Micromagnetic Simulation and X-ray Microscopy of Field- and Current-Induced Magnetization Dynamics in Ferromagnetic Nanostructures

Dissertation
zur Erlangung des Doktorgrades
des Departments Physik
der Universität Hamburg

vorgelegt von
Markus-Andreas Bolte
aus
Henstedt-Ulzburg

Hamburg, 2007

Gutachter der Dissertation: Professor Dr. Ulrich Merkt
Professor Dr.-Ing. Dietmar P. F. Möller
Professor Hans-Christoph Siegmann

Gutachter der Disputation: Professor Dr. Ulrich Merkt
Professor Dr. Detlef Heitmann

Datum der Disputation: 31. Oktober 2007
Vorsitzender des Prüfungsausschusses: Professor Dr. Alexander Lichtenstein

Vorsitzender des Promotionsausschusses: Professor Dr. Günter Huber

Dekan der MIN-Fakultät: Professor Dr. Arno Frühwald

To my dear wife Shimara, my very best friend and the joy of my life,

and our wonderful children Jonathan, Talitha, Lilianne, and Celesta.

To my parents who have implanted in me the love for learning,
and to Him who always inspired and guided me.

Abstract

This thesis deals with the static and dynamic properties of nano- and micrometer-sized ferromagnets in interaction with time-dependent electric currents and magnetic fields studied by micromagnetic simulation, magnetoresistance measurements, and X-ray microscopy. First equilibrium magnetization configurations of iron, nickel and permalloy microelements in arrays were studied depending on inter-element distance, film thickness, as well as strength and direction of applied magnetic fields. The magnetization dynamics of thin permalloy squares in response to nanosecond short magnetic field pulses was then investigated with an enhanced micromagnetic simulation code, and the extracted spin-wave spectrum was compared to current theories of spin-wave eigenmodes. The magnetic eigenmodes of a thin permalloy platelet to periodic field excitation were also studied by micromagnetic simulation and compared to X-ray microscopy data. Then I investigated the influence of the local magnetization on the electric current by means of micromagnetic simulations and measurements of the anisotropic magnetoresistance (AMR) effect. These studies were done by comparing measured AMR signals to those from micromagnetic simulations as well as performing AMR measurements and X-ray microscopy simultaneously on the same samples. Finally, these topics and techniques are brought together in a study of the magnetization changes in permalloy wires and rectangles due to spin-polarized currents and magnetic fields. Domain-wall oscillations driven by spin-polarized ac-currents and the interaction of nanosecond current pulses with domain walls were investigated numerically and by X-ray microscopy. Time- and phase resolving X-ray microscopy and micromagnetic simulations were used to study the dynamics of magnetic vortices and antivortices driven by ac-currents and magnetic fields.

This thesis encompasses the work of several people from different research groups through a number of collaborations. In the individual chapters I focussed on my contributions within these collaborations from the work of the other members. However, as the nature and beauty of scientific collaborations is the mutual sharing and learning that is beneficial and inspiring for all participants, it is impossible to fully isolate my part from the final results. In the individual chapters of this thesis I nevertheless tried to clarify my contributions.

Kurzfassung

Diese Arbeit behandelt die statischen und dynamischen Eigenschaften von Nano- und Mikrometer-großen Ferromagneten in Wechselwirkung mit zeitabhängigen Strömen und Magnetfeldern. Die Untersuchungen wurden mit Hilfe von mikromagnetischen Simulationen, Magnetowiderstandsmessungen und Röntgenmikroskopie durchgeführt.

Zunächst wurden die magnetischen Grundzustände von Eisen, Nickel und Permalloy-Mikroelementen in Arrays in Abhängigkeit von Abstand, Filmdicke sowie Stärke und Richtung des externen Feldes untersucht. Die Magnetisierungsdynamik dünner Permalloy-Quadrate, die durch Nanosekunden-Magnetfeldpulse angeregt wurden, wurde dann mit Hilfe mikromagnetischer Simulations studiert. Das sich ergebende Spinwellenspektrum wurde mit aktuellen Theorien verglichen. Die magnetischen Eigenmoden in dünnen Permalloy-Plättchen, die durch periodische Anregung entstehen, wurden ebenfalls simuliert und mit Röntgenmikroskopie-Daten verglichen. Dann habe ich den Einfluß der lokalen Magnetisierung auf elektrische Ströme mit Hilfe von Simulationen und Messungen des Anisotropen Magnetowiderstands (AMR) sowie durch gleichzeitige Detektion des AMRs und der Domänenstruktur durch Röntgenmikroskopie untersucht. Schließlich wurden alle Themen und Meßmethoden zusammengeführt, um die Magnetisierungsänderungen durch spin-polarisierte Ströme und Magnetfelder zu bestimmen. Domänenwand-Oszillationen durch spin-polarisierte ac-Ströme und der Einfluß von Nanosekunden-Strompulsen auf Domänenwände wurden numerisch und mit Hilfe von Röntgenmikroskopie untersucht. Zeit- und phasen-auflösende Röntgenmikroskopie und mikromagnetische Simulationen halfen, die Dynamik von strom- und feldgetriebenen magnetischen Vortizes und Antivortizes zu verstehen.

Diese Arbeit ist in Zusammenarbeit mit vielen Wissenschaftlern aus mehreren Forschungsgruppen entstanden. In den einzelnen Kapiteln habe ich mich auf meinen Beitrag in diesen Kollaborationen konzentriert. Es liegt jedoch in der Natur und im Zweck der Sache begründet, dass gegenseitiges Mitteilen und Lernen zu einer Vermischung von Gedankengut führen. Deshalb ist es oft nicht möglich, eine vollständige Trennung der Beiträge durchzuführen. In den einzelnen Kapiteln habe ich mich dennoch bemüht, die einzelnen Beiträge zu trennen.

Contents

1 Introduction

Even though magnetism has been known to mankind for more than two millenia, it still holds exciting surprises today. In fact, due to the applications like touchless magnetic sensors, ultra-dense magnetic data storage, and permanent magnets in motors and generators, ferromagnetic systems enjoy an unprecedented popularity, and each household owns literally dozens of them. Research on the origin and behavior of magnetism in ferromagnetic materials under external influences such as temperature, stress, pressure, magnetic fields, electric currents, etc. is currently one of the most active fields in solid state physics. The development of semiconductor-based computers and mass data storage via magnetic harddisk media have profoundly changed the world in which we live. Directly they have brought forth new technologies such as the internet, mobile telephony, digital photography, digital video, and many others. Indirectly, they have spawned the rise of countless innovations through the millionfold increase in computing power and storage capacity over the last fifty years. Without the help of computers to solve complex calculations or to simulate the behavior of new materials and designs, space flight, decisive advances in physics [1, 2, 3, 4], chemistry [5], medicine [6], and material science [7], to just name a few, would have been impossible. In fact, the advances in all technologies of the last decades, also in the semiconductor and magnetic storage technology themselves, would not have been possible without the increasing ability to model and simulate complex physical systems with the advent of computer-aided hardware design (CAD) [8] and the ability to store vast amounts of data.

Magnetic data storage constitute the "memory of humanity". Everything from vital records over personal memories like photos, correspondence, and videos to trivial data such as consumer or internet statistics and spam emails is nowadays stored digitally on these media. The millionfold increase in storage capacity has reduced the size of one bit to less than one-thousandth of the width of a hair, and the total capacity of all the magnetic storage now amounts to a staggering sum of 166 exabytes (10^{18} bytes)[9]. This represents 6 tons of paper per person on this planet. It is estimated that this number will increase sixfold to almost one zetabyte (10^{21} bytes) by 2010. Hitachi Global Storage Technologies, for example, has recently started to sell harddisks with a capacity over 1 Terabyte (10^{12}

bytes) each [10]. The harddisk industry's goal is to produce magnetic storage devices with an areal storage density of 1 Terabit per square inch (Tb/in^2) by 2010 with an average bit size of 25 nm in diameter. In order to constantly expand the limits of what is possible required the ingenuity of corps of engineers but also fundamentally new storage paradigms. For example, the newest development that led to the 1 Terabyte harddisk was to store the information in vertical bits instead of horizontally on the surface. This paradigm is called *perpendicular recording* [11]. The next major advance will likely require that bits are no longer written on continuous magnetic films, but in very small separate magnetic islands - in so-called *bit patterned media* [12]. But is has been shown that the maximum storage capacity of bit patterned media is limited, both by the *superparamagnetic effect* as well as by limits in switching speeds to about 5 Tb/in^2 [13].

New approaches are needed to continue the current increase of 40% more storage capacity per year and thus satisfy the ever-growing demand for storage space. Over the past years, new magnetic storage concepts have been suggested, such as the magnetic bubble memory [14, 15], magnetic random access memory devices (MRAM) [16], the magnetic domain-wall storage devices [17] or the *magnetic racetrack memory* [18]. Some even suggested to use magnetic cells as basic computation units to unite data storage and computation unit and create new computer architecture concepts [17, 19, 20, 21]. While bubble memory and MRAM devices have been and are being delivered to serve in niche markets, the other technologies are still in earlier stages of research and development in which the underlying physics is yet to be understood to the degree that reliable storage applications can be implemented.

Recently, one key discovery was made that could change the way magnetic storage media are conceptualized. It was discovered that spin-polarized electric currents can alter the magnetization of MRAM cells [22, 23] as well as move magnetic domain walls forward [24, 25, 26, 27, 28, 29]. In this way MRAMs could be made much smaller and thus potentially compete with current volatile storage technologies such as DRAM or SRAM. This would make the main memory of a computer non-volatile and could lead to many new hardware architectures. On the other hand, magnetic domain walls could be moved by these currents in threedimensional arrays of ferromagnetic stripes and increase the storage capacity by many times. Despite the intense research on current-induced magnetization switching and domain-wall motion, or *spin-transfer torque*, as the underlying mechanism is called, much of the exact physics remains unknown. For example, it is currently hotly debated how fast current-induced domain-wall motion can be [30, 31, 28, 32] and if the motion is continuous or stochastic. Also, the influence of time dependent electric currents and magnetic fields on the magnetization is under intense investigation. The latter topic is closely related to the magnetic system's inherent dynamic states, its eigenmodes [33]. This thesis deals with the static and dynamic behavior of nano- and micrometer-sized ferromagnets in interaction with time-dependent electric currents and magnetic fields. The fundamental concepts of magnetism are explained in Chapter2 along with two models that allow to numerically simulate the dynamic behavior of nanomagnets. This chapter also expounds on the interaction between electric currents and the local magnetization, namely magnetoresistance and spin-transfer torque. In Chapter3 I introduce the methods used to obtain the results presented in this thesis. These methods are micromagnetic simulation, magnetoresistance measurements, and X-ray microscopy. The results constitute work in a research field that was new for our group and were obtained in collaboration with other groups from the University of Hamburg, the Johann-Gutenberg University of Mainz, the Technical University of Kaiserslautern, the Advanced Light Source in Berkeley, USA, the Chungbuk National University, South Korea, the Max-Planck Institute of Metal Research, Stuttgart, and Ghent University, Belgium. Since the work developped towards the final field of current-induced magnetization dynamics, I will also present the results from intermediate topics categorized into four sections as follows:

In Section 4.1 I investigate the magnetic interaction between ferromagnetic elements in dot arrays to study the minimum distance between magnetic storage cells. In Section 4.2 the dynamics of such elements due to pulsed or periodic field excitations was studied with the help of micromagnetic simulations. The effect of the magnetization on an electric current was examined in Section 4.3. Finally, in Section 4.4 I combined the experience gained in the previous experiments to study current-induced domain-wall motion and magnetic vortex and antivortex rotation. As far as the results have been published in scientific journals, they are reprinted with permission from the corresponding publishers. Some parts of the thesis have not been published yet and will therefore be included in this thesis in more detail.

In Chapter 5 I will give an outlook on ongoing and future projects that could be done based on this thesis, and in Chapter 6 the published journal articles, conference contributions, and invited talks are listed.

2 Theoretical Concepts

2.1 Magnetism

The earliest references of magnetism are from the 6^{th} century BC Greek philosopher Thales of Milet mentioning that lodestone (now known as magnetite - Fe_3O_4) attracts iron. The name is thought to come from the Magnesia region in today's Turkey where this magnetic ore is found. The Chinese scientist Shen Kuo (1031-1095 AD) invented the compass when he described that small iron needles would align to the earth's magnetic field [34]. Much later, in the early 19^{th} century AD, scientific research on magnetism began with the discovery of Hans Christian Oersted that an electric current influences a compass needle. Ampére later quantified the strength of the influence in a mathematical equation. This and other relations were unified by James C. Maxwell into the four Maxwell equations that macroscopically describe the static and dynamic interactions of electric charges, fields, and currents with magnetic fields.

The magnetic properties of matter can be classified by its susceptibility χ to a magnetic field $\mathbf{H}$. The magnetization

$$\mathbf{M} = \mathbf{m}\frac{N}{V} = \chi \cdot \mathbf{H} \tag{2.1}$$

is defined as the dipole moment $\mathbf{m}$ per unit volume V. For negative χ, the material is called *diamagnetic*, for small positive χ, one speaks of *paramagnets*, and when a field induces strong magnetic moments ($\chi \gg 1$) the material is called a ferromagnet. The overall susceptibility of a material is the sum of all susceptibilities

$$\chi = \chi_{dia} + \chi_{para} + \chi_{ferro} + \dots . \tag{2.2}$$

As the Maxwell equations are normally given for the magnetic induction $\mathbf{B}$, the relation

$$\mathbf{B} = \mu_0 \ (\mathbf{H} + \mathbf{M}) = \mu_0 \ \mu_r \mathbf{H} \tag{2.3}$$

with the magnetic permeability $\mu_r = 1 + \chi$ is also defined.[1]

---

[1] There exists a great confusion in the magnetism community as to the units of magnetic properties [35]. This text uses the SI units as suggested by Hubert and Schäfer [36]. Thus the magnetization of a body and the magnetic field strength are given in A/m.

2.1.1 Diamagnetism

In analogy to Lenz' rule the diamagnetism acts against its driving field. Electrons on a circular orbit of radius r around the nucleus are equivalent to a current loop and thus to a magnetic moment

$$|\mathbf{m}| = \pi r^2 \frac{q}{T} = -\pi r^2 \frac{Ze\omega}{2\pi} = -\frac{1}{2} Zer^2 \omega. \tag{2.4}$$

Here q=-Ze is the charge of the electrons and T the period. When subject to a magnetic field, the rotation frequency is the Larmor frequency $\omega_L = \frac{eB}{2m_e}$, and we use the quantum mechanical square mean distance to the nucleus $\frac{2}{3}\bar{r}^2$ (for spherical symmetry). Thus the susceptibility is

$$\chi_{dia} = -\frac{\mu_0 N Z e^2 \overline{r^2}}{6 m_e V} \propto -Z\overline{r^2} < 0. \tag{2.5}$$

This relation is valid to good extent, e.g., for nobel gases [37] where $\chi \approx -10^{-6}\ Z$ is proportional to the atomic number Z. Every material has a diamagnetic term to its susceptibility since a magnetic field always induces circular motion of electrons, but in general its contribution to the total susceptibility is small in comparison to the other terms. In some cases the diamagnetism is so strong that the induced current completely cancels the applied magnetic field, i.e., $\chi = -1$. This is true for superconductors in which electrons with opposite spin and k-vector couple via interaction with the atomic lattice to a current that suffers no measurable resistance [38]. The current remains after the field is switched off, and the superconductor emanates a magnetic field up the critical magnetic field (Meissner-Ochsenfeld-effect).

2.1.2 Paramagnetism

Paramagnetism is a material's tendency to align its existing magnetic moments parallel to a magnetic field to reduce the Zeeman energy. The susceptibility of paramagnets is usually in the order of 10^{-3} to 10^{-5}. Depending on the electronic band structure of the material the origin of paramagnetism is described by either the Pauli model or the Langevin model.

The Langevin model

According to the Langevin model for materials with non-interacting localized spins the net magnetic moment of each atom is randomly distributed due to thermal excitation over the surface of a unit sphere. An external magnetic field brings an alignment of the magnetic moments proportional to the field strength (see Figure 2.1). Hence the susceptibility

χ_{para} is positive. For increasing temperatures T the alignment lessens according to the Curie law

$$\chi_{para,L} = \frac{C}{T} \tag{2.6}$$

where C is the material dependent Curie constant.

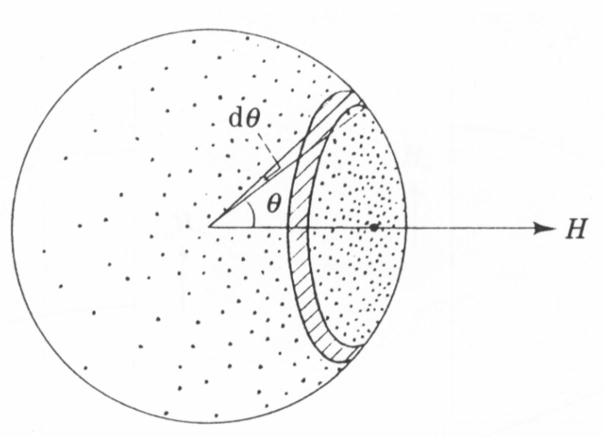

Fig. 2.1: Sketch of the alignment of the magnetic moment in a paramagnet (dots on a sphere) due to an external field. From Ref. [39].

The Pauli model

The Pauli model is true for materials with free electrons in a conduction band. This is valid for most paramagnetic materials. An external magnetic field causes a spin-dependent shift in the density of states proportional to the field strength. The difference in the occupied states is equal to the magnetic moments aligned parallel to the field. The temperature dependence of this type of paramagnetism is due to the changes in the band structure; therefore the Curie law (Eqn. 2.6) is generally not valid for Pauli paramagnets.

2.1.3 Ferromagnetism

Ferromagnetism is the form of magnetism that is most familiar to man. In a ferromagnet the magnetic moments align even without an external field. The susceptibility χ_{ferro} is not a constant, but depends on the history of the magnet. Strong fields can completely align all magnetic moments in a ferromagnet. Then the strength of the magnetization $\mathbf{M}$ assumes its maximum value which is called the *saturation magnetization* M_s, a material and temperature dependent macroscopic parameter. If the field is reduced, some moments relax into other directions while the others remain aligned, reducing the magnetization to the *remanence magnetization* M_r. If a field in reverse direction is applied, the magnetization slowly realigns itself to the field. At a field strength called the *coercive field* H_c half the magnetic moments have switched from their original direction. At negative saturation, all magnetic moments have switched from their original direction. A sufficiently strong field in the original direction will close the so-called *hysteresis* loop. Figure 2.2 shows an exemplary hysteresis loop. Knowledge of a ferromagnet's hysteretic behavior reveals many of its magnetic properties. For example, the area within the hysteresis is equal to the energy needed to switch the ferromagnet or stored in the ferromagnet.

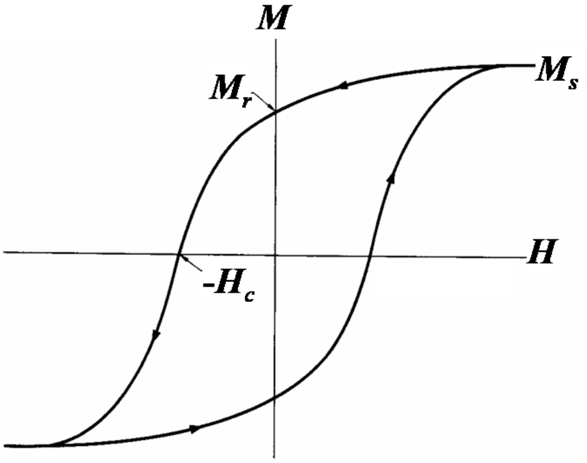

Fig. 2.2: Exemplary hysteresis of a ferromagnetic material. From Ref. [39].

The saturation magnetization is temperature dependent because thermal fluctuation competes against the alignment of the magnetic moments. If a critical temperature, known as the *Curie temperature* T_C, is exceeded, all moments point in arbitrary directions. The ferromagnet behaves as a paramagnet, in other words:

$$\chi = \frac{C}{T - T_C}, \tag{2.7}$$

for $T > T_C$.

Origin of Ferromagnetism

The paramagnetic behavior of ferromagnets above the Curie temperature was found by Pierre Weiss [40] in 1907 when he used a mean-field approximation to explain the strong interaction that constitutes ferromagnetism. He proposed that a strong magnetic field, called the *molecular field, mean field,* or *exchange field*, caused by the magnetic moments themselves act on their nearest neighbors. This field should be much stronger than the dipolar field of the magnetic moments and would cause the moments to co-align. This model explained many phenomena such as the formation of magnetic *domains*, regions in a ferromagnet having the same magnetization direction, and domain walls, the transitions between different domains. It could also give a reasonable estimate for the Curie temperature. However, a closer examination showed that the temperature dependent saturation magnetization below T_c could not be satisfactorily explained by a classical approach [37]. To explain the origin of ferromagnetism, one needs to understand some fundamentals of quantum mechanics. In quantum mechanics, any particle is described by a *wave function* $\Psi(\mathbf{r},t)$ with the following properties:

- The particle's location in space cannot be exactly defined, rather, there is a probability density
$$\Psi^*(\mathbf{r},t)\cdot\Psi(\mathbf{r},t)\,dV \tag{2.8}$$
that the particle is within the volume element dV.

- The wave function can be decomposed into a spatially dependent part and a spin-dependent part
$$\Psi(\mathbf{r},t,\sigma)=\psi(\mathbf{r},t)\cdot\sigma,\text{with } \sigma=\langle\downarrow,\uparrow\rangle\,. \tag{2.9}$$

- As electrons are fermions, the wave function for electrons is antisymmetric, i.e.,
$$\Psi(q_1,q_2)=-\Psi(q_2,q_1)\,. \tag{2.10}$$

Here q denote the space and spin coordinates of an electron. This means that two electrons with all quantum numbers being the same cannot occupy the same single-particle state at the same time. If the space function $\psi(\mathbf{r},t)$ is symmetric, the spin function σ must be antisymmetric and vice versa.

A measurable quantity or *observable* is computed by calculating the expectation value of the corresponding operator. For example, to calculate the energy of an electron, this is done by
$$\langle E\rangle=\int\Psi^*\hat{\mathbf{H}}\Psi dV, \tag{2.11}$$
where $\hat{H}$ is the Hamilton operator of a free electron in a potential
$$\hat{\mathbf{H}}=\frac{(-i\hbar\nabla)^2}{2m_e}+V(\mathbf{r},t)\,. \tag{2.12}$$

Here the first term describes the kinetic energy of the electron as given by the momentum operator $-i\hbar\nabla$ and the potential energy $V(\mathbf{r},t)$. To determine whether a system of many electrons is ferromagnetic, one needs to calculate if the energies are lower for symmetric (parallel spins) or for antisymmetric (antiparallel spins) spins. The energetic difference between the parallel or antiparallel configurations of spins $\mathbf{S_i}$ and $\mathbf{S_j}$ is called the *exchange integral* J_{ij}. It is positive for ferromagnets and negative for antiferromagnets. According to Heisenberg, the ferromagnetic energy is determined by the Hamiltonian of the exchange interaction (see Section 2.2.1)

$$\hat{\mathbf{H}}_{exch} = -\sum J_{ij}\mathbf{S}_i \cdot \mathbf{S}_j. \tag{2.13}$$

Band-Ferromagnetism

To compute the energies of a crystalline solid, it is practical to resort to models such as the *tight binding model* or the *free electron gas model* [37]. In metals *itinerant electrons* are not localized at specific atoms but can freely move throughout the crystal lattice. According to the free electron gas model, the electrons at the Fermi energy can experience a spontaneous band splitting even without an external magnetic field if the resulting loss in potential energy is higher than the increase in kinetic energy (see Fig. 2.3). The increase in kinetic energy

$$\Delta E_{kin} = \frac{1}{2} g\left(E_\mathrm{F}\right)\delta E^2 \tag{2.14}$$

comes about as $\frac{1}{2}g\left(E_\mathrm{F}\right)\delta E$ electrons below the Fermi energy of one spin band are moved by δE above the Fermi energy of the other spin band. $g\left(E_\mathrm{F}\right)$ is the *density of states* at the Fermi energy. This leads to a spin-dependent electron density for each spin band of $n_{\downarrow,\uparrow} = \frac{1}{2}n\left(1 \pm g\left(E_\mathrm{F}\right)\delta E\right)$ and a magnetization $M = \mu_\mathrm{B}\left(n_\downarrow - n_\uparrow\right) = \mu_\mathrm{B} g\left(E_\mathrm{F}\right)\delta E$. $\mu_\mathrm{B} = \frac{e\hbar}{2m_e} = 9.27 \cdot 10^{-27}$J/T is the Bohr magneton. The potential energy decreases due to a parallel alignment of an electron's magnetic moment to the magnetic mean field λdM and forms a positive feed-back. The more electrons are aligned the stronger is the mean field

$$\begin{aligned} \Delta E_{pot} &= -\int \mu_0 M \lambda dM = -\tfrac{1}{2}\mu_0\lambda M^2 \\ &= -\tfrac{1}{2}\mu_0\lambda\mu_\mathrm{B}^2\left(n_\downarrow - n_\uparrow\right)^2 = -\tfrac{1}{2}U\left(g\left(E_\mathrm{F}\right)\delta E\right)^2. \end{aligned} \tag{2.15}$$

with $U = \mu_0\lambda\mu_\mathrm{B}^2$, the *Stoner exchange integral.* Spontaneous ferromagnetism occurs when $\Delta E_{tot} = \Delta E_{kin} + \Delta E_{pot} = \frac{1}{2}g\left(E_\mathrm{F}\right)\delta E^2\left(1 - Ug\left(E_\mathrm{F}\right)\right) \leq 0$ or

$$Ug\left(E_\mathrm{F}\right) \geq 1 \tag{2.16}$$

This is the so-called *Stoner criterion* for ferromagnetism. It turns out that the only ferromagnetic elements at room temperature are iron, cobalt, and nickel [37].

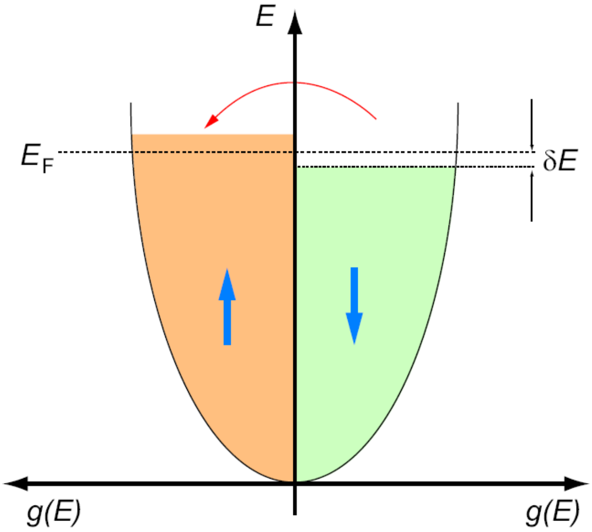

Fig. 2.3: Spontaneous band splitting for up- and down-spins without an external field. From [41].

2.2 Micromagnetic theory

The computation of the energies of even the smallest magnetic systems with quantum mechanical methods requires approximations and is limited in the number of atoms or cells that can be computed in reasonable time. The micromagnetic theory simplifies the exact quantum mechanical model by using standard material parameters such as the exchange integral J_{ij} and the saturation magnetization M_s as spatially continuous scalar functions. The magnetization $\mathbf{M}$ and the magnetic field $\mathbf{H}$ are spatially continuous vector functions. The micromagnetic model describes the magnetic behavior of ferromagnetic systems on the nano- and micrometer scale. It can correctly model the static structure of ferromagnets, the formation of magnetic domains and domain walls, but also the dynamics up to the THz-regime, the magnetic hysteresis, the switching of small magnetic grains, etc. In 1935, Landau and Lifshitz [42] laid the foundation to this theory, with major contributions also coming from Gilbert [43], Néel [44], Bloch [45], Brown [46], and many others. Several excellent reviews and books [47, 36, 48] describe this theory in great detail.

2.2.1 Magnetic fields and energies

There are four important contributions to the Gibbs free energy of a ferromagnetic body: The exchange energy, the demagnetization energy, the crystalline anisotropy energy, and the energy due to an external magnetic field, the Zeeman energy. All magnetic interactions can be written as a magnetic field interacting with local magnetic moments, even though the origins of the fields differ. For example, the exchange interaction as already mentioned is of quantum mechanical nature, but can be described by the mean field mentioned in Section 2.1.3. The interactions are briefly explained in the following sections.

The relation between a magnetic field due to an interaction and its energy is generally given by

$$E = -\int \mu_0 \, \mathbf{M} \cdot \mathbf{H} dV. \tag{2.17}$$

In the simplest way the field can be seen as an external magnetic field, also called Zeeman field, e.g., from a magnetic coil or from the write head of a magnetic hard drive. The field is potentially inhomogeneous in space and can alter over time. Sometimes it is easier to calculate the interaction energy first. Following the definition of the Gibbs free energy, the corresponding field is then

$$\mathbf{H} = -\left(\frac{\partial E}{\mu_0 \, \partial \mathbf{M}}\right). \tag{2.18}$$

Exchange energy

The exchange integral J_{ij} introduced in Section 2.1.3 vanishes rapidly with increasing distance between the atoms i and j so that normally only the nearest neighboring atoms have to be taken into account in Eqn. 2.13 to calculate the exchange energy

$$E_{exch} = -\sum_{NN} J_{ij} \, \mathbf{S_i} \cdot \, \mathbf{S_j}. \tag{2.19}$$

Approximating the cosine of the scalar product by its Taylor series up to second order and using the magnetization $\mathbf{M}$ instead of the spin, one arrives at

$$E_{exch} = \int \frac{A}{M_S^2} \left(\left(\frac{\partial \mathbf{M}}{\partial \, x}\right)^2 + \left(\frac{\partial \mathbf{M}}{\partial \, y}\right)^2 + \left(\frac{\partial \mathbf{M}}{\partial \, z}\right)^2 \right) dV, \tag{2.20}$$

with material dependent *exchange constant* $A = \frac{c}{a_0} J S^2$ where a_0 is the lattice constant and $c \in \{1,2,4\}$ describes the lattice symmetry (*sc*, *bcc*, and *fcc*, respectively). Using Eqn. (2.18) and some vector analysis, one finds that the interaction between the electron spins of neighboring atoms can be mimicked by a magnetic field of the strength

$$H_{exch} = \frac{2A}{\mu_0 M_S^2} \, \nabla^2 \mathbf{M}. \tag{2.21}$$

Demagnetizing energy

Magnetic moments interact also via their magnetic fields. With the Maxwell equations in the absence of electric field and currents $\nabla \cdot \mathbf{B} = 0$ and $\nabla \times \mathbf{H} = 0$ the field in a magnetized body can be written as

$$\mathbf{H} = -\nabla \Phi_m, \tag{2.22}$$

with the scalar potential determined by the magnetization [49]

$$\Phi_m(\mathbf{r}) = \frac{1}{4\pi} \int \mathbf{M}(\mathbf{r}') \cdot \nabla' \left(\frac{1}{|\mathbf{r} - \mathbf{r}'|} \right) dV'. \tag{2.23}$$

For uniformly magnetized bodies $\mathbf{H}$ can be defined as

$$\mathbf{H} = -\mathbf{M} \cdot \hat{\mathbf{N}}, \tag{2.24}$$

where $\hat{\mathbf{N}}$ is the demagnetization tensor with the elements

$$\mathbf{N}_{ij} = \frac{1}{4\pi V} \int_V dV \int_{V'} \nabla_i' \nabla_j' \left(\frac{1}{|\mathbf{r} - \mathbf{r}'|} \right) dV'. \tag{2.25}$$

$\hat{\mathbf{N}}$ is symmetric and its trace is one if V and V' are identical. The trace is zero if V and V' are dissimilar. For highly symmetric bodies such as ellipsoids there exist analytical solutions for $\hat{\mathbf{N}}$ [47, 36]. For example, a sphere has tensor elements $N_{ii} = \frac{1}{3}$ for all symmetry axes, while for an elongated ellipsoid (thin wire), $N_{ii} = 1$ in the direction of the long axis and zero in the direction of the other axes. This means that due to the demagnetizing field, the magnetization tends to align itself parallel to any surfaces. This is easy to understand: Any magnetization vector pointing out of a surface leads to magnetic charges that are the origin for a magnetic field, in analogy to the electric field in a capacitor. The energy contained in this magnetic field increases the energy of the ferromagnet. For general bodies a numerical solution was derived by Newell *et al.* [50, 51]. The demagnetizing energy is found by inserting Eqn.2.24 into Eqn.2.17:

$$E_{demag} = -\frac{\mu_0}{2} \mathbf{M} \cdot \hat{\mathbf{N}} \cdot \mathbf{M}' V \tag{2.26}$$

Here, $\mathbf{M}$ and $\mathbf{M}'$ are the magnetization vectors of two disjoint volumes V and V'.

Anisotropy Energy

Equation 2.19 assumes that the spins are localized classical spins. However, the electrons' positions are not defined with arbitrary exactness, rather they are situated in orbitals that surround the nuclei. Through spin-orbit interaction, the orbits for 3d-electrons that constitute the magnetization in typical ferromagnets are anisotropic. One usually defines a preferred direction of the electron spins due to the crystal structure of the ferromagnet called the *easy axis* of the magnetization. For materials with hexagonal atomic lattices such as cobalt, there is one easy axis (*uniaxial anisotropy*), for iron and nickel there are three (*cubic anisotropy*). An extra energy term can be defined that corrects the exchange energy. For uniaxial anisotropy the term is written as a Taylor series up to first order as

$$E_{Aniso} = \int K_1 sin^2 \theta dV, \tag{2.27}$$

where θ is the angle between the magnetization and the easy axis. In Section 2.3 the anisotropy is used to define a simple model for the switching behavior of single-domain ferromagnets. Section 2.5.2 describes how the anisotropy can cause an angle-dependent change in magnetoresistance.

Zeeman Energy

The Zeeman field is the field an experimentator can use to purposely alter the magnetization. It is the superposition of all (temporally and spatially varying) external fields. The Zeeman energy can be calculated by Eqn. 2.17.

2.2.2 Equation of motion

From Eqns. 2.21, 2.24, and the Zeeman field, an effective field can be defined at every point in a magnetic body:

$$\mathbf{H}_{eff} = \frac{2A}{\mu_0 M_S^2} \nabla^2 \mathbf{M} - \mathbf{M} \cdot \hat{\mathbf{N}} + \mathbf{H}_{ext} \tag{2.28}$$

For parallel alignment of $\mathbf{M}$ and $\mathbf{H}_{eff}$, i.e., $\mathbf{M} \times \mathbf{H}_{eff} = 0$, the energy of the ferromagnet is minimal. This criterion for equilibrium is known as Brown's equation [46]. If, due to sudden changes in the effective field, the magnetization is no longer parallel to $\mathbf{H}_{eff}$, a torque $\mathbf{L} = \mathbf{M} \times \mathbf{H}_{eff}$ acts on the magnetization and causes it to precess around $\mathbf{H}_{eff}$. Torque is defined as the change in angular momentum $\mathbf{g}$ over time. The magnetization is linked to $\mathbf{g}$ by the *gyromagnetic ratio* $\gamma = \frac{\mu_0 g|e|}{2m_e} = 2.21 \cdot 10^5$ m/As, where $g \approx 2$ is the Landé factor of the free electron. This leads to

$$\frac{d\mathbf{M}}{dt} = -\gamma \mathbf{M} \times \mathbf{H}_{ext} \tag{2.29}$$

The magnetization $\mathbf{M}$ precesses around the local magnetic field $\mathbf{H}_{eff}$ with the Larmor frequency $\omega_{\mathrm{L}} = \gamma \mathbf{H}_{eff}$. It is clear that the precession cannot continue for infinitely long times. The magnetic energy stored in the precession angle dissipates through interaction

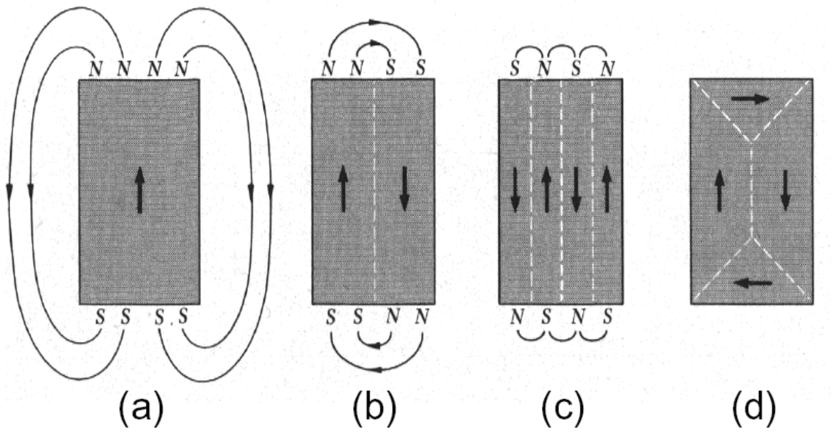

Fig. 2.4: Formation of domains reduces the magnetic stray field. From left to right, the demagnetizing energy is reduced by the formation of domains, especially by closure domains. Modified from Ref.[36].

of the magnetization with the crystal lattice. The magnetization is damped towards equilibrium which is parallel to the effective field. A damping term was originally added into Eqn. 2.29 with a phenomenological damping parameter called *Gilbert damping* α to form the *Landau-Lifshitz equation* [42, 43, 46]

$$\frac{d\mathbf{M}}{dt} = -|\gamma|\mathbf{M}\times\mathbf{H}_{eff} - \frac{|\gamma|\alpha}{M_S}\mathbf{M}\times\left(\mathbf{M}\times\mathbf{H}_{eff}\right). \tag{2.30}$$

The microscopic origin of this damping is still subject of research. Spin-orbit-interaction [52], phonon-mediated spin-flip scattering [53], and magnon-magnon interaction [54] have been proposed as contributors to intrinsic damping.

2.2.3 Domain walls

The energy terms mentioned in Section 2.2.1 act differently on the magnetization. Depending on the material and the geometry of a ferromagnetic body one or the other energy term dominates, leading to different magnetic behavior. While the exchange energy is minimal when all magnetic moments are parallel, the demagnetizing energy is the smallest when the fewest magnetic moments point perpendicular to the surface. For small bodies the exchange energy dominates so that the magnetization is aligned. This state is called the *single-domain limit*. For larger structures it becomes favorable for the magnetization to break down into regions of different magnetization alignment with transition regions called *domain walls*. In this way the magnetic field, also called the *stray field* due to magnetic charges at the surfaces is reduced as depicted in Fig. 2.4. The width of the domain wall is determined by the *exchange length*

$$\lambda = \sqrt{\frac{A}{K_D}} \tag{2.31}$$

where $K_D = \frac{1}{2}\mu_0 N M_S^2$. λ here determines the width of a domain wall in a particular material and is not to be confused with the mean field constant in Section 2.1.3 that was assigned the same symbol. In iron, $\lambda \approx 3.4$ nm, in cobalt $\lambda \approx 4.9$ nm, and in permalloy, $\lambda \approx 5.3$ nm. In the domain wall the magnetization rotates. In thin films the rotation axis depends on the thickness of the film: For thinner films the magnetization rotates around the surface normal because it would be energetically more expensive to create magnetic charges at the surfaces by turning the magnetization out-of-plane. This type of domain wall was first found by Louis Néel [44], hence it is called a *Néel wall* (see Fig. 2.5(a)). The rotation out of-plane costs less exchange energy since the angles between two neighboring spins are smaller than for the in-plane rotation. In thicker films the decrease in exchange energy compensates the increase in demagnetization energy due to surface charges, so that *Bloch walls* [45] (see Fig. 2.5(b)) with out-of-plane magnetization components are predominant. In permalloy ($Ni_{80}Fe_{20}$) of thicknesses between 20 nm and 40 nm Bloch walls appear [55, 56, 57]. For even thicker films, combinations of Néel and Bloch walls are visible. In *asymmetric Bloch walls* [58], the magnetization turns in-plane at the surfaces to reduce the demagnetizing energy and out-of-plane in the films to reduce the exchange energy (see Fig. 2.5(c)). In *cross-tie walls* [59, 60], the Néel-wall-like in-plane rotation at the surfaces changes signs periodically so as to curl around singular points (see Fig. 2.5(d)). These points are called curling Bloch lines or *magnetic vortices* [36]. Half-way between two vortices the magnetization points to and away from singular points to form a magnetization pattern that looks like a cross – hence the name cross-tie wall. These singular points are called cross Bloch lines or *magnetic antivortices*. In the center (*core*) of either vortices or antivortices the exchange energy forces the magnetization out-of-plane. A magnetic (anti-)vortex can be described by the out-of-plane orientation of the magnetization in the core, the *(anti-)vortex polarization*, and the sense of rotation of the in-plane magnetization around the core, called the *chirality*. Recently, vortices have attracted a lot of attention as it was shown that magnetic fields and spin-polarized currents can cause vortices to gyrate around their equilibrium position [61, 62, 63] and even switch their polarization [64, 65]. Our contributions to understanding the dynamics of magnetic vortices and antivortices are presented in Section 4.4.

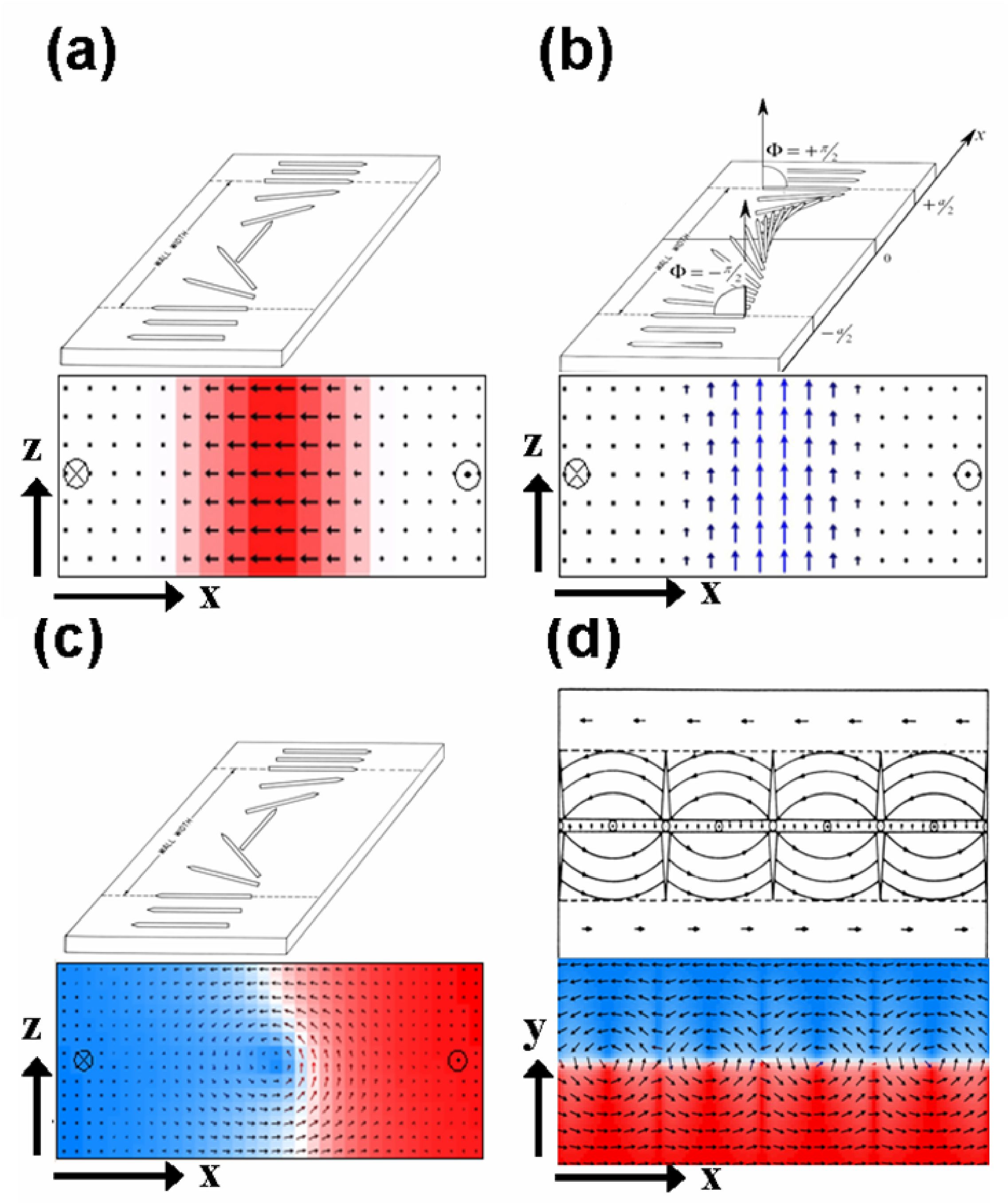

Fig. 2.5: Domain wall types. (a) Néel wall, (b) Bloch wall, (c) asymmetric Bloch wall, and (d) cross-tie wall. Modified from Ref. [36].

2.3 Stoner-Wohlfarth Theory

The domain theory described in the previous section allows the analytical treatment of multi-domain ferromagnets. It is often useful to deal with single-domain particles, e.g., ferromagnetic grains on the surface of a hard disk. The corresponding model has been

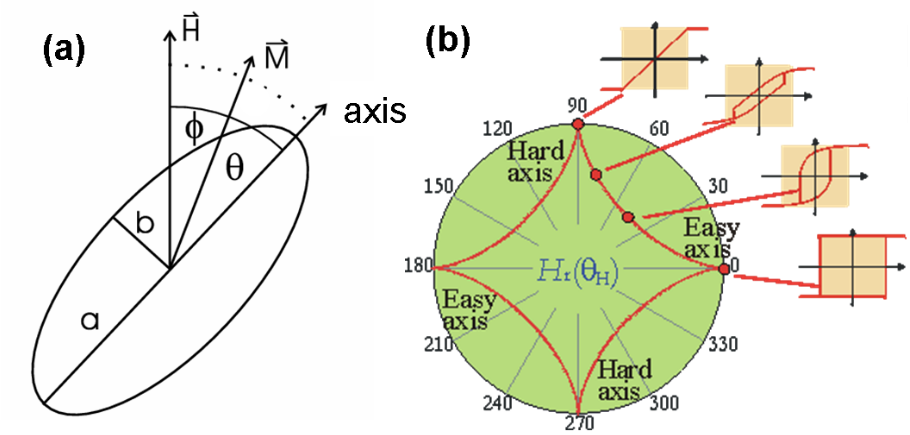

Fig. 2.6: The Stoner-Wohlfarth model. From Ref. [66]. (a) The ferromagnetic particle sketched as an ellipsoid. (b)Stoner-Wohlfarth-asteroid. From Ref. [67].

developed by E. C. Stoner and E. P. Wohlfarth [66]. In the *Stoner-Wohlfarth-model*, the particle has a uniform magnetization and a uniaxial anisotropy so that the particle has two preferred magnetization directions (see Fig. 2.6(a)). With the assumption of uniform magnetization, exchange interaction is assumed to be constant, and the shape or crystal anisotropy competes against an applied magnetic field. With Eqns. 2.27 and 2.17 the energy of the particle is

$$E = K_1 V sin^2\theta - \mu_0 M_S H V cos\phi, \tag{2.32}$$

where θ is the angle between magnetization and easy axis and ϕ the angle between easy axis and applied field. The energy of the particle is minimal when the magnetization is either parallel or antiparallel to the anisotropy axis. The magnetization has to move through the hard axis when switching from one stable state to the other. The energy barrier is calculated by differentiation of Eqn. 2.32 in θ for a set ϕ:

$$E_{Barrier} = K_1 V \left(1 + \left(\frac{H}{H_K}\right)^2\right) \tag{2.33}$$

with the switching field $H_K = \frac{2K_1}{\mu_0 M_S}$. The second derivative in θ for all ϕ yields the region in which a magnetization state has minimal energy. The limiting field, given by $H_{sw} = \left(|H_x|^{\frac{2}{3}} + |H_y|^{\frac{2}{3}}\right)^{\frac{3}{2}}$, forms the so-called *Stoner-Wohlfarth* or *switching asteroid* as shown in Fig. 2.6(b).

2.4 Magnetization Dynamics - Spin Waves

To understand the fundamental nature of spin waves, whose quanta are called *magnons*, we shall begin with spin-$\frac{1}{2}$ moments in a one-dimensional chain with a lattice constant a (*Ising-model*)[68, 37]. As described in Section 2.2.1 and 2.4, the magnetization configuration with minimal energy in a single-domain particle is reached when all magnetic moments are aligned parallel. One might think that the energetically next higher configuration would be with one magnetic moment flipped in opposite direction. Following Eqn. 2.19 that would increase the exchange energy by $\Delta E = 8J_{ij}S^2$. Instead, the minimal change in magnetic moment by $\hbar$ is distributed over all the magnetic moments of the ferromagnet (see Fig. 2.7). The magnetic moments change continuously by precessing around the local effective field to form a complete rotation over the distance L, the extension of the ferromagnet. In this way, the angle between two moments is always very small. The next higher configuration is a change in magnetic moment by two complete rotations and so forth. A wave length $\lambda = \frac{L}{n} = \frac{2\pi}{k}$ can be assigned for the n-th quantized increase in energy. The increase in exchange energy depends on the wave vector $k = \frac{2\pi n}{L}$ and is with $E_n = \left(n+\frac{1}{2}\right)\hbar\omega\left(k\right) = 4J_{ij}S\left(1-cos(ka)\right)$ usually very small. In a three-dimensional ferromagnet, the propagation direction of a spin wave is identified by the normal to the wave front, i.e., magnetic moments having the same phase in their precession. According to the ansatz of Kalinikos and Slavin [69] the magnetization can be written as

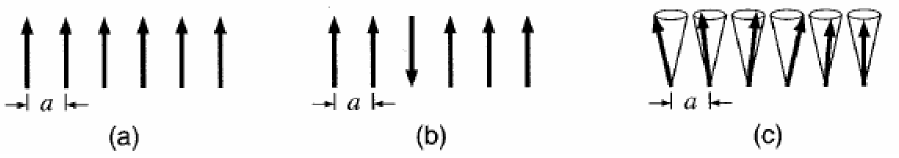

Fig. 2.7: Sketch explaining why the introduction of a magnon requires less energy than switching one magnetic moment. (a) Fully aligned moments, a being the lattice constant. (b) One magnetic moment switched. (c) All magnetic moments turn a little to create a 360° rotation. From Ref. [37].

$$\mathbf{M} = M_s\hat{\mathbf{e}}_\mathbf{z} + \mathbf{m}\left(x,y\right)e^{i\left(k_\zeta\zeta-\omega t\right)}, \tag{2.34}$$

where ζ is the propagation direction of the spin wave. We have here assumed that the magnetization's deviation from the effective field in z-direction is small. The Landau-Lifshitz-Gilbert-equation (Eqn. 2.30) describes the precession of the magnetization. To find the spin-wave dispersion, Kalinikos and Slavin neglected the damping term since

$\alpha \ll 1$ and used the same ansatz for the effective field in Eqn. 2.28 as for the magnetization in Eqn. 2.34 (see also Ref. [70]). With the Rado-Weertman boundary conditions [71, 72] describing the amplitude of $\mathbf{m}$ at the surfaces one can after lengthy calculations derive the general dispersion relation for spin waves in thin films [69]

$$\omega\left(k_\zeta,\varphi\right)=\gamma\left[\left(H+\frac{2A}{M_s}k^2\right)\left(H+\frac{2A}{M_s}k^2+4\pi M_sF_{00}\right)\right]^{\frac{1}{2}}. \tag{2.35}$$

The dipole-dipole matrix elements $F_{00}=1-P_{00}cos^2\left(\varphi\right)+4\pi M_s\frac{P_{00}(1-P_{00})sin^2(\varphi)}{H+\frac{2A}{M_s}k^2}$ take the dipolar field of the magnetic surface charges into account. φ is the angle between the static magnetization and the in-plane component $k_{||}$ of the spin-wave vector, d the thickness, and $P_{00}=1-\frac{1-e^{-k_{||}d}}{k_{||}d}$. Here we have only considered the spin-wave modes that are homogeneous in z-direction, hence the index 0. Higher order modes which occur in films due to a reflection at the surfaces are called *perpendicular standing spin waves (PSSW)*. For bulk-like volumes, Eqn. 2.35 becomes the Herring-Kittel-formula [73]

$$\omega\left(k,\varphi\right)=\gamma\sqrt{\left(H+\lambda_{ex}k^2\right)\left(H+\lambda_{ex}k^2+4\pi M_ssin^2\varphi\right)}. \tag{2.36}$$

In the limit of zero wave number($k=0$) Eqn. 2.36 simplifies to the Kittel-formula for ferromagnetic resonance [74]

$$\omega=\gamma\sqrt{H\left(H+4\pi M_ssin^2\varphi\right)}. \tag{2.37}$$

One can see that the frequency of a spin wave greatly depends on its propagation direction with respect to the static magnetization. For $\varphi=90°$, i.e., spin waves propagating perpendicular to the static magnetization, the dispersion relation has a monotonously increasing slope. These spin waves are historically called *Damon-Eshbach modes* [75] or *magnetostatic surface waves (MSSW)*. Their group velocity is always positive, while the spin waves propagating in the direction of the static magnetization have negative group velocities for small wave vectors, i.e., $k_{||}d<1$. Hence they are called *magnetostatic backward volume waves (MSBVW)*. For higher wave vectors the exchange interaction dominates the dispersion and the group velocity becomes positive.

Recently, a quantization of the spin waves due to their lateral confinement has been observed [76, 77]. It was also shown [78], that an inhomogeneity in the local effective field, e.g., through the demagnetizing field at domain walls or surfaces, would lead to a localization and even trapping of spin waves. In Section 4.2 we will show the influence of the effective field in Landau patterns on the spin-wave dispersion.

2.5 Electronic Transport in Metals

In the presence of an electric field $\mathbf{E}$ the electrons experience the force $\mathbf{F} = -e\mathbf{E}$. In a perfect conductor this would lead to continuous acceleration and thus infinitely high currents. In real conductors the conductance is finite as the electrons interact with lattice oscillations (phonons), impurities, or other electrons. In the Drude-Sommerfeld model of the free electron gas [79, 80] the distance that an electron in a real conductor can travel before it is scattered is expressed by the *mean free path* λ. The conductance electrons are moving at a velocity v_F, the velocity of the electrons at the Fermi energy, $\approx 10^5$ m/s. Thus the average time before an electron is scattered due to the various interactions is given by the *scattering time* $\tau = \lambda / v_F$. The scattering is random so that the average velocity is zero in the absence of an electric field. Due to their negative charge $-e$ electrons in an applied electric field $\mathbf{E}$ move opposite to the direction of the field with a nonzero average velocity called the *drift velocity*

$$\mathbf{v_D} = \frac{e\mathbf{E}}{m}\tau. \tag{2.38}$$

For n_e electrons per unit volume in a conductor, a current density

$$\mathbf{j} = n_e e \mathbf{v_D} = \frac{n_e e^2 \tau}{m}\mathbf{E} \tag{2.39}$$

results. Comparing Eqn. 2.39 to Ohm's law $\mathbf{j} = \sigma\mathbf{E}$ yields the conductance

$$\sigma = \frac{n_e e^2 \tau}{m} \tag{2.40}$$

of a free electron gas in a conducting material. In semiconductors, one often defines the electron (hole) mobility $\mu = \mp e\tau/m$ so that $\sigma = ne\mu$. The resistivity $\rho = 1/\sigma$ is inversely proportional to the mean free path, i.e., $\rho \propto 1/\lambda$. According to the Matthiesen rule the resistivities due to the different scattering mechanisms are added up to obtain the total resistivity of a material. Gold, for example, has a total resistivity of $2.2 \cdot 10^{-8}\Omega$m, while permalloy as a typical ferromagnet has a resistivity of $14 \cdot 10^{-8}\Omega$m. These values can differ depending on the quality of the samples. Williams *et al.* have shown [81] that high sputter rates greatly deteriorate the conductance of thin films as they become more and more inhomogeneous and large clumps of material form with little connecting surfaces.

Thickness-Dependent Conductance

The film thickness also affects the conductance. As first predicted by Fuchs and Sondheimer [82, 83] diffusive scattering occurs at the surfaces of the film in addition to the scattering in the bulk of the film. The model predicts that to first order the resistivity depends on the thickness t as

$$\rho(t) = \rho_0 + \frac{3}{8}\frac{\lambda_0}{t}. \tag{2.41}$$

Here ρ_0 is the total resistivity of bulk material and λ_0 is the total mean free path as given by the Matthiesen rule. The model has been experimentally confirmed in its general correctness [81, 84, 85]. Mayadas and Shatzkes improved the model to include also scattering at grain boundaries [86]. The model yields a homogeneous resistivity and mean free path throughout the thickness of the thin film. However, it has been stated [84] that for a more appropriate description the requirement of a uniform resistivity and mean free path must be dropped. Indeed, in the course of this thesis, we have found experimental indications that the current density in permalloy microelements is inhomogeneous in thickness, resulting in a nonzero average Oersted field caused by a current passing through the permalloy. The methods and results are described in detail in Section. 4.4.

2.5.1 Electronic Transport in Ferromagnets

The above considerations are valid for materials with partially filled conduction bands. In ferromagnets, the density of states for the two spin configurations spin-↑ and spin-↓ are shifted due to the exchange interaction. Following Mott's *two-channel model* [87] the spin-↑ and spin-↓ electrons can be seen as two separate sets of charge carriers with separate transport properties. Hence their transport can be described as occurring through two separate channels. If one of the conduction channels has a lower *scattering rate* τ^{-1} and thus a lower resistivity, its total resistivity is lower. This model is valid as long as the interexchange between the channels is small, i.e., as long as the *spin-diffusion length* $\lambda_{sf} = \sqrt{\frac{\lambda_0 v_F \tau_{sf}}{3}}$ is longer than the electron mean free path λ_0 [88, 89]. Typical values for λ_{sf} in common ferromagnetic transition metals or alloys are 3.3 nm to 5.3 nm in permalloy [90], 45 nm to 60 nm in cobalt [91], and 21 nm in nickel [92].

2.5.2 Magnetoresistance

Magnetic fields applied to a conductor can either lead to an increase of the electric resistance through a localization of the conduction electrons, or to a decrease in resistance. The positive magnetoresistance is due to the Lorentz force that forces the electrons on circular paths and is called *normal magnetoresistance (NMR)*. It is described in more detail in the next paragraph. Examples for negative magnetoresistances are the *anisotropic* *magnetoresistance* (AMR), the *giant magnetoresistance* GMR, and the *tunnel magnetoresistance* TMR which are not explained here.

Normal Magnetoresistance

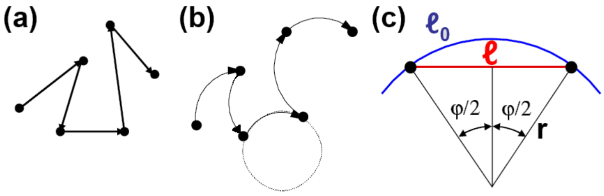

Fig. 2.8: Illustration of the normal magnetoresistance effect. From Ref. [93].

An applied magnetic field $\mathbf{H}$ causes a Lorentz force $\mathbf{F} = -e\mathbf{v} \times \mu_0\mathbf{H}$ on the electrons of a conducting material. Instead of a linear motion between two scattering sites the electrons move on circular paths with the radius $r = v/\omega_c$, where ω_c is the cyclotron frequency $\omega_c = eB/m$ (see Fig. 2.8). The effective mean free path is decreased to the length $\lambda_{eff} = 2r \cdot sin\,(\lambda_0/2r)$ where $\lambda_0 = v_F\tau$ is the mean free path without the magnetic field (see Fig. 2.8(c)). Except for very pure metals or very high magnetic fields the radius is much larger than the mean free path. This means that the sine can approximated by the Taylor series expansion up to third order. This yields the effective mean free path

$$\lambda_{eff} = 2r \cdot \left(\frac{\lambda_0}{2r} - \frac{1}{6} \cdot \frac{\lambda_0^3}{8r^3}\right) = \lambda_0 \left(1 - \frac{1}{24}\tau^2\omega_c^2\right). \tag{2.42}$$

It is reduced by $\frac{1}{24}\tau^2\omega_c^2$. With Eqn. 2.40 and the definitions of ω_c and τ the relative change in resistivity due to the normal magnetoresistance can be written as

$$\frac{\Delta\rho}{\rho_0}_{NMR} \equiv \frac{\rho - \rho_0}{\rho_0} = \frac{1}{24 n_e^2 e}\left(\frac{B}{\rho_0}\right)^2. \tag{2.43}$$

Figure 2.9 shows this parabolic field dependence of the relative resistivity for high magnetic fields.

Anisotropic Magnetoresistance

The *anisotropic magnetoresistance (AMR)* occurs in ferromagnetic materials and describes the dependence of the ferromagnet's resistivity as a function of the angle between the electric current and the magnetization. This effect has been used in magnetic angle and rotation rate sensors and in read heads for magnetic data storage. In the latter application, it has been replaced by read heads utilizing the much more sensitive GMR.

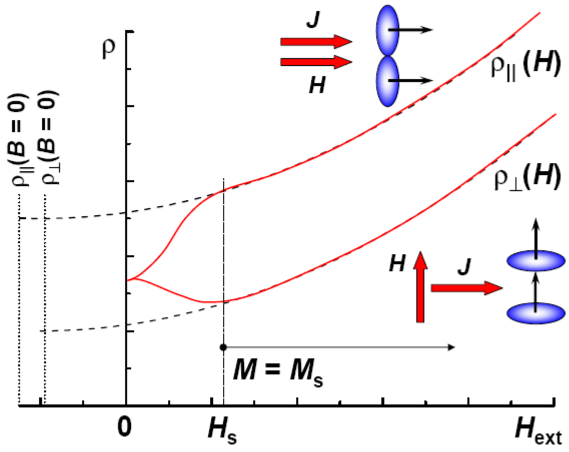

Fig. 2.9: For the explanation of the *anisotropic* and the *normal magnetoresistance*. From Ref. [93].

The AMR is due to the anisotropic distribution of the electronic orbits of the 3d-electrons in ferromagnets [94, 95, 96] that also account for crystal anisotropy (see Section 2.2.1). As the spin direction defines also the symmetry axis of the orbits, a rotation of the spin moments due to an external field causes also a reorientation of the charge densities around the nuclei. This causes a different scattering cross-section for conduction electrons (shown by the blue ellipsoids in Fig. 2.9). When applying a magnetic field to a ferromagnet one measures different resistivities $\rho_{||}$ and $\rho_{\perp}$ whether the field is applied parallel or perpendicular to the electric current. Figure 2.9 shows that for strong fields the normal magnetoresistance (see Section 2.5.2) is dominant while the angle dependent splitting for fields below the saturation field H$_s$ is due to the AMR. To derive the values for $\rho_{||}$ and $\rho_{\perp}$ from measurements one needs to extrapolate the resistivities for vanishing fields as shown in the figure by the dashed lines. The difference between the resistivity $\rho_{||}$ in a perpendicularly aligned magnetic field and the resistivity in a parallel magnetic field $\rho_{\perp}$ in permalloy is typically a few percent at room temperature. With the so-called *spontaneous resistivity anisotropy (SRA)* $\Delta\rho = \rho_{||} - \rho_{\perp}$ and the *average resistivity* $\frac{1}{3}\left(\rho_{||} + 2\rho_{\perp}\right)$ the AMR is defined as

$$\mathbf{AMR} = \frac{\Delta\rho}{\rho_{ave}}\left(cos^2\theta - \frac{1}{3}\right), \tag{2.44}$$

where θ is the angle between the magnetization and the current. It should be mentioned that the general cos^2-dependence applies only to large magnetic systems or single domain structures [97]. In ferromagnets with only a few domains the switching of individual domains or the motion of single domain walls will cause a deviation from this approximation. In Section 4.3 the AMR of multidomain structures as investigated by resistance measurements, micromagnetic simulation, and magnetic force and X-ray microscopy will be described in detail.

2.5.3 Spin-Transfer Torque

In 1996, L. Berger [22] and J. Slonczewski [23] independently found that a high-density electric current would induce a strong torque on magnetic multilayers. In their model, one magnetic layer would polarize the spin of the conduction electrons, and, separated by an non-magnetic layer, another layer potentially having a different magnetization direction, would filter the conduction electrons. Part of the spin is reflected if the magnetization of the two layers is not aligned, in analogy to the GMR and accumulate in the non-magnetic layer. The transmitted electrons have their spin aligned to the second magnetic layer. The change in spin of the transmitted conduction electrons causes an inverse torque on the magnetization of the second layer to conserve the total angular momentum. This effect has become known as *spin-transfer torque* and was first experimentally verified by the Cornell group [98]. It is currently one of the most actively studied fields in solid state physics due to its potential application in magnetic random access memory devices (MRAM).

In the following I shall outline a somewhat different model since the geometry is different in our experiments. In our case, the current is applied laterally in a single magnetic layer. An inhomogeneous magnetization can occur at domain walls in which the magnetization gradually changes. L. Berger predicted [24] that the 4s-conduction electrons would feel a changing potential due to s-d exchange interaction when passing through the domain wall. The spins would adiabatically rotate to align with the magnetization; in turn the domain walls would experience a torque compensating the spin rotation [99, 26, 27]. He predicted the driving force on the domain wall and its resulting speed. Domain-wall motion by spin-polarized currents has since been shown experimentally [25, 100, 101, 102, 103, 30, 104, 105, 106, 31, 107]. It was found that the experimentally observed domain-wall velocities were two orders of magnitude smaller than the ones theoretically predicted [27, 28, 32]. It was also found that high-density currents can change the internal structure of domain walls [105, 106, 108, 109, 110], e.g., from a Néel wall into a vortex wall [105, 106].

I shall here follow the model of S. Zhang and Z. Li [28] which was recently extended for time-dependent currents by B. Krüger *et al.* [29]. It is currently the most general model for the description of current-induced domain-wall motion. S. Zhang and Z. Li found that another torque term could be accountable for the discrepancy between theory and experiment. This torque term is due to a spatial lag of the conduction electron spin behind changes of the local magnetization and is termed *nonadiabatic spin-torque*. They assumed s-d-electron interaction to be the predominant influence of the current on the magnetization, but they also took time- and spatially varying local moments for a full description of the magnetization dynamics into account. By considering variations from the adiabatic process up to first order and a domain-wall width (see Eqn. 2.31) larger than the transport length scale, they derived four new torque terms for the LLG-equation (Eqn. 2.30)

$$\begin{aligned} T = \;& \tfrac{1}{1+\xi^2}\left[-\tfrac{m_0}{M_\mathrm{s}}\tfrac{\partial\mathbf{M}}{\partial t} + \tfrac{\xi m_0}{M_\mathrm{s}^2}\mathbf{M}\times\tfrac{\partial\mathbf{M}}{\partial t}\right] \\ & -\tfrac{1}{1+\xi^2}\left[\tfrac{\mu_\mathrm{B}P}{eM_\mathrm{s}^3}\mathbf{M}\times\left[\mathbf{M}\times\left(\mathbf{j}_e\cdot\nabla\right)\mathbf{M}\right] + \tfrac{\mu_\mathrm{B}P\xi}{eM_\mathrm{s}^2}\mathbf{M}\times\left(\mathbf{j}_e\cdot\nabla\right)\mathbf{M}\right] \end{aligned} \tag{2.45}$$

where m_0 is the local equilibrium spin density of the conduction electrons and P the spin-polarization of the current $\mathbf{j_e}$. The ratio between exchange relaxation time τ_{ex} and spin-flip relaxation time τ_{sf}

$$\xi = \frac{\tau_{ex}}{\tau_{sf}} \tag{2.46}$$

is called the *degree of nonadiabaticity*. The first two terms in Eqn. 2.45 which are independent of the current can be eliminated by renormalizing γ and α. By defining $\mathbf{j_e} = j_e\mathbf{e_x}$ and $b_j = Pj_e\mu_\mathrm{B}/eM_\mathrm{s}^3\left(1+\xi^2\right)$, Eqn. 2.45 can be placed into the LLG equation (Eqn. 2.30) to yield the spin-torque dependent LLG in Gilbert form [32, 29]

$$\begin{aligned} \frac{d\vec{M}}{dt} = & -\gamma\mathbf{M}\times\mathbf{H}_\mathrm{eff} + \frac{\alpha}{M_s}\mathbf{M}\times\frac{d\mathbf{M}}{dt} \\ & -\frac{b_j}{M_s^2}\mathbf{M}\times(\mathbf{M}\times(\mathbf{j_e}\cdot\nabla)\mathbf{M}) \\ & -\xi\frac{b_j}{M_s}\mathbf{M}\times(\mathbf{j_e}\cdot\nabla)\mathbf{M}. \end{aligned} \tag{2.47}$$

The first spin-torque term describes the adiabatic torque on a domain wall in the direction of the current, the second term describes the nonadiabatic torque perpendicular to it. The nonadiabatic spin-torque term has also been introduced by Waintal *et al.* as based on Larmor precession of the conduction electron around the axis of the local magnetization vector [108] and by Thiaville *et al.* who suggested an influence of surface roughness [32]. The magnitude of ξ has been estimated as either $\xi \approx 0$ or $\xi \approx \alpha$. In Chapter 4.4 I will describe X-ray microscopy experiments that we performed. These experiments indicate that $(\xi = 0.95 \pm 0.02)\,\alpha$ [110]. We measured domain-wall velocities of about 100 m/s confirming the theoretical predictions. We also observed a high measure of randomness in the domain-wall motion. We could show, however, that this is due to pinning sites and not due to thermal effects as suggested by other authors [111, 112, 113, 114].

3 Simulation and Measurement Techniques

In this chapter I will describe the main methods used to acquire the results summarized in this thesis, namely micromagnetic simulations, magnetoresistance measurements, and X-ray microscopy. As depicted in Fig. 3.1, each method works on completely different principles and has different advantages, disadvantages, and constraints. Optimally, a combination of these methods magnifies the advantages of each method and therefore makes the interpretations more reliable than each method alone. In the worst case the constraints of each method add up so that the study is impeded and no meaningful conclusion can be drawn. Performing micromagnetic simulations gives one immense control over the material and simulation parameters, but one needs to ensure that the parameters

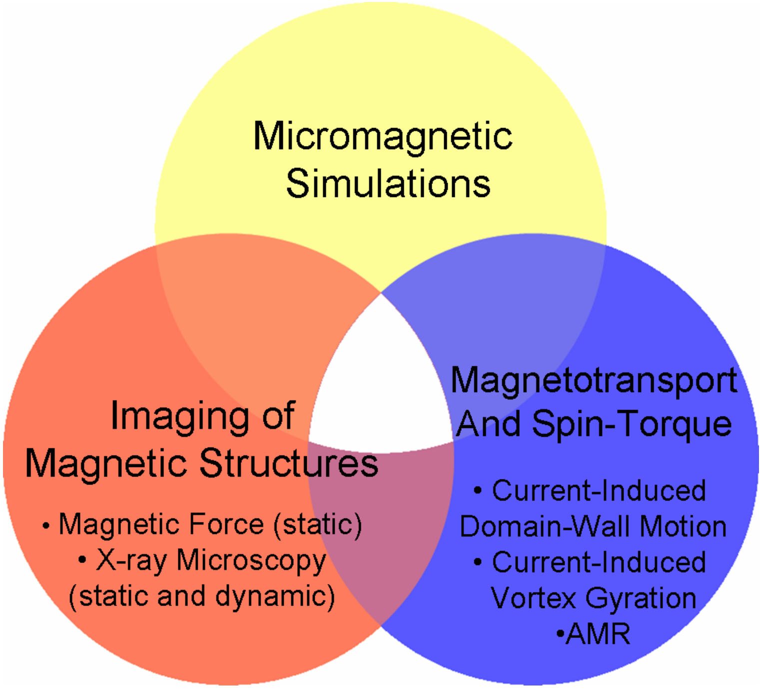

Fig. 3.1: The combination of micromagnetic simulations and different measurement techniques lead to a greater depth of understanding than each method alone.

used are also physically meaningful. There are also a number of constraints that could invalidate the results or greatly prolong the computing time. Magnetoresistance measurements are extremely sensitive to small changes in the magnetization and can potentially give ps-time resolution [115]. On the other hand, the integrated signals are ambiguous due to the cos^2-dependence of the AMR, and the true AMR-signals can be obscured by unwanted side effects as shown for example in Section 4.3.2. Finally, X-ray microscopy allows domain imaging in applied fields without interaction with the magnetization. It is element-specific and potentially time-resolving down to $\approx$ 70 ps, but these advantages come at the cost of difficult preparation processes as the samples need to be placed on 100 nm thin Si_3N_4 membranes. Also there are only a half-dozen X-ray microscopes world-wide that can deliver the temporal and spatial resolution at the right energy required for meaningful inquiries, so that beam time is difficult to obtain. In the following I shall explain the fundamental principles and modi operandi of each method.

3.1 Micromagnetic Simulation

Originally it was the purpose of the micromagnetic theory (see Section 2.2) to analytically estimate the energetically favored magnetization states. These laws are still the foundation to micromagnetic simulations today, the exact analytical calculation of the magnetization, however, is possible only for ferromagnetic bodies of high rotational symmetry [116, 117, 118]. For more complex geometries the magnetization cannot be described analytically, instead one must employ numerical computation. Over the past three decades computing power has increased exponentially, and micromagnetic simulation as simulation in general has become well established as "a third pillar of research next to experiment and (analytical) theory" [1]. In the 1990s the methodology and algorithms constituting micromagnetic frameworks were still a matter of research and discussion [119] and led to the establishment of so-called *standard problems* [120] with which the simulation results from different codes could be compared. While the first standard problems showed that there was much left to be desired in terms of agreement between different codes [120], today, more than eleven years later, there is little discussion about micromagnetic simulation as an eligible scientific tool. Each year, hundreds of articles [121] in scientific journals are published in which the results heavily rely on insights gained by micromagnetic simulation. In this thesis I have used micromagnetic simulations in every study I performed. The advantages of using micromagnetic simulation in combination with experiment and theory was fourfold:

- verification of experimental results or theoretical predictions,
- interpretation of experimental data by varying simulation parameters,
- analysis of the magnetization dynamics' dependence on internal parameters,
- and prediction of behavior, thus being able to give suggestions for the design of samples used in experiments.

Over the years, several individuals and groups have developed their own versions of a micromagnetic simulation program. The most widely used publicly-available simulation codes are *OOMMF* by M. Donahue and D. Porter from NIST [121], M. Scheinfein's *LLG Micromagnetics Simulator* [122], D. Berkov's *Micromagus* [123], *MagPar* from W. Scholz [124], and more recently K. Rivkin's *RKmag* [125]. In the course of my thesis, as well as previously in my Master's theses [126], I have mainly used the OOMMF code because it is open-source and thus extendible, even though we also had the commercial LLG program available for comparison. I extended the OOMMF code by a faster integration method, a component computing the AMR, and a component for the calculation of the spatially resolved spin-wave spectra. I contributed to Benjamin Krüger's expansion of the OOMMF code who included the spin-transfer-torque model from Zhang and Li [28] and to Massoud Najafi's development of a micromagnetic simulation framework in Matlab [127] for his Masters thesis [51].

The micromagnetic equations noted in Section 2.2 cannot be solved analytically for any shape and with arbitrary accuracy on finite precision computers. To numerically solve the micromagnetic behavior of ferromagnets, all micromagnetic codes implement certain approximations: First, a spatial discretization of the ferromagnetic body for discrete computation. Secondly, and connected to that, ways to calculate the effective magnetic fields. Thirdly, the main equation is solved numerically, either by minimizing the total magnetic energy with Brown's equation (see Section 2.2.1) or by solving the equation of motion, the LLG-equation (see Eqn. 2.30). These approximations are explained in more detail in the following sections.

3.1.1 Spatial Discretization

The investigated volume needs to be discretized into smaller volumes or points in which the magnetization assumes a finite value. For the spatial discretization one uses either the *finite-element (FE) method* or the *finite-difference (FD) method.* Since in this thesis I extended and used mainly the OOMMF code which applies the finite-difference method, it is explained in greater detail.

Finite-Element Method

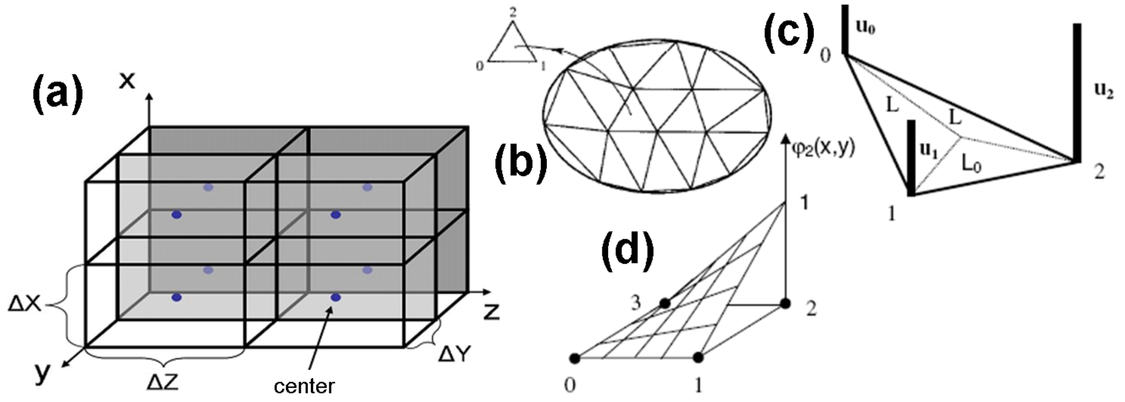

Fig. 3.2: Spatial discretization via the finite-difference method (a) and via the finite-element method (b) - (d) as described in the text. Modified from Ref. [128].

The FE method originated in civil and aeronautical engineering out of a need to solve complex problems regarding the elasticity of bodies and has since been successfully applied to electromagnetism, fluid dynamics and many other fields. It has the advantage that it can model arbitrary geometries. This however, comes at the cost of higher computation complexity.

Three main steps are necessary for the solution of a partial differential equation (PDE) with the FE method (see Ref. [128] and references therein). The first step is to discretize the space, on which the PDE should be solved, into finite elements. These can be triangles or squares in two dimensions or tetrahedrons or cubes for three-dimensional problems as shown in Fig. 3.2(b). Hence this process is called *triangulation*. Secondly, the solution of the PDE, in the case of micromagnetics the poisson equation for the scalar potential of the magnetization $U = \nabla \mathbf{M}$ [129], has to be found for every nodal point. The values within the elements are derived by interpolation from the nodal points of each element (see Fig. 3.2(c)). The solution of the PDE is approximated by piecewise continuous polynomials and the PDE is hereby discretized and split into a finite number of algebraic equations. In the third step, the unknown coefficients of these polynomials are determined in such a way, that the distance from the exact solution becomes a minimum [128, 129].

Finite-Difference Method

The FD method, on the other hand, partitions the volume into rectangular prisms of equal size, and the function value in each prism, in this case the magnetization, is averaged to a value at the center of the prism (see Fig. 3.2 (a)). The interaction between the magnetization and the effective field can now be expressed by a finite sum over all elements. In the following, the FD-computation of the exchange energy and the demagnetization energy shall be explained in greater detail. The computation of the anisotropy and the Zeeman energies are left out as they can be directly derived from the corresponding equations in Section 2.2.1 by substituting integrals by sums.

Computation of the exchange and demagnetization fields

To compute the exchange field one must find an efficient discretization of computing the partial differential in Eqn. 2.21. This is done by using a Taylor-polynomial to determine the change in magnetization between two cells. As the exchange interaction is of a very short-ranged nature it is generally sufficient to limit the computation to nearest neighbors. For the j-th simulation cell one then gets

$$\mathbf{H}_{exch,j} = \frac{2A}{\mu_0 M_S^2} \sum_{i \in NN} \frac{\mathbf{M_i}}{\left(\mathbf{r}_i - \mathbf{r}_j\right)^2} \tag{3.1}$$

where the sum i is over the nearest neighbors, which, for three-dimensional problems, would typically be the six cells with common surfaces [130].

To discretize the demagnetization field one must first solve the demagnetization tensor $\hat{\mathbf{N}}$ (see Eqn. 2.25) for every cell. Newell *et al.* [50] first delivered a solution for the demagnetization tensor of rectangular bodies. By applying Gaussian's integral law, Newell reduced the demagnetization tensor elements to the surface integrals of a simulation cell. The diagonal elements, $\mathbf{N_{ii}}$, describe the interaction of the magnetization at opposite surfaces of a cell, and the non-diagonal elements $\mathbf{N_{ij}}$ describe the interaction between the corresponding other surfaces. Applying some mathematics, Newell *et al.* derived a closed formula for the tensor elements. The demagnetization field

$$\mathbf{H}_{demag,j} = \sum_{i=1}^{N} \hat{\mathbf{N}}_{\mathbf{ij}} \cdot \mathbf{M}_i \tag{3.2}$$

needs to be computed for all j cells at every time step, making it by far the costliest part of the computation. To reduce the computing time, one can make use of the regular grid of the FD method and Fourier transform the tensor and the magnetization vectors. The convolution integral can then be substituted by a discrete convolution sum. Since the geometry of the simulated volume does not change in the course of the simulation, the demagnetization tensor elements need only be computed once, at the initialization phase and is stored as its Fourier transform. At every simulation step, M is Fourier transformed and the field is computed and then inversely transformed back into real space.

As each dimension of the simulated volume is to be divided into an integer number of cells, only rectangular structures can be effectively and correctly simulated. Consequently, errors occur on the edges of curved geometries as the approximated solution potentially differs significantly from the correct one. Several correction algorithms have been suggested [131, 132]. However, for the rectangular structures mainly investigated in this thesis, the FD method is considerably faster than the FE method.

3.1.2 Numerical Solution by Time Integration of the LLG Equation

The time evolution of the magnetization of a ferromagnetic element follows the LLG-equation. By employing numerical integration, one can calculate the magnetization dynamics to a high degree of accuracy. For the numerical integration of the LLG-equation one needs to define an initial magnetization configuration as starting value of the function to be integrated (*initial value problem*). The next time steps are computed from either the current function value (*single-step methods*) or from several values in the past (*multi-step methods*). Some multi-step methods even use predictions of future values (*predictor-corrector methods*). Explicit methods use only known function values to compute the next step, while implicit methods find the function values of the next step by solving an equation involving both the current and the future function values. For example, the LLG-equation as written in Eqn. 2.30 could be solved explicitly, while the Gilbert-form [43, 46] of the LLG-equation could be solved by implicit methods. Depending on the exact nature of the problem, each method would have different convergence, stability, and performance.

The classical fourth-order Runge-Kutta method is one of the most reliable and fastest integration methods for micromagnetic problems [133]. It is a single-step multi-stage explicit numerical integration method. It is an extension of the 1^{st}-order explicit Euler method (see Fig. 3.3(a)) which approximates the magnetization in each cell $\mathbf{M}_{i,t_{n+1}}$ at the next time step t_{n+1} by adding the derivative $\frac{d\mathbf{M_{i,t_n}}}{dt}$ multiplied by the time step δt_n to the current magnetization $\mathbf{M}_{i,t_n}$. Runge-Kutta methods use midpoints at which the function values are approximated via the Euler method. The first midpoint is then used as a starting point for the second stage and so forth (see Fig. 3.3(b)). The number of midpoints or iterations (called stages) corresponds to the order of the algorithm. The final function value for one step is the weighed sum of the derivatives at the midpoints. The advantage of higher-order Runge-Kutta algorithms lies in the higher accuracy of the approximation which allows to expand the step size of the integration. The open-source OOMMF code uses an explicit Euler-method [121]. For my Masters thesis I implemented an adaptive-time step Runge-Kutta method [133] which increased the speed of the simulation by an order of magnitude [126].

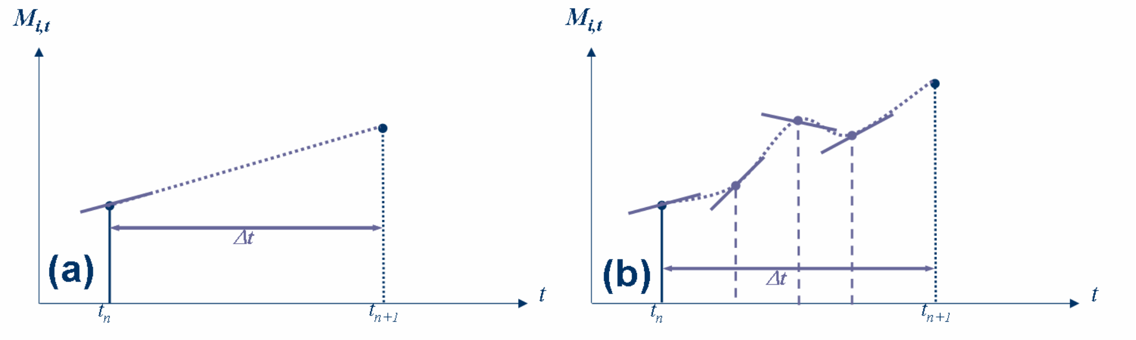

Fig. 3.3: (a) A 1^{st}-order Runge-Kutta (explicit Euler) method and (b) a higher order Runge-Kutta method with three midpoints.

There are also completely different ways to derive the magnetization configuration. For example, by minimizing the total energy via Brown's equation (see Section 2.2.1) and conjugate gradient methods [134], the magnetization state in equilibrium can be determined. Iterative methods such as the Gauss-Seidel methods [135, 136, 137] or Jacobi methods can also be used to approximate the solution.

Having explained the main components of a micromagnetic simulation program, one can now understand how they work together to compute longer periods of the magnetization dynamics. Figure 3.4 shows a simplified flow diagram of an exemplary simulation code. The different codes might vary in detail, but the basic structure remains. A simulation run can be broken down into hierarchical levels of execution, the *stages* and *steps*. A simulation step forwards the numerical integration of the LLG-equation by one time step in the following way: Starting from an initial magnetization configuration, the corresponding magnetic fields, e.g., exchange or stray fields, are computed. From the effective field and the current magnetization the LLG-equation is solved. Then the magnetization for the next time step is computed by numerical integration. Finally, an error estimate and the step size for the next steps are computed. If the error is below a predetermined boundary, the simulation continues, otherwise, the step is repeated with a smaller time step. The simulation continues with the same outer parameters until some stopping criterion, e.g., time duration, number of steps, or change in magnetization, is met. Then some simulation parameters are changed and the simulation continues again or stops altogether. A stage defines a number of steps with the same outer parameters. Stages are especially useful to incorporate into a simulation framework when one wants to simulate magnetic hysteresis, frequency sweeps and the like.

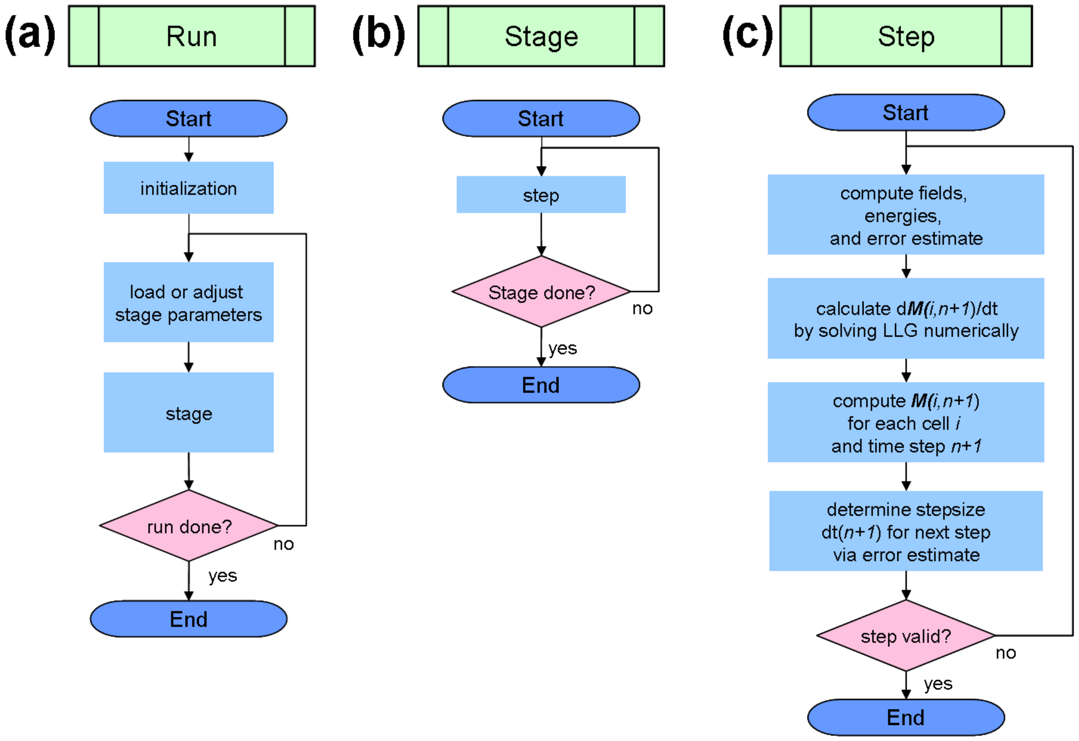

Fig. 3.4: Flow diagram of a micromagnetic simulation program solving the LLG-equation: (a) flow diagram of a simulation run consisting of possibly several stages, (b) flow diagram of a stage consisting of many steps, and (c) flow diagram of the necessary procedures to advance the simulation by one time step.

3.2 Measurement Techniques

There are numerous ways today to investigate the magnetization configuration of magnetic thin films. They can roughly be divided into electronic probing and domain imaging techniques. Electronic probing techniques are those in which electric currents are used to test the interaction between the conduction electrons and the local magnetization or their stray fields. These interaction are detected by a change in voltage. Examples are magnetoresistance measurement techniques (see Section 2.5.2) such as AMR, GMR, and TMR measurements, but also micro-Hall-magnetometry [138, 139] and Hall-measurements [140, 61]. In all these methods, the local interaction is integrated to one voltage value. Electronic signals are very sensitive but conceal the local magnetization pattern.

Domain-imaging techniques, on the other hand, disclose the local magnetic structure but are subject to noise. Excellent reviews on domain-imaging techniques are found in Refs. [36, 141, 142, 143]. I shall here focus on the techniques that were used for this thesis, namely magnetic-force and transmission X-ray microscopy.

Method	contrast origin	max. resolution	depth-sensitivity	max. magn. Field	vacuum needs	exposure time
Kerr	**M**	200 nm	20 nm	any	no	10 ns - 1 s
Holography	**B**, ϕ	1 nm	z_{sample}	no	HV	0.03 - 10 s
SEMPA	**B**	10 nm	2 nm	32 mT	UHV	1 - 100 min
MFM	**B**	10 nm	20-500 nm	400 mT	no	30 min
SP-STM	**M**	0.1 nm	<0.3 nm	any	UHV	20 min
X-PEEM	**M**	50 nm	2-20 nm	1.5 mT	HV	0.03 - 600 s
MTXM	**M**	15 nm	z_{sample}	any	no	0.2 - 200 s

Fig. 3.5: Selected domain-imaging techniques and their properties. ϕ is the phase shift between two electron beams due to magnetic stray fields. (U)HV stands for (ultra) high vacuum. (modified from Ref. [143]).

3.2.1 Magnetoresistance Measurements

For magnetoresistance measurements, one usually uses the lock-in technique in four-point geometry. The latter puts the current and voltage contacts in close proximity of the magnetic structure to be investigated, thereby reducing any serial resistances of the wires and connectors. For lock-in measurements the input signal, here the current, is modulated by low-frequency (mHz to a few hundred Hz) alternating signals. The output signal, i.e., the voltage, is multiplied by the same alternating signal and is integrated over several periods. Only components of the output signal with the same frequency and phase as the input signal remain while other contributions are attenuated. In this way very small voltage changes can be detected. Our lock-in measurements were performed with a Stanford Research SR830 lock-in amplifier typically at currents of 10μA, supplied by a Keithley 2400 current source. In our simultaneous magnetoresistance/X-ray microscopy investigations, we had to greatly increase the integration time of the lock-in amplifier to ensure it was longer than the exposure time of the CCD-chip ($\approx 1-2$s). More details to simultaneous magnetoresistance/X-ray microscopy are given in Section 4.3.2. Usually AMR measurements are performed at low temperatures to reduce thermal noise. The studies presented in Section 4.3.1 were done by Marcus Steiner at liquid helium temperatures. At the XM-1 beam line all measurements were done at room temperature.

3.2.2 Magnetic-Force Microscopy

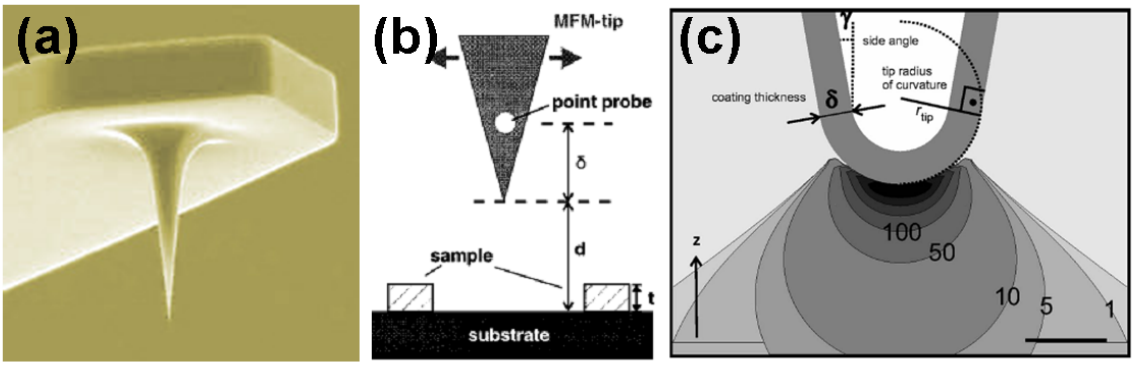

Fig. 3.6: (a) Electron microscopy image of a Co-coated MFM tip (from Ref. [144]). (b) Approximation of the magnetic coating of the tip as a dipole within the tip volume (from Ref. [145]). (c) Finite-element computation of the magnetic stray field of the tip. The field values are in mT and the length scales are given by the bar in the bottom right corner which is 100 nm long (from Ref. [146]).

Y. Martin and H. K. Wickramasinghe first used magnetic tips in scanning-force microscopy to image magnetic domains [147]. Since then it has become possible to use magnetic-force microscopy (MFM) also to quantitatively investigate magnetic systems [145, 146, 138, 139]. With MFM, a magnetic tip (see Fig. 3.6(a)) is positioned at the end of a cantilever that oscillates in resonance (*tapping mode* [148]). The cantilever reflects a laser beam onto a photo diode which detects the oscillations. When the tip interacts with the stray field of a magnet, the frequency of the oscillation slightly changes as [146]

$$\Delta\omega = \frac{\omega_0 F'}{2k} \tag{3.3}$$

with the force gradient of the stray field H

$$F' = \mu_0 \int_{tip} \left[M_{z,tip}\left(\mathbf{r}'\right) \cdot \frac{\partial^2}{\partial z^2} H_z\left(\mathbf{r}-\mathbf{r}'\right) d^3\mathbf{r}' \right] \tag{3.4}$$

where k is the cantilever's spring constant (typically ≈ 3 N/m), $M_{z,tip}$ the z-component of the magnetization of the MFM tip, and ω_0 its resonance frequency ($60-80$ kHz). The tip scans the surface of a sample and the frequency shift is recorded as a function of location to create an image. Alternatively, the oscillation amplitude or the phase shift, which are also linear functions of the force gradient, can also be utilized for MFM imaging [55]. As shown by Eqn. 3.4, the MFM signal is sensitive to the second derivative of the sample's stray field z-component in the tip volume. To first approximation, the interaction can be calculated by seeing the magnetization in the tip as a point dipole located somewhere within the tip volume [145] (see Fig. 3.6(b)). More precise finite-element calculations yielded a stray field of the tip of more than 50 mT for hard-magnetic tips (see Fig. 3.6(c)). These strong local fields have been shown to be sufficient to alter the magnetization of the investigated sample [149]. MFM must therefore be seen as a partially invasive technique. However, with precaution MFM is a very useful technique for the characterization of magnetic samples.

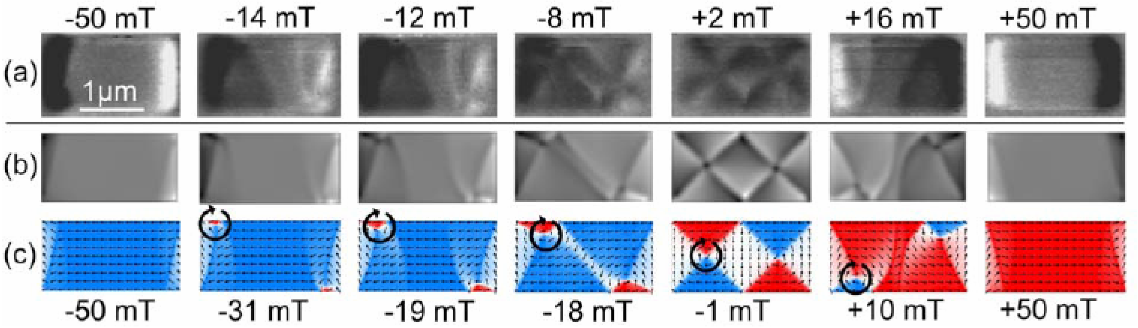

Fig. 3.7: Comparison of MFM measurements (a) to simulations (b) and (c) for the 1×2 μm^2 structure with a thickness of 70 nm in external magnetic fields between -50 mT and +50 mT. (b) Simulations of the MFM signal. (c) Underlying magnetization. One of the vortices driven through the magnetization configuration by the external magnetic field is indicated by circular arrows. From **[P5]**.

In our group the simplified dipole model was implemented in an extension of the OOMMF code to compute MFM images of micromagnetic magnetization states (see for example Fig. 3.7). The detailed algorithm for this procedure is presented in Appendix A of Ref. [55]. The magnetic-force microscope used in our group is a Nanoscope III microscope by Digital Instruments with integrated Helmholtz coils that provide external magnetic fields of up to 100 mT. Both the simulation code and the MFM were used for the preliminary studies for this thesis (see Refs. [150, 151, 152] and Section 4.1) and for precharacterizing the samples for X-ray microscopy studies.

3.2.3 Magnetic Transmission X-ray Microscopy

Magnetic transmission X-ray microscopy works by a completely different contrast mechanism than magnetic-force microscopy: The interaction of soft X-ray photons with the core electrons of ferromagnets. In this energy regime ($\approx$ 1 keV) the thickness-dependent absorption of photons by matter is governed by Beer's law [143]:

$$I(E,Z) = I_0 e^{-\mu(E,Z)z} \tag{3.5}$$

where E is the energy of the photons, Z the atom number of the transmitted material and z its thickness. The absorption coefficient μ can be calculated by Fermi's Golden Rule [153]. For the transition metals investigated here, this involves the integral over the density of unoccupied states. When the energy of the photons is sufficiently high, the core electrons can be excited into the $2p_{1/2}$ and $2p_{3/2}$ states. At the corresponding energies, called the L_2 and L_3 edges, respectively, the absorption is greatly enhanced (see Fig. 3.8). Absorption at these edges depends on the polarization of the photons. This effect, called the *X-ray magnetic circular dischroism* (XMCD) [154], can be used to image magnetic

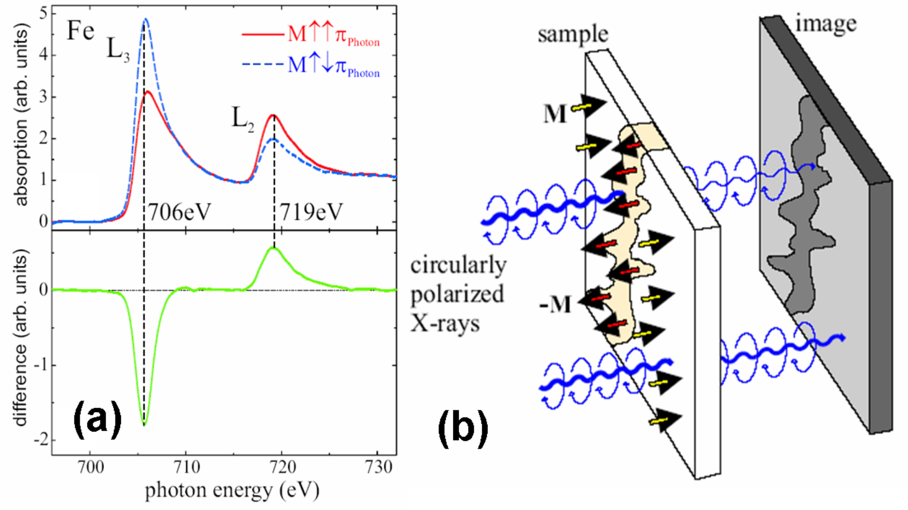

Fig. 3.8: (a) Absorption spectrum of iron at the L_3 and L_2 edges. The absorption of right- and left-circularly polarized X-ray light differs at these edges, resulting in a detectable difference in absorption (bottom graph of (a)). (b) When imaging magnetic domains, the different magnetization directions then appear as gray color contrast. From Ref. [143]

domains by alternating the X-ray polarization. The XMCD contrast is then defined as

$$\frac{\mu_s}{\mu_0}(E) = \frac{\mu^+ - \mu^-}{\mu^+ + \mu^-}(E) \tag{3.6}$$

where $\mu_s = \frac{1}{2}(\mu^+ - \mu^-)$ is the spin-dependent absorption coefficient. Equation 3.6 can be rewritten as

$$\frac{\mu_s}{\mu_0}(E) = \frac{\sigma_s}{\sigma_0}(E)\,\frac{(\mathbf{M}\cdot\mathbf{P})}{|\mathbf{M}|} \tag{3.7}$$

where **P** is the direction and degree of polarized light, and σ_s and σ_0 are the magnetic and atomic absorption cross sections, respectively [155, 143]. Equation 3.7 says that the XMCD contrast is proportional to the component of the sample magnetization in direction of the X-ray beam. Thus if one wants to study materials with perpendicular magnetization such as CoPd-multilayers or FeGd thin films, the sample is placed normal to the X-ray beam (see Figure 3.8). When one wants to study thin films with an in-plane anisotropy (Fe, Ni, Co, and Py), the sample needs to be placed at an angle to make the magnetization visible. With the XCMD contrast mechanism, one can even separate the spin- and the orbital contributions to the material's magnetic moments [156] by calculating the probability of the different transitions according to the so-called *sum rules*, provided that the microscope has sufficiently high energetic resolution, but this has not been pursued in this thesis. But in alloys, the XMCD can be used to identify the magnetic moments of the alloy compounds by measuring at different transition energies [157, 158]. XMCD's companion contrast mechanism, the X-ray magnetic *linear* dichroism (XMLD), allows to observe also antiferromagnetic magnetic moments [159, 160].

The resolution of X-ray microscopes is achieved with the help of Fresnel zone plates [161, 162] that consist of concentric rings of alternating transparent and opaque material.

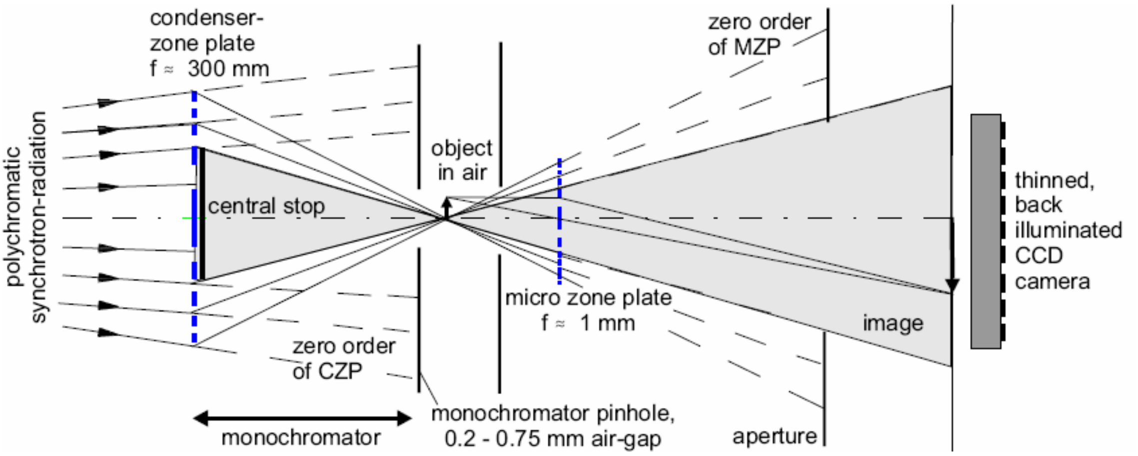

Fig. 3.9: Optical setup of the XM-1 microscope (not drawn to scale). From Ref. [143]

For soft X-rays the zone plates are typically made of nickel or gold. One zone plate, called the *condenser zone plate (CZP)*, focusses the beam onto the sample (see Fig. 3.9). Together with a pinhole it also serves as a monochromator for the X-rays since the focal length is inversely proportional to the photon wave length. A central stop blocks out the direct light from the synchrotron ring so that only refracted light of the *m*-th order comes throught the pinhole. The other zone plate, the *micro zone plate (MZP)*, projects the transmitted beam onto a CCD chip. The resolution of the microscope is given by the Rayleigh criterion for incoherent illumination and is proportional to the width of the outermost transparent rings of the MZP. To achieve a high degree of refraction and high resolution, thick zone plates with small outer ring widths are desirable. Even though this presents severe requirements for the zone plate preparation, zone plates having a resolution of better than 15 nm have been reported recently [163].

At synchrotron light sources, the X-rays are not continuous but are generated in packages called bunches. They are created as bunches of electrons circulate in the storage ring at

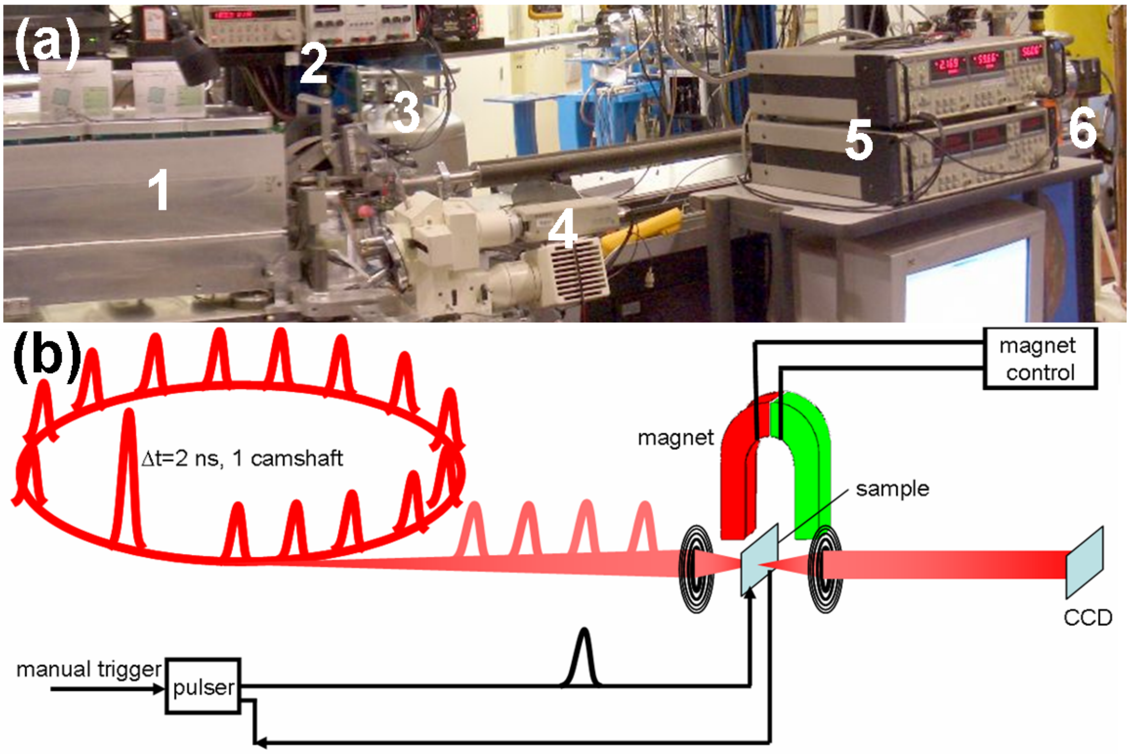

Fig. 3.10: Set-up of the XM-1 X-ray microscope at beam line 6.1.2 of the Advanced Light Source in Berkeley, CA. (a) Photo of the beam line with its main components as described in the text. (b) Sketch of the timing and control units in quasi-static measurements.

almost the speed of light and are deflected by bending magnets or undulators. At the Advanced Light Source (ALS), the 1.5 mA electron bunches have a full width at half maximum (FWHM) of about 70 ps representing the optimal time resolution for dynamic measurements at the ALS. In the normal multibunch mode, the bunches arrive at the endstation every 2 ns. 328 bunches fit in the 196 m long storage ring. To enable time calibrations in multibunch mode, one bunch, the *camshaft* (see the sketch in Fig. 3.10(b)), carries 10 mA current, surrounded by 20 ns gaps. The bunches have a life time of ≈ 8 hours so that currently three times a day the measurements need to be interrupted to refil the storage ring. There is also a special *two-bunch mode* during which only two bunches circulate in the ring and give off light every 328 ns. The storage ring facility sends a synchronized timing signal to each beam line to allow time calibrations of the detection electronics (see Fig. 3.11 and Fig. 3.12(c)).

Full-field X-ray Microscopy at the XM-1 beam line (BL 6.1.2)

The magnetic transmission X-ray microscope XM-1 of beam line 6.1.2 of the Advanced Light Source in Berkeley, is set-up as shown in Fig. 3.9 and Fig. 3.10. For higher intensity the X-rays are transmitted in vacuum except for a 0.75 mm air gap in which the sample is positioned. The CZP is located in the condenser box ('1' in Fig. 3.10(a)) to allow shifts in the focal length for energy selection. The transmitted beam is directed through the MZP stage ('3') to the CCD camera ('6') that is situated 2 m from the sample. An electromagnet ('2') can apply up to 100 mT for in-plane fields and 400 mT for out-of-plane fields, depending on the pole shoes used. The visible light microscope ('4') is needed to adjust the optical path of the microscope and can be swung into the optical axis in place of the condenser box. Finally, the SR830 lock-in amplifiers used in the simultaneous AMR/domain imaging studies are shown in '5' (see Section 4.3.2). For our investigations on stochastic domain-wall motion described in Section 4.4.2 we applied the current pulses manually with the help of an Agilent 33250A 80 MHz Function/Arbitrary Waveform Generator and an Avtech AVN-3 Ultra High Speed Pulse Generator. The outgoing and reflected pulses were detected by a Tektronix TDS 640A Digital Real-Time Oscilloscope.

The time-resolved measurements at the XM-1 beam line are done during the two-bunch mode in pump-probe technique (see Fig. 3.11). In this mode the magnetization is excited by a current or field pulse or a laser beam. With a delay line the excitation (pump) can be varied with respect to the fixed probe flash of the X-ray. The two-bunch mode is necessary to allow the magnetic system to relax back before the next X-ray pulse probes again. The

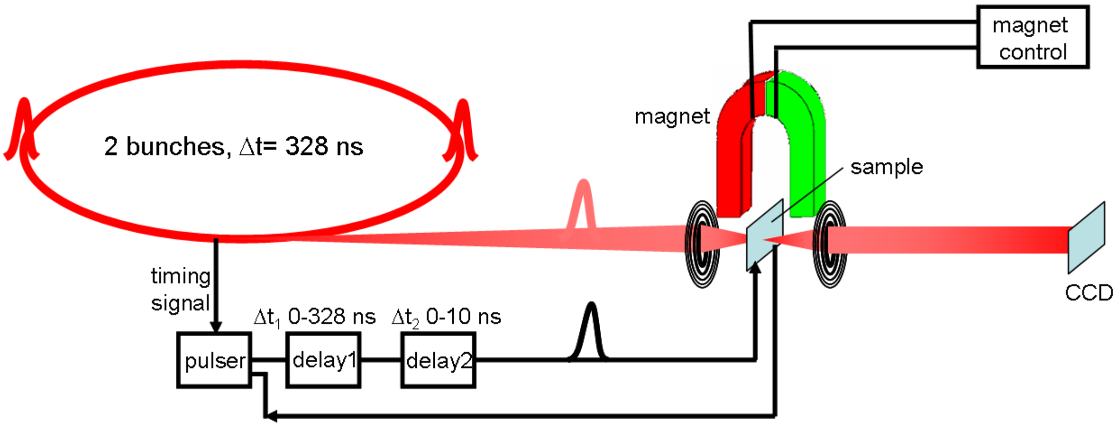

Fig. 3.11: Set-up for time-resolved measurements at the XM-1 beam line. The time delay is realized by a coarse and a fine delay line and synchronization of the pulser to the synchrotron timing signal.

CCD camera collects the transmitted X-rays until the signal-to-noise is sufficient. Varying the time delay between excitation and probing allows to measure the time response of the magnetic system to the excitation with a resolution of approximately 100 ps.

Time-resolved X-ray Microscopy at the STXM beam line (BL 11.0.2)

The Scanning Transmission X-ray Microscope (STXM), beam line 11.0.2, at the ALS does not project the X-ray beam onto a CCD chip. Instead the monochromatic, circularly polarized X-rays from the undulator beam line are focused to a spot of ca. 30 nm onto the sample with the help of a condenser zone plate. The sample is scanned in the xy-plane with a high resolution scanning stage under interferometric control (see in Fig. 3.12(a)). For greater accuracy and higher intensity, the STXM is situated in a vacuum chamber filled with Helium (see Fig. 3.12(b)). The transmitted intensity is recorded by a fast avalanche photo diode (APD). The APD's short recombination time ($\approx$ 1 ns) is many orders of magnitude shorter than that of a CCD chip ($1-2$ s) and allows to detect each photon bunch individually. With programmable hardware, sequences of X-ray bunches can be channeled and stored in arbitrary order (see Fig. 3.12(c)). At beam line 11.0.2 the channeling was done by a FPGA (field programmable gate array) and software supplied by Y. Acremann from the Stanford Linear Accelerator Center (SLAC).

To excite magnetic structures by alternating spin-polarized currents or fields as described in Section 4.4.3 the detection of the magnetization at constant phases was guaranteed by selecting an excitation frequency, and integer multiples of the excitation frequency corresponded to the synchrotron frequency of 500 MHz. Figure 3.12(c) shows how the response of the magnetization at eight different phases is recorded in eight different channels simultaneously. In principle the set-up allows for an arbitrary number of channels. The determination of the absolute phase between the recorded images and the excitation is made possible by sending a short pulse through the detector electronics. The alignment of its arrival to the pulse produced by the photons of the camshaft yielded our time zero. This procedure yields an accuracy in time of better than 160 ps.

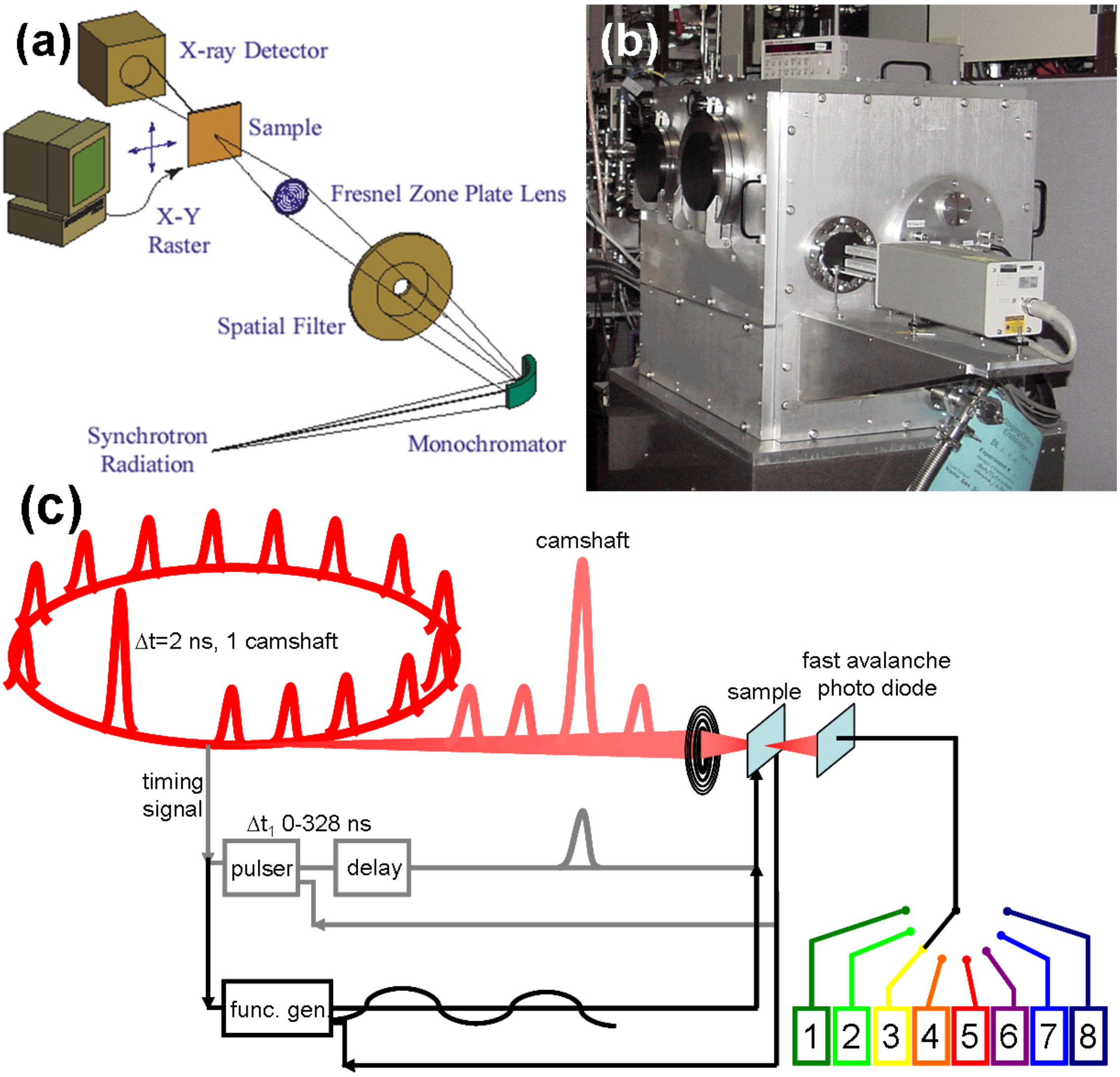

Fig. 3.12: Set-up of the scanning transmission X-ray microscope (STXM) beam line 11.0.2 at the ALS. (a) Sketch of the optical path of the STXM. (b) Photo of the vacuum chamber containing the STXM. (c) Sketch of the timing and control units of the STXM.

4 Results

In this chapter the results achieved by the methods outlined in the previous chapter are summarized. The results are divided into different topics. In Section 4.1, I studied the static magnetization configuration of ferromagnetic microelements by micromagnetic simulation as well as by magnetic force and X-ray microscopy. In Section 4.2 an enhanced micromagnetic simulation code was used to study the dynamics of such elements and to identify their spin-wave eigenmodes. In Section 4.3 the influence of the magnetization of ferromagnetic microelements and wires on the conduction electrons via the anisotropic magnetoresistance effect was investigated. The studies were done by micromagnetic simulation, magnetoresistance measurements, and X-ray microscopy. Finally, these topics and techniques are interwoven to study spin-torque driven domain-wall motion and vortex gyration in Section 4.4.

4.1 Magnetic Domains

As described in Chapters 2.1.3 and 2.2.3, the energetic ground state of a ferromagnet depends on its material parameters as well as on its history. In ferromagnetic thin films, these ground states are unique magnetization patterns or domain-wall types. They can change when one or more parameters are altered. The ferromagnetic system then crosses a phase boundary. For example, depending on the thickness of magnetic films, different domain-wall types occur, separated by phase boundaries [56]. In permalloy microstructures the domain-wall type changes from single-domain over Néel wall, Bloch wall, and asymmetric Bloch wall to cross-tie wall for increasing film thicknesses. In permalloy nanowires the domains are aligned parallel to the wire. For thin and narrow wires, *transverse domain walls* appear which are essentially Néel walls separating domains in which the magnetizations point head-to-head or tail-to-tail to each other. For thicker (> 15 nm) or wider wires, vortex domain walls are known to exist [57, 164, 165, 166]. For even thicker (> 60 nm) and wider wires multi-vortex walls appear [110]. In magnetic rings transverse, vortex or multi-vortex domain walls [167] can be present in the onion state, depending on the width and thickness of the ring [168, 97].

In the following subsections I summarize the results on the static and hysteretic behavior of magnetic domains in ferromagnetic micro- and nanoelements. Starting in Section 4.1.1 I briefly summarize our findings about the comparability of two domain-imaging techniques and micromagnetic simulation. I do so to lay a reliable foundation to the interpretation of the subsequent results as there I use these techniques interchangeably. In Section 4.1.2 I describe the results on the distance-dependent stray-field interaction between ferromagnetic squares in arrays. This is an important issue for the design of MRAM cells as one wants to minimize the interaction between neighboring storage units. We then optimized the geometry of the individual ferromagnetic elements and investigated the angle- and distance-dependent switching distribution of these elements in rectangular and hexagonal arrays.

4.1.1 Comparison of Domain-Imaging Techniques

In the first part of my thesis I continued the work of my diploma thesis [126] and Miriam Barthelmeß' dissertation [55] to compare the energetic ground states of ferromagnetic rectangles of various materials and thicknesses as derived by micromagnetic simulations to those found by magnetic-force microscopy (MFM). The goal was to map out a phase diagram for the domain-wall types in films of different thicknesses for various materials. During my diploma thesis we had already started this study and published three articles on our results. I will briefly outline the content of the three articles as they constitute the starting point for this thesis.

In the first article, we compared the magnetic images of Ni-Fe bilayered rectangles made by MFM to those taken at the X-ray microscope at the ALS in Berkeley, USA, to study the magnetostatic interaction between neighboring ferromagnetic elements [150]. The X-ray microscope shows magnetic domains parallel and antiparallel to the X-ray's polarization in bright and dark contrast while domains perpendicular to the polarization remain gray. The gray-scale contrast in the MFM images, on the other hand, is proportional to the second derivative in the stray field perpendicular to the surface [145, 55] so that domain walls give high contrast. As the stray fields of a domain wall often yield ambiguous signals, MFM images cannot be directly compared to the domain images due to the XMCD contrast. So we had to extend the OOMMF code to produce MFM images besides the magnetization images the code already produced. We then compared the magnetization images to the X-ray images and the corresponding simulated MFM images to the measured MFM images. We found good agreement between the two experimental techniques. The work was published as **[P3]** in G. Meier, R. Eiselt, M. Bolte, M. Barthelmeß, T.

Eimüller, and P. Fischer, *"Comparative study of magnetization reversal in isolated and strayfield coupled microcontacts"*, Appl. Phys. Lett. **85**, 1193 (2004) and presented at international conferences as **[C2]** and **[C3]**.

We then used the same techniques to evaluate the strength of the magnetostatic coupling between the elements [151]. The X-ray images revealed that the magnetization was not in its ground state, and we simulated the magnetization pattern. This allowed the exact calculation of the magnetic field between the elements. In this way we could show that the coupling amounted to several Millitesla. We could also show that the magnetization pattern observed in the X-ray images could only be explained when assuming that part of the magnetization was pinned. This article was published as **[P4]** in M. Bolte, R. Eiselt, T. Eimüller, P. Fischer, and G. Meier, *"Micromagnetic simulation as a bridge between magnetic-force and magnetic-transmission x-ray microscopy"*, J. Magn. Magn. Mat. **290-291**, 723-726, Copyright Elsevier (2005), and presented at an international workshop as **[C4]**.

In a third publication, I calculated the MFM images from micromagnetic simulations of permalloy rectangles of various thicknesses in externally applied magnetic fields and compared them to the MFM images taken by Christian Pels [152]. For this the simulated magnetization was relaxed for every field step in the hysteresis loop. Because the magnetization is hysteretic, the simulation had to be done sequentially and was very time consuming. Simulation and experiment both showed the same transition behavior of the magnetization: When the field is applied along the long axis of a $1 \times 2\ \mu\text{m}^2$ large and 70 nm thick permalloy rectangle, the magnetization reverses with increasingly negative fields by two magnetic vortices entering at the long edges at opposite sides of the rectangle. At remanence, the magnetization is in a double-Landau state with the vortices halfway between the two long edges. When further decreasing the field, the vortices travel through the rectangle and leave the rectangle at the other long edge, thereby reversing the magnetization. Simulation and experiment agree qualitatively on the MFM images as well as quantitatively on the field values at which the transitions occur. This work was published as **[P5]** in C. Pels, M. Barthelmeß, M. Bolte, A. Thieme, and G. Meier, *"Thickness and magnetic-field dependence of domain switching in isolated and interacting permalloy contacts"*, J. Magn. Magn. Mat. **293**, 885-891, Copyright Elsevier (2005). The findings confirm the valid description of experimental magnetization configurations by micromagnetic simulations for static multi-domain systems.

4.1.2 Domain Imaging of Magnetic Dot Arrays

I contributed to the previous articles by performing the micromagnetic simulations and helping with the subsequent analysis. The X-ray microscopy measurements were done by Peter Fischer from the Center for X-ray Optics, Berkeley, USA, and the MFM images were taken by Christian Pels and Miriam Barthelmeß from our group. René Eiselt and Christian Pels prepared the samples. At the beginning of my doctoral thesis I started to also perform the X-ray microscopy measurements at the Advanced Light Source in Berkeley, USA. We first measured at the full-field magnetic transmission X-ray microscope *XM-1* beam line 6.1.2 and later also at the scanning transmission X-ray microscope *STXM* at beam line 11.0.2. Altogether, I spent about 80 eight-hour shifts in measurements at the Advanced Light Source. The results are presented in the following sections as well as in sections 4.3.2 and 4.4.

Distance-Dependent Dipolar Interaction of Iron Elements

In our first X-ray microscopy experiment we investigated the stray-field interaction in arrays of iron, nickel, and permalloy microelements with different inter-element distances [169]. We experimented with different element geometries, namely squares and ellipsoids flattened on one of their sides. They were arranged in hexagonal and square lattices. The inter-element distances in all the geometries were varied by preparing arrays with minimal distances ranging from 100 nm over 200 nm, 300 nm, 400 nm, 600 nm, 800 nm, and 1 μm to 2 μm between neighboring elements. Since the square elements turned out to be qualitatively the best from the preparation process, we focused our studies on those arrays. Figure 4.1.2 shows an image of one of the samples investigated.

With the magnet built into the XM-1 we applied magnetic fields to run hysteresis loops. We then imaged the field dependent magnetization and analyzed the gray-scale contrast of the images with a self-written MATLAB image processing script to derive the average value for the gray-scale of a defined region. This value is proportional to the magnetic moments aligned parallel to the X-ray polarization. In this way we could both image the exact domain patterns and also determine the magnetic hysteresis of the arrays, i.e., the remanence magnetization and the coercive field. We found in the images as well as in the hysteresis that the magnetization reversal in the array elements was affected by stray-field interaction (see Fig. 1 and Fig. 3 of Ref. [169]). We compared the distance-dependent coercive fields and remanence magnetizations and found good qualitative agreement with an analytical model by Zhang *et al.* [170] in which the stray-field interaction decreases sharply with increasing distance. We also performed micromagnetic simulations of in-

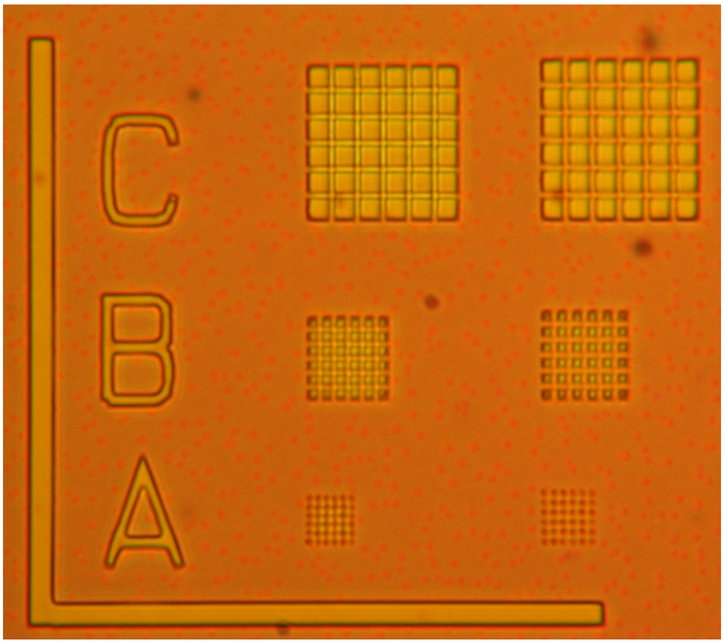

Fig. 4.1: Optical micrograph of a Si_3N_4 membrane with arrays of iron elements on it. The letters indicate different array types, here the size of the squared elements of the array, and the inter-element distance increases from left to right.

dividual Fe microelements and computed their stray field for the different magnetization states of a hysteresis loop. We found that the stray field at a distance of 250 nm from the microelement can still exceed 10 mT strong. Depending on the magnetization state, the stray field is inhomogeneously distributed around the microelement, leading to an anisotropic interaction of the elements in a square array (see Fig. 2 of Ref. [169]). I here reprint the article as **[P10]** with permission from Markus Bolte, René Eiselt, Guido Meier, Dong-Hyun Kim, and Peter Fischer, *"Real space observation of dipolar interaction in arrays of Fe microelements",* J. Appl. Phys. **99**, 08H301-1 - 08H301-3, Copyright (2006), American Institute of Physics. It was presented at the 10^{th} Magnetism and Magnetic Materials Conference in San Jose, CA, USA. It was also presented at a workshop on synchrotron radiation sources in Hamburg **[C9]**.

JOURNAL OF APPLIED PHYSICS **99**, 08H301 (2006)

Real space observation of dipolar interaction in arrays of Fe microelements

Markus Bolte, René Eiselt, and Guido Meier[a]
Institut für Angewandte Physik und Zentrum für Mikrostrukturforschung, Universität Hamburg, Jungiusstrasse 11, 20355 Hamburg, Germany

Dong-Hyun Kim and Peter Fischer
Center for X-Ray Optics, Lawrence Berkeley National Lab, 1 Cyclotron Road, Mail Stop 2R0400, Berkeley, California 94720

(Presented on 2 November 2005; published online 17 April 2006)

Square lattice arrays of thin microelements of Fe are investigated by magnetic transmission x-ray microscopy. The influence of dipole interaction is analyzed by varying the interelement distance. For comparison isolated elements are prepared on the same sample. The magnetostatic field caused by interelement interaction leads to a substantial stabilization of the elements in the center of the array comparable to the magnetization process previously found by numerical solution of the Landau-Lifshitz equation for magnetic dot arrays. Micromagnetic simulations show that for high field strengths the dipolar interaction is collinear with the external field while in the low-field regime the strayfields have significant perpendicular components leading to a complex reversal mechanism. © *2006 American Institute of Physics*. [DOI: 10.1063/1.2158387]

I. INTRODUCTION

Arrays of magnetic micro- and nanoelements are the basis for magnetic data storage and magnetic memory applications.[1–3] Dipolar interactions in dense arrays are important to consider because the magnetic properties such as magnetization process, remanence, and coercive field can be significantly different from those of noninteracting systems.[4–6] Arrays of magnetic elements exhibiting dipolar interactions have been studied theoretically[4–8] and experimentally.[1,3,9,10] Dipole interactions significantly affect the high-frequency response and the reversal dynamics of coupled arrays.[11] A nontrivial variation of the switching time as a function of the packing density is predicted. Because of its relevance for magnetic random access memory cells, it is interesting to use time resolved microscopy techniques to measure directly the expected influence on the reversal dynamics.

Here we focus on the real space observation of the effects of dipolar interaction on the static magnetic properties and the magnetization process in arrays of Fe microelements.

II. SAMPLE PREPARATION AND MEASUREMENT SETUP

We have prepared arrays of Fe microelements on Si_3N_4 membranes consisting of 5 nm Al as a seed layer and 20 nm Fe as a ferromagnetic layer. A 3 nm thick Al cap serves as protection. The microelements are defined by electron-beam lithography, electron-beam evaporation of the Fe layer at a rate of 0.1 nm/s with a base pressure in the 10^{-8} mbar range, and lift-off processing.

We use magnetic transmission x-ray microscopy (MTXM) in external magnetic fields of up to ±100 mT.[12] MTXM is an excellent tool to investigate the fragile and complex dipolar magnetic interaction in arrays of micro- and nanostructured elements. It allows noninvasive exploration of magnetic reversal within large arrays due to the full-field scope with a high spatial resolution.[13,14]

The MTXM images taken at the Fe L_3 absorption edge at a photon energy of 706 eV exhibit a contrast reversal from dark to light when the external field is reversed from +100 to −100 mT. With a proper normalization of each image to the saturated images, MTXM can be used as a highly sensitive local magnetometer. To achieve this, the mean value of the gray scale data in the magnetic part of an image is offset by the corresponding mean value of the nonmagnetic neighborhood and normalized with it. By this method, possible spatial fluctuations of the synchrotron light intensity are significantly reduced and hysteresis loops of a single microelement can be measured. The magnetic moment of one Fe microelement of 1.36×10^{-13} A m^2=0.136 nemu illustrates the ultrahigh sensitivity.

III. RESULTS AND DISCUSSION

Figure 1 shows representative images of four arrays with different interelement spacings at equal external magnetic field. The field is applied in the horizontal direction indicated by the arrow. The dichroic contrast measures the projection of the local magnetization onto the photon propagation direction; i.e., the gray scale of the MTXM image is proportional to their scalar product. For in-plane magnetizations as in the present case, the sample has to be tilted so as to obtain a nonvanishing projection.[15] Areas of magnetization in Fig. 1 pointing to the right appear white, while the ones in the opposite direction appear dark gray. Domains in the perpendicular, i.e., in the vertical direction in Fig. 1, exhibit an intermediate gray value. An example of a magnetization state of a single element interpreted using this gray scale is given in the inset of Fig. 1(d).

Before discussing the hysteresis loops inferred from the sequences of images we estimate the interelement spacing,

---

[a] Electronic mail: meier@physnet.uni-hamburg.de

0021-8979/2006/99(8)/08H301/3/$23.00 © 2006 American Institute of Physics

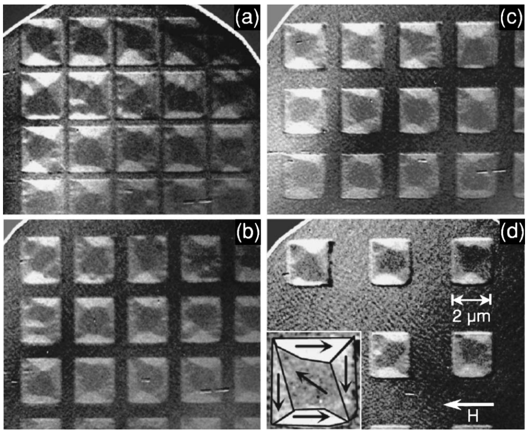

FIG. 1. MTXM images of arrays of Fe microelements with (a) 200 nm, (b) 600 nm, (c) 800 nm, and (d) 2000 nm interelement spacing in a magnetic field of $\mu_0 H = +8.7$ mT (state A in Fig. 3). Its direction is indicated by the arrow. The inset in (d) is an enlarged zoom of one microelement of this array with the magnetization indicated by arrows.

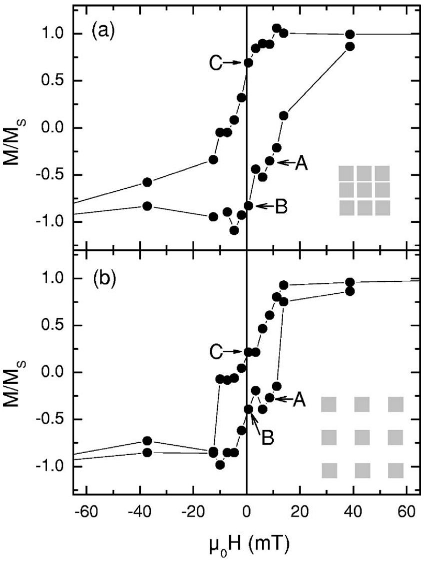

FIG. 3. Normalized hysteresis curves of the arrays determined from MTXM images at different fields for an interelement distance of (a) 200 nm and (b) 2000 nm.

where significant dipolar interaction is expected. For this, an isolated Fe microelement and its strayfield was simulated. We use the object oriented micromagnetic framework (OOMMF)[16] with standard iron parameters (saturation magnetization 1.700 kA/m, anisotropy constant 48.0 kJ/m^3, exchange constant 21×10^{-12} J/m), and a cell size of 5 nm in each direction. The evaporation process yields polycrystalline films with virtually no texture, thus justifying the choice of a random distribution of anisotropy axes in the simulations. Two representative results are shown in Fig. 2, where the magnetization of the microelement is plotted on top of the strayfield distribution. Although the exact magnetization state as measured in the nearly noninteracting elements of the array in Fig. 1(d) could not be reproduced by the micromagnetic simulation, it is worth calculating the strayfields. Significant field strengths of 16 and 6.5 mT at distances of 200 and 400 nm, respectively, are obtained. While at saturation the strayfield is almost completely aligned in the direction of the external field [see Fig. 2(b)], it has significant perpendicular components at zero applied field [see Fig. 2(a)]. This will cause a complex interaction while reversing the magnetization of an array of such elements. Although there is a long tradition in using computer simulations to understand the magnetic dipole interaction problem,[7] the simulation of arrays of real microelements is even today a time- and resource-consuming task. Often the elements of the array are assumed to be uniformly magnetized. If essential features of the magnetic ordering are governed by the net magnetic moment of the particle this is a reasonable assumption.[4] However, in the present case we can merely expect a qualitative description of the magnetization process by such an approach.

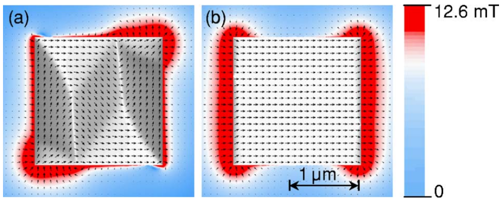

FIG. 2. (Color online) Micromagnetic simulation of the magnetization and the strayfield of an isolated element at zero field (a) and next to saturation at 100 mT (b). The color scale indicates the strength of the strayfield outside the element. A field strength of more than 10 mT is present up to a distance of 250 nm indicated by the sharp transition from red to white.

In the following, we discuss hysteresis loops inferred from MTXM images like the ones in Fig. 1 that were taken at 29 magnetic fields in the ±100 mT range. The hysteresis curves of the arrays with interelement spacings of 200 and 2000 nm are shown in Fig. 3. Magnetization state A corresponds to the images in Fig. 1. It is obvious that the hysteresis loops widen as the interelement distance is decreased. This is due to the dipolar coupling and is theoretically predicted.[4–6]

For a more quantitative interpretation it is interesting to study the dependence of the dipolar interaction characterized by the interelement distance on the reduced remanence M_R/M_S and the reduced coercive field H_C/M_S. The values can either be directly read off the raw data or deduced from sigmoidal fits. Results are shown in Fig. 4. The reduced coercive field H_C/M_R goes up steadily when dipolar interaction becomes stronger. This implies that a substantial additional field is required to change the ferromagnetic order of the magnetic moments. The reduction of coercivity with decreasing interaction strength is confirmed by micromagnetic simulations of interacting chains of Permalloy™ elements.[6]

A remanence $M_R \approx 0.6 M_s$ is measured when the dipolar interaction is strong; i.e., at a spacing of 200 nm. The remanence sharply drops as the interelement distance is increased

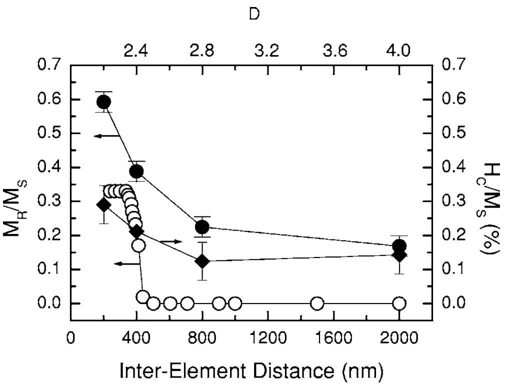

FIG. 4. Measured reduced remanent magnetizations (solid circles) and coercive fields (solid diamonds) of the arrays versus interelement distance. Open symbols are reduced remanences taken from numerical calculations by Zhang *et al.* (see Ref. 5). Lines are guides to the eye.

(spacing $\geqslant 400$ nm). This is in good qualitative agreement with the results of Zhang *et al.*[5] Using their notation $D = a/R$ with the lattice constant a, the element radius R, and by describing the size of the microelements by the radius R, our arrays range from $D=2.2$ to $D=4$. Thus, a direct comparison of the reduced remanences of our arrays with this theory is possible. They agree qualitatively well as can be seen in Fig. 4. It is clear that a quantitative agreement cannot be expected because the model describes arrays of interacting single-domain dots. However, the sharp decrease of the reduced remanence is seen in the calculation as well as in our experiment. The offset in the measured remanence in comparison to the calculated one is presumably caused by the additional shape anisotropy of our Fe microelements. When subtracting the anisotropy offset from the experimental remanences, an almost perfect quantitative agreement is obtained.

The high value of the reduced remanence at a spacing of 200 nm represents the tendency of the magnetization to stabilize itself at zero field. This effect can be observed directly in the images shown in Fig. 5, where magnetization states next to zero field are shown. They correspond to states B and C of Fig. 3. In case of stronger interaction, i.e., for an interelement spacing of 200 nm, an almost saturated state is kept [see Figs. 5(a) and 5(c)], while in case of nearly isolated elements irreversible magnetization processes have already switched significant parts of the element's magnetization [see Figs. 5(b) and 5(d)].

IV. CONCLUSION AND OUTLOOK

With MTXM we have directly observed the influence of dipolar interaction on dense arrays of Fe microelements. The magnetization processes are in qualitative agreement with the theoretical predictions. Arrays of increased density and reduced interelement spacing will be accessible with a new type of zone plates.[17] Future time-resolved investigations of nanostructured magnetic arrays prepared on strip lines with MTXM in the pump-and-probe mode are very tempting and of great interest for fast magnetic memories.

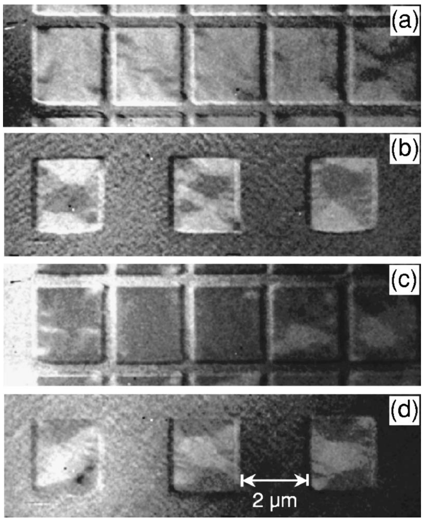

FIG. 5. Magnetization states next to zero applied field. State B in the upward sweep of the array with an interelement distance of (a) 200 nm and (b) 2000 nm. (c) and (d) corresponding magnetization in the down sweep (state C, see Fig. 3).

ACKNOWLEDGMENTS

We would like to thank Ulrich Merkt for valuable discussions. Financial support of the Deutsche Forschungsgemeinschaft via the Sonderforschungsbereich 508 "Quantenmaterialien" and the Sonderforschungsbereich 668 ″Magnetismus vom Einzelatom zur Nanostruktur″ is gratefully acknowledged.

[1] D. W. Abraham and Y. Lu, J. Appl. Phys. **98**, 023902 (2005).
[2] S. Chou, IEEE Trans. Magn. **85**, 652 (1997).
[3] C. A. Ross *et al.*, J. Appl. Phys. **91**, 6848 (2002).
[4] R. L. Stamps and R. E. Camley, Phys. Rev. B **60**, 11694 (1999).
[5] L. F. Zhang, C. Xua, P. M. Hui, and Y. Q. Ma, J. Appl. Phys. **97**, 103912 (2005).
[6] P. Wadhwa and M. B. A. Jalil, J. Magn. Magn. Mater. **294**, 83 (2005).
[7] R. Moskowitz and E. Della Torre, J. Appl. Phys. **38**, 1007 (1967).
[8] D. Süß, T. Schrefl, J. Fidler, and J. Chapman, J. Magn. Magn. Mater. **196–197**, 617 (1999).
[9] G. Meier, M. Kleiber, D. Grundler, D. Heitmann, and R. Wiesendanger, Appl. Phys. Lett. **72**, 2168 (1998).
[10] D. Grundler, G. Meier, K.-B. Broocks, C. Heyn, and D. Heitmann, J. Appl. Phys. **85**, 6175 (1999).
[11] R. L. Stamps and R. E. Camley, Phys. Rev. B **60**, 12264 (1999).
[12] P. Fischer, Curr. Opin. Solid State Mater. Sci. **7**, 173 (2003).
[13] G. Meier, R. Eiselt, M. Bolte, M. Barthelmess, T. Eimüller, and P. Fischer, Appl. Phys. Lett. **85**, 1193 (2004).
[14] M. Bolte, R. Eiselt, T. Eimüller, P. Fischer, and G. Meier, J. Magn. Magn. Mater. **290–291**, 723 (2005).
[15] P. Fischer, T. Eimüller, G. Schütz, M. Köhler, G. Bayreuther, G. Denbeaux, and D. Attwood, J. Appl. Phys. **89**, 7159 (2001).
[16] M. Donahue and D. Porter, Interagency Report NISTIR 6376, National Institute of Standards and Technology, Gaithersburg, MD, Sept. 1999.
[17] W. Chao, B. Harteneck, J. Liddle, E. Anderson, and D. Attwood, Nature (London) **435**, 1210 (2005).

4.2 Magnetization Dynamics in Confined Systems

After I had investigated the static magnetization configuration of ferromagnetic microelements, I studied the dynamic behavior of permalloy microelements due to pulsed or harmonic magnetic-field excitation via micromagnetic simulation. I had already optimized the micromagnetic simulation code during my masters thesis by using a Runge-Kutta algorithm with adaptive time steps [126]. This allowed me to simulate much longer time intervals ($\approx$ 100 ns) and larger elements than I could have with the normal OOMMF code. For the computation of a static magnetization configuration, one would usually choose a highly damped system, i.e., $\alpha \approx 0.1$ or even larger, to achieve critical damping and thus to arrive at the equilibrium state in minimal computation time. For a study of the dynamic behavior, such a high damping parameter would of course be unreasonable. As shown in my masters thesis, the Runge-Kutta integrator outperforms the Euler integrator for very small dampings by one to two orders of magnitude, depending on the problem size. For the present studies, damping parameters of α =0.005 [171] to α =0.008 [172] were used to conform to realistic values.

It was found that many modes superpose each other so that the observation of the spin-wave eigenmodes in real space is extremely difficult. I therefore programmed a spin-wave analysis tool in MATLAB that transformed the simulated magnetization states into Fourier space and thus allowed a detailed analysis of mode amplitudes and phases. MATLAB [127] has a long history in providing software for signal processing, and its near-mathematical notation made it an ideal language for this analysis tool. The resolution in the Fourier space $\Delta f = 1/T$ is limited by the length of the time interval T for which data is available, i.e., the simulation run [173]. Due to the *Nyquist–Shannon sampling theorem* [173] the sampling frequency $f_s = 1/\Delta t$ must be at least twice the maximum frequency f_{Ny} (*Nyquist frequency*) that one wants to investigate. This is because the spectrum is mirrored around f_{Ny} and the higher frequencies would otherwise overlap (*alias-effect*).

These limitations outline the constraints on the simulation – a short simulation run will yield a rough resolution in the frequency space, and making the time intervals too large reduces the cut-off frequency or introduces aliases into the spectra. For example, in Section 4.2.2 where I describe the simulation of 16×32 μm^2 large and 10 nm thick permalloy rectangles, excited by an oscillatory magnetic field at a frequency of 500 MHz, the constraints made it necessary to spatially partition the simulation data and compute the amplitude and phase images for individual regions before reassembling them for the final results.

Also, in comparing the calculated Fourier or spin-wave spectra to measured spectra, e.g., from ferromagnetic resonance experiments, one must be careful to not misinterpret the results. From the micromagnetic simulations one can compute the spectrum of the spatially averaged magnetization by Fourier transforming the averaged magnetization. Alternatively, one can first Fourier transform the magnetization for every magnetization vector and then average the amplitudes and phases. In this case one would preserve the modes with even spatial symmetry that cancel out in the spatial average. These two routes of computation correspond to spatially averaging methods such as ferromagnetic resonance spectroscopy [174] or spatially resolving measurement methods such as Kerr microscopy [175, 176], photoemission electron microscopy [171, 177], or time resolved X-ray microscopy [178].

Inspired by an experimental work done by the Regensburg group [175] I began my dynamic micromagnetic simulations with the investigations of Landau domain patterns excited by short field pulses with different spatial symmetries. The results of this study are outlined in Section 4.2.1. In Section 4.2.2 I report the results of a magnetic system driven by harmonic field excitation, leading to an unexpected excited state. The understanding gained in these two projects proved invaluable when we investigated magnetic structures excited by spin-polarized current pulses (see Section 4.4.2) and ac-currents (see Sections 4.4.1 and 4.4.3).

4.2.1 Spin-Wave Eigenmodes of Landau Domain Patterns

As a test case for my extended micromagnetic simulation code I simulated a permalloy square of the same dimensions as Perzlmaier *et al.* studied in their experimental work [175]. At remanence the magnetization in these squares forms a so-called *Landau domain pattern*, four triangular domains with ×-shaped 90° domain walls and a vortex at the center. Perzlmaier *et al.* used time-resolved scanning Kerr microscopy [176] and micro-focus Brillouin light scattering [179] to detect the magnetic response to short field pulses created by a microcoil (see Fig. 4.2(a)) so that the field acting on the magnetization was out-of-plane. They observed standing spin waves in the domains of the Landau patterns and could identify distinct modes (see Fig. 4.2(b)) that they called "transversal" and "longitudinal" modes. In my simulations I could observe those same mode but also identified other modes with even number of antinodes, that were not observed experimentally. In collaboration with Christian Bayer from the Technical University of Kaiserslautern I could show [180] that the spin-wave modes observed in the experiments and in the simulations could be described analytically by Damon-Eshbach Modes and magnetostatic backward volume spin-wave modes (see Section 2.4). This is evident from the dispersion relation computed from the simulation. I could also show that the symmetry and the frequencies of the spin-wave modes are determined by the symmetry of the exciting torque and the symmetry of the magnetization [172, 180].

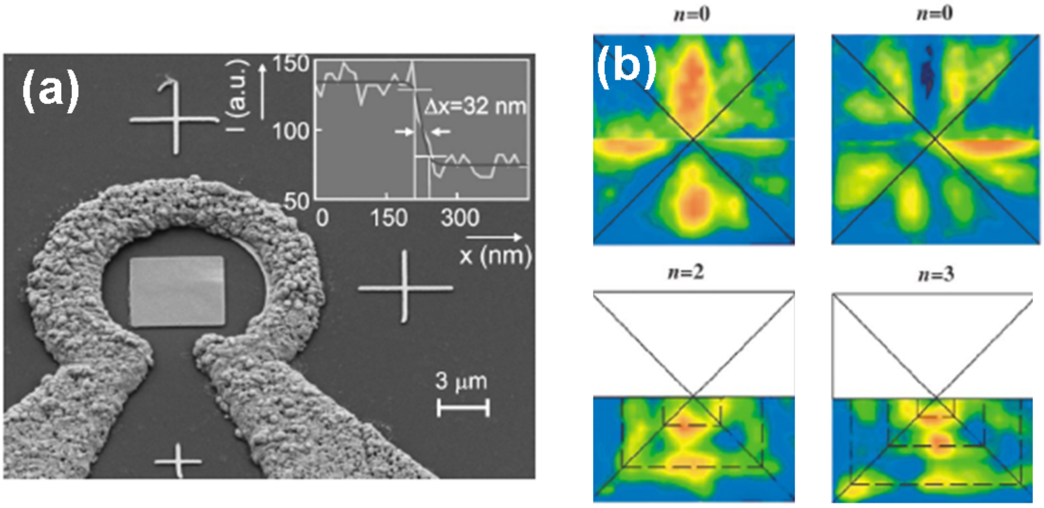

Fig. 4.2: Setup and results of the experiments of Perzlmaier *et al.* [175]. (a) Microcoil with the permalloy square, here from another experiment [178]. The coil is not a closed loop leading to a spatial inhomogeneity of the out-of-plane field pulse. (b) Results from Kerr microscopy (top halves of the images) and Brillouin light scattering (bottom halves) for different transversal quantization numbers denoted by n. From Ref. [175].

The work was published as **[P9]** and is reprinted here with permission from M. Bolte, G. Meier, and C. Bayer, Phys. Rev. B **73**, 052406 (2006), with Copyright (2006) by the American Physical Society. A conference article with a focus on the symmetry-dependence was published as **[P13]** in M. Bolte, G. Meier, and C. Bayer, *"Symmetry dependence of spin-wave eigenmodes in Landau-domain patterns"*, J. Magn. Magn. Mat. **316**, e526, Copyright Elsevier (2007). This work was presented at the Joint European Magnetism Symposia 2006 in San Sebastian, Spain. The work was also presented at other international workshops and conferences as **[C6]** and **[C7]**, at the Ludwig Maximillian University in Munich **[I2]**, the Johannes Gutenberg University in Mainz, **[I3]**, the Technical University of Kaiserslautern **[I4]**, and at a user meeting at the Advanced Light Source in Berkeley, CA, USA **[I5]**.

PHYSICAL REVIEW B **73**, 052406 (2006)

Spin-wave eigenmodes of Landau domain patterns

M. Bolte* and G. Meier
Institut für Angewandte Physik und Zentrum für Mikrostrukturforschung, Universität Hamburg, Jungiusstrasse 11, 20355 Hamburg, Germany

C. Bayer
Fachbereich Physik und Forschungsschwerpunkt MINAS, Technische Universität Kaiserslautern, Erwin-Schödinger-Strasse 56, 67663 Kaiserslautern, Germany

(Received 28 October 2005; published 17 February 2006)

We present micromagnetic simulations of the spin-wave spectra in Landau domain patterns. Ultrashort field pulses of various spatial symmetries are used to excite distinct spin-wave eigenmodes. The frequencies as well as the symmetry of the mode patterns depend on the symmetry of the exciting torque. The latter is determined by the symmetries of the field pulse and the magnetic ground state. Landau domain patterns have collective excitations, i.e., the spin-wave modes cannot be considered for each domain individually. We find transversal modes as well as longitudinal modes as observed experimentally. From the mode profiles an effective dispersion relation is deduced which resembles the dispersion relation for infinitely extended thin films.

DOI: 10.1103/PhysRevB.73.052406 PACS number(s): 75.30.Ds, 75.40.Gb, 75.75.+a, 75.40.Mg.

Understanding the magnetization dynamics of nano- and micrometer sized ferromagnets has been the aim of many recent experimental[1–6] and theoretical[5,7–10] studies. The interest is driven by potential applications in ultrafast nonvolatile magnetic storage cells[11] and logical units.[12] Ultrafast switching and reliable magnetization states require an accurate knowledge of the underlying eigenmodes and eigenfrequencies in micro- or nanomagnets. Micromagnetic simulation has become a powerful tool to study the static and dynamic magnetization processes in all these structures.[7,8,13,14]

The spectrum of confined spin waves in magnetic elements reflects the static magnetization and the internal field in these elements. So far several different effects have been discovered and described theoretically. First, the quantization of spin waves due to the spatial confinement was observed.[15,16] Then it was found that the inhomogeneous internal field in nonellipsoidal elements leads to localization of spin-wave modes.[8,17–20] Substantial effort has also been made in the understanding of inhomogeneously magnetized microstructures. Examples of these structures are inhomogeneously magnetized stripes,[21,22] ferromagnetic disks with a vortex and well-defined cylindrical symmetry,[1,2,5,7,9,10,13,23] rings with different spin-wave eigenmodes in varying magnetic field directions,[24] or squares.[1,3,4,6]

The study of Landau domain patterns which form in squares at remanence to minimize the magnetic stray-field energy[25] is of great interest because it allows the investigation of the basic magnetic constituents and properties in structured ferromagnets, namely, domains, domain walls, vortices, and their dynamics. It has been shown by Brillouin light scattering,[4] time-resolved scanning Kerr-effect microscopy,[1,4,6] and magnetic transmission x-ray microscopy,[3] that domains, domain walls, and vortices evoke distinct spin-wave modes. Experimentally, a number of factors such as the rise and fall times of exciting field pulses and the limited spatial and temporal resolution influence the spectra of observable spin-wave eigenmodes.

In this Brief Report, we present micromagnetic simulations of thin permalloy squares to identify their fundamental spin-wave eigenmodes. Our claim is that even small spatial asymmetries in the exciting field pulses can evoke different observable mode patterns and that properly chosen spatial symmetries of the pulses give access to the rich set of eigenmodes in ferromagnetic micro- and nanostructures. By using spatially inhomogeneous field pulses, we excite different modes and show that they reflect the symmetry of the exciting torque. We study the fundamental spin-wave eigenmodes of high symmetry as well as those that occur frequently in experiments due to an inhomogeneous spatial field distribution, e.g., in microcoils. In order to explain the basic principles, we here focus only on the fundamental modes with high symmetry. The discussion is also restricted to modes with maximum amplitude within the four domains. The discussion of low-frequency domain wall and vortex modes will be published elsewhere. The simulations show two main quantization directions for spin waves in each domain, perpendicular to and along the static magnetization. Both have been observed experimentally.[4] We count the maxima in the local power density with the mode numbers m and n. By m we denote the number of maxima perpendicular to the magnetization. As the four domains are triangular, the length of each domain along the magnetization is smaller close to the center of the square than at its edge. Therefore, we need m numbers $n_1, \dots, n_m$ to count the maxima along the magnetization from the center outward. The spin-wave modes need to be considered for the whole square and not for the individual domains. From the mode profiles an effective dispersion relation is derived which is linear in the wave vectors along the magnetization direction. We show that the spatial symmetry of the field pulses leads to corresponding rotational symmetries of the spin-wave eigenmodes and directly affects their spectra.

With NIST's micromagnetic framework OOMMF,[26] the time evolution of the magnetization was computed. We extended OOMMF with a fifth-order Runge-Kutta integrator with an adaptive time step for the Landau-Lifshitz equation in-

©2006 The American Physical Society

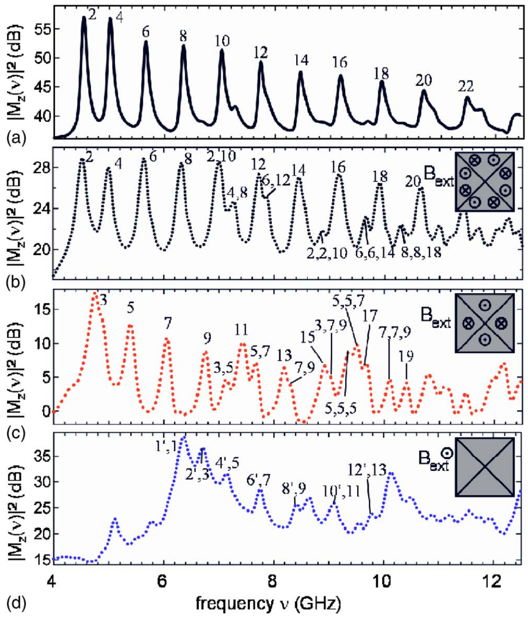

FIG. 1. (Color online) Spin-wave spectra for three out-of-plane excitations. All excitations were done on a 1×1 μm^2 16-nm-thick permalloy square with a sharp pulse of a FWHM of 2.5 ps. (a) Relaxation without pulse from a nonequilibrium initial state, and excitation (b) with a 20 mT pulse having a $\pi/2$ rotational symmetry (see inset), (c) with a 20 mT pulse having a π rotational symmetry (inset), and (d) with a 20 mT spatially uniform pulse (inset) on a fully relaxed ground state. The peaks in the spectra are identified for the transversal orders $m=1$, 2, and 3 (see also Figs. 2 and 3).

stead of the standard Euler evolver. This accelerated the simulations by about two orders of magnitude.[27] Permalloy parameters were used, i.e., exchange constant $A=1.3\times 10^{-11}$ J/m, saturation magnetization $M_s=8\times 10^5$ A/m, uniaxial anisotropy $K_1=100$ J/m^3, and damping constant $\alpha=0.008$. Squares of four lateral sizes 750 nm, 1 μm, 2 μm, and 4 μm and a thickness of 16 nm were simulated. The lateral cell size was 5 nm except for the 4 μm square where it was 10 nm. The ground state was determined for each size separately. The magnetization was excited by out-of-plane field pulses with full width at half maximum (FWHM) of 2.5 ps and a peak amplitude of 20 mT. The pulses have exponentially rising and falling edges to account for a gradual change in the simulation's time step. The frequency response of the field pulse is virtually constant between zero and well over 100 GHz. The pulse lengths and heights were chosen small enough to ensure that all spin-wave modes are in the linear regime. The external field pulses are simulated to be in the out-of-plane direction to prevent unwanted domain wall or vortex motion. Such motion would change the magnetic state and thus the spin-wave spectrum.[14] Because the magnetization precesses around the effective internal field, a small in-plane excitation can be simulated by a corresponding out-of-plane field if the resulting torque remains the same. The pulse was spatially modulated to locally invert its direction and thus to allow the excitation of spin-wave eigenmodes of distinct symmetries. The magnetization response to the excitation was recorded for simulation times T between 20 and 45 ns, long enough to achieve the frequency resolution $\Delta\nu=1/T$ necessary to resolve adjacent modes in the spectra. The magnetization precession was first locally Fourier transformed and then the local power density was integrated over the square to yield the global power density.[1,7,22,28]

Figure 1 shows the global power density of four different simulations. The peaks correspond to spin-wave eigenmodes. Their intensities are at least four times higher than the background level. Figure 2 shows the local power densities (top) and the corresponding phases (bottom) for exemplary eigenmodes [compare peaks in Figs. 1(b) and 1(c)]. The most prominent feature in Fig. 1 is the variation of the spectra for different spatial symmetries of the exciting pulse fields. To understand how modes are affected by the symmetry of a pulse field, it is important to realize that even a spatially homogeneous magnetic pulse $\vec{H}_{\text{pulse}}$ can lead to inhomogeneous modes. If the magnetization is inhomogeneous, an inhomogeneous torque $\vec{M}(\vec{r},t)\times\vec{H}_{\text{pulse}}(t)$ is created by a homogeneous pulse.[22] In Figure 1(a) the initial state was taken artificially so that the static magnetization rotates around the center without any out-of-plane components. The relaxation to the ground state leads to a radially homogeneous torque in the domains. Only modes with even indices n are excited. As the Fourier transform of the torque perpendicular to the static magnetization has its maximum at $k_\perp=0$, only waves with wave vectors $k_\perp\approx 0$, i.e., $m=1$ modes, are excited. Along the magnetization the torque contains higher Fourier components due to the domain walls. Oscillations of the vortex do not contribute to the eigenmodes shown in Fig. 2 since there is no intensity in the center of the structure but only inside the domains. Nevertheless, the existence of the vortex substantially determines which kind of modes are excited. In

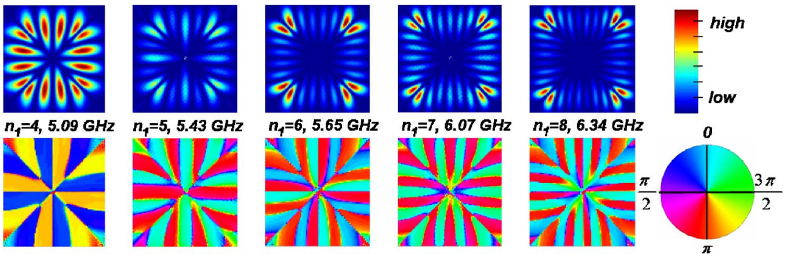

FIG. 2. (Color online) Spatial images of the squared amplitude (top row) and the phases (bottom row) of five exemplary longitudinal eigenmodes of the 1×1 μm^2 square. The numbers n_1 indicate the order of the longitudinal modes for the first transversal mode $m=1$ (see Fig. 1).

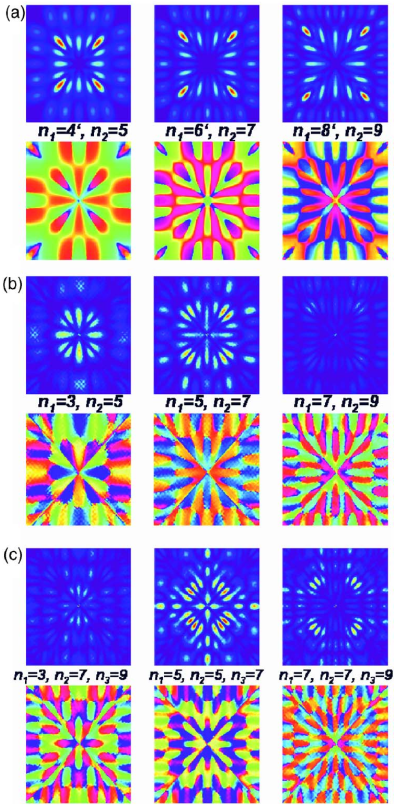

FIG. 3. (Color online) Spatial images of the squared amplitudes (top row) and the phases (bottom row) for a 1×1 μm^2 square. (a) $m=2$ transversal modes excited by a uniform field pulse [see Fig. 1(d)]. Dashes indicate modes with maximum excitation in a domain wall. $m=$(b) 2 and (c) 3 transversal modes excited by the field pulses shown in the insets of Fig. 1(c).

Fig. 1(b), the completely relaxed ground state with a vortex is taken as the initial state for the simulation, excited with a pulse of $\pi/2$ rotational symmetry. The same modes as in Fig. 1(a) and also additional higher-order transversal eigenmodes appear. This supports the assumption that the relaxation creates spin waves of opposite phase that propagate parallel and antiparallel to the static magnetization on both sides of a domain wall. It also shows the impact of the vortex, even though it is not excited.

The modes in Fig. 1(b) show the same $\pi/2$ rotational symmetry as the exciting torque. The odd modes in Figs. 1(c) and 2, on the other hand, were obtained after applying a pulse field with π rotational symmetry. Their magnitudes and phases show the same spatial symmetry as the exciting torque. This is true for all investigated excitations. Modes that result from the torque due to a homogeneous out-of-plane field pulse are depicted in Figs. 1(d) and 3. In this case, the exciting torque is $\pi/2$ rotationally symmetric and inhomogeneous perpendicular to the static magnetization. Waves with $k_\perp > 0$ and transversal modes, i.e., mixtures of Damon-Eshbach and backward volume modes, are excited because the maximum in the Fourier transform of the exciting torque is at $k_\perp > 0$. Figure 3 shows the local power density and the corresponding phases for some modes which have nodes perpendicular to the magnetization. Also simulated were excitations with 2π rotational symmetry, with the transition line between different pulse-phase regions lying either diagonally or along one of the in-plane axes of the square. The eigenmodes that result when two opposing domains are excited exactly out of phase show an odd number of maxima in these domains and an even number in the domains over which the pulse phase changes its sign, because a nodal line has to be in the latter domains. Similar modes have been experimentally observed before [see the bottom part of Fig. 4(b) of Ref. 4]. Due to space limitation, the results for 2π rotationally symmetric pulses cannot be shown here.

These excitation properties have several interesting implications. For odd modes, the outermost maxima of each domain are in phase, while for the even modes they are exactly out of phase. Furthermore, in the domains with an odd number of maxima there is a nonzero average amplitude, while in the case of even modes the averaged amplitude over one domain is always zero. For π and $\pi/2$ rotationally symmetric excitations, the neighboring outer maxima of adjacent domains always exhibit a phase shift of π to minimize the stray-field energy.[29] In other words, the spin-wave excitations discussed here are excitations of the whole structure that cannot adequately be discussed when restricting oneself to an individual domain. Since in experiments typically only

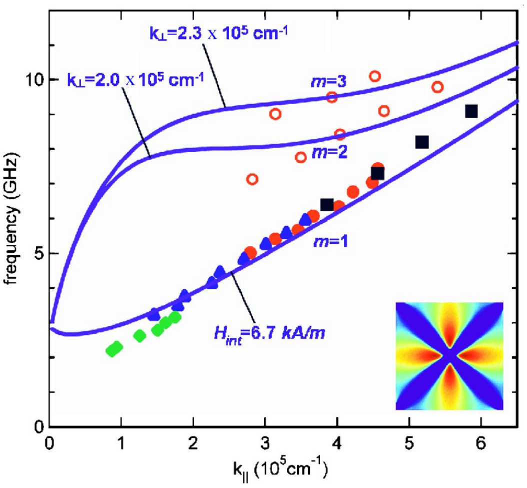

FIG. 4. (Color online) Dispersion relations of the longitudinal eigenmodes for different squares and transversal orders $m=1-3$. Closed symbols denote $m=1$ modes. (Green) diamonds are for the 4×4 μm^2, (blue) triangles for the 2×2 μm^2, (red) solid circles for the 1×1 μm^2, and (black) squares for the 750×750 nm^2 pattern. The higher transversal modes [open (red) circles] $m=2$ and 3 are for the 1×1 μm^2 square. Lines represent analytical predictions for an infinite thin film. The inset shows the local internal field with the colors ranging from fields with values below zero (blue) up to 6.7 kA/m (red).

one type of pulse is used, not all modes are necessarily observed. Actually, it is very difficult to predict which modes will be observed, as even a slight asymmetry in the experimental setup will affect the excitation. Equally, small deviations in the micromagnetic structure of a sample can lead to the excitation of measurably altered modes.

Another interesting feature is that the modes are nearly equidistant in frequency as a function of n for constant m. From spatial mode profiles as in Figs. 2 and 3 the effective wave vectors of a specific mode can be deduced from the distance between maxima parallel ($k_{\parallel}$) or perpendicular ($k_{\perp}$) to the static magnetization. The eigenfrequencies and wave vectors of the individual eigenmodes lead to their effective dispersion relations. In Fig. 4. the dispersion relations for the spin waves of Landau patterns with lateral dimensions of 750 nm, 1 μm, 2 μm, and 4 μm as well as higher-order transversal modes for the 1×1 μm^2 square are shown. There are two remarkable features. The dispersion relation for $m=1$ is linear and the modes for structures of different sizes have the same dispersion relation. The solid lines are from analytical results for an infinite thin film[30] with the same material parameters as for the micromagnetic simulation of the squares. The lower line was calculated with $k_{\perp}=0$ for a maximum internal field strength of $H_{\text{int}}=6.7$ kA/m. This value was determined from the simulation (see inset of Fig. 4). The simulation and the analytical description agree very well, even though it has to be remembered that the internal field is inhomogenenous as shown in the inset. The $m=2$ and 3 transversal modes are fitted by spin waves with larger perpendicular components $k_{\perp}$ and an H_{int} of 6.7 kA/m within the same model. The slopes of these curves do not fit the simulated results. This implies that one cannot conclusively calculate the spin-wave eigenmodes for Landau domain patterns within the infinite film model, but that the dispersion relation depends on the location of the eigenmodes within the square.

To conclude, we describe spin-wave eigenmodes in Landau domain patterns of different lateral dimensions. The modes are excited with pulse fields of various spatial symmetries. The spin-wave eigenmodes of Landau domain patterns are collective excitations, and cannot be considered for each domain individually. The eigenmodes are quantized and localized in the domains along and perpendicular to the static magnetization. They are equidistant in frequency and lead to linear effective dispersion relations. The excited modes reflect the spatial symmetry of the magnetic pulse field. Small deviations of the micromagnetic initial state can lead to different modes.

We thank B. Hillebrands, M.P. Kostylev, and U. Merkt for fruitful discussions. Financial support of the Deutsche Forschungsgemeinschaft via the Sonderforschungsbereich 508 “Quantenmaterialien” and the Sonderforschungsbereich 668 “Magnetismus vom Einzelatom zur Nanostruktur” (M.B. and G.M.) and the Studienstiftung des Deutschen Volkes (C.B.) is gratefully acknowledged.

---

*Electronic address: mbolte@physik.uni-hamburg.de

[1] J. P. Park *et al.*, Phys. Rev. B **67**, 020403(R) (2003).
[2] M. Buess *et al.*, Phys. Rev. Lett. **93**, 077207 (2004).
[3] H. Stoll *et al.*, Appl. Phys. Lett. **84**, 3328 (2004).
[4] K. Perzlmaier *et al.*, Phys. Rev. Lett. **94**, 057202 (2005).
[5] X. Zhu *et al.*, Phys. Rev. B **71**, 180408(R) (2005).
[6] J. Raabe *et al.*, Phys. Rev. Lett. **94**, 217204 (2005).
[7] M. Buess *et al.*, Phys. Rev. B **71**, 104415 (2005).
[8] M. Grimsditch *et al.*, Phys. Rev. B **69**, 174428 (2004).
[9] R. Zivieri and F. Nizzoli, Phys. Rev. B **71**, 014411 (2005).
[10] B. A. Ivanov and C. E. Zaspel, Phys. Rev. Lett. **94**, 027205 (2005).
[11] S. Tehrani *et al.*, Proc. IEEE **91**, 703 (2003).
[12] A. Ney *et al.*, Nature (London) **425**, 485 (2003).
[13] K. Yu. Guslienko *et al.*, Phys. Rev. B **71**, 144407 (2005).
[14] A. Krasyuk *et al.*, Phys. Rev. Lett. **95**, 207201 (2005).
[15] J. Jorzick *et al.*, Phys. Rev. B **60**, 15194 (1999).
[16] Y. Roussigné *et al.*, Phys. Rev. B **63**, 134429 (2001).
[17] J. Jorzick *et al.*, Phys. Rev. Lett. **88**, 047204 (2002).
[18] J. P. Park *et al.*, Phys. Rev. Lett. **89**, 277201 (2002).
[19] C. Bayer *et al.*, Appl. Phys. Lett. **82**, 607 (2003).
[20] C. Bayer *et al.*, Phys. Rev. B **72**, 064427 (2005).
[21] M. Bailleul *et al.*, Phys. Rev. Lett. **91**, 137204 (2003).
[22] C. Bayer *et al.*, Phys. Rev. B **69**, 134401 (2004).
[23] L. Giovannini *et al.*, Phys. Rev. B **70**, 172404 (2004).
[24] F. Giesen *et al.*, Appl. Phys. Lett. **86**, 112510 (2005).
[25] L. D. Landau and E. M. Lifshitz, Phys. Z. Sowjetunion **8**, 153 (1935).
[26] M. J. Donahue and D. G. Porter, Interagency Report No. NISTIR 6376, National Institute of Standards and Technology, Gaithersburg, Maryland, 1999 (unpublished).
[27] M. Bolte, G. Meier, and D. P. F. Möller, in Proceedings of the 19th European Conference on Modelling and Simulation, 2005, edited by Y. Merkuryev, R. Zobel, and E. Kerkhoffs (SCS Publishing House, Ghent, 2005), pp. 574–579.
[28] R. D. McMichael and M. D. Stiles, J. Appl. Phys. **97**, 10J901 (2005).
[29] M. P. Kostylev *et al.*, Phys. Rev. B **69**, 064408 (2004).
[30] B. A. Kalinikos and A. N. Slavin, J. Phys. C **19**, 7013 (1986).

Available online at www.sciencedirect.com
ScienceDirect
Journal of Magnetism and Magnetic Materials 316 (2007) e526–e528
Journal of magnetism and magnetic materials
www.elsevier.com/locate/jmmm

Symmetry dependence of spin-wave eigenmodes in Landau-domain patterns

M. Bolte[a,*], G. Meier[a], C. Bayer[b]

[a]Institut für Angewandte Physik und Zentrum für Mikrostrukturforschung, Universität Hamburg, Jungiusstraße 11, 20355 Hamburg, Germany
[b]Fachbereich Physik und Forschungsschwerpunkt MINAS, Technische Universität Kaiserslautern, Erwin-Schödinger-Straße 56, 67663 Kaiserslautern, Germany

Available online 12 March 2007

Abstract

Spin-wave eigenmodes in thin permalloy squares with Landau-domain patterns are investigated by micromagnetic simulation. Both the spatial symmetry of an exciting field pulse and the symmetry of the internal field determine the frequency and spatial distribution of the spin waves. With each symmetry, only a subset of all the possible eigenmodes can be observed. Our findings confirm the presence of longitudinally and transversally localized modes. Comparison with dispersion relations from analytical theory allows the unambiguous identification of the modes as backward volume and Damon–Eshbach modes, respectively.
© 2007 Elsevier B.V. All rights reserved.

PACS: 75.30.Ds; 75.40.Gb; 75.75.+a; 75.40.Mg

Keywords: Spin wave; Micromagnetic simulation; Eigenmode; Symmetry

Author's personal copy

1. Introduction

The magnetization dynamics of small ferromagnetic particles are actively studied experimentally [1–4] and theoretically [3–5] due to their potential application as ultrafast magnetic storage elements. Reliable switching and thermally stable magnetization states require an accurate knowledge of the underlying eigenmodes and eigenfrequencies. In recent years, micromagnetic simulation has become a powerful tool to study the static and dynamic magnetization processes in small magnetic particles [4–5].

The spectrum of confined spin waves in magnetic elements reflects the energy density given by the static magnetization and the internal field. Standing spin waves in finite structures are known to be energetically quantized [6] and, in case of an inhomogeneous internal field distribution, spatially localized [4,7,8]. Landau-domain patterns (LDP) which form in squares at remanence to minimize the magnetic stray-field energy allow the investigation of the basic magnetic constituents in structured ferromagnets, namely domains, domain walls, and vortices. It is known that these constituents evoke distinct spin-wave modes. Recently, we presented results from micromagnetic simulations of thin permalloy squares that showed that the spatial symmetry of the exciting torque leads to corresponding symmetries of the spin-wave eigenmodes and directly affect their spectra, i.e., the eigenfrequencies of the magnetic system [5]. Here we demonstrate how due to the symmetries of a field pulse only distinct spin-wave vectors are excited so that only a subset of the possible eigenmodes can be observed. As an example, we focus on transversal modes in such squares and show that they can be approximated by the spin-wave dispersion relation for infinite thin films.

To accomplish this, we used the micromagnetic simulation package OOMMF [9], extended with a fifth-order adaptive time step Runge–Kutta, to compute the influence of a magnetic field pulse on the magnetization over time. Standard parameters for permalloy were used, i.e., exchange constant $A = 1.3 \times 10^{-11}$ J/m, saturation magnetization $M_S = 8 \times 10^5$ A/m, uniaxial anisotropy $K_1 = 100$ J/m^3, and damping constant $\alpha = 0.008$. The simulated

---

*Corresponding author. Tel.: +49 40 42838 3629; fax: +49 40 42838 3954.
E-mail address: mbolte@physik.uni-hamburg.de (M. Bolte).

0304-8853/$ - see front matter © 2007 Elsevier B.V. All rights reserved.
doi:10.1016/j.jmmm.2007.03.008

squares had the dimensions of 750 nm, 1, 2, and 4 μm in the lateral direction and a thickness of 16 nm. The lateral cell sizes were 5 and 10 nm. The magnetization was excited by out-of-plane field pulses with full widths at half maximum of 2.5 ps and a peak amplitude of 20 mT. The pulse was periodically modulated in space to locally invert its direction and thus to allow the excitation of spin-wave eigenmodes of distinct symmetries. The magnetization was Fourier transformed for each simulation cell individually after zeropadding and applying a Hamming window to ensure minimal alias frequencies in the spectrum. The local power density was then integrated over the volume of the square to yield the global power density. Just as in Ref. [5], the eigenmodes were determined by selecting frequencies at which the averaged oscillation amplitude is enhanced and the spatial phase distribution shows abrupt phase transitions hinting at standing spin waves.

2. Results

Fig. 1 shows the local power densities (top rows) and the corresponding phases (bottom rows) for three different exciting torques. The symmetry of the torques is indicated on the right. The most prominent feature in Fig. 1 is the variation of the local power density for different spatial symmetries of the exciting field pulses. In Fig. 1(a) the Landau state is excited with a pulse of $\pi/2$ rotational symmetry. The modes show the same symmetry as the exciting torque, and adjacent oscillation maxima are exactly out-of-phase, suggesting the presence of standing spin waves for given frequencies. The odd modes in Fig. 1(b) were obtained after applying a pulse field with π rotational symmetry. Modes that result from a torque due to a homogeneous out-of-plane field pulse are depicted in Fig. 1(c). They show longitudinal as well as transversal components in the spin-wave vector, visible by nodes and antinodes both parallel and perpendicular to the static magnetization. In the following, we focus on modes originating from this excitation.

Fig. 2 shows power density maps of 750 nm (a)–(c) and 2 μm (d)–(f) sized LDPs excited by phase-uniform out-of-plane field pulses at 9.6 GHz (a), 10.5 GHz (b), 10.9 GHz (c), 5.4 GHz (d), 10.0 GHz (e), and 15.7 GHZ (f). The uniform out-of-plane excitation causes a discretization of the spin-wave modes perpendicular to the static magnetization. Even though the modes are a combination of longitudinal and transversal modes, the modes presented here, with the exception of Fig. 2(f), are mainly parallel to the static magnetization.

The triangular geometry of the domains in LDPs leads to a varying number of longitudinal antinodes for each transversal antinode if the spin-wave vector is to remain constant. Therefore, the nomenclature in Fig. 1 assigns each mode pattern a tuple of integer numbers representing the number of maxima along the static magnetization in the first, second, etc. transversal mode, counted from the edge inward. The nomenclature shall not infer such quantization to be present in all the possible modes, as

My personal copy

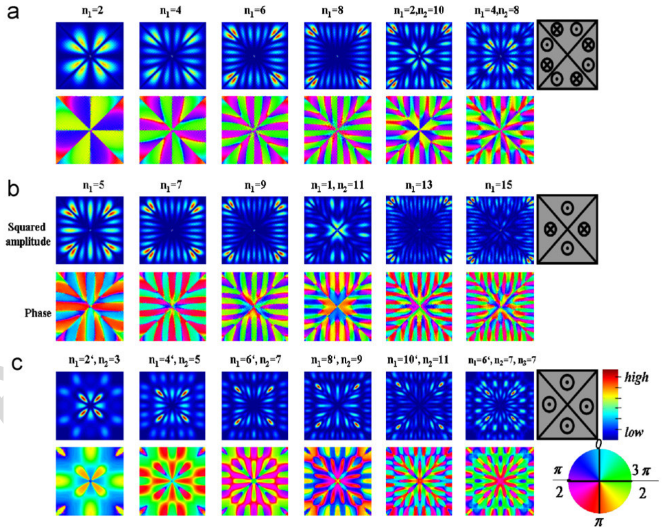

Fig. 1. Squared amplitudes (top rows) and phases (bottom rows) of a $1 \times 1\,\mu\mathrm{m}^2$ 16 nm thick permalloy square excited by a 20 mT out-of-plane field pulse with three different spatial symmetries. (a) Excitation pulse having a $\pi/2$ rotational symmetry, (b) a π-rotational symmetry, and (c) homogeneous excitation. Shown are the first six modes and their mode numbers (cf. Fig. 2 of Ref. [5]).

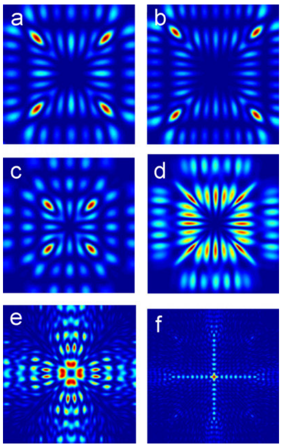

Fig. 2. Power densities of a 750 × 750 nm^2 (a)–(c) and a 2 × 2 μm^2 (d)–(f) square excited by a homogeneous out-of-plane field pulse for selected frequencies.

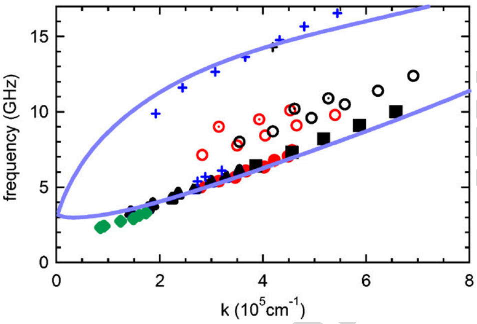

Fig. 3. Effective spin-wave dispersion relation for thin permalloy squares of 750 nm (black), 1 μm (red), 2 μm (blue), and 4 μm (green) lateral sizes. The shapes denote the number i of maxima perpendicular to the static magnetization (see Fig. 1): $i = 1$—solid shapes, $i = 2$—circles, $i = 3$—circles with dots. Crosses represent wave vectors almost perpendicular to the static magnetization (see Fig. 2(f)).

other, e.g., radial symmetries are evident in LDPs (see Fig. 2(c) of Ref. [10]). The distance between two maxima in the direction of the magnetization, or perpendicular to it in the case of the transversal modes such as shown in Fig. 2(f), was used to determine the wave length and thus the wave vector. The wave vectors were plotted against the respective eigenfrequency. The resulting effective spin-wave dispersion relations are seen in Fig. 3. It shows that the first three longitudinal orders (filled shapes, circles, and circles with dots) have linear dispersions, thus justifying them to be called backward-volume modes. The frequency difference between them can be understood by the varying internal fields in the center of a domain or closer to the vortex core. The dispersion relation, indicated by crosses, originates from predominantly transversal spin waves (see Fig. 2(f)). Fitting the data points with the analytical theory for infinite thin films [11] yields good agreement justifying them to be called Damon–Eshbach modes.

3. Conclusion

We simulated spin-wave eigenmodes in Landau-domain patterns of different lateral dimensions. The spatial localization, the amplitude, and the phase of the modes are derived by Fourier transformation. By analyzing their effective dispersion relations, the longitudinal and transversal modes can be unambiguously linked to backward-volume and Damon–Eshbach modes of infinitely extended thin films.

Acknowledgments

We thank B. Hillebrands, U. Merkt, and J. Podbielski for fruitful discussions. Financial support of the DFG via SFB 668 “Magnetismus vom Einzelatom zur Nanostruktur” and GrK 1286 “Functional Metal-Semiconductor Hybrid Systems” (M.B. and G.M.) and the Studienstiftung des Deutschen Volkes (C.B.) is gratefully acknowledged.

References

[1] J.P. Park, et al., Phys. Rev. B 67 (2003) 020403(R).
[2] K. Perzlmaier, et al., Phys. Rev. Lett. 94 (2005) 057202.
[3] X. Zhu, et al., Phys. Rev. B 71 (2005) 180408(R).
[4] M. Grimsditch, et al., Phys. Rev. B 69 (2004) 174428.
[5] M. Bolte, G. Meier, C. Bayer, Phys. Rev. B 73 (2006) 052406.
[6] J. Jorzick, et al., Phys. Rev. B 60 (1999) 15194.
[7] J. Jorzick, et al., Phys. Rev. Lett. 88 (2002) 047204.
[8] J.P. Park, et al., Phys. Rev. Lett. 89 (2002) 277201.
[9] M.J. Donahue, D.G. Porter, OOMMF User’s Guide Version 1.0, in Interagency Report No. NISTIR 6376, National Institute of Standards and Technology, Gaithersburg, MD, 1999.
[10] M. Yan, et al., Phys. Rev. B 73 (2006) 014425.
[11] B.A. Kalinikos, A.N. Slavin, J. Phys. C 19 (1986) 7013.

Author's personal copy

4.2.2 Mode-Trapping in Landau Flux-Closure Structures

I also investigated large ($16 \times 32\ \mu\text{m}^2$) and 10 nm thin permalloy rectangles with a Landau domain pattern that were excited by magnetic field pulses with a repetition rate of 500 MHz. These pulses were applied through a copper stripline on which the samples lay. The magnetic structures were imaged by X-ray photoemission electron microscopy performed at the Berlin Light Source (BESSY) by Alexander Krasyuk and coworkers from the Johannes Gutenberg University of Mainz during the so-called *low α-mode*. In this mode, the X-rays had an extremely short full width at half maximum (FWHM) of only 3 ps which allowed them with their microscope and special electronic equipment to have an excellent time resolution. They observed a puzzling phenomenon that they at first could not understand: Under the influence of the stroboscopic field pulses the center domain wall was moved in the direction of the field pulses proportional to the strength of the field pulses. One would expect that the domains with parallel magnetic moments would be enlarged so that the wall would move perpendicular to the field direction.

Alexander Krasyuk approached me during tthe IFF Spring School in Jülich, and we started a collaboration in the course of which I simulated the dynamics of such a permalloy rectangle. In the simulations I had to deal with severe constraints: The exact damping parameter and saturation magnetization were not known. Also, to observe the effect I knew I had to simulate longer than the settling time of the magnetization (more than 50 periods, i.e., 100 ns). In addition, the sample was unusually large. This meant either making the simulation cell size much larger than the exchange length λ making the results less reliable or taking much more time and computer memory. I approached the problem by simulating the dynamics of the permalloy rectangles with varying cell sizes for short periods of time. Then I compared the magnetization oscillations, i.e., their eigenfrequencies. I found that for cell sizes smaller than 10 nm the time-dependent magnetization was virtually the same. Due to memory constraints I simulated a $8 \times 16\ \mu\text{m}^2$ rectangle instead of the $16 \times 32\ \mu\text{m}^2$ which still took many weeks to simulate.

My simulations showed several details that helped to solve the riddle: First an initial asymmetry was needed to cause the domain wall motion in the right direction. Second, by performing Fourier transforms of the oscillations I could show that the same modes exist in the experiment as in the simulation (see Figs. 4.3(a) and (b), respectively). Professor Hans Joachim Elmers then came up with a model that explained the observations: A self-trapping of the dominant spin-wave mode when the system is excited just below resonance. Assuming an initial asymmetry of the domain wall to the right, the left domain has a slightly lower resonance frequency than the right domain and is thus closer to the

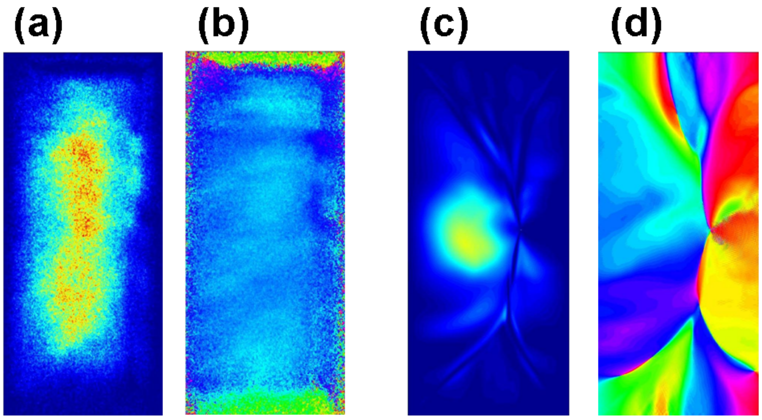

Fig. 4.3: Amplitudes and phases of the second eigenmode of a permalloy platelet. The colors in (a) and (c) represent the amplitude of the mode, ranging from blue for low intensity over yellow to red for high intensity. The corresponding phases ((b) and (d)) range from $-\pi$ (blue) over 0 (green) to π (red). (a) and (b): Amplitudes and phases at 1.25 MHz, derived by Fourier transforming the photoemission electron microscopy images. (c) and (d): Amplitudes and phases at 1.5 MHz derived from micromagnetic simulation.

excitation frequency. This results in a higher oscillation amplitude in the left domain, and the domain expands. Counteracting is the increase in magnetostatic energy from the increase of the domain so that the new equilibrium position of the domain wall is input-power dependent. The work was published as **[P7]** and is reprinted here in its entirety with permission from A. Krasyuk, F. Wegelin, S. A. Nepijko, H. J. Elmers, G. Schönhense, M. Bolte, and C. M. Schneider, Phys. Rev. Lett. **95**, 207201 (2005). Copyright (2005) by the American Physical Society. The results were also presented at a workshop on synchrotron radiation (see **[C8]**) and at a talk at the University of Mainz (see **[I3]**).

PRL **95,** 207201 (2005) PHYSICAL REVIEW LETTERS week ending 11 NOVEMBER 2005

Self-Trapping of Magnetic Oscillation Modes in Landau Flux-Closure Structures

A. Krasyuk, F. Wegelin, S. A. Nepijko, H. J. Elmers,* and G. Schönhense
Institut für Physik, Universität Mainz, D-55128 Mainz, Germany

M. Bolte
Institut für Angewandte Physik und Zentrum für Mikrostrukturforschung, Universität Hamburg, Jungiusstrasse 11, Hamburg D-20355, Germany

C. M. Schneider
Institut für Festkörperforschung IFF-6, Forschungszentrum Jülich GmbH, D-52425 Jülich, Germany

(Received 29 July 2005; published 7 November 2005)

We investigated the magnetodynamics in rectangular Permalloy platelets by means of time-resolved x-ray photoemission microscopy. 10 nm thick platelets of 16×32 μm size were excited by an oscillatory field along the short side of the sample with a fundamental frequency of 500 MHz and considerable contributions of higher harmonics. Under the influence of the oscillatory field, the Néel wall in the initial classical Landau pattern shifts away from the center, corresponding to an induced magnetic moment perpendicular to the exciting field. This phenomenon is explained by a self-trapping effect of the dominating spin-wave mode when the system is excited just below the resonance frequency. The basic driving mechanism is the maximization of entropy.

DOI: 10.1103/PhysRevLett.95.207201 PACS numbers: 75.40.Gb, 75.60.−d, 75.75.+a

Excitations of magnetic moments in nanostructures have recently attracted considerable attention [1–5] due to their relevance to high-frequency applications of magnetic particles in data storage devices. Advanced magnetic recording technology pushes the switching time into the gyromagnetic regime. For mesoscopic elements, the high-frequency behavior is governed by confined spin-wave eigenmodes as visible, e.g., in Brillouin light scattering [2,6]. So far, most studies have addressed the simplest case of elements in an almost monodomain state [6,7]. In larger microstructures, magnetic stray fields are minimized by the formation of multidomain configurations. Thin rectangular platelets of Permalloy often exhibit a Landau flux-closure structure comprising a Néel wall in the center [8].

The magnetization dynamics is quantitatively described by the Landau-Lifshitz-Gilbert equation [9] that resembles the equation of motion for a spinning top, because the magnetic moment is accompanied by an angular momentum. In the ultrafast regime, the torque acting on the local magnetization $\vec{M}$ becomes the dominant factor. This torque may initiate a precessional motion of $\vec{M}$, which can be observed, if the Fourier spectrum of the excitation by an external field comprises significant components of the precessional eigenfrequency of the system. In particular, $\vec{M}$ should not be affected, if the local torque disappears.

In this Letter, we report on the striking phenomenon of a magnetic moment induced perpendicular to an exciting ac magnetic field. This phenomenon occurs for a Landau flux-closure structure excited slightly off resonance. We show that the induced perpendicular moment, which leads to a domain wall shift despite zero local torque, is caused by a self-trapping of an oscillating mode, thus maximizing the energy exhausted off the exciting field.

The time dependent spatial distribution of the magnetization was measured using a photoemission electron microscope (PEEM) [10]. The PEEM measures the spatial distribution of the x-ray absorption via the electron yield of secondary electrons [11]. When the energy of circularly polarized (polarization vector $\vec{P}$) photons is tuned to the Ni-L_3 absorption edge, the electron yield varies with the relative orientation of magnetization ($\vec{M}$) and $\vec{P}$. X-ray magnetic circular dichroism (XMCD) images are obtained from two images taken with opposite polarization (+ and −). In order to visualize magnetic domains, we calculated the asymmetry $I_i = (I_i^+ - I_i^-)/(I_i^+ + I_i^-)$ at each pixel (Fig. 2), which is proportional to $\vec{M} \cdot \vec{P}$. The samples are Permalloy ($Ni_{80}Fe_{20}$) platelets with 16 μm width, 32 μm length, and 10 nm thickness, placed on a coplanar waveguide (Cu, 50 μm width, 200 nm thickness) with the long side parallel to the waveguide. The in-plane direction of the x-ray beam (incident angle 65°) was oriented perpendicular to the waveguide and parallel to the exciting field. Because of the grazing incidence of the x rays, we are most sensitive to the in-plane magnetization component along the short side of the platelet.

An externally triggered pulse generator injected the high-frequency current pulses into the waveguide. The actual pulse shape [see curves I, II, and III in Fig. 1(a)] was derived from the apparent change of the sample size, when the current pulse passes the field of view. The voltage pulse accompanying the current pulse slightly changes the magnification of the electron optical lens [12]. An absolute value for the magnetic field results from the voltage signal measured at the output of the waveguide using a fast

© 2005 The American Physical Society

oscilloscope. The maximum field values are of the order of 2 Oe [Fig. 1(a)]. The output shield of the pulse generator was set to floating ground. Thus, the mean current through the waveguide remains zero, and we merely apply a 500 MHz ac signal with considerable contribution of higher harmonical components [Fig. 1(b)] and synchronized with the x-ray pulses from the synchrotron.

Time-resolved experiments are performed by stroboscopic illumination of the sample by x-ray pulses produced by electron bunches in the synchrotron ring ($t_{\mathrm{FWHM}} = 3$ ps, low α mode [13]) with a repetition rate of 500 MHz. The ac driving current and the probe pulses are synchronized via a variable electronic delay t. The sample is thus excited and probed every 2 ns. To acquire an image, we typically integrate the signal for 30 s, thus averaging over 1.5×10^{10} pump-probe cycles.

Snapshots of the time evolution of the magnetization $\vec{M}$ in the Permalloy platelet comprising a Landau flux-closure pattern are shown in Fig. 2 for the smallest field pulse. Micromagnetic simulations [14] were used to verify the experimental findings. Permalloy rectangles of the same aspect ratio were excited with periodic pulses of the same magnetic pulse shapes and strengths as the experimental samples [see Fig. 1(a)]. The time evolution of the magnetization was stored, until the oscillations converged. The spin-wave eigenfrequencies were then determined by local Fourier transformations, and the local power density was integrated over the volume to a global power density. The local power density yields the location and relative phases of specific eigenmodes.

The domains oriented parallel and antiparallel to $\vec{P}$ appear black and white, while the two domains oriented perpendicular to $\vec{P}$ both appear gray. A 180°-Néel wall along the y axis separates the two large domains with $\vec{M}$ upward (left) and downward (right). In the Néel wall, $\vec{M}$ is oriented to the left; thus, the Néel wall appears black. Because of the high driving frequency, the image at $t = 0$ corresponding to the onset of the field pulse does not represent the equilibrium case before the excitation. The system does not have enough time to relax back into the equilibrium state before the next pulse arrives. Instead, the image shows already a dynamical state of the magnetization pattern.

At $t = 600$ ps, the intensity has increased in the left and right domains, indicating a rotation of the magnetization vector towards the direction of the applied field, i.e., clockwise in the left domain and counterclockwise in the right domain. At $t = 1100$ ps, the left and right domains appear dark, because $\vec{M}$ has rotated in the opposite direction. A second oscillation is indicated by the snapshot at $t = 1400$ ps. Micromagnetic simulations yield very similar oscillations of the magnetization, even though the exact pattern has not been reproduced.

In our experiment, the predominant excitation mode is a precession of the magnetization in the two large domains. It is excited by the external field pulse directed perpendicular to $\vec{M}$ in these domains. Our observation of two pronounced maxima of the magnetization component parallel to the field confirms the dynamical motion of $\vec{M}$. In our case, the excitation field can be described as an oscillating field with considerable contribution of overtones rather than a field pulse. Thus, the system resembles a

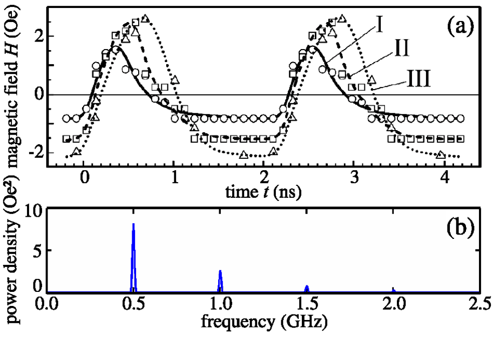

FIG. 1 (color online). (a) Time dependence of the exciting magnetic field $H_x(t)$. Two periods are shown in order to emphasize the repetition rate. (b) Fourier transformation of 50 periods of amplitude I into frequency space.

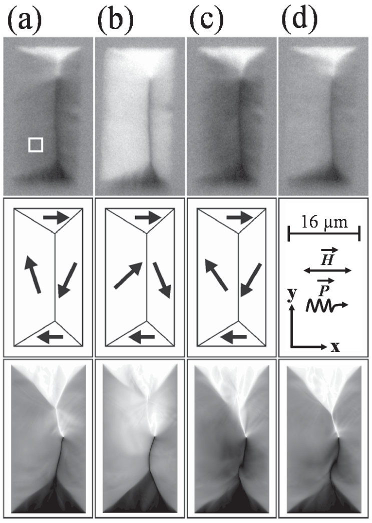

FIG. 2. Selected XMCD images showing the time evolution of the x component of the magnetization (bright areas are magnetized to the right, dark areas to the left) in a Permalloy platelet (16 μm × 32 μm) for delay times $t = 0$ ps (a), 600 ps (b), 1100 ps (c), and 1400 ps (d). The orientation of the exciting ac field and the photon polarization $\vec{P}$ are in the x direction. Sketches of the corresponding domain patterns are shown in the second row. In the third row, micromagnetic simulation results are shown for a Permalloy platelet with linearly reduced dimensions (8 μm × 16 μm × 5 nm, cell size 10 nm).

driven oscillator, and we observe the dynamical answer of the system to the periodic excitation instead of a damped oscillatory relaxation to equilibrium.

To determine the frequencies and amplitudes of the data shown in Figs. 2(a)–2(d), we analyze the rotation angle $\phi(t) = \pm \arccos(M_x/M)$ by averaging over the boxes shown in Fig. 2(a). The intensity of the small closure domains was taken as a reference, since no initial torque acts on the magnetization within these domains. The rotation angle shows pronounced extrema at $t = 600$, 1100, 1450, and 1900 ps in the left domain [Fig. 3(a)]. A rough estimate of the eigenfrequency can be made from the second oscillation of $\vec{M}$ (indicated by the period T). In this case, the least altering of the eigenfrequency can be expected. For the left domain, we thus estimate a value of 1.25 GHz.

The domain walls and, particularly, the 180°-Néel wall move only very little throughout the series shown in Figs. 2(a)–2(d). Close to the maximum of the field pulse at $t = 600$ ps, the upper triangular domain [$\vec{M} \parallel \vec{H}(t)$] grows while the lower black domain shrinks. This occurs through a bulging of the 90° domain walls downwards. This bulging behavior is similar to an observation in square particles [1]. The wall velocity [Fig. 3(b)] does not exceed 10^3 m s^{-1} in agreement with Ref. [1]. The 180°-Néel wall movement is in close relation to the oscillation of the magnetization in the left and right domains. We do not observe a significant movement of the vortex. This is not a contradiction to previous observations of a vortex motion perpendicular [1] or parallel to the applied field [3], because in our case the excitation frequency is too high for the slow velocity of the vortex.

The most interesting phenomenon is the mean shift of the 180°-Néel wall out of its symmetrical position to the right [see Figs. 4(b)–4(d)]. This shift increases with the amplitude of the exciting field. This shift cannot be caused by the external field directly, because the field is directed parallel to the magnetization in the domain wall and, thus, causes no torque. Moreover, the field is oscillating and the mean field averaged over one cycle disappears. Of course, a movement of the wall could be induced by a magnetic field along the y axis. Since the domain walls can move freely in our low-anisotropy sample, the walls will adjust in a quasistatic external field such that the sum of the demagnetizing field H_d and the external field is zero. $H_d = N_y M \epsilon$ is given by the magnetic moment $m = MV\epsilon$ of the particle ($\epsilon = 2\Delta x/w$, denoting the relative shift of the 180° domain wall) and the demagnetizing factor $N_y \approx t/l$ (thickness t and length l) roughly approximated assuming an ellipsoidal particle. The required external field for a domain wall shift to the right edge ($\epsilon = 1$) is 3 Oe, i.e., on the same order of magnitude as the field amplitude. Such a large field component can certainly not be caused by a misalignment of the particle and the waveguide or by stray fields from the leads. The presence of static fields can also be excluded (the vacuum chamber itself is made out of μ metal in order to shield external fields fields), as the shift of the domain wall would then be independent of the exciting field. However, Fig. 4 clearly shows that ϵ increases with the field amplitude. For the largest field amplitudes applied in this experiment, the platelet is nearly saturated with the magnetization vector pointing upwards [Fig. 4(d)].

The observed effect can be explained only by the following dynamic response of the system on the periodic excitation: As a general physical principle, a system with a continuous source (exciting field) and sink (spin damping) of power assumes a state with maximum energy stored in the system and, thus, maximizes the entropy production.

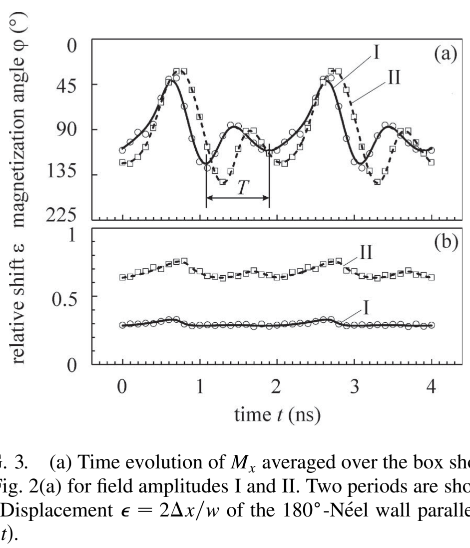

FIG. 3. (a) Time evolution of M_x averaged over the box shown in Fig. 2(a) for field amplitudes I and II. Two periods are shown. (b) Displacement $\epsilon = 2\Delta x/w$ of the 180°-Néel wall parallel to $H_x(t)$.

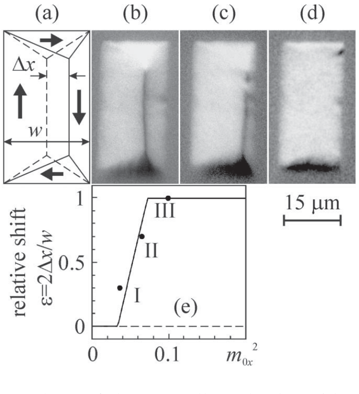

FIG. 4. Snapshots of the Permalloy platelet with the domain pattern sketched in (a) at the time $t = 600$ ps excited with three different amplitudes [see Fig. 1(a)] denoted as I (b), II (c), and III (d). In (c), the domain wall comprises additional vortices appearing aperiodically, in some cases at higher amplitudes. A comparison of the numerical solution obtained from Eq. (3) and the experimentally determined mean domain wall shift ϵ is shown in (e).

The energy stored in our particle is given mainly by the magnetization precession in the large domains. The system is excited with a significant oscillating field component of 1 GHz, i.e., just below the resonance frequency of the free-running system. If the domain wall is shifted to the right, the effective field determining the precession frequency and, consequently, the resonance frequency will be reduced in the left domain and vice versa in the right domain. As a consequence, the amplitude of the precession will increase in the left domain and decrease in the right domain. Since the precession energy is proportional to the square of the amplitude, the total energy has increased. Moreover, the domain with the larger amplitude has grown, which also helps to increase the stored energy. The stored precession energy is finally balanced by the stray field energy, because of the resulting finite magnetic moment of the particle. The initial domain wall movement can occur to the left or to the right. However, we observed exclusively a shift to the right. Small inhomogeneities or a small vortex motion as described in Ref. [3] could be the reason.

In order to substantiate this qualitative picture, we estimate the contributing energies in the following. The amplitude of a forced oscillator with small damping is given by $A(\xi) = C(1 - \xi^2)^{-1}$ at the exciting frequency $\xi = \omega/\omega_0$ normalized to the resonance frequency ω_0. If ω_0 is varied, the amplitude will change by:

$$\beta = \frac{A'(\xi)}{A(\xi)}\Delta\omega_0 = -\frac{2\xi^2}{1-\xi^2}\frac{\Delta\omega_0}{\omega_0}. \qquad (1)$$

The resonance frequency ω_0 of the two large domains can be derived from the Landau-Lifshitz-Gilbert equation: $\omega_0(\epsilon) = \gamma\mu_0 M\sqrt{N_x - N_y} \approx \gamma\mu_0 M\sqrt{\pi t/w(1+\epsilon)}$, assuming demagnetization factors N_i for an ellipsoidal particle of similar dimensions as the magnetic domains. The resonance frequency decreases with increasing shift $\epsilon = 2\Delta x/w$ of the domain wall: $\Delta\omega_0/\omega_0(0) = [(1+\epsilon)^{-1/2} - 1]$. We calculate the change of the precession energy when the domain wall is shifted by ϵ as

$$\Delta E_p/E_p = \beta^2 + 2\beta\epsilon, \qquad (2)$$

where E_p denotes the total precession energy of the excited mode. Using the experimentally accessible amplitude of the magnetization component $M_x = Mm_x$ along the x axis and the demagnetization factor N_x, we can express the energy as $E_p = \frac{1}{2}V\mu_0 N_x M^2 m_x^2$. The stray field energy ΔE_s balancing ΔE_p also increases with increasing domain wall shift: $\Delta E_s = \frac{1}{2}V\mu_0 N_y M^2\epsilon^2$. From the equilibrium condition $\Delta E_p = \Delta E_s$, one obtains the implicit equation:

$$(N_x/N_y)(\beta^2 + 2\beta\epsilon)m_x^2 = \epsilon^2, \qquad (3)$$

determining the shift ϵ as a function of the oscillation amplitude m_x. If m_x exceeds a critical value, a nontrivial solution $\epsilon \neq 0$ exists. As expected, ϵ increases with increasing amplitude of the oscillation. A comparison of $\epsilon(m_x)$ obtained from Eq. (3) to the experimental data is shown in Fig. 4(e) with the parameter $2\xi^2/(1-\xi^2) = 3.8$ corresponding to a relative exciting frequency $\xi = 0.81$, i.e., $\omega/2\pi \approx 1$ GHz. Even though we performed a rough approximation of the contributing energies, the experimental data can be described by our model quite well, thus confirming our assumptions. Micromagnetic simulations confirm the basic assumptions of this model, as will be discussed in more detail in a forthcoming publication.

In conclusion, we found an induced magnetic moment in a rectangular platelet oriented perpendicular to an exciting oscillatory magnetic field. This phenomenon can be explained by a self-trapping spin-wave mode. When the system is excited just below the resonance frequency, the magnetization distribution adapts itself to gain more energy out of the exciting field. In the dynamically steady state of feeding constantly energy into the platelet by the exciting field that finally dissipates into the heat bath by magnon-phonon interaction, the increase of entropy is thus maximized. Above a threshold, the near-resonance spin-wave mode thus causes an effective force perpendicular to the 180°-Néel wall in the center of the particle that is balanced by the restoring force due to the stray field energy.

This work was supported by the DFG (priority program "magnetization dynamics") and BMBF (03N6500). Thanks are due to the BESSY staff and, in particular, H. Schmitz (HMI, Berlin) for excellent support and I. Mönch and J. Vinzelberg (IFW Dresden) for sample preparation. M. B. thanks G. Meier (Universität Hamburg) for fruitful discussions and insights and the DFG (Sonderforschungsbereich 508 "Quantenmaterialien") for financial support.

---

*Electronic address: elmers@uni-mainz.de

[1] J. Raabe *et al.*, Phys. Rev. Lett. **94**, 217204 (2005).
[2] K. Perzlmaier *et al.*, Phys. Rev. Lett. **94**, 057202 (2005).
[3] S.-B. Choe *et al.*, Science **304**, 420 (2004).
[4] H. Stoll *et al.*, Appl. Phys. Lett. **84**, 3328 (2004).
[5] J. P. Park *et al.*, Phys. Rev. B **67**, 020403(R) (2003).
[6] S. O. Demokritov *et al.*, Phys. Rep. **348**, 441 (2001).
[7] T. M. Crawford *et al.*, Phys. Rev. B **67**, 024411 (2003).
[8] See, for example, A. Hubert and R. Schäfer, *Magnetic Domains* (Springer, Berlin, 1998).
[9] L. Landau *et al.*, Phys. Z. Sowjetunion **8**, 153 (1935).
[10] C. M. Schneider *et al.*, Appl. Phys. Lett. **85**, 2562 (2004).
[11] C. M. Schneider *et al.*, Rep. Prog. Phys. **65**, 1785(R) (2002).
[12] D. Neeb *et al.*, J. Phys. Condens. Matter **17**, S1381 (2005).
[13] J. Feikes *et al.*, in *Proceedings of the 9th European Particle Accelerator Conference (EPAC 2004), Lucern, Switzerland* (European Physical Society Accelerator Group, Lucern, Switzerland, 2004), p. 1954; www.BESSY.de.
[14] http://math.nist.gov/oommf/. For the simulations, standard Permalloy parameters ($A = 1.3 \times 10^{-12}$ J/m, $M_s = 8.6 \times 10^5$ kA/m, $\alpha = 0.005$) were used.

4.3 Anisotropic Magnetoresistance in Permalloy Microstructures

As mentioned in Chapter 3, magnetoresistance measurements can sensitively detect small changes in the magnetization of a ferromagnetic material. However, the measured signals are often ambiguous as they are derived by the interaction between the local magnetization and the conduction electrons integrated along their paths. For an AMR signal the cosine-square dependence of the resistance gives rise to further ambiguity. There are in essence two ways to increase the significance of AMR measurements: One way is to make the sensitive volume smaller so that the measurement approaches a local probing of the magnetization instead of an average of a large volume. Then there is less variability in the magnetization configuration possible. This approach was followed in the study outlined in Section 4.3.1 as well as in a number of studies by other authors [61, 181]. We investigated the AMR response in a permalloy rectangle if the voltage contacts encompass only a small region of the magnetic structure.

The other way to increase the significance of AMR measurements is to directly compare the AMR signal at a certain external magnetic field to the actual magnetization configuration at that field. The latter can be obtained either by domain imaging techniques (see Section 3) or via micromagnetic simulation. This is the path we pursued in Section 4.3.1 as well as in Section 4.3.2. This path has been applied by other groups as well [31, 182].

4.3.1 Comparison of Micromagnetic Simulation and Experiment

Marcus Steiner had been working on the switching behavior of single-domain ferromagnetic electrodes for spin injection into semiconductors for spintronic applications [183]. He also studied the transport characteristics of larger, multi-domain permalloy structures. For an investigation of the change of anisotropic magnetoresistance due to different magnetization states, he contacted micrometer-sized permalloy rectangles of various thicknesses and measured the output voltage for fixed input currents. The voltage contacts overlapped approximately only one-fourth of the permalloy rectangles. He measured the AMR for magnetic fields perpendicular and parallel to the long axis of the rectangles and for various temperatures (see Section 5.2 of Ref. [183]).

I completed his study by comparing his measured data to results from micromagnetic simulations. For this I extended the OOMMF code with a tool that calculates the AMR for simulated magnetization patterns. For a physically correct calculation it was required that the assumed current flow through the rectangles was homogeneous in one direction, even though the software interface allowed for general vector fields. The scalar product of the magnetization of each cell with the local current vector was added along each of the three coordinate axes for the total AMR contribution. The code does not allow for setting boundary conditions, i.e., spatially separating current and voltage contacts. For our simple model the current was assumed to be homogeneous in the x-direction, we defined the current to be only between the voltage probes. An exemplary correlation between a ferromagnet's magnetization and the corresponding AMR signal in shown in Fig. 4.4.

I simulated hysteresis sweeps for several initial magnetization states (S-state and C-state, see Ref. [36, 134]) and thicknesses. The qualitative agreement between the measurements and the simulations was already good, but a discrepancy in the absolute values caused us to turn to Matthias Holz, who from a diffusive transport model calculated the expected current density distribution in our measured and simulated samples. We found that due to the low-ohmic gold voltage contacts on top of the higher-ohmic permalloy most of the current flowed through the contacts causing a high current density in the permalloy adjacent to the gold contacts. Thus in these regions the AMR was measured with greater sensitivity than in the others, and in other regions the magnetization would have no influence on the AMR as no current passed through the voltage probes. With this advanced model we recalculated the expected AMR signals from the simulated hysteresis sweeps and found a much better correlation between measurement and simulation. We confirmed our simulated magnetization states with magnetic-force microscopy images taken from samples with similar aspect ratios. Thus we have shown that AMR can be used to locally detect magnetization changes and that with the help of micromagnetic simulation one can obtain information about a ferromagnetic system not accessible by AMR measurements alone.

The work was published as **[P8]** and is reprinted here in its entirety with permission from M. Bolte, M. Steiner, C. Pels, M. Barthelmeß, J. Kruse, U. Merkt, G. Meier, M. Holz, and D. Pfannkuche, Phys. Rev. B **72**, 224436 (2005). Copyright (2005) by the American Physical Society. The work was also presented at the DPG Spring conference in Berlin (Germany) in 2005 **[C5]** and at the Technical University of Eindhoven, NL (see **[I1]**).

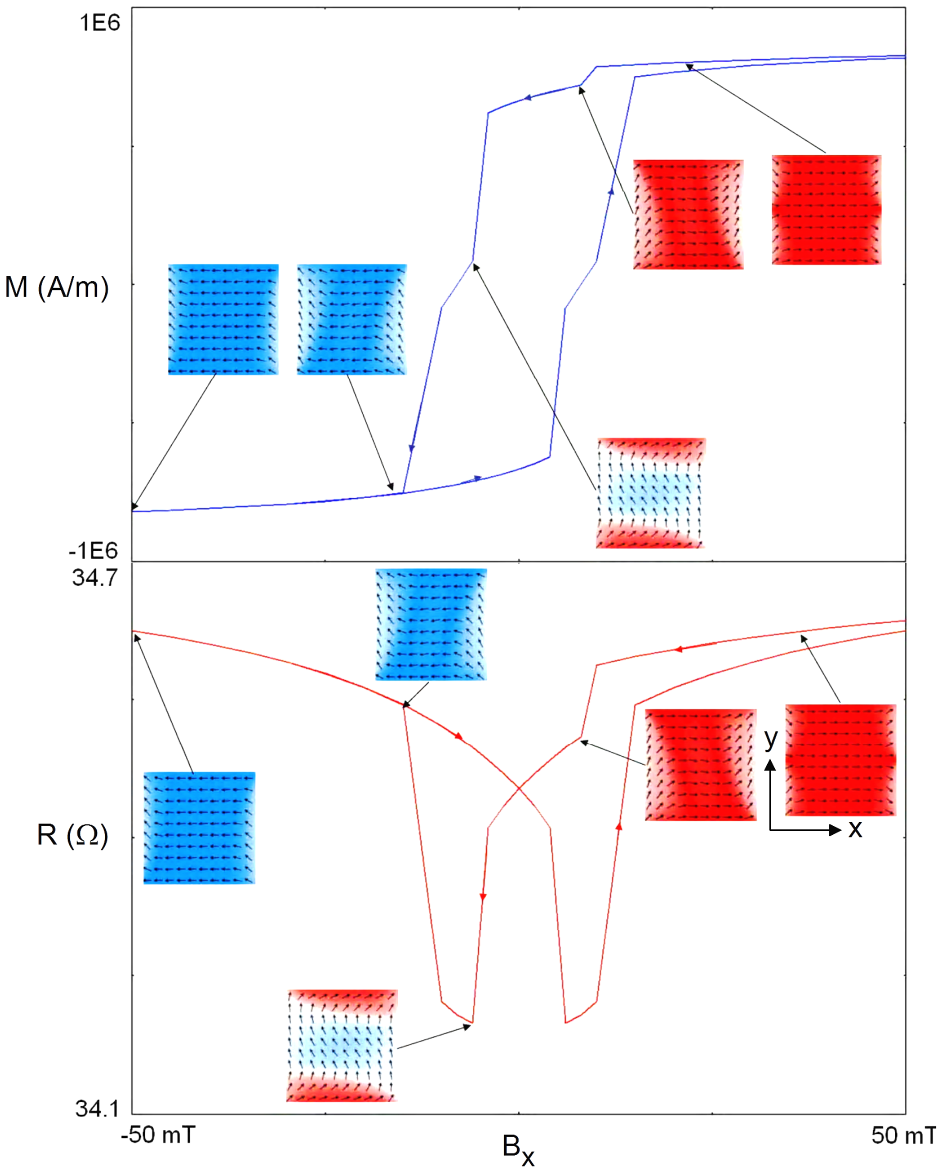

Fig. 4.4: (a) Hysteresis and (b) corresponding AMR for a 400×400 nm^2 and 10 nm thick permalloy sample. The simulation started at +50 mT in a flower-state and went into an S-state at -50 mT to reverse into another S-state at +50 mT. Therefore the up–sweep and the down–sweeps are not symmetric.

PHYSICAL REVIEW B **72**, 224436 (2005)

Magnetotransport through magnetic domain patterns in permalloy rectangles

M. Bolte,* M. Steiner, C. Pels, M. Barthelmeß, J. Kruse, U. Merkt, and G. Meier
Institut für Angewandte Physik und Zentrum für Mikrostrukturforschung, Universität Hamburg, Jungiusstrasse 11, 20355 Hamburg, Germany

M. Holz and D. Pfannkuche
Institut für Theoretische Physik, Universität Hamburg, Jungiusstrasse 9, 20355 Hamburg, Germany

(Received 31 May 2005; published 30 December 2005)

We study the influence of multidomain configurations on the magnetoresistance of rectangular permalloy microstructures with various thicknesses. The anisotropic magnetoresistance (AMR) is the dominating resistance contribution in these systems. Reversible and irreversible magnetization reversals lead to complex AMR signals. Appropriate positioning of the voltage probes allows the local detection of the magnetoresistance. Two methods for calculating the local AMR, the uniform-current model and diffusive transport calculations, are described. The latter takes potential differences and inhomogenous current paths into account. By comparing magnetoresistance measurements, micromagnetic simulations, and images of magnetic-force microscopy for various film thicknesses, we can exactly link the transitions between magnetic configurations to changes observed in the magnetoresistance.

DOI: 10.1103/PhysRevB.72.224436 PACS number(s): 75.47.−m, 75.50.Bb, 75.60.Ch, 75.60.Jk

I. INTRODUCTION

Electron transport through ferromagnetic microstructures and nanostructures is a hot issue due to its relevance for magnetic memories.[1,2] At present, a lot of progress in understanding the interaction between itinerant and localized electrons is being made.[3–8] With high current densities, the local magnetization can be controlled by the spin-transfer torque which is most attractive as a direct writing process in magnetic random access memory devices (MRAM).[9] In the regime of low current density, the resistance of a ferromagnetic metal can be probed without deteriorating the local magnetization.[7,8] Low current densities are thus used to read out information. Experiments have been performed to analyze the access memory devices (AMR)[10,11] and the resistance caused by a domain wall.[12–17] For the latter there is an ongoing discussion about its sign and existence. Negative as well as positive domain-wall resistances have been theoretically predicted and experimentally demonstrated. It has also been stated that without impurities the resistance of a domain wall vanishes.[18] A possible reason for the contradictive interpretation of the experimental work might be the presence of a local AMR that dominates the domain wall contribution. Thus a proper description and a detailed understanding of the local AMR is essential. To this aim, micromagnetic simulations have proven to be an important tool.[19–23]

We measure the magnetoresistance of permalloy microstructures with local voltage probes and compare the experimental data with simulations. We use the three-dimensional version of the micromagnetic simulation package OOMMF (Ref. 24) which we extended in order to be able to describe local AMR and inhomogeneous current distributions. Thus it is possible to calculate the magnetoresistance of simulated magnetic configurations and to observe transitions between magnetic states through reversible and irreversible changes. The results are compared with AMR measurements and cross-checked by magnetic-force microscopy (MFM).

II. SAMPLE PREPARATION

We have prepared permalloy rectangles with thicknesses between 10 and 100 nm. The different domain patterns that arise due to the distinct thicknesses and lateral sizes of these rectangles have been described in earlier publications.[21,25,26] Gold contacts for magnetoresistance measurements were added to the 4×2-μm^2-sized rectangles with thicknesses 20, 40, and 70 nm as can be seen in Fig. 1. The voltage probes were prepared to cover a rectangle approximately one-fourth of its width. This way we are able to resolve local magnetic configurations with a mirror symmetry along the long axis (the x direction in Fig. 1). External fields can be applied in-plane under an arbitrary angle φ with respect to the long axis. All transport measurements were performed in a helium cryostat at temperatures between 2 and 50 K.

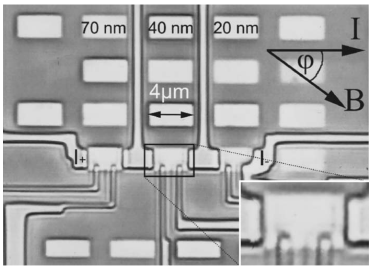

FIG. 1. Array of 4×2 μm^2 permalloy rectangles, three of them contacted. The current contacts are labeled with $\boldsymbol{I}_+$ and $\boldsymbol{I}_-$. The in-plane angle φ between the magnetic field $\boldsymbol{B}$ and the current $\boldsymbol{I}$ is illustrated. The inset shows the 40 nm thick element with its current and voltage probes. The voltage probes are $l=1$ μm apart and reach $w=500$ nm across the sample.

©2005 The American Physical Society

III. MICROMAGNETIC SIMULATIONS

For the simulations, the AMR with its well-known $\cos^2$ dependence between the magnetization and the current,

$$\rho = \rho_\perp + \Delta\rho \cos^2 \theta, \tag{1}$$

is used.[10,27] Here, θ is the angle between the local magnetization and the local current, since the AMR is calculated for every simulation cell and not according to the macrospin model, $\Delta\rho = \rho_\parallel - \rho_\perp$ is the change in resistivity due to the AMR, and $\rho_\perp$ and $\rho_\parallel$ are the resistivities of the thin film when the magnetic field is perpendicular ($\varphi = 90°$) and parallel ($\varphi = 0°$) to the current direction, respectively. An average value, $\rho_{\text{ave}} = (2\rho_\perp + \rho_\parallel)/3$ is defined for the resistivity at remanence for bulk material and $\rho_{\text{ave}} = (\rho_\perp + \rho_\parallel)/2$ for extended thin films.[10] The AMR typically adds about 2% to the total resistivity of permalloy.[27,28]

To calculate the domain patterns, the $4 \times 2\ \mu\text{m}^2$ elements were simulated by applying a finite-difference mesh with a cubic cell size of 10 nm. The material parameters for the simulation are as follows: The anisotropy constant 100 J/m^3, the saturation magnetization 8.6×10^5 A/m, and the exchange constant 1.3×10^{-11} J/m. For the 20-nm-thin rectangles, the simulations were repeated for the *s*-ground state using a conjugate gradient algorithm for the magnetization relaxation and a cell size of 5 nm. The magnetization patterns are virtually unaltered and lead to almost identical AMR curves as the 10 nm cells. The damping coefficient α was set to 0.5 and the precession term of the Landau-Lifshitz equation was turned off to minimize computation time. In quasistatic state transitions such as the present ones, the precession term does not lead to different results since the angle between effective field and magnetization remains small, and the magnetization can move straight towards the direction of the effective field. Also to optimize performance, the conventional Euler evolver as opposed to a more sophisticated Runge-Kutta scheme was used for the present quasistatic problem.[19]

Two different approaches are used to simulate the local AMR. The first one, hereafter called the uniform-current model, assumes that the electric current density is uniform and propagates along the x direction through the ferromagnet, thus neglecting the influence of the magnetization and the impact of the low-ohmic gold contacts on the current. The AMR was computed separately for each simulation cell and not simply integrated over the whole sample volume as in the macrospin model. The macrospin model averages out local effects which often leads to wrong results. The voltage calculated between the voltage probes is the sum of all cell-wise resistivities multiplied by the incoming current and the ratio l/wt of the distance $l = 1\ \mu$m between the voltage probes and the product of the probes' extension across the rectangle $w = 500$ nm and the thickness t of the film.

The second approach computes the actual, nonhomogeneous current density by taking the gold contacts and the influence of the AMR on the current into account. This is done by solving the diffusive transport equation,[29] thereby extending the model that has previously been applied for ferromagnetic disks.[30] It generates a finite-element mesh and uses the local magnetization from the micromagnetic simulation. The potential difference between the voltage contacts is computed from the resistivities $\rho_\perp$ and $\rho_\parallel$ by taking into account the geometry of the permalloy and gold structures.

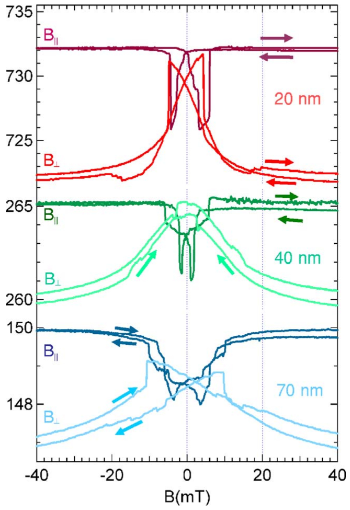

FIG. 2. (Color online) Magnetoresistance measurements of the 20 nm (red), 40 nm (green), and 70 nm (blue) permalloy element at $T = 50$ K. The AMR is measured in magnetic fields parallel and perpendicular to the principal direction of the current.

The resistivities of the permalloy were determined by mapping the real geometry of the magnetic structure and its contacts onto a three-dimensional finite-element (FE) mesh. The thicknesses of the permalloy and of the gold (40 nm) were taken into consideration. A current matching the input current of the experiment (50 μA) was placed between the left and right current contacts. By solving the diffusive transport and Poisson's equation, the potential at every node of the FE mesh was derived (see Sec. VII). The resistivity $\rho_\parallel$ was thereby used as a fit parameter to adjust the resulting potential difference at the voltage contacts to the values of the measurements. This yielded a value for $\rho_\parallel$ of 44 $\mu\Omega$ cm. For the resistivity of gold, 2.2 $\mu\Omega$ cm was used.

The AMR ratios $\Delta\rho/\rho_{\text{ave}}$ were determined experimentally. The magnetoresistances for angles $\varphi = 0°$ and close to 90° are depicted in Fig. 2. The curvature of the AMR signals due to the Lorentz force can be neglected. All curves show irreversible and reversible transitions in the magnetization marked by abrupt and gradual changes in the resistivity, respectively. For 20-, 40-, and 70-nm-thick rectangles, we obtain AMR ratios of 1.4%, 1.9%, and 2.4%, respectively. The highest resistances are observed in saturation for $\varphi = 0°$, when the magnetic field is parallel to the current. For decreasing field strengths, the magnetization turns out of the long axis to reduce the stray-field energy and states with magnetization components perpendicular to the x direction appears. These states decrease the resistivity. At saturation in transverse geometry, when φ is close to 90° (Ref. 31), all magnetic moments are oriented perpendicular to the current resulting in the lowest possible resistance. In the thicker structures, the

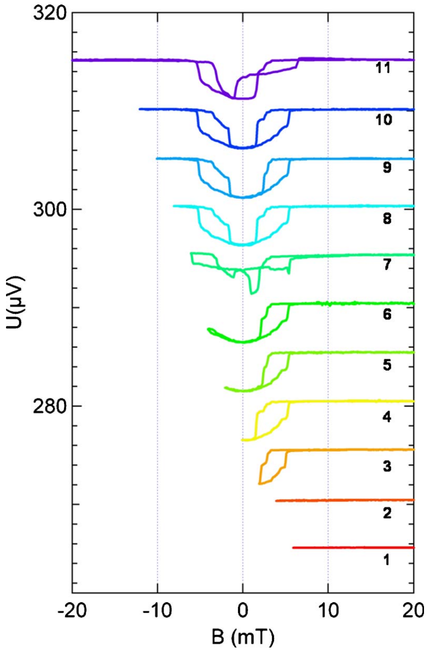

FIG. 3. (Color online) Minor loops of the 40-nm-thick element at $T=2$ K. The traces 2 to 11 are successively shifted upwards by 5 μV.

$\cos^2$ term dominates the irreversible magnetization changes. Also noticeable in Fig. 2 is the different shape of the corresponding curves for different thicknesses. For the thin element, the transitions are abrupt and occur within a narrow field interval. In thicker films vortices can nucleate easier than in thinner films, causing wider field intervals in which the transitions can occur. Because the absolute value of the AMR increases less (from 1.4% to 2.4%) than the interval width (from 7 to 30 mT), the average slopes decrease from 4×10^{-3}/mT to 1.6×10^{-3}/mT. This corresponds to the fact that there are less geometric constraints acting on the magnetization in thicker films so that the vortices can move more easily.[23]

IV. MINOR LOOPS

To understand the interplay between reversible and irreversible magnetization reversals, minor-loop measurements were performed in longitudinal geometry ($\varphi=0°$) for all thicknesses at 2.0 K. In Fig. 3 results are shown for the 40-nm-thick element. In curves 1 and 2 the magnetoresistance remains virtually constant at fields higher than 4 mT. An irreversible change is recorded in curve 3 between 2 and 5 mT with the typical hysteretic signature. Curves 4 to 6 reveal a subsequent reversible magnetization change. In curve 7, the loop is different from the previous ones, in particular it is asymmetric. In curves 8 to 10, the reversible and irreversible changes occur at the same field strengths and the AMR signals have the same shape. Hence it can be assumed that the sequence of magnetic configurations remains the same. An irreversible change is noted at about -6 mT, so that curves 8 to 10 become symmetric. Finally, curve 11 shows a sweep into saturation and back. Its transition pattern is like the one in curves 8 to 10 for the downward sweep, but different for the upward sweep. The assumed cause for this deviation as well as for the deviation in curve 7 are the different paths the magnetic configuration follows on the energy surface. Impurities such as oxides at the surface can pin the magnetization with an unknown strength. Such pinning on oxide particles was observed on deteriorated samples by MFM. This assumption is investigated further in Sec. VIII with temperature-dependent experiments.

V. UNIFORM-CURRENT MODEL

It has been known for years that only a very limited number of magnetic transitions are possible in soft magnetic rectangles.[32–34] The so-called *c*, *s*, and flower states are the high-remanent ground states for thin permalloy rectangles. The flower state can be disregarded because its total energy is much higher than the ones for the *c* or *s* state.[32,33] In the following, results from micromagnetic simulations are compared to experimental resistances.

In Fig. 4 simulated and measured AMR curves of a 4×2 μm^2 permalloy element with 20 nm thickness are shown in external fields ranging from -20 to 20 mT. The simulations were done according to the uniform-current model with the resistivities determined by diffusive transport calculations (see Sec. III). The geometry of the voltage probes and strength of the current were taken from the experiment. As the actual magnetic configuration in the real sample is unknown and since only the *c* and *s* states exist as high-remanent ground states,[32] these states were used to initialize the simulations. Figures 4(a) and 4(b) refer to the *c* and the *s* state, respectively.

The transitions between magnetization states can be reversible or irreversible. Experimentally, reversible and irreversible transitions are defined from minor loops. For the simulations, the definition is derived from the underlying magnetization states. We consider a transition irreversible when a vortex or a domain wall nucleates or dissolves. Reversible transitions are vortex or domain wall propagations. The measurements were performed at 2.0 K and repeated 20 times for each thickness in positive and negative field direction. Due to temperature and training effects, individual measurements of the same element yield different curves for the first cycles (see Sec. VIII). After about 10 cycles, the AMR curves became stable. Exemplary successive measurements are shown in the lower parts of Figs. 4(a) and 4(b). The step size of the external field for the measurements was 0.1 mT, while the discretization in the simulation was 5 mT between -40 and -10 mT and between 10 and 40 mT, and 1 mT between -10 and 10 mT in Fig. 4(a). For the *s* state, 0.25 mT steps were chosen between 2 and 9 mT.

Figure 4(a) shows two simulated AMR curves for an initial *c* state. To account for mirror-symmetric states, bottom and top contacts at the vertical edges of the boxes enclosed

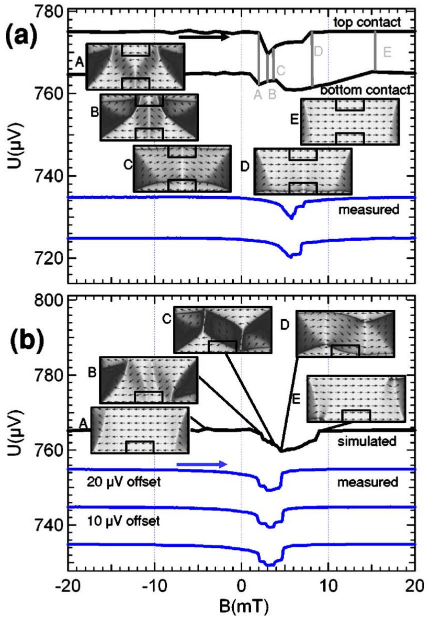

FIG. 4. (Color online) Simulated and experimental traces of the AMR of a 4×2 μm^2 large and 20-nm-thick permalloy structure with two different initial magnetic configurations. (a) Top curves show the simulated AMR for the initial *c*-state, with the upper one offset by $+10$ μV for clarity. The bottom curves are two corresponding measured AMR signals, the lower one offset by -10 μV. (b) Simulated sweep for the initial *s*-state (top curve) and measurements (bottom) akin to the simulation. Between configurations *A* to *E* irreversible changes occur. The small outlined boxes represent the regions in which the AMR is measured (see voltage probes in Fig. 1) and simulated.

by solid lines were assumed in the calculations. Because of the symmetric positions of the voltage probes with respect to the long edge of the sample, the two possible *s* states yield the same AMR.

When the strength of the external field increases from -40 mT towards zero, the diagonal end domains grow. At a field strength of about 1 mT (state *A*), the domain walls are ε shaped.[35] This causes a noticeable reduction in resistance in the bottom box (bottom curve), while the top region remains uniformly magnetized parallel to the current density. Towards 2 mT (state *B*), the legs of the ε pattern are pushed towards the center of the element. In this situation, the walls enter the top box and a drastic drop in resistance occurs (top curve). The bottom probes notice no major change between states *A* and *B*. For even higher fields (3 mT), the domain between the outer legs of the ε state collapses and the outer domain walls merge into a vortex. This vortex moves towards the bottom edge of the structure until it reaches equilibrium in state *C*. This transition has been previously demonstrated for similar geometries by simulation[35] and x-ray microscopy.[36] It does not result in significant changes in the AMR signal as can be seen in the top two curves of Fig. 4(a) because the average angle of the magnetization with respect to the current density remains basically the same in both regions. In the bottom region, the resistance even increases slightly because the vortex has not entered the bottom box. The unexpected configuration in state *C*, in which a rather thin area is pinned against the edge of a structure, is explained by the torque acting on the magnetic moments due to the strong shape anisotropy at the edges.[35] This torque prevents the magnetic moments from switching into an energetically more favorable direction until the external field is strong enough to overcome the energy barrier between the parallel and the antiparallel configuration. The simulation shows that the domain wall between the pinned domain and the center domain is of a Néel type, with a wall width of about 120 nm. The existence of this narrow edge domain was substantiated by simulations with a smaller cell size (5 nm) and with an external field that was tilted by 0.6° off the long axis. By further increasing the external field, the vortex is moved toward the edge of the sample until, in state *E* (15 mT), the vortex has left the structure and a state close to saturation is reached. This is seen in the bottom contact. The top contact, however, seems to detect a transition into saturation already at point *D*, when the upper domain wall is dissolved. When increasing the thickness of the structure to 40 nm, the domain at the edges dissolves already at about 6 mT.

The measurements in Fig. 4(a) closely correspond to the simulated curve for the top contacts. The same reversible and irreversible resistance changes can be seen, even though the first change, from the initial state over state *A* to *B*, occurs more smoothly in the measurement and at a slightly higher field strength compared to the simulations. An intermediate state *C* and a subsequent jump to a final state *D* can be assumed from the measurements. No further transitions can be seen. Assuming the same underlying transitions in the measurement and in the simulation, we conclude that a *C* state with top-contact arrangement was present in the measurements shown in Fig. 4(a).

In the simulation of Fig. 4(b) which starts with an *s* state at -40 mT, the change of state *A* to *B* appears because a domain wall forms in the sensitive region. From state *B* to *C*, the configuration changes irreversibly by uniting the outer two legs of the *N*-shaped domain pattern into one. The center domain enlarges, while the upper and lower closure domain reduce until at point *D* the 180° walls break apart. At this instance, vortices form at the lower left and upper right ends of the 180° walls. The vortices then move up and down, respectively, through the element to irreversibly form state *D*. This drastic change in magnetization is barely visible in the AMR, because the average angle between local current and magnetization remains almost constant. With increasing field strength, the vortices move towards the upper left and lower right corner of the element, respectively, until the thin Néel walls at the element's upper right and lower left edges collapse. Then the magnetization state is irreversibly transformed into state *E*. The AMR signal does not change any further from that point on because the vortices are well outside the voltage probes. In the measurements, two to three distinct intermediate states can be inferred from the transitions. Even though the measured curves are confined to a smaller field region, the shapes are alike.

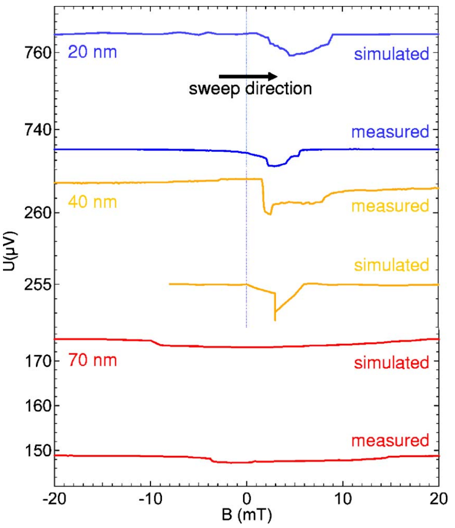

FIG. 5. (Color online) Comparison of measurements at 2 K and simulations for 20-nm- (blue), 40-nm- (yellow), and 70-nm- (red) thick rectangles.

Simulated and measured data for different thicknesses are compared in Fig. 5 in the field range of −20 to 20 mT. The field was applied in the *x* direction, increasing from −40 to 40 mT. Figure 5 shows good agreement in the absolute values of the AMR as well as in the shapes and locations of the transitions. For the 70 nm-thick rectangles, the magnetization reversal takes place over an extended field interval of about 30 mT, starting with a sharp change in resistance. Changes occur within the same regime for simulation (−10 to 20 mT) and measurement (−6 and 12 mT). For the thinner elements, the transitions are confined to more narrow field ranges. Due to limitations in storage space, the simulations for the 70-nm-thick element were done for a $2\times 1\ \mu\text{m}^2$ rectangle. This approach is justified because the magnetization depends more on thickness than on lateral size for elements several microns wide.[20,21,37,38] A more detailed comparison of measurement and simulation follows in Sec. VI.

For the 40-nm-thick element, the measured AMR shows a gradual increase in resistance between −10 and 0 mT, a sharp drop at 2 mT, and a smaller but also sharp increase at 3 mT. The resistance stays almost unchanged up to a field of +8 mT, where the configuration irreversibly changes again and slowly saturates. Two intermediate magnetic states between 2 and 3 mT and between 3 and 8 mT are likely. The simulated transitions are quite similar: between 0 and 3 mT the resistance decreases slowly and at 3 mT it drops sharply. Due to the 1 mT resolution of the simulation, the transition moves from the initial state to the higher intermediate state in one simulation stage as can be seen by the vertical line at 3 mT. The transition shows about the same resistance change as the measurements (0.6 μV). A gradual change from the second intermediate state to the final state is also not seen in the simulation, again due to the limited field resolution. It may also be possible that the vortices in the real sample could not leave the sensitive area between the contacts due to edge roughness[39] or strain caused by the contacts. That would explain the irreversible jump at +8 mT in the experiment. Experiments and simulations for the 20 nm-thin rectangle have already been compared in Fig. 4.

VI. MAGNETIC-FORCE MICROSCOPY

To derive more conclusive information about the magnetization configurations that result in the measured AMR signals, MFM was employed. There is an inherent difficulty to carry out magnetoresistance and MFM measurements simultaneously due to the interaction of the magnetic tip with the sample, which creates a stray field of up to 50 mT.[40,41] Hence, micromagnetic simulations serve as a bridge between AMR and MFM.

In Fig. 6(a), measured (first row) and simulated MFM images (second row) together with their underlying magnetic

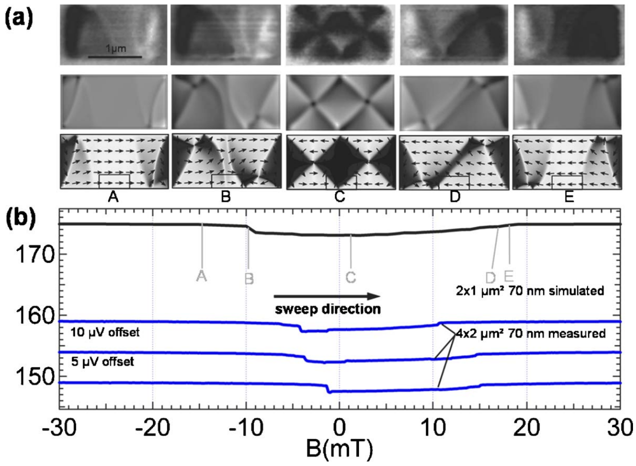

FIG. 6. (Color online) (a) 2×1-μm^2-large and 70-nm-thick permalloy rectangles, measured by MFM (top row). The middle and lower rows show simulated MFM images according to Ref. 26. The gray scale of the lower row ranges from white (magnetization along the long axis) to black (magnetization perpendicular to long axis). (b) Three consecutive AMR measurements (lower curves) performed at 2.0 K on a 4×2-μm^2-large and 70-nm-thick rectangle and an AMR curve simulated for the rectangle in (a).

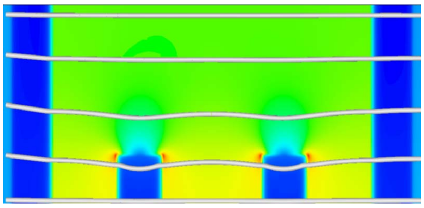

FIG. 7. (Color online) Current distribution just below the surface of the 20-nm-thick permalloy rectangle. The current contacts are attached on the left- and right-hand sides, while the voltage probes lie in the lower part of the figure, on top of the structure. The bright lines illustrate five current paths. Colors represent absolute values of the current density between 0 A/m^2 (blue) and 2.0×10^9 A/m^2 (red).

configurations (third row) are shown for a 2×1 μm^2 large and 70 nm-thick rectangle. Labels *A* to *E* correspond to strengths of the magnetic field as indicated in Fig. 6(b). The calculated MFM images were derived by our OOMMF extension[21,26] according to the algorithm described in Ref. 41. The simulated AMR signal in Fig. 6(b) considers only the region within the black boxes (see also Fig. 4). For comparison, three distinct AMR measurements on a structure with the same lateral aspect ratio and thickness (4×2 μm^2, 70 nm thick) are shown. These measurements show that the transitions observed by MFM coincide almost exactly with the simulated magnetic states (third row) and their MFM images (second row). The simulated magnetizations, in turn, cause the local AMR [Fig. 6(b), top curve]. That AMR curve agrees with the principle shape of the measured signals. The good agreement of measurement and simulation in Fig. 6 demonstrates that the simulated magnetic states *A* to *E* actually occur in real samples and that they lead to AMR signals expected from the geometric positions of the voltage probes in Fig. 1.

VII. DIFFUSIVE TRANSPORT CALCULATIONS

To understand the impact of the low-resistive voltage contacts on the current paths and to calculate the influence of the local AMR more accurately, the conductivities of permalloy and gold, the geometric boundary conditions as well as the local AMR were included in a diffusive transport calculation of the local electric potentials and the current density. The calculations were used first of all to determine the resistivity. For this, the potential difference between the voltage probes was calculated and compared to the measured voltage. The fitting resulted in a resistivity of 44 $\mu\Omega$ cm. The result of such a calculation is shown in Fig. 7. The background color coding reveals a spatial variation of the current density at the top of the permalloy rectangle of about an order of magnitude. It ranges from the permalloy regions right below the highly conductive gold current and voltage contacts (blue, 0 A/m^2 to regions in the permalloy at the corners of the voltage contacts (red, 2.0×10^9 A/m^2.

The calculation of the local current densities and of current paths reveal a noticeable deviation from the uniform-current model. In comparison to the uniform-current model, the current paths change little due to the local AMR, but are largely influenced by the shape and position of the gold contacts. Future work would allow determining the quantitative values of the influences.

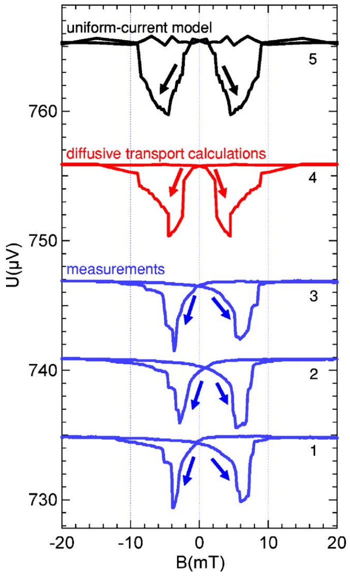

FIG. 8. (Color online) Comparison of the AMR of the two simulation models with experiments: Bottom three curves (blue) are measured AMR signals for the 4×2-μm^2-large and 20-nm-thick permalloy rectangle at 2 K, the top curve (black) shows the results of the uniform-current approach and an initial *s* state, and the middle curve (red) results from the diffusive-transport calculation. Curves 2 to 4 are shifted upwards by 6, 12, and 21 μV.

The potential difference between the voltage contacts was computed for hysteresis loops and yielded results such as the center (red) curve in Fig. 8. The bottom three curves depict measurements. These curves differ in their details due to the low temperature as will be discussed in Sec. VIII. However, the down-sweeps all show two to three irreversible jumps hinting at intermediate magnetic states. The diffusive transport calculation (center curve) shows a similar decrease in resistance with decreasing field strength down to the minimum resistance between −4 and −5 mT, then an increase with two sharp irreversible jumps. The magnetic transitions are more pronounced than for the uniform-current approach (top curve in black). This is even though identical magnetization patterns were used to compute the AMR. The conclusion is that the local AMR is weighed by the absolute value of the current density. In Fig. 7, the corners of the voltage contacts contribute most, so that any resistance changes in these areas, e.g., caused by passing vortices, are amplified in comparison to other regions of the sample.

VIII. TEMPERATURE DEPENDENCE

Temperature-dependent AMR measurements for the 70-nm-thick element are shown in Fig. 9. The hysteretic

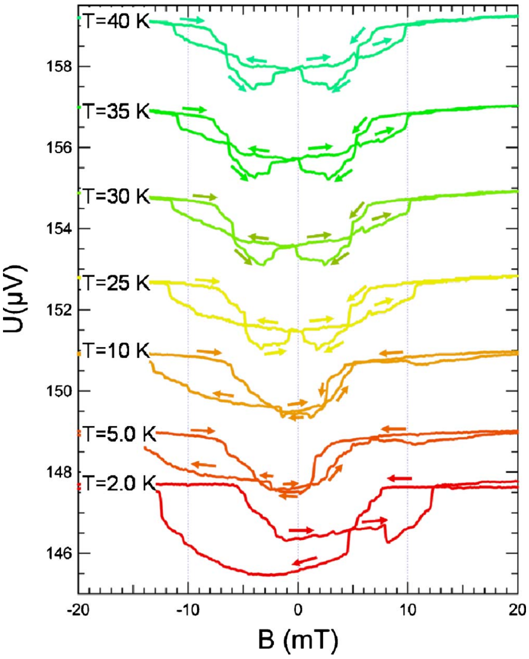

FIG. 9. (Color online) Temperature-dependent AMR measurements of the 70-nm-thick permalloy element. The curves are successively shifted upwards by 2 μV for clarity.

magnetoresistances become more symmetric when the temperature is increased. The transition temperature from asymmetric to symmetric reversals decreases with increasing thickness from about 50 K (20 nm) over 35 K (40 nm) to 25 K (70 nm). This behavior originates from the complex magnetization patterns of the multidomain configurations. The curves will never be completely symmetric, though, due to the random nature of Barkhausen jumps. Samples with simpler magnetic configurations such as nanorings[42–45] do not show a significant temperature-dependence in the AMR curve in the temperature range between 2 to 50 K. This is because the geometrical constrictions in nanorings allow only a very limited number of ground states, namely the onion, the global vortex, and the local vortex state.[45] Such magnetization states are very robust, i.e., they are separated by large energy barriers.

Thermal excitation energies are very small compared to the total energy of the micromagnets. However, the energy differences between different reversal paths can be tiny. This may explain the asymmetry of the magnetoresistance curves for lower temperatures. In the picture of an energy landscape, the system follows local paths for low temperatures. For a flat landscape near equilibrium, a small thermal energy suffices to reach global minima which correspond to symmetric magnetization reversals. In thin films, the energy barriers between distinct magnetic configurations increase. Hence, thin elements show more pronounced irreversible resistance changes and the hysteresis becomes symmetric at higher transition temperatures.

IX. CONCLUSIONS

In conclusion, we have investigated permalloy rectangles with different thicknesses by magnetotransport measurements and compared the results to local AMR simulations. We employed uniform current and diffusive transport calculations. The latter were used to determine the resistivity of the permalloy, the current density, and the current paths through the element. There is good agreement of both calculations with the experiment in respect to the overall value and shape of the AMR signals. However, one must include in the calculations both the presence of the current and voltage contacts and the variation in the local current density to arrive at the absolute values of the resistance and a more precise shape of the hysterectic AMR curves. The reversible and irreversible jumps observed in the measurements can be linked to changes in the magnetic states observed in micromagnetic simulations. The magnetic configurations found in the simulations are supported by MFM. Deviations in the AMR curves are linked to temperature effects. Future investigations would allow the study of interactions between nonuniform currents and the local magnetization with the aid of diffusive-transport calculations in combination with magnetotransport measurements and simulations, e.g., the study of the influence of "hot-spots" in magnetic trilayers[46] or the current flow through nanoconstrictions.

ACKNOWLEDGMENTS

We would like to thank J. Gancarz for his superb technical assistance. Financial support of the Deutsche Forschungsgemeinschaft via the Graduiertenkolleg "Physik nanostrukturierter Festkörper" and the BMBF via the Verbundprojekt 13N8283, via the Sonderforschungsbereich 508 "Quantenmaterialien" and the Sonderforschungsbereich 668 "Magnetismus vom Einzelatom zur Nanostrucktur" is gratefully acknowledged.

---

*Electronic address: mbolte@physik.uni-hamburg.de

[1] J. C. Slonczewski, J. Magn. Magn. Mater. **159**, L1 (1996).
[2] J. A. Katine, F. J. Albert, R. A. Buhrman, E. B. Myers, and D. C. Ralph, Phys. Rev. Lett. **84**, 3149 (2000).
[3] P. M. Levy and S. Zhang, Phys. Rev. Lett. **79**, 5110 (1997).
[4] G. Tatara and H. Fukuyama, Phys. Rev. Lett. **78**, 3773 (1997).
[5] R. P. van Gorkom, A. Brataas, and G. E. W. Bauer, Phys. Rev. Lett. **83**, 4401 (1999).
[6] S. Zhang and Z. Li, Phys. Rev. Lett. **93**, 127204 (2004).
[7] Z. Li and S. Zhang, Phys. Rev. B **70**, 024417 (2004).
[8] A. Thiaville, Y. Nakatani, J. Miltat, and Y. Suzuki, Europhys. Lett. **69**, 990 (2005).

[9] K. Yagamia, A. A. Tulapurkar, A. Fukushima, and Y. Suzuki, Appl. Phys. Lett. **85**, 5634 (2004); K. Ounadjela (unpublished); M. Kläui, P.-O. Jubert, R. Allenspach, A. Bischof, J. A. C. Bland, G. Faini, U. Rüdiger, C. A. F. Vaz, L. Vila, and C. Vouille, Phys. Rev. Lett. **95**, 026601 (2005).

[10] T. R. McGuire and R. I. Potter, IEEE Trans. Magn. **11**, 1018 (1975).

[11] D. Buntinx, A. Volodin, and C. Van Haesendonck, Phys. Rev. B **70**, 224405 (2004).

[12] U. Rüdiger, J. Yu, S. Zhang, A. D. Kent, and S. S. P. Parkin, Phys. Rev. Lett. **80**, 5639 (1998).

[13] C. Yu, S. F. Lee, J. L. Tsai, E. W. Huang, T. Y. Chen, Y. D. Yao, Y. Liou, and C. R. Chang, J. Appl. Phys. **93**, 8761 (2003).

[14] T. Taniyama, I. Nakatani, T. Namikawa, and Y. Yamazaki, Phys. Rev. Lett. **82**, 2780 (1999).

[15] J. F. Gregg, W. Allen, K. Ounadjela, M. Viret, M. Hehn, S. M. Thompson, and J. M. D. Coey, Phys. Rev. Lett. **77**, 1580 (1996).

[16] U. Ebels, A. Radulescu, Y. Henry, L. Piraux, and K. Ounadjela, Phys. Rev. Lett. **84**, 983 (2000).

[17] R. Danneau, P. Warin, J. P. Attané, I. Petej, C. Beigné, C. Fermon, O. Klein, A. Marty, F. Ott, Y. Samson, and M. Viret, Phys. Rev. Lett. **88**, 157201 (2002); H. Sato, R. Hanada, H. Sugawara, Y. Aoki, T. Ono, H. Miyajima, and T. Shinjo, Phys. Rev. B **61**, 3227 (2000).

[18] V. A. Gopar, D. Weinmann, R. A. Jalabert, and R. L. Stamps, Phys. Rev. B **69**, 014426 (2004).

[19] J. Fidler and T. Schrefl, J. Phys. D **33**, R135 (2000).

[20] R. Hertel and H. Kronmüller, Phys. Rev. B **60**, 7366 (1999).

[21] M. Barthelmeß, C. Pels, A. Thieme, and G. Meier, J. Appl. Phys. **95**, 5641 (2004).

[22] G. Meier, R. Eiselt, M. Bolte, M. Barthelmeß, T. Eimüller, and P. Fischer, Appl. Phys. Lett. **85**, 1193 (2004).

[23] A. Hubert and R. Schäfer, *Magnetic Domains: The Analysis of Magnetic Microstructures* (Springer, Berlin, 1998).

[24] M. Donahue and D. Porter, National Institute of Standards and Technology, Interagency Report No. NISTIR 6376, Gaithersburg, MD, 1999 (unpublished).

[25] C. Pels, M. Barthelmeß, M. Bolte, A. Thieme, and G. Meier, J. Magn. Magn. Mater. **293**, 885 (2005).

[26] M. Barthelmeß, A. Thieme, R. Eiselt, and G. Meier, J. Appl. Phys. **93**, 8400 (2003).

[27] T. G. S. M. Rijks, S. K. J. Lenczowski, R. Coehoorn, and W. J. M. de Jonge, Phys. Rev. B **56**, 362 (1997).

[28] T. G. S. M. Rijks, R. Coehoorn, M. J. H. de Jong, and W. J. M. de Jonge, Phys. Rev. B **51**, 283 (1995).

[29] M. Holz, O. Kronenwerth, and D. Grundler, Phys. Rev. B **67**, 195312 (2003).

[30] P. Vavassori, M. Grimsditch, V. Metlushko, N. Zaluzec, and B. Ilic, Appl. Phys. Lett. **86**, 072507 (2005).

[31] M. Steiner, C. Pels, and G. Meier, J. Appl. Phys. **95**, 6759 (2004).

[32] R. Hertel, Z. Metallkd. **93**, 957 (2002).

[33] W. Rave and A. Hubert, IEEE Trans. Magn. **36**, 3886 (2000).

[34] D. Goll, G. Schütz, and H. Kronmüller, Phys. Rev. B **67**, 094414 (2003).

[35] See Fig. 20 in Ref. 32.

[36] M. Bolte, R. Eiselt, G. Meier, D.-H. Kim, and P. Fischer, J. Appl. Phys. (to be published).

[37] S. Middelhoek, J. Appl. Phys. **34**, 1054 (1963).

[38] T. Trunk, M. Redjdal, A. Kákay, M. F. Ruane, and F. B. Humphrey, J. Appl. Phys. **89**, 7606 (2001).

[39] Y. Nakatani, A. Thiaville, and J. Miltat, Nat. Mater. **2**, 521 (2003).

[40] J. M. García, A. Thiaville, J. Miltat, K. J. Kirk, J. N. Chapman, and F. Alouges, Appl. Phys. Lett. **79**, 656 (2001).

[41] M. Barthelmeß, Ph.D. thesis, University of Hamburg, 2003.

[42] M. Steiner and J. Nitta, Appl. Phys. Lett. **84**, 939 (2004).

[43] M. Steiner, G. Meier, U. Merkt, and J. Nitta, Physica E (Amsterdam) **24**, 124 (2004).

[44] J. Rothman, M. Kläui, L. Lopez-Diaz, C. A. F. Vaz, A. Bleloch, J. A. C. Bland, Z. Cui, and R. Speaks, Phys. Rev. Lett. **86**, 1098 (2001).

[45] M. Kläui, C. A. F. Vaz, L. Lopez-Diaz, and J. A. C. Bland, J. Phys.: Condens. Matter **15**, R985 (2003).

[46] E. R. Nowak, R. D. Merithew, M. B. Weissman, I. Bloom, and S. S. P. Parkin, J. Appl. Phys. **84**, 6195 (1998).

4.3.2 Simultaneous X-ray Microscopy and Magnetoresistance Measurements

In Section 4.3.1 we have shown that micromagnetic simulation in connection with AMR measurements can be used to obtain detailed information of a sample's magnetization configuration. In real samples, however, several magnetization states are often energetically close together. Also, due to the $\cos^2$-dependence of the AMR several magnetization states with identical AMR values can exist so that an AMR signal cannot always be unambiguously interpreted. We have used the excellent spatial resolution of X-ray microscopy in combination with the sensitivity of AMR measurements to discriminate between two domain wall types in permalloy wires. The measurements were performed simultaneously, so that changes in the AMR could be matched with corresponding X-ray images. Similar experiments have been successfully done on Nickel strips in a combination of AMR and Lorentz microscopy [182].

The combination has allowed us to control the type of domain wall in ferromagnetic nanowires for spin-torque driven domain-wall motion as will be described in Section 4.4. In those measurements, domain walls in permalloy wires were imaged quasi-statically, i.e., a nanosecond pulse was applied and then an image of the domain structure was taken. It also enabled a study of the training effect in permalloy microwires. In the following paragraphs preliminary results are presented.

Sample Preparation

The samples for these experiments were prepared by René Eiselt. Permalloy rings with a diameter of 40 μm and ring widths of 200 nm, 300 nm, 500 nm, and 1000 nm were prepared by electron-beam lithography, electron-beam evaporation, and lift-off processing on 1×1 mm^2 large and 200 nm thick Si_3N_4 membranes to allow for minimal X-ray absorption by the substrate. Permalloy thicknesses varied between 20 nm, 40 nm, 60 nm, and 80 nm. The rings were contacted by 40 nm thick gold wires, leading from the rings on the membrane to bond pads on the 500 μm thick frame. Four contacts for every ring allow for four-point resistance measurements. The inner contacts were $\approx$ 4.2 μm apart, constituting the region in which the AMR is detected. The samples were bonded to a PC board, and the current lines of individual rings were connected to the lock-in amplifier, as shown in Fig. 4.5.

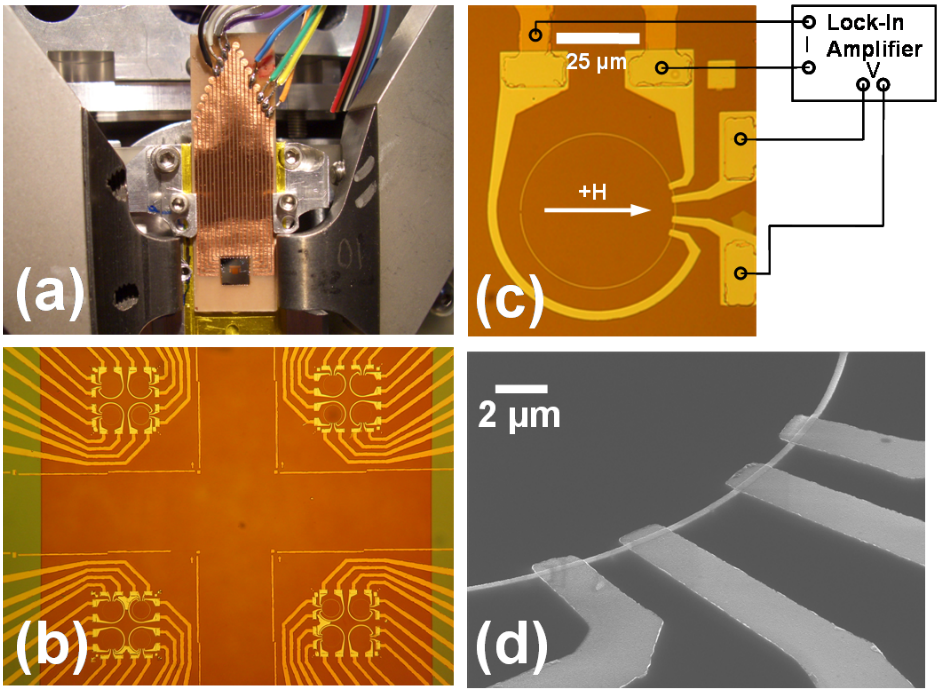

Fig. 4.5: (a) Image of the sample holder and the Si_3N_4 membrane placed in the XM-1 microscope with wires leading to the lock-in amplifier. The pole shoes on the left and right create the in-plane magnetic field. (b) Optical micrograph of the gold wiring on the membrane with four write fields having four permalloy ring structures each. (c) Magnification of one permalloy ring with its current and voltage contacts. (d) Electron micrograph image of the region sensitive to the AMR measurements.

Measurement Setup

The samples were placed in the X-ray microscope as shown in Fig. 4.5 and connected to the lock-in amplifier. The lock-in measurements were performed with a Stanford Research SR830 lock-in amplifier at a frequency of 377.3 Hz and a current of 10 μA. A Keithley 2400 was used for a current source to be able to automatically sweep the magnetic fields with high accuracy. The limited photon flux of the X-ray microscope necessitates $\approx$ 30 exposures for one high-resolution image. The exposure time is limited by the recombination time of the CCD-chip which is $\approx$ $1-2$ two seconds long. It was found that the X-ray photons created enough photoemission electrons in the permalloy to significantly influence the AMR measurements. When an X-ray image has been taken, a shutter opens for the time of exposure, and the measured voltage would increase. When the shutter closes after the image was taken, the AMR voltage slowly reduces to its original value. To reduce this parsitic effect we increased the integration time of the lock-in. It had to be longer than the exposure time of the CCD-chip and was set to 3 s. The field sweep rate was also increased to $\approx$ 50 mT/min as the X-ray beam spot on the sample was only stable for about an hour. In this way a whole AMR sweep could be run without unacceptable deterioration of the XMCD contrast in the images. Therefore we measured in two modes: To run repeated AMR sweeps without spatially resolving the domain structure, a finer field scan (10 mT/min) and a shorter integration time (0.1 s) was used. For AMR sweeps in synchronization with the XM-1 microscope, the aforementioned compromise of 50 mT/min sweep rate and 3 s integration time was used. Since the samples were placed in the microscope, all measurements were performed at room temperature.

Results and Discussion

In Fig. 4.6(a) the first five AMR sweeps on a 300 nm wide and 40 nm thick permalloy ring segment are shown. Clearly visible is the typical $\cos^2$-shape of the curves according to the model for the AMR in single-domain elements, overlayed with jumps in the resistance that are caused by changes in the domain structure. Especially the first curve exhibits many of such jumps, while consecutive sweeps have smoother curves but also at least one large jump for each sweep direction. Even after multiple sweeps (see Fig. 4.6(b)) the curves are not completely identical. The change in resistance due to the AMR was 0.8 Ω on a total resistance of 139 Ω ($\rho = 40\ \mu\Omega$cm), so that the AMR ratio was 0.58 %. Figure 4.7 shows five consecutive AMR sweeps of a 500 nm wide and 60 nm thick permalloy ring segment. The resistance of the samples was 569 Ω ($\rho = 41\ \mu\Omega$cm) and the change in resistance due to AMR was 3 Ω, leading to an AMR ratio of 0.53 %. The individual sweeps are non-repetitive, but some transitions always occur at the same field values, e.g., at ±15 mT. During the fifth sweep (blue curve) the X-ray microscope was imaging the domain structure. The effect of the opening and closing of the shutter for the CCD chip can be clearly seen, even though the long integration of the lock-in already averages out most of the oscillations.

The previous AMR measurements show that the magnetization took several paths through the energetic landscape as the external magnetic field was swept from one saturation direction to the other. The transition states cannot be identified from the AMR alone. A system that showed only two transition paths was the 1000 nm wide and 80 nm thick ring segment. Its AMR is shown in Fig. 4.8. The sharp jumps in AMR for four consecutive sweeps occur in seven out of eight magnetization reversals at exactly the same fields (±21.5 mT and ±24 mT), even though the intermediate transitions differed (see blue curve). This suggests that pinning at the surfaces is one source of randomness in the

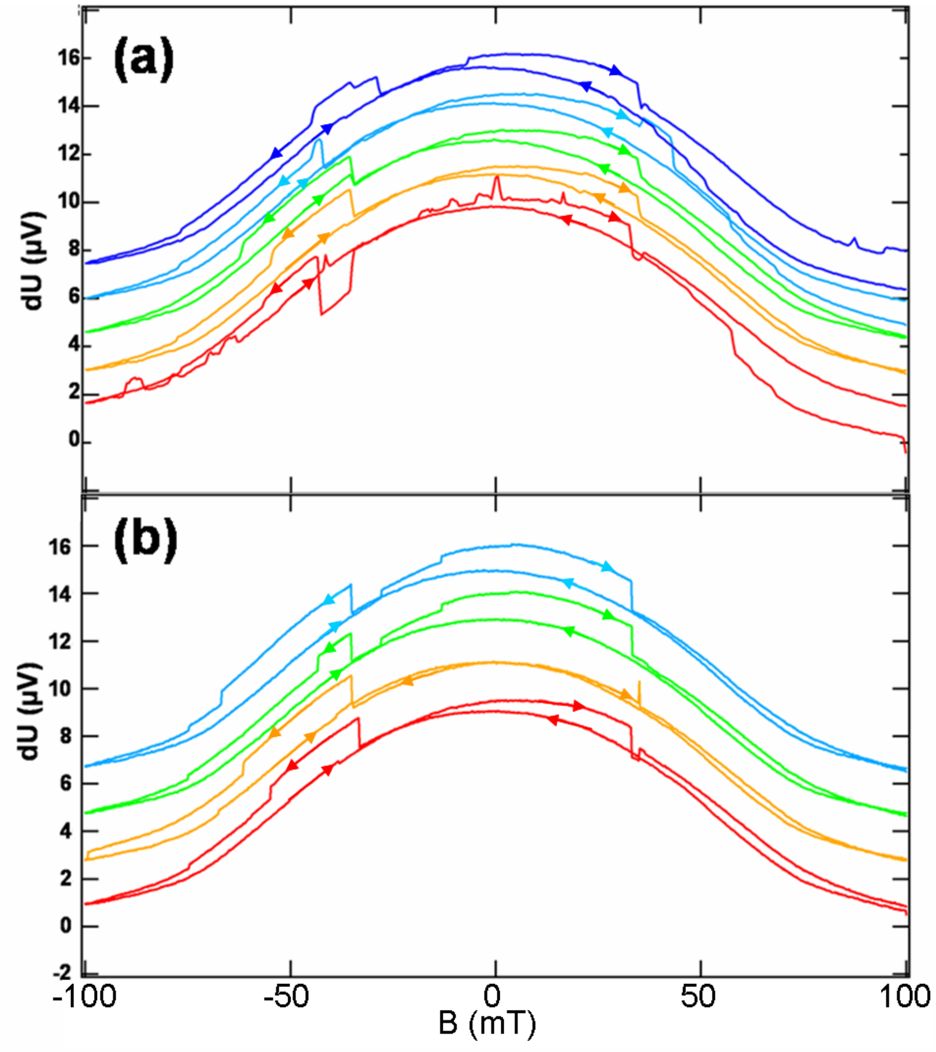

Fig. 4.6: (a) AMR sweeps No. 1-5 of the 300 nm wide and 40 nm thick permalloy ring section. A strong variation in the signal reveals a training effect of the magnetization. (b) sweeps No. 19-23. The agreement is better but still not complete. The curves are off-set for clarity.

magnetization switching since the magnetic volume of this sample is larger in comparison to its surface than the two other samples previously discussed. One jump occured at lower fields (+18.5 mT instead of +21.5 mT).

Several AMR curves were measured simultaneously to X-ray imaging. A part of one of the AMR curves is shown in Fig. 4.9(a). It shows transitions at the two different fields. Figure 4.9(b) shows the corresponding magnetic XMCD contrast in the sample at the field values identified by colored markers. Figure 4.9(c) shows a sketch of the magnetization states at these fields. The X-ray images show that, sweeping down from positive saturation, the magnetization contains a double-vortex wall. Such a wall is known

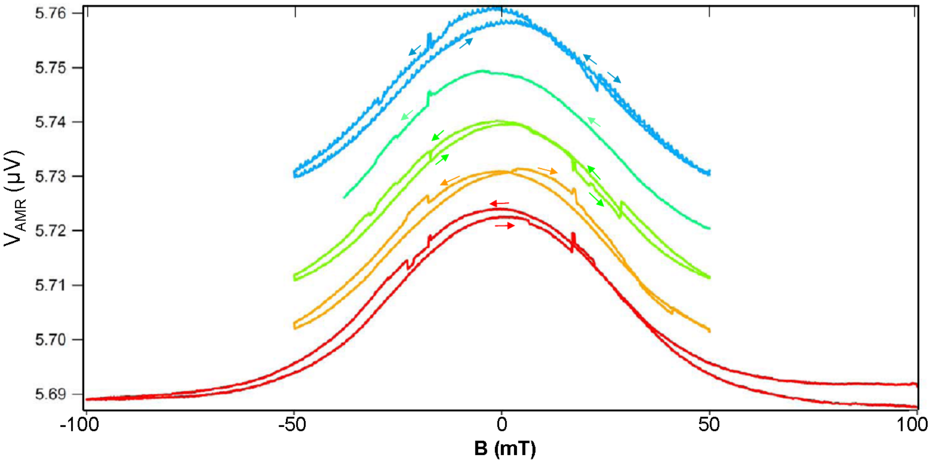

Fig. 4.7: Five AMR curves for a 500 nm wide and 60 nm thick permalloy ring segment. The curves are off-set for clarity. The fifth AMR sweep (blue curve) shows the jitter due to the periodic opening and closing of the beam shutter.

to be present in permalloy rings thicker than 65 nm [167]. In the positive sweep direction the domain wall consists of a vortex elongated to an asymmetric Bloch wall as is visible by the bright line reaching towards the upper contacts from the bright domain in the center. The magnetic contrast in these images is very limited due to the short exposure time, but

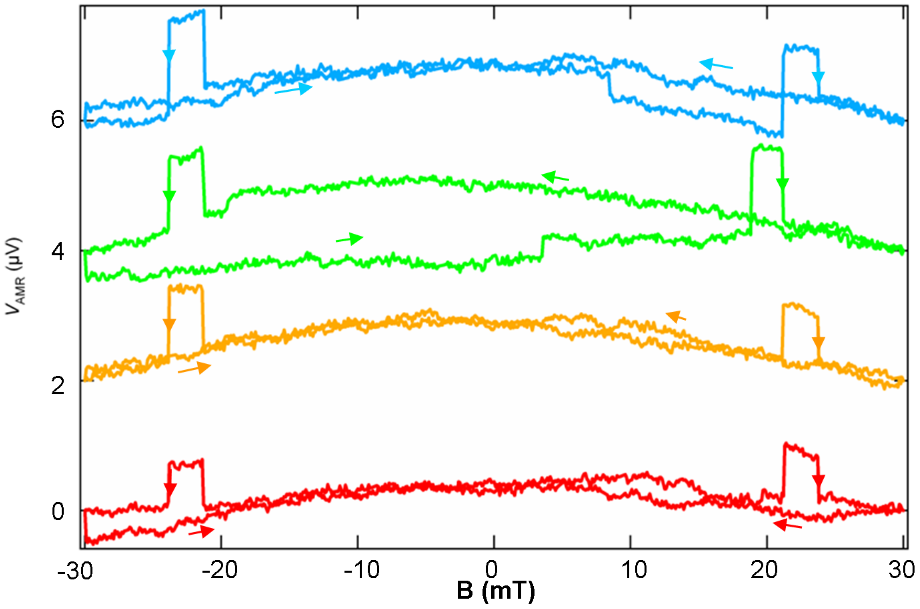

Fig. 4.8: Four AMR sweeps of a 960 nm × 80 nm permalloy wire from positive magnetic field to negative field and back.

can be enhanced to the human eye when viewing successive images as a movie.

To confirm that these domain wall types, the asymmetric Bloch wall and the double-vortex wall can both exist in permalloy rings having the same dimensions as in our samples, we performed micromagnetic simulations. Figure 4.10 shows a comparison of the domain walls seen in X-ray images and in simulation. The double-vortex wall appeared as the magnetization initially pointing in the y-direction was relaxed.

These preliminary results have been presented at the 51st Conference on Magnetism and Magnetic Materials (MMM) in Baltimore, MD, USA in January 2007 (see **[C15]**) and

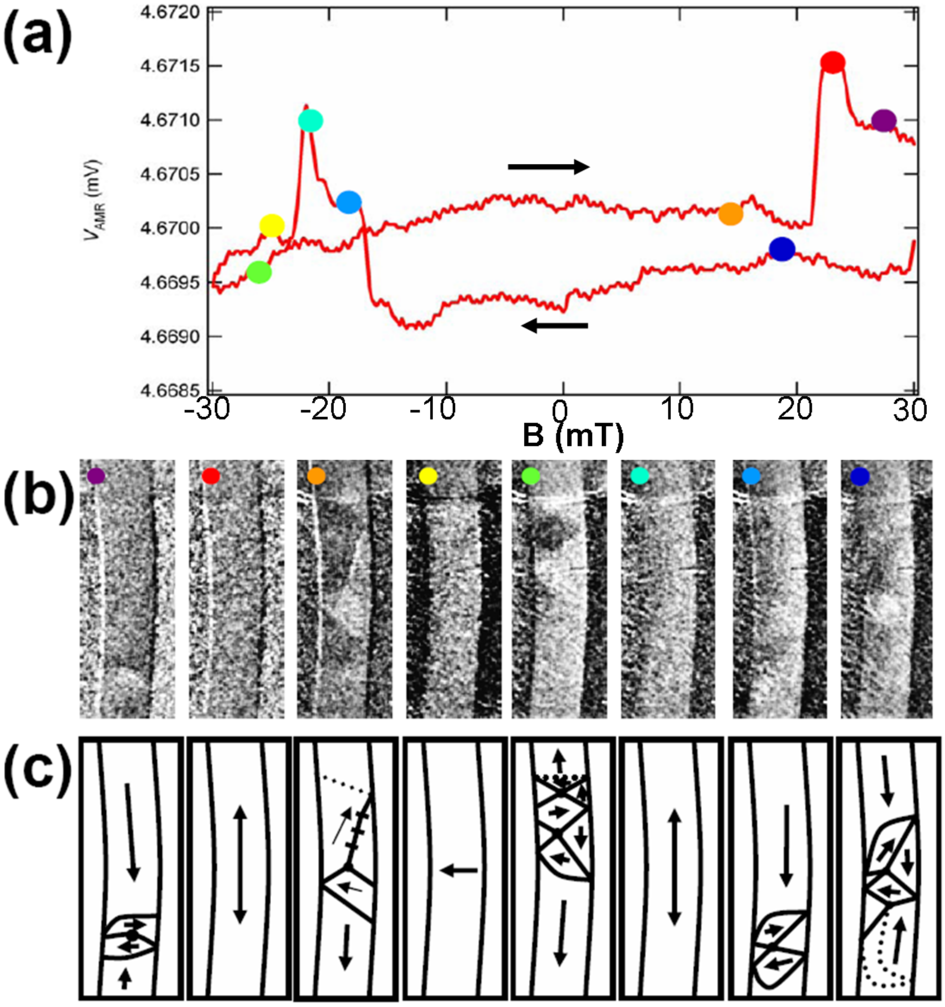

Fig. 4.9: (a) AMR sweep of a 960 nm × 55 nm permalloy wire from positive magnetic field to negative field and back. Eight exemplary magnetic states as distinguished by their magnetoresistance are marked by colored dots. (b) X-ray microscopy images taken at these field values show distinct magnetic contrast. (c) Sketches of the magnetization pattern from the images in (b). Note the different domain-wall types around the peaks in the AMR.

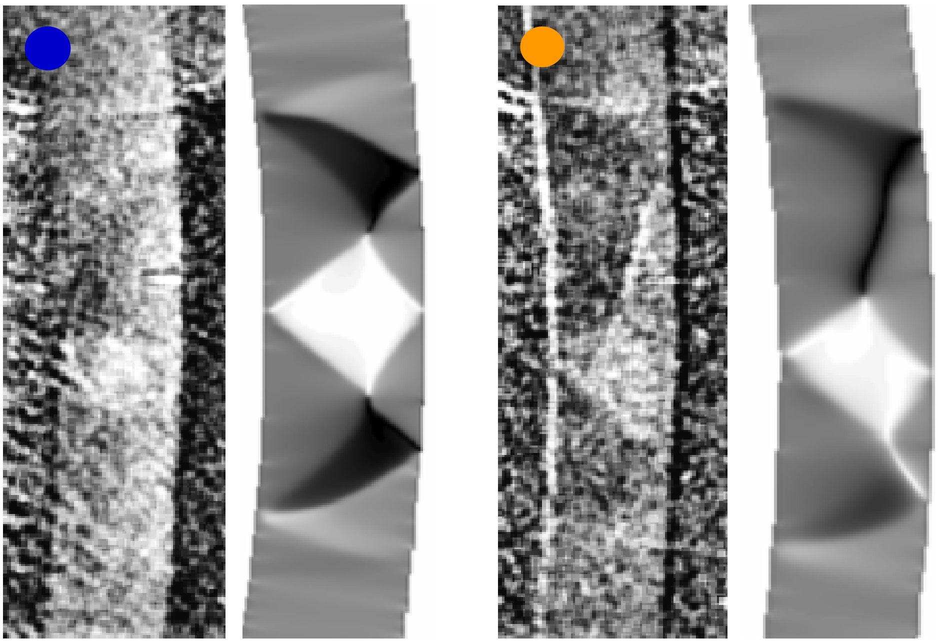

Fig. 4.10: (a) Comparison of the two domain wall types in Fig. 4.9(b) with micromagnetic simulations. Shown on the left is the double-vortex wall, on the right a cross-tie wall in combination with a vortex wall.

during a talk at the group of Stuart Parkin at the IBM Research Center in Almaden, San Jose, CA, USA, **[I6]** but have not been published in a journal so far.

4.4 Spin-Torque Induced Magnetization Dynamics

With the experience in the static and dynamic behavior of magnetic domains and domain walls as well as in the influence of the local magnetization on the magnetoresistance in permalloy microelements described in the previous sections I investigated the changes in magnetization due to high-density currents. Magnetization switching induced by spin-transfer torque [23, 22, 98, 101] and domain-wall motion [30, 109, 184, 100, 103, 185, 186] has recently drawn a lot of attention as it is currently viewed as a promising solution for the realization of magnetic random access memories [187, 101, 188]. Current-induced domain-wall motion has potential application in spintronic data storage devices, e.g. in the racetrack memory [18], or data transfer schemes [189, 21, 190]. Several theoretical models have been established to explain the electronic origin of current-induced magnetization changes and to predict their effects (see Section 2.5.3). However, many aspects are still under active discussion, for example, the microscopic mode of domain-wall propagation: Do domain walls propagate continuously or discretely in form of a series of random pinning-depinning processes? How does temperature influence domain-wall propagation? Does the nonadiabatic spin-torque really exist and if so, how strong is it?

Also, a number of advanced issues have emerged, e.g., the influence of dynamic spin-polarized currents on the magnetization: What happens when the risetime of a current pulse becomes very short? And what if the frequency of an ac-current matches the eigenfrequency of a magnetic object, i.e., a domain wall or a magnetic vortex? What if a domain wall experiences a periodic potential as for example in the racetrack memory where bits are stored in regions of same magnetization separated by domain wall pinned by periodic notches?

In this thesis I have focussed on spin-torque phenomena in single-layer permalloy systems with lateral current flows. These systems constitute the ideal testbeds for studying the fundamental physics of current-induced domain-wall motion. In the following I subdivided the results of my studies into four categories that address one or more of the questions stated above.

First, I describe the influence of ac-currents on the dynamics of a domain wall with the help of micromagnetic simulations and an analytic model in Section 4.4.1. In Section 4.4.2 I describe our observations from X-ray microscopy on the current-induced domain-wall motion with nanosecond short current pulses. Our results on the gyration of magnetic vortices and antivortices induced by spin-torque are summarized in Section 4.4.3.

4.4.1 Spin-Torque Induced Domain-Wall Dynamics

I began to numerically investigate the spin-torque induced magnetization dynamics in 2005 when I worked with Benjamin Krüger for his Masters thesis dealing with "Current-Induced Domain-Wall Dynamics in Ferromagnetic Nanowires" [191]. He used my Runge-Kutta micromagnetic simulation code and extended it further by implementing the adiabatic and the non-adiabatic spin-torque terms suggested by S. Zhang and Z. Li [28] into the LLG equation. We tested the improved code on a system for which both an analytical approximation and experimental data exist: The ac-current driven domain-wall oscillation in thin ferromagnetic nanowires. Saitoh *et al.* have presented data for Néel walls in thin curved nanowires in an external magnetic field [184]. The wire curvature and the field created a parabolic potential for the wall in which the wall could oscillate if excited at resonance. They showed resonance peaks in the ac resistances for different field strengths.

Benjamin Krüger established an analytical model in which this spin-torque driven domain-wall oscillation was seen as an harmonic oscillator. We compared the numerical results from simulations with the extended code to predictions from the analytical model and derived the parameters that unambiguously define an harmonic oscillator, i.e., domain-wall mass, resonance frequency, damping constant, and the force acting on the wall. The ability to calculate the force acting on a magnetic object due to spin-torque has proven important for the analysis of further studies of spin-torque driven magnetization dynamics. The difference between Saitoh's model and ours is that Saitoh *et al.* assumed the wall to behave as an harmonic oscillator and arrived at several incorrect conclusions. Our only assumption was that the domain wall in thin nanowires remains rigid, which we verified numerically (see Ref. [29] **[P12]** for details).

The work was published as **[P12]** and is reprinted in its entirety with permission from B. Krüger, D. Pfannkuche, M. Bolte, G. Meier, and U. Merkt, Phys. Rev. B **75**, 054421 (2007). Copyright (2007) by the American Physical Society. It was presented at an international workshop, an international conference, and in an invited talk (see **[C12]**, **[C19]**, and **[I6]**). A conference article for the Joint European Magnetism Symposia 2006 (JEMS2006) in San Sebastian, Spain, focussing on the computed domain-wall eigenmodes and the domain-wall velocities was published as **[P14]** in G. Meier, M. Bolte, U. Merkt, B. Krueger, and D. Pfannkuche, *"Current-induced domain-wall motion in permalloy semi rings"*, J. Magn. Magn. Mat., **316**, e966, Copyright Elsevier (2007). It is also reprinted here.

PHYSICAL REVIEW B **75**, 054421 (2007)

Current-driven domain-wall dynamics in curved ferromagnetic nanowires

Benjamin Krüger and Daniela Pfannkuche
I. Institut für Theoretische Physik, Universität Hamburg, Jungiusstrasse 9, 20355 Hamburg, Germany

Markus Bolte, Guido Meier, and Ulrich Merkt
Institut für Angewandte Physik und Zentrum für Mikrostrukturforschung, Universität Hamburg, Jungiusstrasse 11, 20355 Hamburg, Germany

(Received 30 August 2006; revised manuscript received 30 November 2006; published 26 February 2007)

The current-induced motion of a domain wall in a semicircle nanowire with applied Zeeman field is investigated. Starting from a micromagnetic model we derive an analytical solution which characterizes the domain-wall motion as a harmonic oscillation. This solution relates the micromagnetic material parameters with the dynamical characteristics of a harmonic oscillator: i.e., domain-wall mass, resonance frequency, damping constant, and force acting on the wall. The time derivative of the current density greatly contributes to the force on the domain wall. For wires with strong curvature the dipole moment of the wall as well as its geometry influence the eigenmodes of the oscillator. Based on these results we suggest experiments for the determination of material parameters which otherwise are difficult to access. Numerical calculations confirm our analytical solution and show its limitations.

DOI: 10.1103/PhysRevB.75.054421 PACS number(s): 75.60.Ch, 72.25.Ba, 76.50.+g

I. INTRODUCTION

The field-driven dynamics of magnetic domain walls has been intensely studied over the last decades.[1,2] The topic has recently regained interest by the discovery that spin-polarized currents of high density can alter magnetization configurations[3–6] and move domain walls.[7–11] Current-induced magnetic switching is viewed as a promising solution for the realization of magnetic random access memories,[6,12,13] while current-induced domain-wall motion has potential applications in spintronic data storage devices: e.g., in the racetrack memory[14] or data transfer schemes.[15–17] Several models of current-driven magnetization dynamics have been established to explain the electronic origin of current-induced magnetization changes and to predict their effects.[3,4,18–21] At first it was assumed that for finite domain walls the spins of the conduction electrons adiabatically follow the local magnetic moments.[18,22] Later the theoretical model was extended to include a nonadiabatic mismatch between the polarization of the current and the direction of the magnetization.[19–21]

The measured and calculated velocities of current-driven magnetic domain walls in thin nanowires vary by several orders of magnitude even for the same material.[7,21,23–25] While it has been originally suggested that the discrepancy could be due to thermal activation[11,25–28] or surface roughness,[25] it has recently been found that the domain-wall velocity depends on the type of the domain wall[26,29] which can be changed by a spin-polarized current.[8,26,30,31] Recently it has been observed that the velocity of field-driven domain-wall motion[32] can be altered by ±100 m/s by a pulsed spin-polarized current[33] and that the motion can even be halted completely.[34] It is now assumed that the adiabatic term is largely responsible for the acceleration of the domain wall while the nonadiabatic term will cause the wall to continually move.[21]

In this paper we use an alternating current to excite transverse walls in thin narrow rings. From a micromagnetic description we derive a hitherto phenomenological harmonic oscillator model which well describes the wall motion in this geometry. Experimentally it has been shown that domain-wall oscillations excited with an alternating current at their resonance frequency require current densities one to two orders of magnitude less (10^{10} A/m^2; see Refs. 9 and 35) than for pulsed excitations (10^{11}–10^{12} A/m^2; see Refs. 6, 7, 11, and 26). Our calculations show that the time derivative of the current density greatly contributes to the force on the domain wall which could be an explanation for this phenomenon. Experimentally alternating current excitation is advantageous because it allows for time-resolved imaging of the domain-wall motion by its periodic return to the initial state.

This work is organized in two parts presenting an analytical model for the description of domain walls in curved nanowires and a numerical investigation supporting the analytical model as well as showing its limitations. The analytical model used to describe the motion of a domain wall in a nanowire is developed in the framework of the one-dimensional (1D) approximation as done previously for field-driven motion[36] and direct-current-driven spin torque.[21,25,34] We here limit ourselves to the spin-transfer torque. This approach is valid to describe ferromagnetic metals where the Fermi wavelength is much smaller than the size of the magnet and the width of the domain wall.[18] Solving analytically the Landau-Lifshitz-Gilbert equation extended by the current corrections due to Zhang and Li[21] we are able to express the properties of the driven oscillator by the quantities determining the micromagnetic model. Furthermore, we are able to include the influence of alternating current excitation, i.e., the time derivative of the current density. A comparison of the numerical calculations with our analytical solution confirms the importance of the geometry due to the curved wires. Finally, we suggest experiments which can determine the values of the nonadiabatic spin torque and the Gilbert damping parameter from the phase of the oscillation with respect to the exciting current.

©2007 The American Physical Society

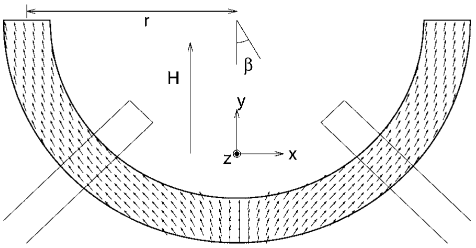

FIG. 1. Scheme of the semicircle nanowire with radius r in a magnetic field H. The static magnetization in the absence of a current is indicated by small arrows. The two rectangles under angles $\beta = \pm 45°$ are the electrical contacts.

II. MODEL

Figure 1 shows a ferromagnetic semicircle nanowire with a domain wall at its bottom placed in an external magnetic field.[37] The wall is excited by an oscillating current flowing between the two contacts.[9]

The magnetization dynamics of a magnetic wire is well described by the Landau-Lifshitz-Gilbert (LLG) equation.[38] In the presence of a spin-polarized current density $\vec{j}$, the interaction between the itinerant electrons and the magnetization $\vec{M}$ leads to an extension of the LLG equation. This extension was derived from a quantum mechanical model by Zhang and Li.[21] Their semiclassical approximation results in the extended LLG equation in Gilbert's form

$$\frac{d\vec{M}}{dt} = -\gamma\vec{M}\times\vec{H}_{\mathrm{eff}} + \frac{\alpha}{M_s}\vec{M}\times\frac{d\vec{M}}{dt} - \frac{b_j}{M_s^2}\vec{M}\times[\vec{M}\times(\vec{j}\cdot\vec{\nabla})\vec{M}] - \xi\frac{b_j}{M_s}\vec{M}\times(\vec{j}\cdot\vec{\nabla})\vec{M}, \tag{1}$$

with the gyromagnetic ratio γ, the Gilbert damping parameter α, the saturation magnetization M_s, and the ratio between exchange relaxation time and spin-flip relaxation time $\xi = \tau_{\mathrm{ex}}/\tau_{\mathrm{sf}}$. The effective magnetic field H_{eff} includes the external as well as the internal fields. In this model the spin current is sensitive to the spatial inhomogeneities of the magnetization with a coupling constant $b_j = \frac{P\mu_B}{eM_s(1+\xi^2)}$ where P denotes the spin polarization of the current and μ_B is the Bohr magneton.

Since the saturation magnetization is constant for a given material at fixed temperature, $\vec{M}$ is perpendicular to $\frac{d\vec{M}}{dt}$ and Eq. (1) can be reformulated to an explicit equation of motion for the magnetization

$$\frac{d\vec{M}}{dt} = -\gamma'\vec{M}\times\vec{H}_{\mathrm{eff}} - \frac{\alpha\gamma'}{M_s}\vec{M}\times(\vec{M}\times\vec{H}_{\mathrm{eff}}) - \frac{b_j'}{M_s^2}(1+\alpha\xi)\vec{M}\times[\vec{M}\times(\vec{j}\cdot\vec{\nabla})\vec{M}] - \frac{b_j'}{M_s}(\xi-\alpha)\vec{M}\times(\vec{j}\cdot\vec{\nabla})\vec{M}, \tag{2}$$

with the abbreviations $\gamma' = \frac{\gamma}{1+\alpha^2}$ and $b_j' = \frac{b_j}{1+\alpha^2}$. This equation is the starting point for the analytical as well as for the numerical calculations presented in the following.

III. ANALYTICAL CALCULATIONS OF THE STRAIGHT WIRE

For the analytical treatment of Eq. (2) we transform the semicircle wire in a homogeneous Zeeman field to a straight wire in a spatially varying field. For this we consider the parallel component of the field. The perpendicular component does not contribute to the domain-wall motion in a *straight* wire and is included in the shape anisotropy. In Sec. IV we will investigate the effect of the perpendicular component of the field on the motion of the domain wall in the *curved* wire and the increase of the exchange energy due to the curvature.

The wire is directed along the x axis and the direction of the magnetization is expressed in a polar spin basis $\vec{M} = M_s(\cos\theta, \sin\theta\cos\phi, \sin\theta\sin\phi)$. In the absence of electric current and external magnetic field the energy of a domain wall within the wire is

$$E = S\int\left[A\left(\frac{\partial\theta(x)}{\partial x}\right)^2 + K\sin^2\theta(x)\right]dx, \tag{3}$$

where θ denotes the angle between the wire axis and the magnetization. A and K denote the exchange and shape anisotropy constants. This functional can be minimized by the well known Néel wall described by the angle

$$\theta = \pi - 2\arctan(e^{(x-X)/\lambda}). \tag{4}$$

The center of the wall is at position X, and the width of the domain wall is $\lambda = \sqrt{A/K}$. From Eq. (4) two expressions

$$\cos\theta = \tanh\left(\frac{x-X}{\lambda}\right), \quad \sin\theta = \frac{1}{\cosh\left(\frac{x-X}{\lambda}\right)} \tag{5}$$

can be derived which will be useful in our further calculations.

In the presence of an external field H_{ext} the demagnetization energy $K_\perp\sin^2\theta\sin^2\phi$ caused by the rotation of the wall around the wire axis can no longer be neglected. We include the external field perpendicular to the wire into the shape anisotropy $K_\perp$. The energy functional in Eq. (3) has to be extended to

$$E = \int\left[K\sin^2\theta + A\left(\frac{\partial\theta}{\partial x}\right)^2 + A\sin^2(\theta)\left(\frac{\partial\phi}{\partial x}\right)^2\right]dV + \int[K_\perp\sin^2\theta\sin^2\phi - \mu_0 M_s H_{\mathrm{ext}}(x)\cos\theta]dV. \tag{6}$$

Here we have restricted ourselves to an external field parallel to the wire. Also the crystalline anisotropy has been neglected.[39] From the energy functional in Eq. (6) we derive the effective magnetic field through the relation $\vec{H}_{\mathrm{eff}} = -\frac{1}{\mu_0}\frac{\delta E}{\delta\vec{M}}$.

We can then write the extended LLG equation (2) in the polar spin basis

$$\dot{\theta} = -\frac{\gamma'}{\mu_0 M_s \sin(\theta)}\frac{\delta E}{\delta\phi} - \frac{\gamma'\alpha}{\mu_0 M_s}\frac{\delta E}{\delta\theta} + b_j'(1+\alpha\xi)\vec{j}\cdot\vec{\nabla}\theta + b_j'(\xi-\alpha)\sin(\theta)\vec{j}\cdot\vec{\nabla}\phi \tag{7}$$

and

$$\dot{\phi}\sin\theta = \frac{\gamma'}{\mu_0 M_s}\frac{\delta E}{\delta\theta} - \frac{\gamma'\alpha}{\mu_0 M_s \sin(\theta)}\frac{\delta E}{\delta\phi} + \sin(\theta) b_j'(1+\alpha\xi)\vec{j}\cdot\vec{\nabla}\phi - b_j'(\xi-\alpha)\vec{j}\cdot\vec{\nabla}\theta. \tag{8}$$

Assuming that the moving wall stays a Néel wall (see Sec. VI) we can describe its motion, following the description of Schryer and Walker[2] by two dynamical variables: the position of its center X and its angle around the wire axis $\phi(x)=\phi$, which is uniform along the wire. With Eqs. (5) and (6) we get from Eqs. (7) and (8)

$$\frac{\sin(\theta)}{\lambda}\dot{X} = -\frac{2K_\perp\gamma'}{\mu_0 M_s}\sin(\theta)\sin(\phi)\cos(\phi) - \alpha\gamma'\sin(\theta)H_{\mathrm{ext}}(x) - \frac{b_j'}{\lambda}\sin(\theta)(1+\alpha\xi)j - \frac{2K_\perp\gamma'\alpha}{\mu_0 M_s}\sin(\theta)\cos(\theta)\sin^2(\phi) \tag{9}$$

and

$$\dot{\phi}\sin\theta = \sin(\theta)\gamma' H_{\mathrm{ext}}(x) + \sin(\theta)\frac{b_j'(\xi-\alpha)j}{\lambda} - 2\sin(\theta)\gamma'\alpha K_\perp\sin(\phi)\cos(\phi)\frac{1}{\mu_0 M_s} + \frac{2K_\perp\gamma'}{\mu_0 M_s}\sin(\theta)\cos(\theta)\sin^2(\phi), \tag{10}$$

with the wall width $\lambda = \sqrt{\frac{A}{K+K_\perp\sin^2\phi}} \approx \sqrt{\frac{A}{K}}$.[40] Note that X and ϕ depend on the position x along the wire. In the following we show that a solution consistent with our initial assumptions exists for small exitations.[2] Note that this condition holds for realistic current densities.

Assuming that $H_{\mathrm{ext}}(x)$ varies slowly on the length scale of the domain-wall width $\lambda=\sqrt{A/K}$, $\sin\theta$ is replaced by a δ-function $\pi\lambda\delta(x-X)$ in view of Eq. (5). Also we neglect terms which are nonlinear in ϕ. This approximation holds for angles ϕ smaller than about 10°.

The equations of motion for the domain wall then become

$$\dot{X} = -\lambda 2\gamma' K_\perp\phi\frac{1}{\mu_0 M_s} - \lambda\gamma'\alpha H_{\mathrm{ext}}(X) - b_j'(1+\alpha\xi)j \tag{11}$$

and

$$\dot{\phi} = \gamma' H_{\mathrm{ext}}(X) - 2\gamma'\alpha K_\perp\phi\frac{1}{\mu_0 M_s} + \frac{b_j'(\xi-\alpha)j}{\lambda}. \tag{12}$$

These equations are general equations of motion with a time-dependent current density j. In the limit of a steady current and a homogeneous magnetic field one can calculate the initial velocity of the wall by setting $\phi=0$, the initial condition of the Néel wall. This leads to the initial velocity $\dot{X}_i = -\lambda\gamma'\alpha H_{\mathrm{ext}} - b_j'(1+\alpha\xi)j$ which is exactly the value obtained by Zhang and Li.[21] The terminal velocity $\dot{X}_f = -(\lambda\gamma H_{\mathrm{ext}} + b_j\xi j)/\alpha$ is calculated by setting $\dot{\phi}=0$, i.e., stationary motion. This velocity is also identical to the one calculated by Zhang and Li. Similar relations have recently been found by Dugaev *et al.*[41]

The domain-wall mass is obtained by comparing the ϕ-dependent part of the wall energy in Eq. (6) to the energy E of the domain-wall quasiparticle:

$$\frac{1}{2}m\dot{X}^2 = E = S\int dx K_\perp \sin^2(\theta)\left(\dot{X}\frac{\mu_0 M_s}{\lambda 2\gamma' K_\perp}\right)^2 = \frac{1}{2}\frac{S\mu_0^2 M_s^2}{\lambda\gamma'^2 K_\perp}\dot{X}^2. \tag{13}$$

Here we used

$$\phi = -\dot{X}\frac{\mu_0 M_s}{2\lambda\gamma' K_\perp}, \tag{14}$$

derived from Eq. (11) for stationary motion and in the absence of electric currents and external fields. We arrive at the domain-wall mass

$$m = \frac{S\mu_0^2 M_s^2}{\lambda\gamma'^2 K_\perp}. \tag{15}$$

Note that this result relates the phenomenological domain-wall mass of a Néel wall to the micromagnetic material parameters.

In the case of a curved wire the projection of a uniform external field along the wire is given by $H_{\mathrm{ext}}(x) = H_0\sin(x/r)$. Transferring this to our straight wire model, at small displacements of the domain wall ($X \ll r$) the wall is exposed to the external field $H_{\mathrm{ext}} \approx H_0 X/r$. Then the equations of motion become a system of two coupled linear differential equations of first order:

$$\begin{pmatrix}\dot{X}\\ \dot{\phi}\end{pmatrix} = \gamma'\begin{pmatrix} -\lambda\alpha H_0\frac{1}{r} & -\lambda 2K_\perp\frac{1}{\mu_0 M_s}\\ H_0\frac{1}{r} & -2\alpha K_\perp\frac{1}{\mu_0 M_s}\end{pmatrix}\begin{pmatrix}X\\ \phi\end{pmatrix} + b_j' j\begin{pmatrix}-(1+\alpha\xi)\\ \frac{(\xi-\alpha)}{\lambda}\end{pmatrix}. \tag{16}$$

Except for the nonvanishing first matrix element $-\lambda\alpha H_0/r$ these equations are equivalent to those of a driven harmonic oscillator. For a time-dependent current density of the form $j_0 e^{i\Omega t}$ the general solution

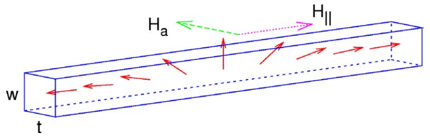

FIG. 2. (Color online) Schematic illustration of the magnetization in the Néel wall (solid red arrows) in a straight wire of width w and thickness t. $H_{\|}$ and H_a are the parallel components of the external field and the anisotropy field, respectively.

$$\begin{pmatrix} X(t) \\ \phi(t) \end{pmatrix} = \begin{pmatrix} X_+ \\ \phi_+ \end{pmatrix} e^{-\Gamma t + i\omega_f t} + \begin{pmatrix} X_- \\ \phi_- \end{pmatrix} e^{-\Gamma t - i\omega_f t} + \frac{1}{\omega_r^2 - \Omega^2 + 2i\Omega\Gamma} \frac{\vec{F}}{m} \tag{17}$$

consists of an exponentially damped starting configuration with the initial conditions described by $X_\pm$ and $\phi_\pm$ and a current-driven oscillation with the driving force $\vec{F}$. The damping constant

$$\Gamma = \alpha\gamma' \left(\frac{\lambda H_0}{2r} + \frac{K_\perp}{\mu_0 M_s} \right) \tag{18}$$

depends on the ratio of applied magnetic field and ring radius. It represents the restoring force acting on the domain wall. This dependence of the damping constant on the restoring force expresses that the damping is spatially dependent. This also leads to a second term in the frequency of the free oscillation,

$$\omega_f = \sqrt{\frac{2\gamma'^2 H_0 \lambda K_\perp}{\mu_0 M_s r} - \alpha^2 \gamma'^2 \left(\frac{K_\perp}{\mu_0 M_s} - \frac{\lambda H_0}{2r} \right)^2}, \tag{19}$$

which is different from Γ. Hence the resonance frequency

$$\omega_r = \sqrt{\omega_f^2 + \Gamma^2} = \sqrt{\frac{2\gamma'^2 H_0 \lambda K_\perp}{\mu_0 M_s r}(1 + \alpha^2)} \tag{20}$$

depends explicitly on the Gilbert damping parameter α and differs from the resonance frequency of a normal harmonic oscillator,

$$\omega_0 = \sqrt{\frac{D}{m}} = \sqrt{\frac{2\gamma'^2 H_0 \lambda K_\perp}{\mu_0 M_s r}}, \tag{21}$$

by the factor $\sqrt{1+\alpha^2}$. The constant D is given by $D = F_H / X$ where F_H is the force on the domain wall due to the external magnetic field. The force

$$\vec{F} = -m b_j j_0 e^{i\Omega t} \left(\frac{2\gamma' K_\perp \xi}{\mu_0 M_s} + \frac{1 + \alpha\xi}{1 + \alpha^2} i\Omega \right) \vec{e}_X - m b_j j_0 e^{i\Omega t} \left(\gamma' H_0 \frac{1}{r} - \frac{\xi - \alpha}{1 + \alpha^2} \frac{i\Omega}{\lambda} \right) \vec{e}_\phi, \tag{22}$$

induced by the current, depends on the frequency Ω of the applied current. The terms in Eq. (22) can be understood as direct forces due to the spin torque and the precessions of the magnetization in the external and anisotropy fields depicted in Fig. 2. The terms proportional to $i\Omega$ express the current-induced spin torque. They are the time derivatives of the inhomogenities in Eq. (16). The H_0-dependent term is a result of the precession of the magnetization in the external field which causes a rotation of the wall around the wire axis. The precession in the anisotropy field, described by the $K_\perp$ term in Eq. (22), causes a change of the wall velocity.

Except that the force depends on the frequency Ω of the applied current the result for the domain-wall displacement [Eq. (17)] is equal to the one in a harmonic oscillator. With increasing Ω the force increases and its phase shifts up to 90°. In the absence of a nonadiabatic spin torque ($\xi = 0$), current and domain-wall displacement at resonance have opposite sign. In case of a nonadiabatic torque the phase at resonance frequency between the current and the magnetization in the z direction is 90° when the ratio ξ of exchange and spin-flip relaxation time equals the Gilbert damping parameter ($\xi = \alpha$). The phase can be used to find out whether a nonadiabatic spin torque exists and to determine the value of ξ in comparison to the damping parameter α.

The influence of the adiabatic torque on the position of the wall is obtained by setting $\xi = 0$ in Eq. (22). The x component of the force $\vec{F}$ due to the adiabatic torque is proportional to the time derivative of the current density. Therefore, the adiabatic torque does not accelerate the wall when the current does not change in time. This explains the observation of Zhang and Li[21] that without a nonadiabatic spin torque a domain wall subjected to a steady current stops moving. In contrast the nonadiabatic contributions to the force are proportional to the current density as well as to its derivative.

In Eq. (17) the starting configuration depends on $\phi_\pm$ and $X_\pm$. The equation that follows from decoupling of Eq. (16),

$$\phi_\pm = \left(\frac{\alpha}{2\lambda} - \frac{\alpha H_0 \mu_0 M_s}{4 r K_\perp} \mp i \frac{\omega_f \mu_0 M_s}{2\lambda\gamma' K_\perp} \right) X_\pm, \tag{23}$$

connects $\phi_\pm$ with $X_\pm$. Hence we have two parameters left for our starting configuration as expected for an oscillation.

With the above analytical model—i.e., Eqs. (15) and (17)–(22)—we are able to derive the hitherto phenomenological oscillator model[9] and to express its characteristics by the micromagnetic material parameters. Likewise, the measurement of the domain-wall motion allows the determination of micromagnetic quantities.

IV. CURVED WIRES

For curved wires in a homogeneous magnetic field its component perpendicular to the wire has to be taken into account. Also the change of the magnetization due to the curvature becomes important. To include the perpendicular field we calculate the force on the domain wall as the spatial derivative of its Zeeman energy. The total magnetic moments parallel to the wire,

$$m_\| = \int M_s \cos[\theta(x)] dV = -2 M_s S X, \tag{24}$$

and perpendicular to the wire,

$$m_\perp = \int M_s \sin[\theta(x)] dV = \pi M_s S \lambda, \tag{25}$$

are volume integrals over its magnetization that are readily calculated using the relations in Eq. (5). Note that $m_\parallel$ is the magnetic moment of an abrupt domain wall. With the magnetic field H_0 in the y direction the Zeeman energy can be written as

$$E_\parallel = \mu_0 M_s H t \int_{r-w/2}^{r+w/2} r' \left[\int_{-\pi/2}^{\beta_0} \sin(\beta) d\beta - \int_{\beta_0}^{\pi/2} \sin(\beta) d\beta \right] dr', \tag{26}$$

where $\beta_0 = \frac{X}{r}$ is the angle of the position of the domain wall (see Fig. 1) and r, w, and t are the radius, the width, and the thickness of the wire. We get

$$E_\parallel = -2\mu_0 M_s S r H \cos(\beta_0) = 2\mu_0 M_s S H Y, \tag{27}$$

with the cross section $S = wt$. One recognizes that the energy is equivalent to the energy of a monopole with magnetic charge $Q_M = 2\mu_0 M_s S$. For small domain-wall displacements we can write the cosine in Eq. (27) as a Taylor series up to second order in X and get

$$E_\parallel \approx -2\mu_0 M_s S r H \left(1 - \frac{X^2}{2r^2} \right). \tag{28}$$

The monopole has been included in the calculations in Sec. III as well as in the calculations of Saitoh *et al.*[9] The perpendicular magnetization contributes to the Zeeman energy by a term

$$E_\perp = -\mu_0 m_\perp H \cos\left(\frac{X}{r}\right) \approx -P_M H \left(1 - \frac{X^2}{2r^2} \right), \tag{29}$$

which can be interpreted as the energy of a magnetic dipole with moment $P_M = \mu_0 \pi M_s S \lambda$. The potential $E = E_\parallel + E_\perp$ is parabolic like for the straight wire.[9,34] However, the resonance frequency is higher. The Zeeman energy of the perpendicular magnetization has previously not been included in the magnetic energy. It gives a correction to the magnetic force on the domain wall,

$$F_x = -\frac{dE}{dX} \approx -\frac{2\mu_0 M_s S H}{r} X - \frac{\pi \mu_0 M_s S \lambda H}{r^2} X = -\frac{Q_M H}{r} X - \frac{P_M H}{r^2} X = -\frac{Q_M}{r} X H \left(1 + \frac{\pi\lambda}{2r} \right). \tag{30}$$

Thus, we include the action of a field component perpendicular to the wire by replacing the field in Eq. (17) by an effective field

$$H_e = H \left(1 + \frac{\pi \lambda}{2r} \right). \tag{31}$$

For example, a ring with a width of 370 nm (Ref. 42) and radius of 500 nm experiences an increase in the effective field of approximately 31%.

We now take into acount the curvature of the wire. With decreasing ring radius the angle between neighboring spins in the domain wall shrinks. This leads to an additional contribution to the exchange energy of the wall when its magnetization points out of the wire plane.

To calculate the new exchange energy we change the spin basis to Cartesian coordinates. To distinguish the spin basis from the basis in space we introduce the coordinates $\chi = \cos\theta$, $\eta = \sin\theta\cos\phi$, and $\zeta = \sin\theta\sin\phi$. Moving along the wire the magnetization performs a rotation in the $-\theta$ direction due to the domain wall as well as a rotation around the ζ axis due to the curvature. For small rotations $\Delta\theta$ and $\Delta\beta$ the Cartesian coordinates are given by

$$\chi = \cos(\Delta\beta)\cos(\theta + \Delta\theta) - \sin(\Delta\beta)\sin(\theta + \Delta\theta)\cos(\phi),$$

$$\eta = \cos(\Delta\beta)\sin(\theta + \Delta\theta)\cos(\phi) + \sin(\Delta\beta)\cos(\theta + \Delta\theta),$$

$$\zeta = \sin(\theta + \Delta\theta)\sin(\phi). \tag{32}$$

The exchange energy density is given by

$$W_{\mathrm{ex}} = A\left[\left(\frac{\partial \chi}{\partial x}\right)^2 + \left(\frac{\partial \eta}{\partial x}\right)^2 + \left(\frac{\partial \zeta}{\partial x}\right)^2 \right]. \tag{33}$$

From Eq. (32) we obtain

$$W_{\mathrm{ex}} = A\left(\frac{\partial\theta}{\partial x}\right)^2 + 2A\frac{\partial\theta}{\partial x}\frac{1}{r}\cos\phi - A\frac{1}{r^2}\sin^2\theta\sin^2\phi + \frac{A}{r^2}. \tag{34}$$

The first term is equal to the exchange energy density of the straight wire. The last term is constant and does not depend on the magnetization. In the approximation for small ϕ the other two terms can be rewritten:

$$\Delta W_{\mathrm{ex}} = A\frac{\partial\theta}{\partial x}\frac{1}{r}(2 - \phi^2) - A\left(\frac{\phi}{r}\right)^2 \sin^2\theta. \tag{35}$$

Integration leads to the contribution

$$\int dV \Delta W_{\mathrm{ex}} = \left(\frac{AS\pi}{r} - \frac{AS2\lambda}{r^2} \right)\phi^2 - \frac{2AS\pi}{r} \tag{36}$$

of the curvature to the anisotropy energy. The last term is a constant which depends neither on X nor on ϕ. The perpendicular anisotropy energy can be written as

$$\int dV W_{\mathrm{a}\perp} = \int dV K_\perp \sin^2\theta \sin^2\phi = K_\perp S 2\lambda \phi^2. \tag{37}$$

Comparing Eqs. (36) and (37) one can see that the additional exchange energy due to the curvature can be included into the perpendicular anisotropy by defining an effective anisotropy constant

$$K_{\perp \mathrm{eff}} = K_\perp + \frac{A\pi}{2\lambda r} - \frac{A}{r^2}. \tag{38}$$

By this equation and Eq. (31) for the effective field we have shown that the modifications result in a higher resonance frequency, higher damping constant, and in a lower domain-wall mass in comparison to the straight wire.

V. NUMERICAL CALCULATIONS

To check the applicability of the approximations made in our analytical model—i.e., the form invariance of the domain wall at small displacements—we have performed micromagnetic simulations. We have modeled current-induced domain-wall oscillations in curved nanowires as described in Sec. II. The current contacts are arranged under an angle of 90° to have sufficient distance to the domain wall as well as to the ends of the wire (see Fig. 1).

We extended the implementation of the Landau-Lifshitz-Gilbert equation in the object-oriented micromagnetic framework[43] (OOMMF) by the additional current-dependent terms of Eq. (2) and implemented Runge-Kutta and Adams-Bashforth-Moulton algorithms of higher order to speed up the calculations. The calculations presented here have been performed using the explicit embedded Runge-Kutta 5(4) algorithm by Cash and Karp.[44] The current density is calculated by locally solving Ohm's law, thus taking the curvature of the wire and the contacts into account. For the spatial discretization a cell size of 1 nm in the x and y directions and 10 nm in the z direction was chosen. Numerical calculations were performed for radii of 45 nm, 55 nm, 65 nm, 70 nm, 85 nm, and 95 nm with different polarized current densities $j_p = jP$. Small radii are chosen so that the corrections from Sec. IV become pronounced. We use the material parameters of Permalloy: i.e., the exchange constant $A = 13 \times 10^{-12}$ J/m and the saturation magnetization $M_s = 8 \times 10^5$ A/m. All wires have a quadratical cross section $S = wt = 100$ nm^2. The applied field in the y direction was chosen to be 125 mT to increase the resonance frequency [see Eq. (20)] and thus to reduce the simulation time necessary for the domain wall to perform several oscillations. Due to the small width of the wire, this high field has virtually no effect on the ground state ($H=0$) of the magnetization. In the ground state we obtain a domain-wall width of $\lambda = 9.25$ nm. The difference in the magnetization orientation θ between the analytical description of the Néel wall and the micromagnetic ground state in the curved wire is less than 5°.

We have determined the eigenmodes of the magnetization in the wire by applying a magnetic δ pulse in the z direction (see Fig. 1), thus exciting all frequencies with equal amplitude. To mimic an applied current, the magnetic field pulse has been chosen to point in the z direction so that the torque of the field points in the same direction as the torque of the applied current [see Eq. (2)]. After this excitation the system performs damped free oscillations. The eigenmodes of the wire are found by spatially resolved discrete Fourier transformation (see Fig. 3).[45,46] The higher harmonics and the standing spin waves in the wire are neglected in the analytical description. The resonance of the ground mode is observed at a frequency of $\Omega = 15.7$ GHz. The higher modes are also indicated in Fig. 3. However, in the following we focus on the ground mode.

We simulated an alternating current with frequencies close to the resonance frequency of the domain wall for different radii r and Gilbert damping parameters α. Figure 4 shows the numerically obtained amplitudes for different radii at fixed $\alpha = 0.05$ and $\xi = 0.01$. For each radius the position and the width of the resonance curve have been fitted to the analytical model, Eq. (17), to determine the parameters $F(r)$, $\omega_r(r)$, and $\Gamma(r)$. Note that all resonance curves are in excellent agreement with the harmonic-oscillator model. The frequencies $\omega_r(r)$ and the damping constants $\Gamma(r)$ have been summarized in Fig. 5 where they are compared to the analytical expressions in Eqs. (18) and (20). The results coincide if we assume $K_{\perp\mathrm{eff}} = K_\perp + \frac{A\pi}{2\lambda r} - \frac{A}{r^2}$ with $K_\perp = 60\,000$ J/m^3 for the perpendicular anisotropy [see Eq. (38)]. The dependence of the resonance frequency ω_r on the radius r according to the phenomenological model of Saitoh *et al.*[9] is also shown. It is visible from Fig. 5 that the analytical model and the phenomenological oscillator model yield the same eigenfre-

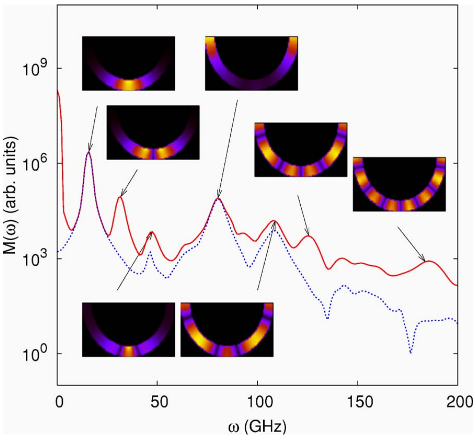

FIG. 3. (Color online) Fourier transform $M(\omega)$ of the simulated magnetization $M_x(t)$ in a curved nanowire with radius $r = 45$ nm and Gilbert damping parameter $\alpha = 0.05$. The wire is excited with a magnetic δ pulse. The lines show the spatially resolved (solid line) and the integral response (dashed line). The insets show the spatially resolved discrete Fourier transforms for seven selected eigenfrequencies.

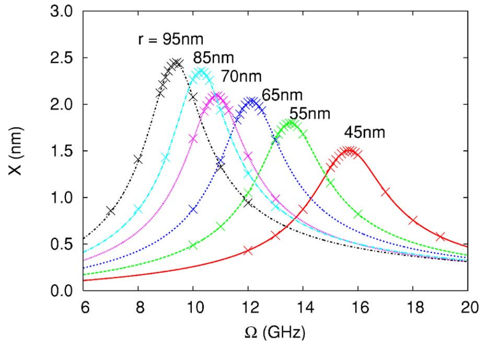

FIG. 4. (Color online) Amplitude of the domain-wall displacement versus frequency of the applied current for different radii r. The Gilbert damping $\alpha = 0.05$, the ratio of the exchange and spin-flip relaxation time $\xi = 0.01$, and the polarized current density $j_p = 10^{11}$ A/m^2 are fixed. The crosses denote numerical values while the lines are fits with the analytical result of Eq. (17).

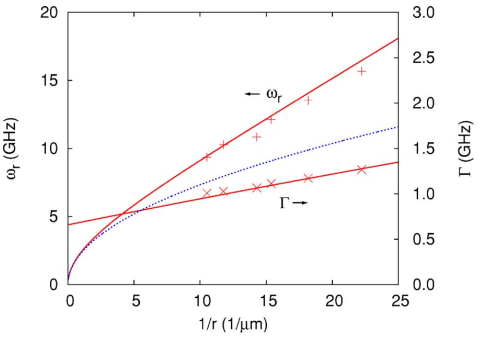

FIG. 5. (Color online) Resonance frequency ω_r and damping constant Γ versus reciprocal ring radius. Shown are the values determined from the fits in Fig. 4 (data points) and the analytical values (solid lines). The dashed line indicates the behavior of the resonance frequency as expected from the phenomenological model of Saitoh *et al.* (Ref. 9)

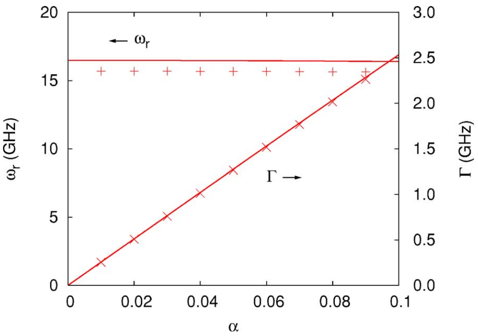

FIG. 7. (Color online) Resonance frequency ω_r and damping constant Γ versus Gilbert damping parameter α. Shown are the values determined from the fits in Fig. 6 (data points) and the analytical values (solid lines).

quencies in the limit of a straight wire ($r \gg 1$ μm). For smaller radii the phenomenological model gives eigenfrequencies which are significantly lower than the ones of the numerical calculations. Our analytical model including the geometrical corrections fits the numerical data very well.

Figures 6 and 7 show the corresponding data for a ring with a radius of 45 nm and different values of the Gilbert damping parameter α. The analytical solutions are calculated with no free fit parameter. While the data points for the damping constant $\Gamma(\alpha)$ coincide with the analytical result, small deviations occur in the resonance frequency $\omega_r(\alpha)$. These deviations can be attributed to the finite cell size in our simulations.

In Figs. 8 and 9 the values for the fit parameter $F(\alpha, r)$ are compared with the analytical result. The analytical values exceed the numerically obtained parameters by up to a factor of 2. This difference has several reasons. In Sec. III we assumed that the ground mode can be described by the motion of the center of the wall X and the magnetization angle ϕ. This neglects spin-wave excitations and higher wall modes. Calculating the mode spectrum excited with a single driving frequency revealed a strong coupling between the ground mode and higher modes. This coupling is enhanced for small radii. Therefore, the force is distributed over several modes, thus decreasing the amplitude of the ground mode. Moreover, in wires with small radii the current distribution is very inhomogeneous with a higher current density at their inner edge. We expect that this leads to an additional deformation of the Néel wall. Another aspect is the finite cell size. In the numerical calculations the curved surface has been approximated with rectangular prisms. The resulting kinks in the wire wall have a measurable effect on the domain-wall motion similar to surface roughness.

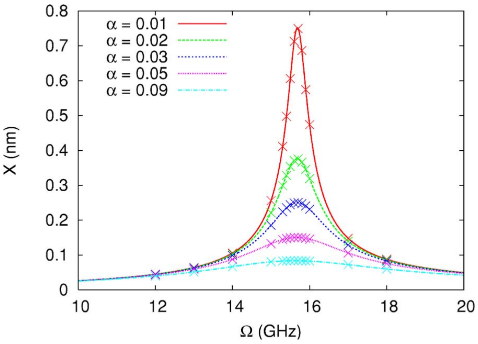

FIG. 6. (Color online) Amplitude of the domain-wall displacement versus frequency of the applied current for different Gilbert damping parameters α. The ring radius $r = 45$ nm, the ratio of the exchange and spin-flip relaxation time $\xi = 0.01$, and the polarized current density $j_p = 10^{10}\,\mathrm{A/m^2}$ are fixed. The crosses denote numerical values while the lines are fits with the analytical result of Eq. (17).

VI. RELATION TO EXPERIMENT

In the analytical calculations we assume the linear approximations $\sin(X/r) \approx X/r$ and $\sin\phi \approx \phi$. Nonlinearities

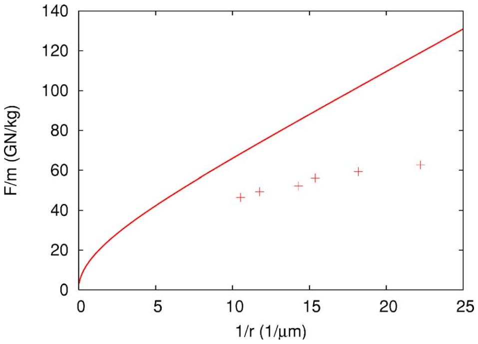

FIG. 8. (Color online) Force per wall mass at the resonance frequency versus reciprocal ring radius. Shown are the numerical values (crosses) and the analytical values (line). The polarized current density is $j_p = 10^{11}\,\mathrm{A/m^2}$.

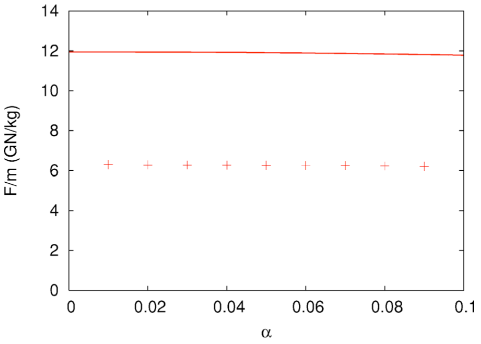

FIG. 9. (Color online) Force per wall mass at the resonance frequency versus Gilbert damping parameter. Shown are the numerical (crosses) and the analytical values (line). The polarized current density is $j_p = 10^{11}\,\text{A/m}^2$.

cause the deviation of the resonance frequency in Fig. 10 from the analytical form at the current density $j_p = 10^{11}\ \text{A/m}^2$ and Gilbert damping parameters below 0.05. Note that these nonlinearities are small ($<5\%$). The presented model clearly fails beyond Walker's breakdown.[2] The current densities at which nonlinearities become important strongly depend on the geometry of the wire. Our analytical model allows us to derive them for typical experimental parameters. In the rest of this section we will assume that the damping constant Γ is not field dependent $\left(\frac{\lambda H}{2r} \ll \frac{K_\perp}{\mu_0 M_s}\right)$ and that the squared Gilbert damping parameter is small ($\alpha^2 \ll 1$). These assumptions usually hold in experiments because the domain-wall width λ is small compared to the radius r and the usual values of the damping parameter α are lower than 0.1. We can express all terms in Eq. (22) with the expressions for Γ and ω_r in Eqs. (18) and (20), respectively, when we assume that the ratio of exchange and spin-flip relaxation time ξ is comparable or less than the Gilbert damping parameter α. In the case of a noncritically damped oscillation ($\omega_r > \Gamma$) the oscillation becomes nonlinear if the current density is approximately

$$j = \min\left(\frac{\Gamma r}{4b_j}, \frac{\Gamma^2 \lambda}{2\alpha\omega_r b_j}\right). \qquad (39)$$

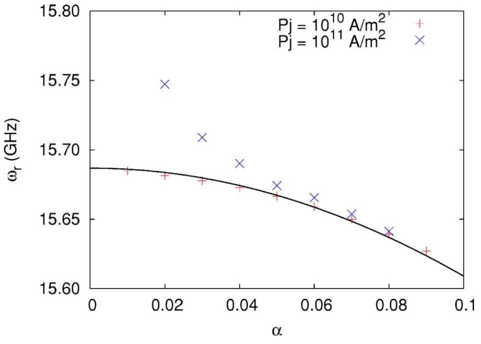

FIG. 10. (Color online) Resonance frequency ω_r versus Gilbert damping parameter α. The data points are the numerical values obtained for a wire with radius 45 nm and two different densities of the polarized current j_p. The line is a fit according to the analytical result $\omega_r = C/\sqrt{1+\alpha^2}$ from Eq. (20) with the fit parameter C.

The experimental current densities which Saitoh *et al.*[9] applied on a wire with cross section $S = 3150\ \text{nm}^2$ and radius $r = 50\ \mu\text{m}$ are well below this current density. They have determined a domain-wall width $\lambda = 70$ nm, a domain-wall mass $m = (6.55 \pm 0.06) \times 10^{-23}$ kg, and a domain-wall relaxation time $\tau = \frac{1}{2\Gamma} = (1.4 \pm 0.2) \times 10^{-8}$ s. Calculating the demagnetization energy for a straight wire numerically and fitting with the expression for the shape anisotropy $K_\perp \sin^2\theta \sin^2\phi$, we get an anisotropy constant of $K_\perp = 76175\ \text{J/m}^3$. This yields an effective anisotropy of $K_{\perp\text{eff}} = 76175\ \text{J/m}^3 + \frac{A\pi}{2\lambda r} - \frac{A}{r^2}$. Using Saitoh's experimental parameters we obtain from Eq. (15) a domain-wall mass $m \approx 1.2 \times 10^{-23}$ kg. Tatara and Kohno's approach[18] used in the paper of Saitoh *et al.*[9] delivers exactly the same result.

As mentioned in Sec. 3 the analytical calculations lead to relations between the micromagnetic material parameters and the parameters of the harmonic oscillator. These can be used to experimentally determine the Gilbert damping parameter α from the experimental data. From Eqs. (18), (20), and (15) one can derive the relation

$$\alpha = \frac{2\Gamma\gamma H\lambda}{\omega_r^2 r} = \frac{m\Gamma\gamma\lambda}{\mu_0 M_s S}. \qquad (40)$$

With the domain-wall mass and the domain-wall relaxation time of the experiment of Saitoh *et al.* we get a Gilbert damping parameter of $\alpha = 0.0114 \pm 0.0017$. This value agrees quite well with the experimental values of Nibarger *et al.*[47] and Schneider *et al.*[48] which range from 0.008 to 0.017 for film thicknesses between 10 nm and 93 nm.

VII. CONCLUSION

The current-induced motion of a domain wall in thin curved nanowires has been investigated. A harmonic-oscillator model which so far had only been introduced phenomenologically is derived from the LLG equations extended by the spin torque according to Zhang and Li.[21] This derivation relates micromagnetic material parameters to the characteristic quantities describing the oscillating domain wall under the influence of an alternating driving current. It is shown that the dipole moment of the wall and the curvature of the wire have an important influence on the resonance frequency and damping constant of the oscillation. The domain wall can be seen as a quasiparticle in a parabolic potential well which is acted upon by a current-induced force. An important result is that the time derivative of the current density greatly contributes to the force on the domain wall. The phase and magnitude of the force depend on the frequency of the current. The analytical results have been compared to numerical simulations. They agree very well. Our analytical solution suggests new methods to determine material parameters which are otherwise difficult to measure: e.g., the nonadiabatic term of the spin torque can be determined from the phase shift between the applied current and the overall magnetization. Moreover, the Gilbert damping parameter α and the domain-wall mass m follow from a measurement of the resonance frequency ω_r and the damping constant Γ of the oscillations.

ACKNOWLEDGMENTS

The authors thank S. S. P. Parkin for sharing his results prior to publication. We appreciate fruitful discussions with U. Gummich. Financial support by the Deutsche Forschungsgemeinschaft via SFB 668 “Magnetismus vom Einzelatom zur Nanostruktur” and via Graduiertenkolleg 1286 “Functional metal-semiconductor hybrid systems” is gratefully acknowledged.

---

[1] A. A. Thiele, J. Appl. Phys. **45**, 377 (1974).

[2] N. L. Schryer and L. R. Walker, J. Appl. Phys. **45**, 5406 (1974).

[3] J. Slonczewski, J. Magn. Magn. Mater. **159**, L1 (1996).

[4] L. Berger, Phys. Rev. B **54**, 9353 (1996).

[5] E. B. Myers, D. C. Ralph, J. A. Katine, R. N. Louie, and R. A. Buhrman, Science **285**, 867 (1999).

[6] J. Grollier, P. Boulenc, V. Cros, A. Hamzi, A. Vaur, A. Fert, and G. Faini, Appl. Phys. Lett. **83**, 509 (2003).

[7] A. Yamaguchi, T. Ono, S. Nasu, K. Miyake, K. Mibu, and T. Shinjo, Phys. Rev. Lett. **92**, 077205 (2004).

[8] H. Koo, C. Krafft, and R. D. Gomez, Appl. Phys. Lett. **81**, 862 (2002).

[9] E. Saitoh, H. Miyajima, T. Yamaoka, and G. Tatara, Nature (London) **432**, 203 (2004).

[10] M. Kläui, C. A. F. Vaz, J. A. C. Bland, W. Wernsdorfer, G. Faini, E. Cambril, and L. J. Heyderman, Appl. Phys. Lett. **83**, 105 (2003).

[11] N. Vernier, D. Allwood, D. Atkinson, M. Cooke, and R. Cowburn, Europhys. Lett. **65**, 526 (2004).

[12] J. A. Katine, F. J. Albert, R. A. Buhrman, E. B. Myers, and D. C. Ralph, Phys. Rev. Lett. **84**, 3149 (2000).

[13] I. N. Krivorotov, N. C. Emley, J. C. Sankey, S. I. Kiselev, D. C. Ralph, and R. A. Buhrman, Science **307**, 228 (2005).

[14] S. S. P. Parkin, US Patent 6,834,005 (2004).

[15] D. A. Allwood, G. Xiong, M. D. Cooke, C. C. Faulkner, D. Atkinson, N. Vernier, and R. P. Cowburn, Science **296**, 2003 (2002).

[16] D. A. Allwood, G. Xiong, C. C. Faulkner, D. Atkinson, D. Petit, and R. P. Cowburn, Science **309**, 1688 (2005).

[17] R. P. Cowburn, Patent Application WO002004077451A1 (2004).

[18] G. Tatara and H. Kohno, Phys. Rev. Lett. **92**, 086601 (2004).

[19] A. Thiaville, Y. Nakatani, J. Miltat, and Y. Suzuki, Europhys. Lett. **69**, 990 (2005).

[20] X. Waintal and M. Viret, Europhys. Lett. **65**, 427 (2004).

[21] S. Zhang and Z. Li, Phys. Rev. Lett. **93**, 127204 (2004).

[22] Z. Li and S. Zhang, Phys. Rev. B **70**, 024417 (2004).

[23] M. Kläui, C. A. F. Vaz, J. A. C. Bland, W. Wernsdorfer, G. Faini, E. Cambril, L. J. Heyderman, F. Nolting, and U. Rüdiger, Phys. Rev. Lett. **94**, 106601 (2005).

[24] T. Ono, H. Miyajima, K. Shigeto, K. Mibu, N. Hosoito, and T. Shinjo, Science **284**, 468 (1999).

[25] Y. Nakatani, A. Thiaville, and J. Miltat, Nat. Mater. **2**, 521 (2003).

[26] M. Kläui, P.-O. Jubert, R. Allenspach, A. Bischof, J. A. C. Bland, G. Faini, U. Rüdiger, C. A. F. Vaz, L. Vila, and C. Vouille, Phys. Rev. Lett. **95**, 026601 (2005).

[27] A. Yamaguchi, S. Nasu, H. Tanigawa, T. Ono, K. Miyake, K. Mibu, and T. Shinjo, Appl. Phys. Lett. **86**, 012511 (2005).

[28] A. Yamaguchi, T. Ono, S. Nasu, K. Miyake, K. Mibu, and T. Shinjo, Phys. Rev. Lett. **96**, 179904(E) (2006).

[29] J. He, Z. Li, and S. Zhang, Phys. Rev. B **73**, 184408 (2006).

[30] M. Kläui *et al.*, Appl. Phys. Lett. **88**, 232507 (2006).

[31] G. Meier, M. Bolte, R. Eiselt, U. Merkt, B. Krüger, D. Pfannkuche, D. H. Kim, and P. Fischer (unpublished).

[32] D. Atkinson, D. Allwood, G. Xiong, M. D. Cooke, C. C. Faulkner, and R. P. Cowburn, Nat. Mater. **2**, 85 (2003).

[33] M. Hayashi, L. Thomas, Y. B. Bazaliy, C. Rettner, R. Moriya, X. Jiang, and S. S. P. Parkin, Phys. Rev. Lett. **96**, 197207 (2006).

[34] L. Thomas, M. Hayashi, R. Moriya, X. Jiang, C. Rettner, and S. S. P. Parkin, Nature (London) **443**, 197 (2006).

[35] G. Tatara, E. Saitoh, M. Ichimura, and H. Kohno, Appl. Phys. Lett. **86**, 232504 (2005).

[36] N. L. Schryer and L. R. Walker, J. Appl. Phys. **45**, 5406 (1974).

[37] Starting with a high magnetic field the wire is saturated in the y-direction. Reducing the magnetic field to a small offset the system ends up with a domain wall at the bottom of the wire. The wall type depends on the width w and the thickness t of the wire (see Ref. 42). In the present study we choose a small cross section $S=wt=100\ \text{nm}^2$ with width $w=10$ nm and thickness $t=10$ nm to get a transverse wall.

[38] L. Landau and E. Lifshitz, Phys. Z. Sowjetunion **8**, 153 (1935).

[39] Uniaxial anisotropy can be taken into acount by replacing the anisotropy constants K and $K_{\perp\mathrm{eff}}$ with the new constants K' and $K'_{\perp}$ given by $K'=K+K_y-K_x$ and $K'_{\perp}=K_{\perp\mathrm{eff}}+K_z-K_y$.

[40] Expanding the expression for λ in terms of ϕ shows that the first nonvanishing ϕ-dependent term is quadratic. Since we linearize the equations of motion, we can neglect all nonlinear terms. Then λ is independent of the magnetization angle ϕ.

[41] V. K. Dugaev, V. R. Vieira, P. D. Sacramento, J. Barnaś, M. A. N. Araújo, and J. Berakdar, Phys. Rev. B **74**, 054403 (2006).

[42] Y. Nakatani, A. Thiaville, and J. Miltat, J. Magn. Magn. Mater. **290**, 750 (2005).

[43] OOMMF User's Guide, version 1.0, M. J. Donahue and D. G. Porter, Interagency Report No. NISTIR 6376, National Institute of Standards and Technology, Gaithersburg, MD, 1999 (http://math.nist.gov/oommf/).

[44] J. Cash and A. Karp, ACM Trans. Math. Softw. **16**, 201 (1990).

[45] R. D. McMichael and M. D. Stiles, J. Appl. Phys. **97**, 10J901 (2005).

[46] M. Bolte, G. Meier, and C. Bayer, Phys. Rev. B **73**, 052406 (2006).

[47] J. Nibarger, R. Lopusnik, and T. Silva, Appl. Phys. Lett. **82**, 2112 (2003).

[48] M. Schneider, T. Gerrits, A. Kos, and T. Silva, Appl. Phys. Lett. **87**, 072509 (2005).

N·H
ELSEVIER

Available online at www.sciencedirect.com
ScienceDirect

Journal of Magnetism and Magnetic Materials ▮ (▮▮▮▮) ▮▮▮–▮▮▮

Journal of magnetism and magnetic materials

www.elsevier.com/locate/jmmm

Current-induced domain-wall motion in permalloy semi rings

Guido Meier[a,*], Markus Bolte[a], Ulrich Merkt[a], Benjamin Krüger[b], Daniela Pfannkuche[b]

[a]*Institut für Angewandte Physik und Zentrum für Mikrostrukturforschung, Universität Hamburg, Jungiusstrasse 11, 20355 Hamburg, Germany*
[b]*I. Institut für Theoretische Physik, Universität Hamburg, Jungiusstrasse 9, 20355 Hamburg, Germany*

Abstract

We have incorporated the model of Zhang and Li [Phys. Rev. Lett. 93 (2004) 127204] for spin-transfer torque into the Landau–Lifshitz–Gilbert equation and have investigated the current-induced magnetization dynamics of permalloy ($Ni_{80}Fe_{20}$) semi rings. The distribution of the current density within the ring is taken into account. Current-induced eigenmodes with distinct resonance frequencies and higher harmonics are observed as well as a dependence of the resonance frequency on the ring radius. The domain-wall mass determined from the micromagnetic simulation and an analytical model is in agreement with recent experiments. Maximum domain-wall velocities between 30 and 34 $\mathrm{m\,s^{-1}}$ are deduced.

© 2007 Published by Elsevier B.V.

PACS: 75.45.+j; 72.25.Ba; 75.60.Ch; 75.40.Mg

Keywords: Spin-transfer torque; Micromagnetic simulation; Magnetization dynamics

---

UNCORRECTED PROOF

The spin-polarized current within a ferromagnet transfers a torque when passing through a locally varying magnetization. This mechanism is currently discussed as a technologically simple writing scheme for magnetic memory devices as it would drastically reduce the complexity of the wiring. Berger [2,3] and Slonczewski [4] described independently the interaction between conduction electrons and localized spins of magnetic multilayers. Recently, current-driven magnetization reversal has been studied experimentally in nanopillars [5,6]. In the last two years considerable progress has been made in understanding the current-induced domain wall motion in magnetic nanowires [1,7–10]. Experimentally the velocity of current-induced domain wall motion in nanowires and other constrained geometries has been investigated with current pulses and subsequent quasi-static detection by magnetic-force microscopy [11] and by scanning-electron microscopy with polarization analysis [12]. The dynamics of a domain wall has been measured with the help of resonant high-frequency current excitation [13]. Domain-wall velocities in the range of $0.3-3\,\mathrm{m\,s^{-1}}$ and threshold current densities from 10^{11} up to $10^{12}\,\mathrm{A\,m^{-2}}$ have been determined. Theoretically there has been extensive effort to expand the existing micromagnetic models to include the influence of spin-polarized currents [1,2,4,7,9,10]. Threshold current densities of $10^{12}\,\mathrm{A\,m^{-2}}$ and wall velocities in the range of $100\,\mathrm{m\,s^{-1}}$ are obtained. So far, the discrepancy to the experimental velocities is not understood. Edge roughness as well as excitation of spin waves have been proposed as possible explanations [7,8].

Current-induced magnetization dynamics of permalloy ($Ni_{80}Fe_{20}$) semi rings as shown in Fig. 1 are studied numerically and fitted with a harmonic-oscillator model [14]. Ferromagnetic semi rings are interesting because they can give access to the dynamic properties of a single domain wall [13]. We have extended the micromagnetic simulation package OOMMF [15] to include spin-polarized currents according to the model of Zhang and Li [1]. In their model the conduction electrons are assumed to propagate without reflection. Their spin direction follows approximately the direction of the local magnetization at the wall. This approach is suitable to describe ferromagnetic metals where the Fermi wavelength is much smaller than the size of the magnet and the width of the domain wall. The corresponding equation of motion is deduced by

---

[*] Corresponding author. Tel.: +49 40 42838 2903; fax: +49 40 42838 4368.
E-mail address: meier@physnet.uni-hamburg.de (G. Meier).

0304-8853/$ - see front matter © 2007 Published by Elsevier B.V.
doi:10.1016/j.jmmm.2007.03.157

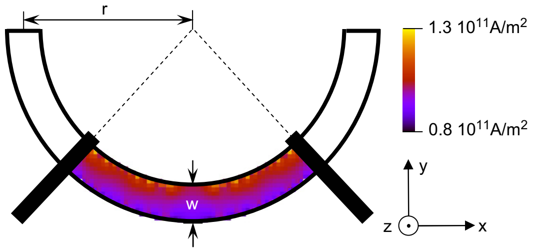

Fig. 1. Geometry of the semi rings. Radii r of 45, 55, 65, 70, 85, and 95 nm have been simulated. The width w of all rings is 10 nm, the thickness t is 10 nm. The current distribution between the contacts is shown as color contour ranging from 0.8×10^{11} to 1.3×10^{11} A/m^2.

adding the adiabatic and the non-adiabatic spin-torque term to the Gilbert form of the Landau–Lifshitz equation. Then, the explicit form of the equation of motion for the local magnetization reads:

$$\frac{\mathrm{d}\mathbf{M}}{\mathrm{d}t} = -\frac{1}{1+\alpha^2}[\gamma\mathbf{M}\times\mathbf{H} + \alpha\gamma\mathbf{M}\times(\mathbf{M}\times\mathbf{H}) + b_j(1+\alpha\xi)\mathbf{M}\times(\mathbf{M}\times(\mathbf{j}\cdot\nabla)\mathbf{M}) + b_j(\xi-\alpha)\mathbf{M}\times(\mathbf{j}\cdot\nabla)\mathbf{M}], \qquad (1)$$

with the local magnetization **M**, the local effective magnetic field **H**, the gyromagnetic ratio γ, the Gilbert damping parameter α, and the local current density **j**. The prefactors b_j and $c_\mathrm{j} = \xi b_\mathrm{j}$ are defined in Ref. [1]. The first and the second terms in Eq. (1) are the well-known precession and damping terms, respectively. The third and fourth terms are the adiabatic and non-adiabatic spin-torque terms.

The two spin-torque terms introduce local derivatives of the magnetization. We have implemented these in the micromagnetic code by a finite difference method considering the nearest and next nearest neighbors. The performance of the code has been improved by a fifth-order Cash–Karp Runge–Kutta algorithm [16]. A gain of performance of up to two orders of magnitude in comparison with an Euler evolver could be obtained depending on the size of the problem and the damping parameter. The calculations are performed with permalloy parameters, i.e. exchange constant $A = 1.3\times10^{-11}$ J/m, saturation magnetization $M_\mathrm{S} = 8.0\times10^5$ A/m, uniaxial anisotropy $K_1 = 0$, and damping constant $\alpha = 0.05$. The cell size used in all simulations is 1, 1, and 10 nm in x, y, and z-direction, respectively.

The detailed current distribution is important when electron transport through ferromagnetic micro- and nanostructures is considered [17]. Therefore the geometry of the ring was included in a diffusive transport calculation of the local electrical potentials and the current density [18]. The current distribution for the semi ring with a radius of 45 nm is shown in Fig. 1. The location of the contacts far away from the domain wall and the ends of the semi ring guarantees a homogeneous static magnetization in the contact area. Note that the current density varies by nearly a factor of two within the ring. A rather small system size has been chosen to enable a thorough study of current-induced magnetization dynamics in rings.

To prepare the magnetization state with the domain wall in the middle of the semi ring a strong static magnetic field of 1 T is applied in y-direction to saturate the magnetization. Then the strong external field in the simulation is reduced to a confining field of 0.125 T. By this procedure a single domain wall, i.e. Néel or transverse wall, is introduced in the middle of the semi ring in a controllable manner. In the next step an alternating current with a specified frequency is applied. The domain wall oscillates with this frequency. The magnitude of the oscillation is expected to have its maximum amplitude when the frequency of the current is close to the eigenfrequency of the domain-wall in the semi ring. To obtain the eigenmode spectrum the permalloy semi ring is excited with a homogeneous magnetic field in z-direction with a full-width-at-half-maximum of 2.6 ps. Such pulses excite all frequencies relevant for spin-wave modes in ferromagnetic micro- and nanostructures. The torque generated by such pulses resembles the torque due to a current through the ring. The eigenmodes of the semi ring are found by spatially resolved discrete Fourier transformation. A sum over all cells yields the spectrum with the eigenmode frequencies. Fig. 2 shows the Fourier transform of the modes excited in the ring with a radius $r = 45$ nm with a current of a frequency of 2.5 GHz. The strong resonance at 2.5 GHz is accompanied by resonances with strongly decreasing intensity at higher harmonics [19]. An image of the amplitude of the current-induced eigenmode is shown in the inset. Fig. 3(a) shows simulated resonances of the magnetization excitation versus frequency of the exciting current. The shape of the curves confirm the description of a domain wall as a particle with a finite mass as predicted by Döring [14]. As expected according to Eq. (1) of Ref. [13] the resonance frequencies increase with increasing confinement, i.e., decreasing ring radius. In Fig.

UNCORRECTED PROOF

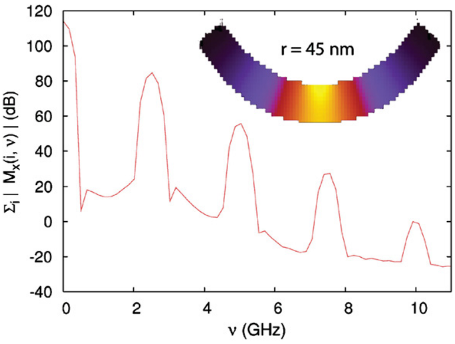

Fig. 2. Fourier transform of the ring modes excited with a current of frequency $\nu = 2.5$ GHz. The inset shows the amplitude of the fundamental mode at 2.5 GHz.

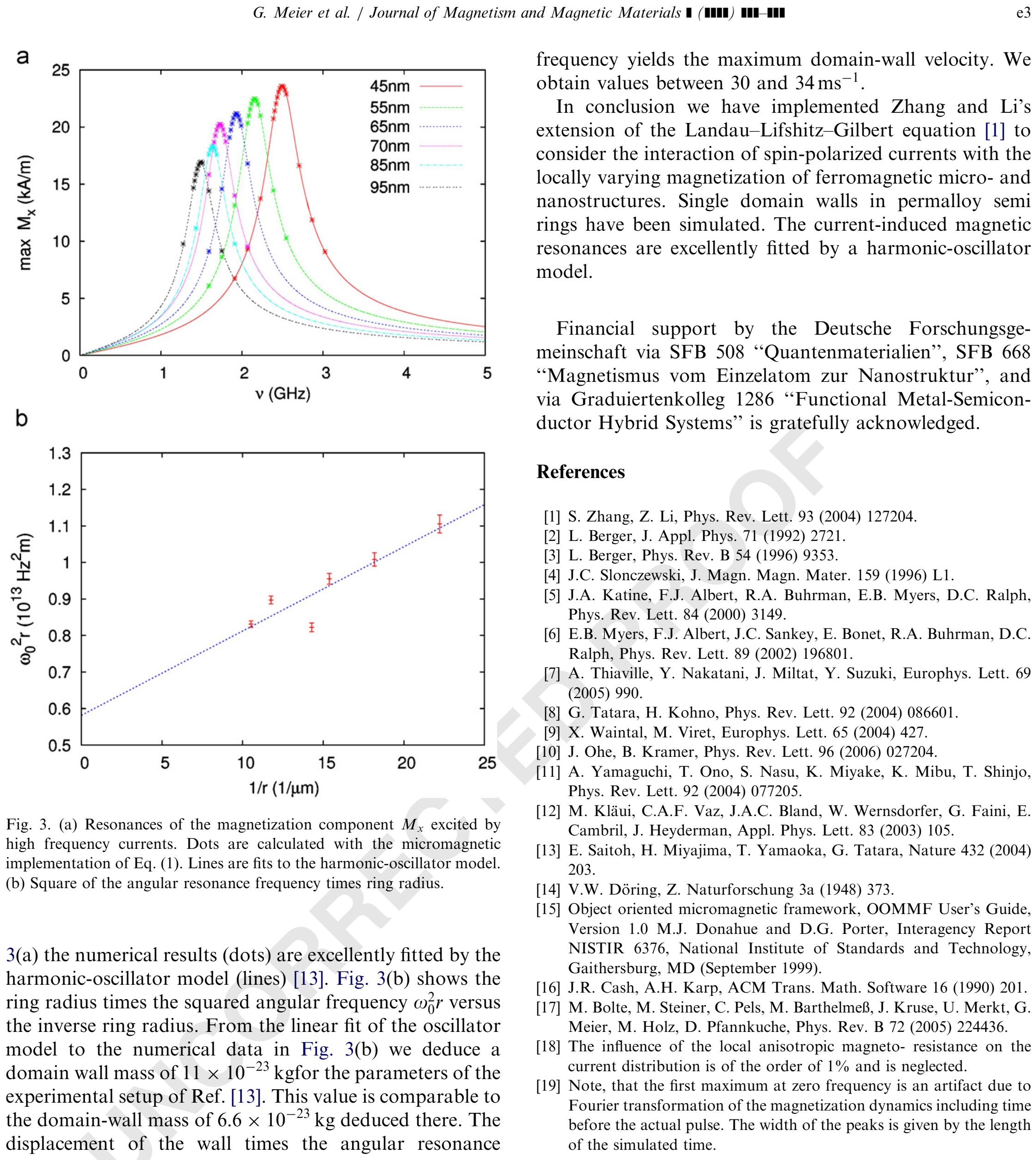

Fig. 3. (a) Resonances of the magnetization component M_x excited by high frequency currents. Dots are calculated with the micromagnetic implementation of Eq. (1). Lines are fits to the harmonic-oscillator model. (b) Square of the angular resonance frequency times ring radius.

3(a) the numerical results (dots) are excellently fitted by the harmonic-oscillator model (lines) [13]. Fig. 3(b) shows the ring radius times the squared angular frequency $\omega_0^2 r$ versus the inverse ring radius. From the linear fit of the oscillator model to the numerical data in Fig. 3(b) we deduce a domain wall mass of 11×10^{-23} kgfor the parameters of the experimental setup of Ref. [13]. This value is comparable to the domain-wall mass of 6.6×10^{-23} kg deduced there. The displacement of the wall times the angular resonance frequency yields the maximum domain-wall velocity. We obtain values between 30 and 34 ms^{-1}.

In conclusion we have implemented Zhang and Li's extension of the Landau–Lifshitz–Gilbert equation [1] to consider the interaction of spin-polarized currents with the locally varying magnetization of ferromagnetic micro- and nanostructures. Single domain walls in permalloy semi rings have been simulated. The current-induced magnetic resonances are excellently fitted by a harmonic-oscillator model.

Financial support by the Deutsche Forschungsgemeinschaft via SFB 508 "Quantenmaterialien", SFB 668 "Magnetismus vom Einzelatom zur Nanostruktur", and via Graduiertenkolleg 1286 "Functional Metal-Semiconductor Hybrid Systems" is gratefully acknowledged.

References

[1] S. Zhang, Z. Li, Phys. Rev. Lett. 93 (2004) 127204.
[2] L. Berger, J. Appl. Phys. 71 (1992) 2721.
[3] L. Berger, Phys. Rev. B 54 (1996) 9353.
[4] J.C. Slonczewski, J. Magn. Magn. Mater. 159 (1996) L1.
[5] J.A. Katine, F.J. Albert, R.A. Buhrman, E.B. Myers, D.C. Ralph, Phys. Rev. Lett. 84 (2000) 3149.
[6] E.B. Myers, F.J. Albert, J.C. Sankey, E. Bonet, R.A. Buhrman, D.C. Ralph, Phys. Rev. Lett. 89 (2002) 196801.
[7] A. Thiaville, Y. Nakatani, J. Miltat, Y. Suzuki, Europhys. Lett. 69 (2005) 990.
[8] G. Tatara, H. Kohno, Phys. Rev. Lett. 92 (2004) 086601.
[9] X. Waintal, M. Viret, Europhys. Lett. 65 (2004) 427.
[10] J. Ohe, B. Kramer, Phys. Rev. Lett. 96 (2006) 027204.
[11] A. Yamaguchi, T. Ono, S. Nasu, K. Miyake, K. Mibu, T. Shinjo, Phys. Rev. Lett. 92 (2004) 077205.
[12] M. Kläui, C.A.F. Vaz, J.A.C. Bland, W. Wernsdorfer, G. Faini, E. Cambril, J. Heyderman, Appl. Phys. Lett. 83 (2003) 105.
[13] E. Saitoh, H. Miyajima, T. Yamaoka, G. Tatara, Nature 432 (2004) 203.
[14] V.W. Döring, Z. Naturforschung 3a (1948) 373.
[15] Object oriented micromagnetic framework, OOMMF User's Guide, Version 1.0 M.J. Donahue and D.G. Porter, Interagency Report NISTIR 6376, National Institute of Standards and Technology, Gaithersburg, MD (September 1999).
[16] J.R. Cash, A.H. Karp, ACM Trans. Math. Software 16 (1990) 201.
[17] M. Bolte, M. Steiner, C. Pels, M. Barthelmeß, J. Kruse, U. Merkt, G. Meier, M. Holz, D. Pfannkuche, Phys. Rev. B 72 (2005) 224436.
[18] The influence of the local anisotropic magneto- resistance on the current distribution is of the order of 1% and is neglected.
[19] Note, that the first maximum at zero frequency is an artifact due to Fourier transformation of the magnetization dynamics including time before the actual pulse. The width of the peaks is given by the length of the simulated time.

UNCORRECTED PROOF

4.4.2 Direct Imaging of Stochastic Domain-Wall Motion Driven by Nanosecond Current Pulses

Following the AMR studies (see Section 4.3.2) Guido Meier, René Eiselt, and I performed our first spin-torque experiments at the XM-1 beam line with the help of the beam line scientist Peter Fischer and his PostDoc Dong-Hyun Kim. After having characterized the switching fields in permalloy rings with AMR measurements and X-ray microscopy (see Fig. 4.5), we applied 1.0 ns short current pulses between the voltage contacts with the help of an Avtech AVN-3 Ultra High Speed Pulse Generator (see Fig. 1(a) of **[P15]**). We imaged the magnetization before and after each pulse to see whether the magnetization had changed. This process was repeated ≈ 50 times. In the thicker rings (960 nm wide and 80 nm thick) multi-vortex domain walls were observed [167], while in the rings with smaller cross sections (300 nm width and 40 nm thickness) single vortex domain walls prevailed [166].

At current densities of 7.5×10^{12} A/m^2 to 1.0×10^{11} A/m^2 we observed stochastic motion of the domain walls in the rings. The jumps in domain-wall position from one image to the next were up to 100 nm, corresponding to domain wall velocities of about 100 m/s, while at other times the walls would not move at all. Most of the times the domain walls did not move as a composite particle, but only regions of the walls changed while others remained unaltered. With the micromagnetic code enhanced by Benjamin Krüger I simulated the magnetic response of permalloy rings of different thicknesses to nanosecond current pulses. Figure 4.11 shows the simulated static magnetization for three ring sections with 20 nm, 60 nm, and 80 nm thickness before and after a 1 ns current pulse of density 1.0×10^{12} A/m^2. The simulations showed transitions from Néel like walls to vortex walls for the thinner rings, in agreement with Kläui *et al.* who had first observed this structural change [105]. In 60 nm thick permalloy the simulated single domain wall was elongated and several vortex-antivortex pairs were created [106], confirming our own observations by X-ray microscopy (see Fig. 2(b) and 2(d) of **[P15]**). The double-vortex wall in the simulated 80 nm thick permalloy ring showed both wall deformation as well as displacement with an average velocity of ≈ 100 m/s. This velocity is remarkably higher than what had been observed with longer current pulses [31], but in line with current-assisted field-driven domain-wall motion [115] as well as what theory predicts [28, 107]. It appears that long current pulses average out the peak velocity that can be discriminated with nanosecond current pulses. Our present point of view is that the time derivative of the current also induces a torque on a domain wall that for nanosecond pulses exceeds the torque of the current itself. This is indicated by the $i\Omega$-dependent terms of Eqn. (22) in

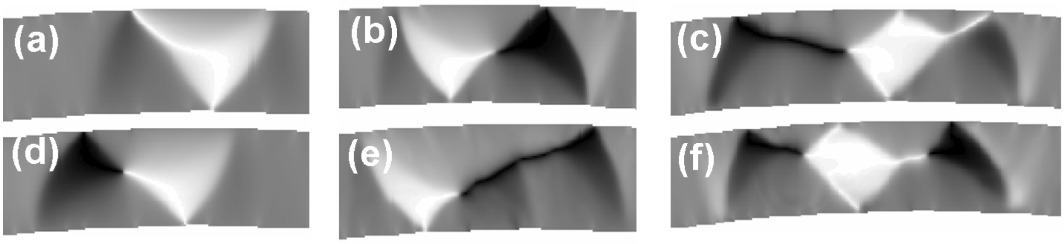

Fig. 4.11: Simulated magnetization in a 960 nm wide permalloy ring segment with a radius of 25 μm before ((a), (b), and (c)) and after ((d), (e), and (f)) a nanosecond current pulse of 1.0×10^{12} A/m^2. The thicknesses of the ring segments are 20 nm ((a) and (d)), 60 nm ((b) and (e)), and 80 nm ((c) and (f)).

[P12] (see previous Section).

The investigation yielded another important contribution to the fundamentals of spin-torque driven domain walls, namely the strength of the nonadiabatic spin-torque. He *et al.* predicted a displacement of a vortex in a vortex wall perpendicular to the current that is linear in the degree of nonadiabaticity ξ. By analyzing the position of the vortices in the double-vortex walls we estimated the strength of the nonadiabatic spin-torque to be roughly proportional to the damping factor α. Finally, we derived a rough estimate for the critical exponent of the stochastic domain-wall motion. The work was published as **[P15]** and is reprinted here with permission from G. Meier, M. Bolte, R. Eiselt, B. Krüger, D.-H. Kim, P. Fischer, Phys. Rev. Lett., **98**, 187202 (2007). Copyright (2007) by the American Physical Society. The work was also presented at several international conferences and invited talks (see **[C13]**, **[C16]**, **[C20]**, **[I6]**, **[I9]**, **[I11]**, and **[I12]**).

PRL **98,** 187202 (2007) PHYSICAL REVIEW LETTERS week ending 4 MAY 2007

Direct Imaging of Stochastic Domain-Wall Motion Driven by Nanosecond Current Pulses

Guido Meier,* Markus Bolte, and René Eiselt
Institut für Angewandte Physik und Zentrum für Mikrostrukturforschung, Universität Hamburg, Jungiusstrasse 11, 20355 Hamburg, Germany

Benjamin Krüger
I. Institut für Theoretische Physik, Universität Hamburg, Jungiusstrasse 9, 20355 Hamburg, Germany

Dong-Hyun Kim
Department of Physics and Institute for Basic Research, Chungbuk National University, Cheongju 361-763, South Korea

Peter Fischer
Center for X-Ray Optics, Lawrence Berkeley National Lab, 1 Cyclotron Road, Mail Stop 2R0400, Berkeley, California 94720, USA

(Received 27 December 2006; published 2 May 2007)

Magnetic transmission x-ray microscopy is used to directly visualize the influence of a spin-polarized current on domain walls in curved permalloy wires. Pulses of nanosecond duration and of high current density up to 1.0×10^{12} A/m^2 are used to move and to deform the domain wall. The current pulse drives the wall either undisturbed, i.e., as composite particle through the wire, or causes structural changes of the magnetization. Repetitive pulse measurements reveal the stochastic nature of current-induced domain-wall motion.

DOI: 10.1103/PhysRevLett.98.187202 PACS numbers: 75.60.Ch, 68.37.Yz, 72.25.Ba, 75.60.Ej

Current-driven domain-wall (DW) dynamics paves the way to novel concepts for memory [1] and logic devices [2]. The underlying physics is still under debate [3–6]. Several models have been proposed to predict the effects of a spin-polarized electric current interacting with a locally inhomogeneous magnetization [3–5,7–11]. It was initially assumed that for DWs wider than the magnetic coherence length the spins of the conduction electrons adiabatically follow the local magnetic moments [4,12]. Later a nonadiabatic term was added [3,4,9] to account for the different DW velocities of theory and experiment [6,13]. It has be shown that the adiabatic term is largely responsible for the initial velocity of the DW while the nonadiabatic term controls its terminal velocity [3]. The velocity of magnetic DWs in thin nanowires has been stated to be between tenths of m/s [3,14,15] up to several 100 m/s [3,16,17]. The velocities reported by experiments tend to be less than those from theoretical predictions. Various suggestions have been proposed to account for this discrepancy, in particular, thermal activation [14,16,18,19] and surface roughness [16]. On the other hand, it has been found that the DW velocity depends on the DW type [14,20] and that a spin-polarized current can change the topology of a wall [14]. Moreover, it has been predicted that fast-changing currents should exert a force on a DW much stronger than the constant current alone [10] which implies that the time structure of the fast-changing current should be considered. Thus, to understand the underlying physics of current-driven DW motion it is required to determine the DW velocity and to simultaneously observe the DW type and topology as well as to accurately control the time structure of the current.

In this Letter we report spatially resolved experiments and micromagnetic simulations of the motion of vortex DWs in curved wires driven by current pulses. Nanosecond current pulses are used to determine the DW velocity. In case of microsecond pulses an average velocity including pinning and depinning of the wall might be measured. We show that DW velocities comparable to the field-driven case are obtained and that the current-driven motion follows a statistical distribution comparable to Barkhausen jumps in the field-driven case.

Curved wires with a radius of 25 μm were patterned by electron-beam lithography and lift-off processing from permalloy films deposited by electron-beam evaporation. Curved wires are most convenient for the field-controlled creation and destruction of a single DW. Four electrical contacts on each wire are patterned from a 60 nm thick Au layer for injection of current pulses and measurement of the dc impedance. Figure 1 shows an optical micrograph of a permalloy wire on a 100 nm thick Si$_3$N$_4$ membrane. The membrane is required for transmission soft x-ray microscopy. The distance between the two inner Au contacts is 4.2 μm.

Measurements of the anisotropic magnetoresistance (AMR) at low current densities of 1.0×10^9 A/m^2 prior to the pulse experiments provide full control over the field-induced generation of a single DW between the inner contacts. An example of an AMR measurement is depicted in Fig. 1(d). The resistance is lowest at saturation and highest at remanence, as expected [21]. For the pulse measurements we use the onion states with either a tail-to-tail or a head-to-head DW between the contacts depending on the magnetic history. From the absolute resist-

© 2007 The American Physical Society

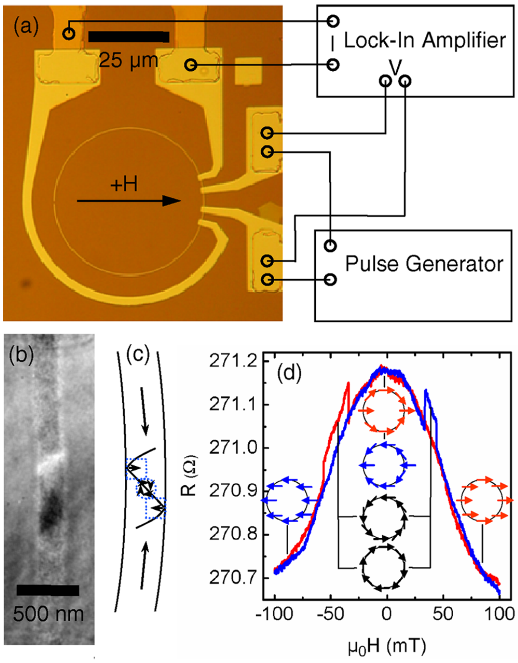

FIG. 1 (color online). (a) Optical micrograph of a curved permalloy wire on a Si_3N_4 membrane with four gold contacts. A slit on the left side avoids dc current flow through this part. (b) MTXM image and (c) scheme of a vortex wall in the section between the inner contacts. (d) Measured AMR. The up-sweep (down-sweep) is plotted in blue (red). The arrows indicate the magnetization states. Shown are schemes of the two saturated states, the two global-vortex states, and the two onion states. At remanence the onion states exhibit either a tail-to-tail (blue) or a head-to-head (red) DW in the region of interest for the pulse experiments.

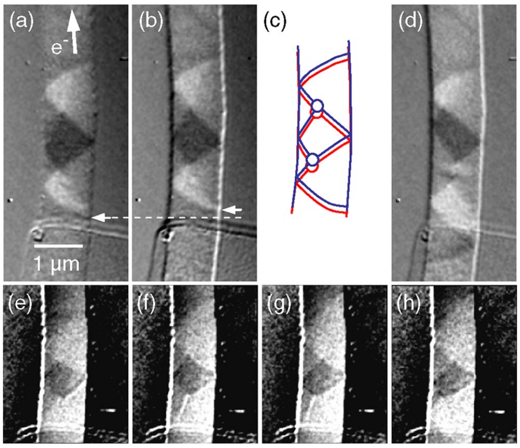

FIG. 2 (color online). (a) MTXM image of a double-vortex wall before and (b) after sending ten current pulses of 1.0 ns duration and 4.0 ns periodicity through the wire. (c) Sketch of the wall positions in (a) and (b) illustrating the motion of the double-vortex wall as composite particle. (d) Another pulse sequence generates a vortex-antivortex pair. (e)–(h) Sequence of MTXM images of a double-vortex wall taken after single 1.0 ns long current pulses with a current density of 1.0×10^{12} A/m^2. The lower vortex moves successively to the left edge of the wire.

ance at zero field, the geometry of the wire, and the distance between the voltage contacts we obtain a specific resistivity of 45 $\mu\Omega$ cm for the permalloy on the Si_3N_4 membrane. After the AMR characterization, magnetic transmission x-ray microscopy (MTXM) [22] with high lateral resolution down to 15 nm utilizing Fresnel zone optics [23] is used to image the magnetization of the wire. Figures 1(b) and 1(c) show an MTXM image and a scheme of a single-vortex wall, respectively.

Figure 2 shows MTXM images of double-vortex walls in the 960 nm wide wire. Prior to each image current pulses of 1.0 ns duration and a density of 1.0×10^{12} A/m^2 are sent through the wire in the direction indicated. In Fig. 2(a) and 2(b) the current-induced motion of a double-vortex wall in the direction of the conduction electrons is observed. Here, the wall moves with an undisturbed shape, i.e., as composite particle as predicted theoretically in Ref. [20]. A sketch of the motion is given in Fig. 2(c). However, in the repetitive pulse experiments also a current-induced distortion of the double-vortex wall is observed as vividly displayed in Fig. 2(d). Note that a vortex-antivortex pair has been created with the current pulse. Figures 2(e)–2(h) show MTXM images of a double-vortex wall which correspond to the results shown in Fig. 3. The current pulses successively move the lower vortex in a Barkhausen-like manner from pinning site to pinning site to the left, i.e., perpendicular to the direction of the conduction electrons.

It is well known that field-driven magnetization reversal is mediated via a sequence of Barkhausen jumps [24]. Disorder plays a significant role in the process of field-driven Barkhausen avalanches as there are pinning sites which cause a local distribution for the probability of DW depinning and motion [25]. We assume a similar mechanism in case of current-driven DW motion and expect a thermally activated process for the room temperature measurements with an energy barrier related to pinning by defects or to wall transformations at the wire borders as demonstrated in Ref. [16]. To analyze the stochastic nature of current-induced DW motion in more detail we have repeatedly imaged a double-vortex wall and sent current pulses of 1.0 ns duration, 100 ps rise time, and 7.5×10^{11} A/m^2 (1.0×10^{12} A/m^2) density through it. In the present experiment the DW width is much larger than the magnetic coherence length of the conduction electrons [11]. Thus the spins of the conduction electrons can follow the direction of the local magnetization [4,9] although the

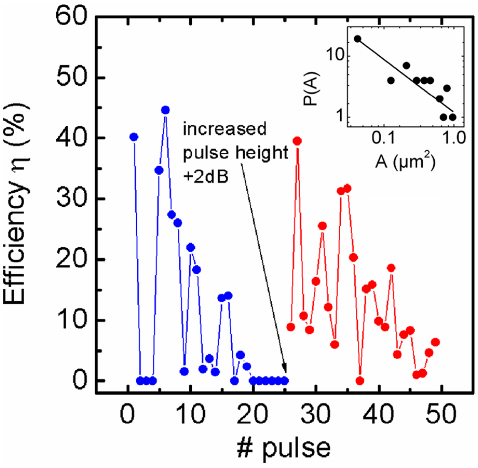

FIG. 3 (color online). Efficiency of DW displacement for 49 pulses of 1.0 ns duration. The current density of the pulses was increased from 7.5×10^{11} A/m^2 to 1.0×10^{12} A/m^2 after pulse No. 25.

nonadiabatic correction introduces an angle between the local magnetization and the magnetic moment of the conduction electrons. From the difference of two successive x-ray images the lateral area A in which the magnetization has been changed by one current pulse is determined. Following the approach of Ref. [6], the efficiency of DW displacement $\eta = \Delta m/m_{\text{current}}$, where $\Delta m = 2M_S A d$ is the change of the magnetic moment in the wire and $m_{\text{current}} = 2P\mu_B wtj\Delta t/e$ is the magnetic moment carried by the current pulse, can be determined. The spin polarization of $P = 35\%$ is determined by point-contact Andreev spectroscopy [26]. With the thickness $d = 80$ nm and the width $w = 960$ nm of the wire, the saturation magnetization $M_S = 800$ kA/m^2, and the pulse duration $\Delta t = 1.0$ ns we calculate the efficiency plotted in Fig. 3 for 49 pulses and two different current densities. It clearly shows the stochastic nature of the process; e.g., for a number of pulses no motion of the DW is observed. We believe that the stochastic nature, i.e., a continuous pinning and depinning, is the reason for the extremely low DW velocities obtained from measurements with long current pulses [14]. It is interesting to compare the distribution $P(A)$ of the current-driven jump size A to the field-driven case of Barkhausen jumps. The inset of Fig. 3 shows a power-law behavior for $P(A)$ akin the field-driven case. The experimental data are fitted by $P(A) \propto A^{-\tau}$ with a critical exponent of $\tau = 0.9 \pm 0.2$. This exponent differs from the universality class for field-driven Barkhausen jumps in thin films of various thicknesses and materials [25]. However, for a final quantitative determination of the critical exponent the number of repetitions must be increased to improve the statistics.

To compare the experimental results with theory we implemented the spin-torque transfer model of Zhang and Li [3] in the micromagnetic framework OOMMF [27] and simulated the influence of current on a DW in curved wires [10]. Here, we apply this code to determine the current-induced DW velocity using the material parameters of permalloy, i.e., an anisotropy constant of $K = 100$ J/m^3, an exchange constant of $A = 1.3 \times 10^{-12}$ J/m, and a saturation magnetization of $M_S = 800$ kA/m, the Gilbert damping parameter $\alpha = 0.01$, the degree of nonadiabaticity $\xi = 0.01$, and the geometry of the approximately 1 μm wide wire of Fig. 2. Figure 4 shows the simulation of a double-vortex wall while a current of density 1.0×10^{12} A/m^2 is sent through the wire. The time difference between Figs. 4(a) and 4(b) is 1.0 ns. Taking the right end of the double-vortex wall as a measure for the motion one obtains a velocity of 110 m/s. A comparison with the experimental data in Fig. 2 reveals that the simulated and the measured static domain structure are consistent [28]. The current-induced DW velocities determined from simulation and experiment are also in good agreement. The simulated DW velocity is not homogeneous in time and space as DW motion occurs in jumps from pinning center to pinning center given by the edge roughness due to the discretization. A strong influence of the edge roughness of the wire on the DW velocity for the field-driven case is well known from the literature [16]. Furthermore, inner excitations of DWs are observed under the influence of the current, e.g., the generation of a vortex-antivortex pair, which is in turn annihilated under emission of spin waves (not shown). Thus micromagnetic simulations support the interpretation of the experimental results and underline the importance of the stochastic nature of current-driven DW motion [29].

In the following, we focus on the perpendicular motion of vortex cores observed repeatedly, e.g., in Fig. 2(e)–2(h).

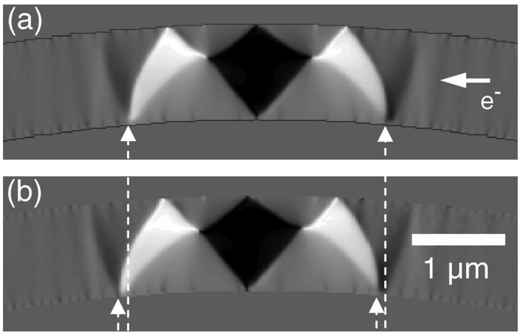

FIG. 4. Micromagnetic simulation of the influence of a spin-polarized current with a current density of 1.0×10^{12} A/m^2 on a double-vortex wall in a curved permalloy wire of 1 μm width and 80 nm thickness. The time difference between (a) and (b) is 1 ns. The right edge of the wall has moved 110 nm.

The perpendicular motion of a vortex core was calculated analytically and by micromagnetic simulation in Ref. [20]. There, the number of vortex cores was reduced by one from a vortex wall to a transverse wall. The description of the vortex motion by a restoring force, i.e., the coupling of vortices via a spring constant, can also be used to describe the more complex walls of the present experiments. The vortex polarity p determines to which edge of the wire the vortex moves. We deduce a perpendicular displacement y_0 of 83 ± 36 nm of the lower vortex core in Fig. 2 for a single 1.0 ns long current pulse of density 1.0×10^{12} A/m^2. If the deduced perpendicular displacement y_0 is applicable we can solve Eq. (21) of Ref. [20] and extract the ratio between the degree of nonadiabaticity ξ and the Gilbert damping parameter α

$$\frac{\xi}{\alpha} = 1 - \frac{\kappa y_0}{G_v b_j^c}, \qquad (1)$$

where $\kappa = \frac{4K^{3/2}}{\pi\sqrt{A}}$ is the spring constant, $G_v = -\frac{2\pi M_S p t}{\gamma}$ the value of the gyrocoupling vector with the gyromagnetic ratio γ, the parameter of the current density $b_j^c = \frac{P j_c \mu_B}{e M_S(1+\xi^2)}$, and j_c the critical current density that moves the vortex to the next pinning site. In the present wire the anisotropy is comparable to the one of an extended film; i.e., the shape anisotropy is small, justifying the value of $K = 100$ J/m^3 in agreement with the phase diagram for DWs in nanowires [30]. Since $\xi^2 \ll 1$ we neglect this term in b_j^c and obtain $\xi = (0.96 \pm 0.02)\alpha$ in good agreement with the experiments of Ref. [17]. This evidences that the nonadiabatic spin-torque term is important for DW motion.

To exclude Joule heating [18] as a possible cause for DW motion we calculate the heat deposited by a single current pulse of 1.0 ns duration and 1.0×10^{12} A/m^2 current density from the sample geometry, the specific resistivity, and the heat capacity of permalloy. A temperature increase of 115 K is calculated which is considerably lower than the Curie temperature of permalloy (850 K) and room temperature where the experiments were performed. In the above estimate the heat flow through the wire is neglected; i.e., the calculated temperature increase is an upper limit that is in agreement with the detailed calculations of Ref. [31] that yield 68 K for our parameters. Thus we conclude that in the present experiments the motion of the DW is caused by the spin-transfer torque and is not much affected by Joule heating.

In conclusion, we have performed soft x-ray microscopy with high spatial resolution to image the current-induced motion of vortex-DWs in curved wires. Nanosecond current pulses were used to determine a DW velocity of 110 m/s which is in agreement with recent theories and is comparable to the case of field-driven motion. We found that the current-driven motion exhibits a statistical distribution like Barkhausen jumps for the field-driven case.

We thank Ulrich Merkt and Daniela Pfannkuche for fruitful discussions and the staff of CXRO and ALS, in particular, Ron Oort, Paul Denham, Bob Gunion, and Erik Anderson for their help with the experiments. Financial support of the Deutsche Forschungsgemeinschaft via the Sonderforschungsbereich 668 "Magnetismus vom Einzelatom zur Nanostruktur" and via the Graduiertenkolleg 1286 "Functional metal-semiconductor hybrid systems" is gratefully acknowledged. This work was supported by the U.S. Department of Energy under Contract No. DE-AC02-05-CH11231.

*Electronic address: meier@physnet.uni-hamburg.de

[1] S. S. P. Parkin, US Patent 309,6,834,005 (2004).
[2] D. A. Allwood *et al.*, Science **309**, 1688 (2005).
[3] S. Zhang and Z. Li, Phys. Rev. Lett. **93**, 127204 (2004).
[4] G. Tatara and H. Kohno, Phys. Rev. Lett. **92**, 086601 (2004).
[5] A. Thiaville *et al.*, Europhys. Lett. **69**, 990 (2005).
[6] A. Yamaguchi *et al.*, Phys. Rev. Lett. **92**, 077205 (2004).
[7] J. Slonczewski, J. Magn. Magn. Mater. **159**, L1 (1996).
[8] L. Berger, Phys. Rev. B **54**, 9353 (1996).
[9] X. Waintal and M. Viret, Europhys. Lett. **65**, 427 (2004).
[10] B. Krüger *et al.*, Phys. Rev. B **75**, 054421 (2007).
[11] Y. Tserkovnyak, H. J. Skadsem, A. Brataas, and G. E. W. Bauer, Phys. Rev. B **74**, 144405 (2006).
[12] Z. Li and S. Zhang, Phys. Rev. B **70**, 024417 (2004).
[13] D. Atkinson *et al.*, Nat. Mater. **2**, 85 (2003).
[14] M. Kläui *et al.*, Phys. Rev. Lett. **95**, 026601 (2005).
[15] T. Ono *et al.*, Science **284**, 468 (1999).
[16] Y. Nakatani *et al.*, Nat. Mater. **2**, 521 (2003).
[17] M. Hayashi *et al.*, Phys. Rev. Lett. **96**, 197207 (2006).
[18] A. Yamaguchi *et al.*, Appl. Phys. Lett. **86**, 012511 (2005).
[19] A. Yamaguchi *et al.*, Phys. Rev. Lett. **96**, 179904 (2006).
[20] J. He *et al.*, Phys. Rev. B **73**, 184408 (2006).
[21] M. Kläui *et al.*, Appl. Phys. Lett. **81**, 108 (2002).
[22] P. Fischer, Curr. Opin. Solid State Mater. Sci. **7**, 173 (2003).
[23] W. Chao *et al.*, Nature (London) **435**, 1210 (2005).
[24] H. Barkhausen, Z. Phys. **20**, 401 (1919).
[25] D.-H. Kim *et al.*, Phys. Rev. Lett. **90**, 087203 (2003).
[26] L. Bocklage *et al.*, J. Appl. Phys. (to be published).
[27] M. Donahue and D. Porter, National Institute of Standards and Technology Interagency Report No. NISTIR 6376, 1999.
[28] Note that the curvature of the wire with respect to the double-vortex wall is reversed between experiment and simulation. However, the curvature is small; i.e., the confining potential in the curved and in the straight wire are very similar.
[29] A simulated Oersted field of several mT perpendicular to the wire caused no DW motion.
[30] Y. Nakatani *et al.*, J. Magn. Magn. Mater. **290–291**, 750 (2005).
[31] C.-Y. You *et al.*, Appl. Phys. Lett. **89**, 222513 (2006).

4.4.3 Spin-Torque Induced Magnetic Vortex and Antivortex Gyration

Observing the time dependence of magnetic configurations with X-rays is a challenge since the photon flux of even 3^{rd} generation synchrotron light sources is too low to yield a enough signal-to-noise ratio in one light flash for an image. There are currently two options: Either one measures quasi-statically before and after an event to detect the changes in the magnetic system as was done in the previous experiment. Alternatively, one needs repeatable processes to perform time-resolved X-ray microscopy. Here one has again two choices as described in Section 3.2.3: Either to detect in pump-probe mode or in harmonic excitation mode. We performed pump-probe measurements at the XM-1 beam line 6.1.2 and harmonic excitation measurements at the STXM beam line 11.0.2 at the Advanced Light Source in Berkeley, CA, USA.

We studied the dynamics of magnetic vortices and antivortices in permalloy thin film structures since the cylindrical symmetry of the vortices allows for a relatively simple analytical description. Magnetic vortices form in laterally confined thin films when it is energetically favorable for the magnetization to point in-plane and parallel to the edges. In the center the magnetization is forced out-of-plane to avoid large angles between magnetic moments that would drastically increase the exchange energy. Antivortices, also called *cross Bloch lines* (see Section 2.2.3 and Ref. [36]), form either in cross-tie walls or when the magnetic thin film is artificially patterned in such a way that the magnetization of four domains meet radially in one point (see Fig. 4.12 and Fig. 3 of Ref. [192]). In both cases, the region with a strong out-of-plane magnetization component is called a (anti-)vortex core and is only a few nanometers in diameter [193, 194]. The direction of the magnetization in the core, also called the (anti-)vortex *polarization*, can only assume two values $p = +1(-1)$ for the (anti-)vortex core pointing out of (into) the plane (see Fig. 4.12). The direction of the in-plane magnetization with respect to the polarization is called the *chirality* $c = +1(-1)$ for counterclockwise (clockwise) in-plane curling of the magnetization. Chirality and polarization unambiguously define the (anti-)vortex configuration as noted by Shibata *et al.* (see Ref. [195]). Vortices and antivortices can be analytically described by the same formalism by introducing a third quantity, the *skyrmion number* $q = n\,p/2$ where n is the winding number.

It has been shown that vortices can be excited to rotate around their equilibrium position by in-plane magnetic field pulses [196] or in-plane alternating fields [197]. The direction of gyration is governed by the vortex polarization according to the right-hand rule. Recently our collaborators from the Max-Planck-Institute for Metal Research in Stuttgart and the University of Ghent, Belgium, have shown that a combination of alternating fields

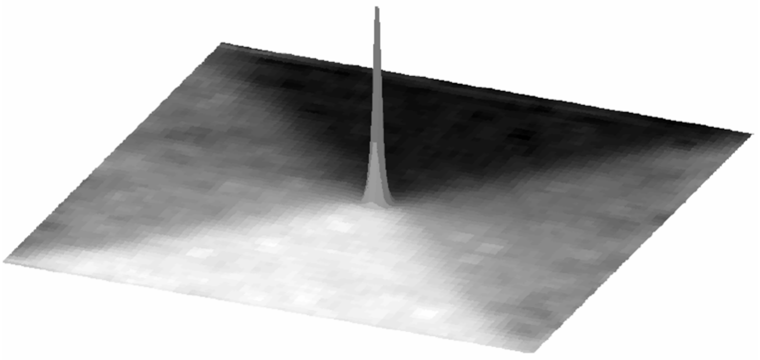

Fig. 4.12: Simulated image of a vortex in a Landau-domain pattern in a permalloy square. The magnetization in the horizontal direction is displayed as gray contrast.

and field pulses of higher field amplitude can switch the polarization of vortices [64]. This opened a way of manipulating the vortex polarization. It has been shown that electric currents of high density can switch the vortex in the same way [198, 65], and micromagnetic simulations have confirmed these findings [199, 200, 201, 202, 203].

In the following I present the results from experimental, numerical, and analytical investigations of magnetic vortex and antivortex dynamics. At first I show the first time-resolved detection of the spin-torque driven vortex gyration in permalloy squares that have been observed at the STXM beam line. This method is very sensitive to the gyration phase with respect to the excitation. From deviations in the phase we could show that in typical permalloy thin film structures the Oersted field of the conducting current induces a phase shift to the gyration even though the field amplitude is rather small ($\approx 40\ \mu$T for a current of 1.2×10^{11} A/m^2). This work has recently been submitted as **[P18]** but has not been published yet. It has been accepted for an oral presentation at the 52^{nd} Conference on Magnetism and Magnetic Materials in Tampa, FL, USA, in November 2007 (see **[C24]**). It was also presented at several international conferences, workshops and in invited talks (see **[C11]**, **[C14]**, **[C18]**, and **[I9]**). It is printed as a preprint on the following pages.

During the writing of the above manuscript Benjamin Krüger, André Drews, and I developed a two-dimensional harmonic oscillator model for the analytical description of field-and current-induced vortex gyration. It has been accepted as **[P17]** in the Physical Review B, but has not been printed yet. It is included as a preprint in this thesis as well.

Parallel to the development of the vortex-oscillator model, André Drews, with the help of Benjamin Krüger and myself, simulated the dynamics of an antivortex excited by field or current. So far, no one has dynamically observed antivortex motion in experiments. Therefore there is no accurate description or prediction for its dynamics. André Drews

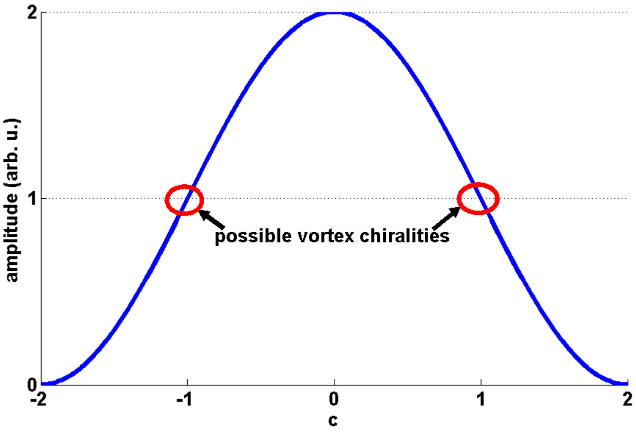

Fig. 4.13: Chirality-dependent enhancement or suppression of gyration amplitude.

has performed numerous simulations, and together we derived a similar analytical model as for the vortex, but found also important differences between vortices and antivortices. Magnetic vortices have integer chirality being either -1 or $+1$, whereas antivortex chiralities can be non-integer within the interval $(-2,2]$. A combination of field- and spin-torque excitation will therefore cause chirality-dependent enhancement or suppression of gyration amplitude as shown in Fig. 4.13. This study has been submitted as **[P19]** and was accepted for oral presentation at the 52^{nd} Conference on Magnetism and Magnetic Materials in Tampa, FL, USA, in November (see **[C23]**). It was also presented at an international conference and during a poster session of the international summer school of the Graduiertenkolleg 1286 in Hamburg (see **[C18]** and **[C21]**, respectively).

Finally, a conference article for the 52^{nd} Conference on Magnetism and Magnetic Materials in Tampa, FL, USA, in November with Benjamin Krüger as first author combines the analytical models for vortex and antivortex gyration driven by magnetic fields and electric currents (see **[C25]**). It has been accepted as **[P20]** in the Journal of Applied Physics and was presented during two invited talks (see **[I9]** and **[I11]**).

Direct Observation of Spin-Torque- and Oersted Field-Induced Magnetic Vortex Gyration with X-ray Microscopy

Markus Bolte,* Guido Meier, René Eiselt, Lars Bocklage, and André Drews
Institut für Angewandte Physik und Zentrum für Mikrostrukturforschung,
Universität Hamburg, Jungiusstrasse 11, 20355 Hamburg, Germany

Benjamin Krüger
I. Institut für Theoretische Physik, Universität Hamburg, Jungiusstrasse 9, 20355 Hamburg, Germany

Tolek Tyliszczak
Advanced Light Source, LBNL, 94720 Berkeley, California, USA

Bartel Van Waeyenberge
Department of Subatomic and Radiation Physics,
Ghent University, Proeftuinstraat 86, 9000 Ghent, Belgium

Kang Wei Chou, Gisela Schütz, and Hermann Stoll
Max Planck Institut für Metallforschung, Heisenbergstrasse 3, 70569 Stuttgart, Germany
(Dated: August 30, 2007)

Spin-polarized currents used for switching the magnetic state of novel data storage cells are a promising alternative to magnetic fields generated by nearby currents. A current in a ferromagnet exerts a torque on the magnetization proportional to the magnetization's spatial derivative. We have imaged the influence of alternating high-density currents on the magnetization dynamics of ferromagnetic vortices via time-resolved X-ray microscopy. Spin-torque induced vortex gyration is observed in micrometer-sized permalloy squares at current densities between $4.7 \cdot 10^{10}$ A/m^2 and $1.2 \cdot 10^{11}$ A/m^2. The phase of the gyration in structures with different chirality were compared to an analytical model and micromagnetic simulations, considering both alternating spin-polarized currents and the current's Oersted fields. This analysis revealed that also effective Oersted fields are present. These are attributed to inhomogeneous current densities within the thin films. In the 20 nm thick squares the driving force of the effective Oersted field is about forty percent of the driving force due to spin-torque. As this might be a general feature of sputtered and evaporated thin films, this finding has implications to magnetic storage devices using spin-torque driven magnetization switching.

PACS numbers: 68.37.Yz, 72.25.Ba , 75.25.+z, 75.40.Mg, 85.75.-d

The discovery that spin-polarized electrons travelling through ferromagnets apply a torque on their local magnetization [1, 2] opened up a new field of research in solid state physics that could potentially result in new magnetic storage media. Random access memories in which magnetic layers are aligned parallel or antiparallel with respect to each other can use this spin-transfer torque to change the direction of the magnetization and thus change the stored magnetic information[3, 4]. Also, magnetic domain walls, i.e., the interfaces between regions of same magnetization, can be driven by spin-polarized currents to store information in bit registers and can even be used for computation [5, 6]. It is now understood that the spin-transfer torque acts on inhomogeneities in the magnetization, e.g., on interfaces between magnetic layers [2], on domain walls [7, 8], or on magnetic vortices [9–12].

Vortices form in laterally confined thin films when it is energetically favorable for the magnetization to point in-plane and parallel to the edges. In the center the magnetization is forced out-of-plane to avoid large angles between magnetic moments that would drastically increase the exchange energy. The region with a strong out-of-plane magnetization component is called a vortex core and is only a few nanometers in diameter [13, 14]. The direction of the magnetization in the vortex core, also called the vortex polarization, can only assume two values. They are separated by a high energy barrier, hence ferromagnetic elements could be used for data storage. To denote the possible vortex configuration, we shall use the chirality $c = +1(-1)$ for counterclockwise (clockwise) in-plane curling direction of the magnetization and the vortex polarization $p = +1(-1)$ for the vortex core pointing out of (into) the plane as was defined by Shibata *et al.* (see Ref. [9]).

It is known that vortices can be excited to gyrate around their center position by in-plane magnetic field pulses [15] or resonantly by alternating fields[16]. The

---

*Electronic address: `mbolte@physnet.uni-hamburg.de` direction of gyration is governed by the vortex polarization according to the right-hand rule (see Fig. 2 of Ref. [15]). Recently it has been shown that sinusoidal in-plane field excitation coupled with a short burst of higher field amplitude can even switch the polarization of the vortices [17] and simulations indicate that very short field pulses might do the same[18]. This opened a way of manipulating the vortex polarization.

It was predicted that also electric currents of high density could excite a vortex in the same way[9] as an external magnetic field. However, the experimental verification requires careful analysis, as all electric currents are accompanied by magnetic fields. For perfectly homogeneous currents the average magnetic field would cancel out while inhomogeneous currents result in an additional field-driven excitation. Generally, a non-uniform resistivity and hence a non-uniform current density along the perpendicular direction might be expected in thin films.

Spin-torque induced vortex gyration does not depend on the chirality, but only on the polarization [9, 11]. This is not the case for field-driven gyration where the phase of gyration depends not only on the vortex core polarization, but also on the curling direction of the in-plane magnetization around the vortex core. Hence, experimentally resolving the absolute phase of the gyration and comparing different magnetization configurations is the way to discriminate between spin-torque driven and field-driven vortex rotation.

Here we show via time- and phase-resolving X-ray microscopy that magnetic vortices in confined structures can be excited to gyration by high-frequency currents of high density passing directly through the sample. By observing the phase of the rotation relative to the excitation, we could discriminate between the current's spin-torque and its Oersted field contributions to the vortex motion. We investigated two 2 × 2 μm^2 large and 20 nm thick permalloy ($Ni_{80}Fe_{20}$) squares. In this geometry Landau patterns (see Fig. 1(A)) with a single vortex are energetically favorable at remanence. To excite the structures with alternating currents, they were contacted by 40 nm thick gold strip lines with an overlap of 150 nm (see Fig. 1(A) and (B)). Thus the current had to pass through the ferromagnetic material. The samples were placed in the scanning transmission X-ray microscope (STXM) of beam line 11.0.2 at the Advanced Light Source (ALS) in Berkeley. This instrument offers a high lateral resolution of about 30 nm, and, by exploiting the pulsed nature of the synchrotron light, temporal resolution of about 70 ps. Magnetic sensitivity is obtained by using the X-ray circular dichroism (XMCD) [19] at the nickel L_3-edge. There the transmitted photon intensity is higher when the magnetic moments and polarization are antiparallel than in the parallel case. The sample plane is set at an angle of 60° with respect to the incident beam (see Fig. 1(A)) so that the microscope can detect the in-plane magnetization. From the polarization of the X-rays we identify the dark (bright) regions in the images to be magnetized in the negative (positive) x-direction. We can thus unambiguously determine the chirality of the vortices. An alternating current with a frequency of 62.5 MHz was sent through the structures (see Fig. 2(A)). Figures 2(B) and 2(C) show the time-resolved magnetic contrast of the different samples (see also *movie1.avi* and *movie2.avi* in the online supporting material). The square in Fig. 2(B) with the chirality $c = +1$ was excited with a current density amplitude $j = 1.2 \cdot 10^{11}$ A/m^2. The vortex performs a counterclockwise gyration. Therefore, it must have a positive polarization $p = +1$. The radius of gyration is 220 nm, i.e., the vortex gyrates at a speed of 87 m/s. The vortex in Fig. 2(C) was excited with $j = 4.7 \cdot 10^{10}$ A/m^2. It has a negative chirality $c = -1$ and also gyrates counterclockwise, i.e., the polarization is positive ($p = +1$). The radius of gyration is much smaller, approximately 60 nm, leading to a vortex velocity of 24 m/s. Even though the two vortices have opposite chiralities, at phase 0° of

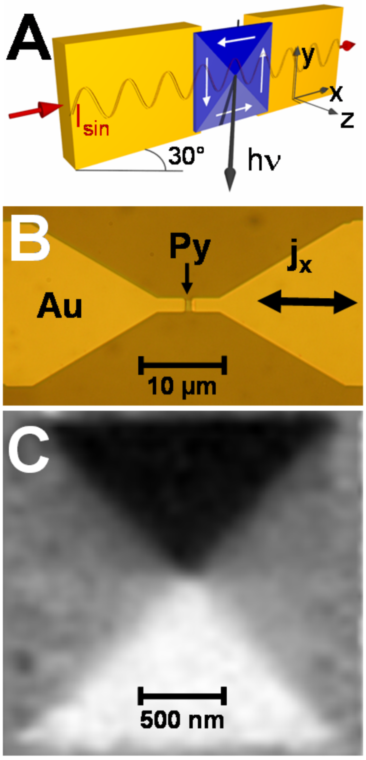

FIG. 1: (A) Scheme of the permalloy square contacted by two gold wires. The sample is tilted by 60° relative to the incident X-ray beam. (B) Optical micrograph of a permalloy square and its contacts on the Si_3N_4-membrane (deep brown). (C) Magnetic contrast of the relaxed permalloy square with a thickness of 20 nm showing the x-component of the magnetization as black-to-white contrast.

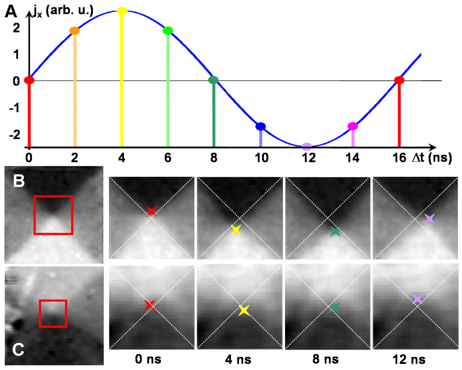

FIG. 2: (A) Sampling of the response to an 62.5 MHz excitation with eight different channels. Colors represent different phases from 0° to 315° in steps of 45°. Shown in (B) and (C) are four channels at 0, 4, 8, and 12 ns corresponding to phases 0°, 90°, 180°, and 270°. (B) X-ray images portraying the magnetization of a 2 × 2 μm^2 permalloy square with 20 nm thickness. The vortex of chirality $c = +1$ and polarization $p = +1$ is excited with a current density of $j = 1.2 \cdot 10^{11}$ A/m^2. (C) Magnetization of a square having $c = -1$ and $p = +1$ excited with $j = 4.7 \cdot 10^{10}$ A/m^2.

the ac-excitation both vortices are in the upper left quadrant. A closer investigation of the gyrations in the two Landau patterns reveals that at phase 0° the $c = +1$ vortex points more in the positive y–direction (to the top of the image) while the $c = -1$ vortex points more in the negative x–direction (to the left of the image). The phase difference between the gyration of these vortices is about 45°. This phase difference is due to a combination of the chirality neutral spin torque and the chirality sensitive Oersted field of the current (see differential images in the online supporting materials). It is clear, however, that the observed vortex gyrations are mainly caused by spin torque since a field-driven gyration would have a phase difference of 180° between the gyrations of the two Landau patterns of Figs. 2(B) and (C).

To better understand the dependence of the phases on current and field excitation, micromagnetic simulations were performed (for a description of the simulations see online supporting material). An ac-excitation of a small permalloy square with either spin-polarized currents j_x or magnetic fields H_y was simulated at different frequencies. The amplitudes of the excitations were found to influence only the radius of the gyration but not its phase. In the simulations the sense of gyration was governed in both cases by the polarization according to the right-hand rule, while its phase with respect to the ac-excitation differs between spin-transfer torque and field-excitation, because the latter depends on the chirality. This is in agreement with previous micromagnetic simulations[9, 10]. Figure 3 shows schematically the simulated phases of the vortex gyration as functions

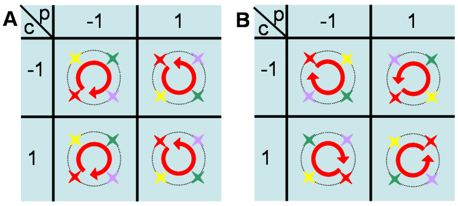

FIG. 3: Expected vortex positions in a square due to the current's spin torque (A) and Oersted field (B) when exciting just below resonance. The current flows from the left to the right. The red arrows depict the sense of rotation of the vortices according to the right-hand rule and the colored stars correspond to gyration phases 0°(red), 90°(yellow), 180°(light blue), and 270°(violet) (see Fig. 2(A)).

of the vortex chirality and polarization for spin-torque induced and field-induced gyration (see Fig. 3(A) and 3(B), respectively). Following the 'rigid model' for magnetic vortices in thin films [20, 21], the vortex gyration due to alternating fields or currents can be described by a two-dimensional harmonic oscillator [11]. An alternating magnetic field or an alternating current forces the vortex to oscillate along the direction of the field or current. The magnetostatic field due to the deviation of the vortex from its equilibrium position drives the oscillator perpendicular to the direction of the field or current. Since in our case the current passes through the permalloy square along the x-direction (see Fig. 1), the Oersted field is along the y-direction. Thus the equation of motion for the vortex in the oscillator model reads[11]

$$\begin{pmatrix} X \\ Y \end{pmatrix} = \frac{e^{i\Omega t}}{\omega^2+(i\Omega+\Gamma)^2} \times \left(\frac{\gamma l}{2\pi} c H_y \begin{pmatrix} -\omega \\ i\Omega p \end{pmatrix} - b_j j_x \begin{pmatrix} i\Omega \\ p\omega \end{pmatrix} \right). \qquad (1)$$

Here, Ω is the excitation frequency, ω the rotation frequency of the free vortex, Γ the damping constant proportional to the Gilbert damping α, and $\gamma = 2.21 \cdot 10^5$ m/As the gyromagnetic ratio for permalloy. The constant $b_j = P\mu_\mathrm{B}/(eM_\mathrm{s})$ with the saturation magnetization M_s and the spin polarization P describes the coupling between the current density and the magnetization. Gilbert damping terms of higher order were neglected as they are at least one order of magnitude smaller than the leading terms. We simulated the relaxation of excited Landau patterns with the experimental dimensions and derived a resonance frequency both vortices that is in good agreement with previous calculations [22]. If the magnetization configuration (p,c) is known Γ and the ratio H_y/j_x are the only variable parameters in Eqn. (1). In the following it is assumed that Γ and H_y/j_x are the same for both vortices because the permalloy squares were prepared from the same thin film. H_y/j_x is found by comparing the relative phase between the vortex gyrations in Fig. (2) to the analytical model. $\Gamma/2\pi$ is derived by fitting the simulated absolute phases of each vortex to the experimental phases (see online supporting material) and is found to be approximately 10 MHz for both vortices. According to the model the phase difference observed in the experiment is due to an Oersted field exercising a force of about 40% of the one due to spin-torque.

The origin of the unexpected Oersted field contribution can be attributed to a thickness dependent resistivity of thin metal films[23]. Using Eqn. (1) to calculate the average Oersted field one derives a strength of approximately $3.0 \cdot 10^{-5}$ T for a current density of $1.2 \cdot 10^{11} \mathrm{A/m^2}$. Micromagnetic simulations were performed using both spin-torque and field excitation with the above parameters and yielded 40°, almost the same phase difference as in the X-ray microscopy measurements. Experimentally field-induced vortex gyration has been observed at field values as low as $5.0 \cdot 10^{-4}$ T. Due to vortex pinning at surfaces[24] the excitation field apparently needs to be stronger to get the vortex moving than if it is already gyrating due to spin torque. Indeed, at slightly lower input powers ($j_x = 1.1 \cdot 10^{11} \mathrm{A/m^2}$) the excitation reached a threshold. At some lines of the scanning X-ray microscope image no gyration was observed while at others the vortex gyrated at approximately the same radius as with the $j_x = 1.2 \cdot 10^{11} \mathrm{A/m^2}$ current.

The existence of Oersted fields due to inhomogeneous current densities is of a general nature and will not be limited to our samples. The observations of the phase of magnetic vortex gyration were possible due to its periodic motion in a confined structure. The dynamics of other magnetic objects, e.g., vortex domain walls, are more difficult to record, but are also subject to Oersted fields from a spin-polarized current. We feel that the Oersted fields of an inhomogeneous current density have not been adequately taken into account in previous measurements and that one must be careful to rule out field-driven or field-assisted magnetization dynamics in spin-torque experiments. As seen from our observations, one cannot safely assume that the change of a magnetic structure is due to a traversing spin-polarized current alone.

With the help of time-resolved X-ray microscopy we have observed magnetic vortex gyration driven by spin-polarized currents that can be described by a harmonic oscillator model. We have also recognized a non-negligible contribution of the current's Oersted field even though the current was transmitted directly through the magnetic layer. In experiments, one needs to resolve the phase and the sense of gyration to separate the contribution of the current's spin-torque to magnetic vortex gyrations from the current's Oersted field. Time-resolved X-ray microscopy has proven to be an excellent method for detecting even small contributions from Oersted fields to the gyration of vortices. These observations are relevant to technological applications since spin-polarized currents that switch the polarization of vortices have been suggested for data storage devices [12].

Acknowledgments

We would like to thank Ulrich Merkt for valuable discussions. Financial support from the Deutsche Forschungsgemeinschaft via the SFB 508 "Quantenmaterialien", the SFB 668 "Magnetismus vom Einzelatom zur Nanostruktur" as well as the GK 1286 "Functional Metal-Semiconductor Hybrid Systems" is gratefully acknowledged.

[1] L. Berger, *Phys. Rev. B* **54**, 9353 (1996).

[2] J. Slonczewski, *J. Magn. Magn. Mater.* **159**, L1 (1996).

[3] I. N. Krivorotov, *et al.*, *Science* **307**, 228 (2005).

[4] E. B. Myers, D. C. Ralph, J. A. Katine, R. N. Louie, R. A. Buhrman, *Science* **285**, 867 (1999).

[5] D. A. Allwood, *et al.*, *Science* **309**, 1688 (2005).

[6] S. S. P. Parkin, *US Patent* **309**, 6,834,005 (2004).

[7] S. Zhang, Z. Li, *Phys. Rev. Lett.* **93**, 127204 (2004).

[8] B. Krüger, D. Pfannkuche, M. Bolte, G. Meier, U. Merkt, *Phys. Rev. B* **75**, 054421 (2007).

[9] J. Shibata, Y. Nakatani, G. Tatara, H. Kohno, Y. Otani, *Phys. Rev. B* **73**, 020403 (R) (2006).

[10] S. Kasai, Y. Nakatani, K. Kobayashi, H. Kohno, T. Ono, *Phys. Rev. Lett.* **97**, 107204 (2006).

[11] B. Krüger, *et al.*, *submitted* (2007).

[12] K. Yamada, *et al.*, *Nature Materials* **6**, 269 (2007).

[13] T. Shinjo, T. Okuno, R. Hassdorf, K. Shigeto, T. Ono, *Science* **289**, 930 (2000).

[14] A. Wachowiak, *et al.*, *Science* **298**, 577 (2002).

[15] S.-B. Choe, *et al.*, *Science* **304**, 420 (2004).

[16] B. E. Argyle, E. Terrenzio, J. C. Slonczewski, *Phys. Rev. Lett.* **53**, 190 (1984).

[17] B. Van Waeyenberge, *et al.*, *Nature* **444**, 461 (2006).

[18] R. Hertel, S. Gliga, M. Fähnle, C. M. Schneider, *Phys. Rev. Lett.* **98**, 117201 (2006).

[19] G. Schütz, *et al.*, *Phys. Rev. Lett.* **58**, 737 (1984).

[20] A. A. Thiele, *Phys. Rev. Lett.* **30**, 230 (1973).

[21] D. L. Huber, *Phys. Rev. B* **26**, 3758 (1982).

[22] V. Novosad, *et al.*, *Phys. Rev. B* **72**, 024455 (2005).

[23] A. F. Mayadas, J. F. Janak, A. Gangulee, *J. Appl. Phys.* **45**, 2780 (1974).

[24] R. L. Compton, P. A. Crowell, *Phys. Rev. Lett.* **97**, 137202 (2006).

Supporting Online Material

Experimental details

The time and space resolved response of the sample magnetization was imaged by a stroboscopic Scanning Transmission X-ray Microscope (STXM) at the Advanced Light Source (ALS, BL 11.0.2). The monochromatic, circularly polarized X-rays from the undulator beam line are focused to a spot of 30 nm onto the sample with the help of a Fresnel zone plate. The sample is scanned in the xy-plane with a high resolution scanning stage under interferometric control and the transmitted intensity is recorded. The photon energy was set at the Ni L_3-absorption edge (852.7 eV), where X-ray circular dichroism (XMCD) [1] gives a high magnetic contrast.

In this stroboscopic technique, the temporal resolution (70 ps) is given by the width of the electron bunches that produce the photon flashes. In the standard multi-bunch operation mode of the synchrotron used here, the flash repetition rate is 500 MHz. To resolve the individual flashes, a fast avalanche photodiode was used as a photon detector. With fast data acquisition electronics, the intensity of the individual bunches could be recorded. An RF signal generator was synchronized with the synchrotron RF main oscillator to deliver an alternating current to the sample. An excitation frequency 500 MHz / 8 = 62.5 MHz was selected. This frequency is close to the expected resonance frequency of the structure and allows us to record the response of the magnetization at eight different phases simultaneously in eight different channels. At the ALS, the synchrotron is not filled uniformly with electrons, but contains a larger electron bunch surrounded by a gap. This bunch produces a brighter flash and is used as a reference marker to align the excitation signal with the data acquisition. The absolute phase relation between the eight recorded images and the excitation current was made by sending a short pulse through the detector electronics. By aligning its arrival to the pulse produced by the photons of the reference marker we achieved an accuracy in the phases of approximately 4°.

Microstructured permalloy squares were prepared on 200 nm thin Si_3N_4 membranes for minimal absorption of the X-rays. The squares were prepared onto the membranes by electron-beam lithography, electron-beam evaporation, and lift-off processing. The permalloy squares were contacted by 40 nm thick gold strip-lines. The overlap of the gold contacts with the permalloy was 150 nm wide (see Fig. 1) ensuring the current to flow through the ferromagnet.

Differential images

The differential images yield the phase and the amplitude of the gyration with greater accuracy than the absolute images. They were calculated by subtracting an image taken at 180° excitation phase from the 0° phase image, the 225° image from the 45° image, and so forth. A white (black) cross in the differential images means that the vortex is positioned opposite to the magnetic domain represented by bright (dark) contrast. For example, the white contrast in phases 270° to 45° in Fig. 1 (see Fig. 2(B) of the main article) represent the vortex being in the upper quadrants, as the domain with bright XMCD contrast is shown at the bottom of the image. Likewise, in Fig. 2 (see Fig. 2(C) of the main article) the black contrast in phases 225° to 0° represent the vortex being in the upper quadrants as the chirality and therefore the contrast is inversed. For detailed information on how to calculate the vortex position from differential images see Ref. [2]. The phases at which maximum white (black) contrast in the differential images occurs yields the estimate for the gyration amplitude. Since the vortices gyrate in the same direction, comparing Fig. 1 and 2 yields the phase difference of ≈ 45° mentioned in the main article.

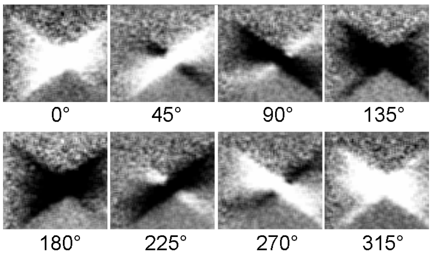

FIG. 1: Differential images of a 2×2 μm^2 large and 20 nm thick permalloy square excited by a current of $j_0 = 1.2 \cdot 10^{11}$ A/m^2 at 62.5 MHz. Compare Fig. 2(B) of the main article.

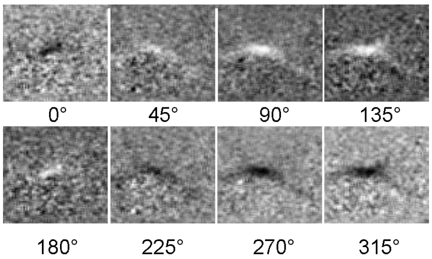

FIG. 2: Differential images of a 2×2 μm^2 large and 20 nm thick permalloy square excited by a current of $j_0 = 4.7 \cdot 10^{10}$ A/m^2 at 62.5 MHz. Compare Fig. 2(C) of the main article.

Micromagnetic simulation parameters

Simulations were performed to investigate the phase between vortex core motion and exciting magnetic field or spin current, and the results are plotted in Fig. 3 of the main article. The simulations were done below resonance, at resonance, and above resonance for all chiralities and polarizations. For this a version of the Object Oriented Micromagnetic Framework *OOMMF* extended by additional spin-torque terms [3] was used. A size of the vortex element of $200 \times 200 \times 20$ nm^3 was chosen. We assumed a saturation magnetization of $M_\mathrm{s} = 8 \cdot 10^5$ A/m, an exchange constant of $A = 1.3 \cdot 10^{-11}$ J/m, a Gilbert damping of $\alpha = 0.01$, and the ration between spin-flip and spin-relaxation time $\xi = \alpha$ [4]. The amplitude of the electrical current was set to $P \cdot j = 1 \cdot 10^{11}$A/m and the amplitude of the magnetic field to $H = 50$ mT. Simulation cells of size $2\times2\times$ 20 nm^3 was chosen. The resonance frequency ω_r of the vortex element was derived from a fit to the relaxed vortex core motion by the equation of motion of a damped harmonic oscillator [5].

Harmonic oscillator model

The use of one resonance frequency for both vortices is justified, even though it is known that pinning sites can cause the resonance frequency to differ by a factor of two or more [6]. As it is stated in Ref. [6], the gyrotropic frequency decreases abruptly to the value expected by the magnetostatic potential, i.e., the resonance frequency for perfect vortex structures, when the radius of the gyrotropic orbit exceeds the range of the pinning centers ($\lesssim$ 25 nm). Since our gyration amplitude is many times the critical value, pinning does not influence the resonance frequency in our experiments.

The magnitude of the Oersted field was estimated in the following way: Starting with the harmonic oscillator model for magnetic vortices (see Ref. [5]) we discarded the terms proportional to Γ/ω to arrive at Eqn.(1) of the present article since $\Gamma \ll \omega$. The position of the vortex is then given by

$$\begin{pmatrix}X\\ Y\end{pmatrix} = -\frac{e^{i\Omega t}}{\omega^2+(i\Omega+\Gamma)^2}\begin{pmatrix}\tilde{H}\omega & + & i\tilde{j}\Omega\\ \tilde{j}\omega p & - & i\tilde{H}\Omega p\end{pmatrix} \qquad (1)$$

with $\tilde{H} = \gamma H_y lc/(2\pi)$ and $\tilde{j} = b_j j_x$. Equation (1) depends on the chirality of the vortex. One can get an expression which is independent of the chirality by rotating the coordinate system of each vortex individually by

$$\tau = -\arctan\left(\frac{\tilde{H}p}{\tilde{j}}\right) = -cp\arctan\left(\frac{\gamma H_y l}{2\pi b_j j_x}\right). \qquad (2)$$

The vortex position then is

$$\begin{pmatrix}X'\\ Y'\end{pmatrix} = -\frac{e^{i\Omega t}}{\omega^2+(i\Omega+\Gamma)^2}\sqrt{\tilde{H}^2+\tilde{j}^2}\begin{pmatrix}i\Omega\\ \omega p\end{pmatrix}. \qquad (3)$$

Due to the different chirality of the vortices, the angles τ_+ ($c = +1$) and τ_- ($c = -1$) have different signs. The phase difference ϕ observed in the experiment is set equal to the difference between the rotating angles

$$\tau_- - \tau_+ = 2\arctan\left(\frac{\gamma H_y l}{2\pi b_j j_x}\right) \equiv \phi \approx \frac{\pi}{4}. \qquad (4)$$

Assuming a spin polarization of $P = 0.5$ this leads to a ratio $H_y/j_x \approx 0.2$ nm which corresponds to the field strengths stated in the main article.

We performed micromagnetic simulations with simultaneous current- *and* field-excitation. We used the same sample dimensions as in the experiment. The current- and field values were determined as described above. We found that the amplitudes and the phases of the gyrations agree very well with the experiment.

Comparison of Eqn. (3) with Eqn. (1) shows that in the rotated system the vortex is driven with an effective current $\tilde{j}_\mathrm{eff} = \sqrt{\tilde{H}^2+\tilde{j}^2}$. The position at phase zero is determined only by Ω, ω, and Γ, leading to the fit for the damping constant Γ. When rotating the coordinate system back and applying the fitted parameters, we find that for a sample thickness slightly smaller than in the experiment (17.3 nm) and a Gilbert damping of $\alpha = 0.01$ the model leads to a gyration amplitude of $\approx$ 160 nm for an excitation with $P \cdot j = 6 \cdot 10^{10}$A/m. The amplitudes and the phases are almost identical to those observed in the simulation and in the experimental data.

[1] G. Schütz, *et al.*, *Phys. Rev. Lett.* **58**, 737 (1984).
[2] A. Puzic, *et al.*, *J. Appl. Phys.* **97**, 10E704 (2005).
[3] S. Zhang, Z. Li, *Phys. Rev. Lett.* **93**, 127204 (2004).
[4] G. Meier, *et al.*, *Phys. Rev. Lett.* **98**, 187202 (2007).
[5] B. Krüger, *et al.*, *submitted* (2007).
[6] R. L. Compton, P. A. Crowell, *Phys. Rev. Lett.* **97**, 137202 (2006).

Harmonic oscillator model for current- and field-driven magnetic vortices

Benjamin Krüger,[1] André Drews,[2] Markus Bolte,[2] Ulrich Merkt,[2] Daniela Pfannkuche,[1] and Guido Meier[2]
[1] I. Institut für Theoretische Physik, Universität Hamburg, Jungiusstr. 9, 20355 Hamburg, Germany
[2] Institut für Angewandte Physik und Zentrum für Mikrostrukturforschung,
Universität Hamburg, Jungiusstr. 11, 20355 Hamburg, Germany

(Dated: June 27, 2007)

In experiments the distinction between spin-torque and Oersted-field driven magnetization dynamics is still an open problem. Here, the gyroscopic motion of current- and field-driven magnetic vortices in small thin-film elements is investigated by analytical calculations and by numerical simulations. It is found that for small harmonic excitations the vortex core performs an elliptical rotation around its equilibrium position. The global phase of the rotation and the ratio between the semi-axes are determined by the frequency and the amplitude of the Oersted field and the spin torque.

PACS numbers: 75.60.Ch, 72.25.Ba

Recently it has been found that a spin-polarized current flowing through a magnetic sample interacts with the magnetization and exerts a torque on the local magnetization. [1, 2] A promising system for the investigation of the spin-torque effect is a vortex in a micro- or nanostructured magnetic thin-film element. Vortices are formed when the in-plane magnetization curls around a center region. In this few nanometer large center region [3], called the vortex core, the magnetization turns out-of-plane to minimize the exchange energy. [4] It is known that these vortices precess around their equilibrium position when excited by magnetic field pulses [5, 6] and it was predicted that spin-polarized electric currents can do the same. [7] The spacial restriction of the vortex core as well as its periodic motion around its ground state yield an especially accessible system for space- and time-resolved measurements with scanning probe and time-integrative techniques such as soft X-ray microscopy or X-ray photoemission electron microscopy. [5, 6, 8–10] Magnetic vortices also occur in vortex domain walls. The motion of such walls has recently been investigated intensively. [11, 12] Understanding the dynamics of confined vortices can give deeper insight in the mechanism of vortex-wall motion. [13] An in-plane Oersted field accompanying the current flow also influences the motion of the vortex core. For the interpretation of experimental data it is crucial to distinguish between the influence of the spin torque and of the Oersted field. [14]

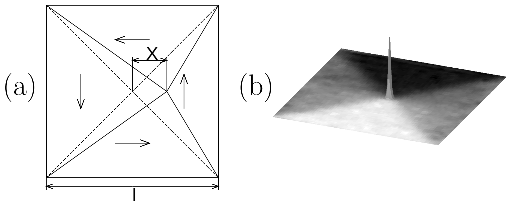

FIG. 1: (a) Scheme of the magnetization in a square magnetic thin-film element with a vortex that is deflected to the right. (b) Magnetization of a vortex in its static ground state. The height denotes the z-component while the gray scale corresponds to the direction of the in-plane magnetization.

In this Letter we investigate the current- and field-driven gyroscopic motion of magnetic vortices in square thin-film elements of size l and thickness t as shown in Fig. 1 and present a method to distinguish between spin torque and Oersted field driven magnetization dynamics. In the presence of a spin-polarized current the time evolution of the magnetization is given by the extended Landau-Lifshitz-Gilbert equation

$$\begin{aligned}\frac{d\vec{M}}{dt} =& -\gamma\vec{M}\times\vec{H}_{\text{eff}} + \frac{\alpha}{M_s}\vec{M}\times\frac{d\vec{M}}{dt}\\ &-\frac{b_j}{M_s^2}\vec{M}\times\left(\vec{M}\times(\vec{j}\cdot\vec{\nabla})\vec{M}\right)\\ &-\xi\frac{b_j}{M_s}\vec{M}\times(\vec{j}\cdot\vec{\nabla})\vec{M}\end{aligned} \qquad (1)$$

with the coupling constant $b_j = P\mu_B/[eM_s(1+\xi^2)]$ between the current and the magnetization where P is the spin polarization, M_S the saturation magnetization, and ξ the degree of non-adiabaticity. [15] If the vortex keeps its static structure, its motion with the velocity $\vec{v}$ can be described using the Thiele equation. [16] This equation was expanded by Nakatani et al. [17] to include the action of a spin-polarized current flowing in the sample,

$$\vec{F} + \vec{G}\times(\vec{v}+b_j\vec{j}) + D(\alpha\vec{v}+\xi b_j\vec{j}) = 0. \qquad (2)$$

Denoting the out-of-plane angle of the magnetization with θ and the angle of the in-plane magnetization with ϕ, the force due to the external and the stray field is

$$\vec{F} = -\mu_0\int dV\,\left[(\vec{\nabla}\theta)\frac{\partial}{\partial\theta} + (\vec{\nabla}\phi)\frac{\partial}{\partial\phi}\right](\vec{H}_{sz}\cdot\vec{M}). \qquad (3)$$

The gyrovector

$$\begin{aligned}\vec{G} &= -\frac{M_s\mu_0}{\gamma}\int dV\ \sin(\theta)(\vec{\nabla}\theta \times \vec{\nabla}\phi) \\ &= -\frac{2\pi M_s\mu_0 tp}{\gamma}\vec{e}_z = G_0\vec{e}_z,\end{aligned} \tag{4}$$

indicates the axis of precession and points out-of-plane. The dissipation tensor is given by

$$D = -\frac{M_s\mu_0}{\gamma}\int dV\ (\vec{\nabla}\theta\vec{\nabla}\theta + \sin^2(\theta)\vec{\nabla}\phi\vec{\nabla}\phi). \tag{5}$$

It is diagonal with

$$D_{xx} = D_{yy} = D_0 \approx -\frac{\pi M_s\mu_0 t\ln(l/a)}{\gamma}, \qquad D_{zz} = 0. \tag{6}$$

The constant a is the lower bound of the integration. It is in the order of magnitude of the radius of the vortex core. [3, 13, 18, 19] A polarization p of $+1$ (-1) denotes that the magnetization in the vortex core is parallel (antiparallel) to the z-axis. The velocity of the vortex core is in-plane and hence perpendicular to the gyrovector. Thus Eq. (2) can be rewritten as

$$\vec{G}\times\vec{F} - G_0^2(\vec{v} + b_j\vec{j}) + D_0\vec{G}\times(\alpha\vec{v} + \xi b_j\vec{j}) = 0. \tag{7}$$

By calculating $\vec{G}\times\vec{v}$ from Eq. (7) and inserting the result in Eq. (2) we can derive the velocity

$$\vec{v} = \frac{\vec{G}\times\vec{F} - D_0\alpha\vec{F} - (G_0^2 + D_0^2\alpha\xi)b_j\vec{j} + b_jD_0\vec{G}\times\vec{j}(\xi-\alpha)}{G_0^2 + D_0^2\alpha^2} \tag{8}$$

of the vortex core. As for any square-symmetric confining potential, the stray-field energy for small deflections can be modeled as a parabolic potential

$$E_s = \frac{1}{2}m\omega_r^2(X^2 + Y^2) \tag{9}$$

with the coordinates X and Y of the vortex core (see Fig. 1a).

In the following a spacially homogeneous current in x-direction is investigated. Due to possible inhomogeneities in real samples the current flow may vary in the out-of-plane direction. This results in an in-plane Oersted field which is perpendicular to the direction of the current flow. In the following this Oersted field is accounted for by a homogeneous magnetic field in y-direction. Both driving forces may depend on time. To estimate the Zeeman energy due to the Oersted field H, the magnetization pattern is divided into four triangles (see Fig. 1a). Assuming that the magnetization is uniform in each of these triangles the total Zeeman energy is given by

$$E_z = \frac{\mu_0 M_s Hltc}{2}\left[\left(\frac{l}{2} + X\right) - \left(\frac{l}{2} - X\right)\right], \tag{10}$$

with the chirality c of the vortex. A chirality of $+1$ (-1) denotes a counterclockwise (clockwise) curling of the magnetization around the vortex core. We will see that this simple approximation describes the field-induced vortex motion sufficiently well. In this case the force is given by

$$\vec{F} = -\vec{\nabla}(E_s + E_z) = -\mu_0 M_s Hltc\vec{e}_x - m\omega_r^2 X\vec{e}_x - m\omega_r^2 Y\vec{e}_y. \tag{11}$$

Inserting Eq. (11) in Eq. (8) yields the equation of motion for the vortex. In the absence of current and field the excited vortex performs an exponentially damped spiral rotation around its equilibrium position with its free frequency

$$\omega = -\frac{pG_0 m\omega_r^2}{G_0^2 + D_0^2\alpha^2} \tag{12}$$

and the damping constant

$$\Gamma = -\frac{D_0\alpha m\omega_r^2}{G_0^2 + D_0^2\alpha^2}. \tag{13}$$

From Eqs. (12) and (13) one easily obtains that

$$D_0\alpha = \frac{\Gamma p G_0}{\omega}. \tag{14}$$

For thin-film systems ($t/l \lesssim 0.1$) the resonance frequency of a vortex is proportional to the inverse lateral dimension $1/l$. [20] Here, we obtain from Eq. (14) that the damping constant Γ also has a characteristic length dependence, $\Gamma \propto \ln(l/a)/l$. Substituting $D_0\alpha$ using Eq. (14) the equation of motion of the vortex can be written as

$$\begin{aligned}\begin{pmatrix}\dot{X}\\ \dot{Y}\end{pmatrix} &= \begin{pmatrix}-\Gamma & -p\omega\\ p\omega & -\Gamma\end{pmatrix}\begin{pmatrix}X\\ Y\end{pmatrix} \\ &+ \begin{pmatrix}\frac{p\omega\Gamma}{\omega^2+\Gamma^2}\frac{\mu_0 M_s Hltc}{G_0} - b_j j - \frac{\Gamma^2}{\omega^2+\Gamma^2}\frac{\xi-\alpha}{\alpha}b_j j\\ -\frac{\omega^2}{\omega^2+\Gamma^2}\frac{\mu_0 M_s Hltc}{G_0} + \frac{p\omega\Gamma}{\omega^2+\Gamma^2}\frac{\xi-\alpha}{\alpha}b_j j\end{pmatrix}.\end{aligned} \tag{15}$$

In the following we assume harmonic excitations, i.e., the magnetic field and the electrical current are of the form $H(t) = H_0 e^{i\Omega t}$ and $j(t) = j_0 e^{i\Omega t}$. The magnetic (Oersted) field and the electrical current are in phase. Assuming that the squared Gilbert damping is small ($\alpha^2 \ll 1$), the damping constant of the vortex is small compared to its frequency ($\Gamma^2 \ll \omega^2$). Then Eq. (15) has the solution

$$\begin{aligned}\begin{pmatrix}X\\ Y\end{pmatrix} &= A\begin{pmatrix}i\\ p\end{pmatrix}e^{-\Gamma t + i\omega t} + B\begin{pmatrix}-i\\ p\end{pmatrix}e^{-\Gamma t - i\omega t} \\ &- \frac{e^{i\Omega t}}{\omega^2 + (i\Omega + \Gamma)^2} \\ &\times \begin{pmatrix}\left(\tilde{H} + \frac{\Gamma}{\omega}\frac{\xi}{\alpha}\tilde{j}\right)\omega + & \left(\frac{\Gamma}{\omega}\tilde{H} + \tilde{j}\right)i\Omega\\ \tilde{j}\omega p & - \left(\tilde{H} + \frac{\Gamma}{\omega}\frac{\xi-\alpha}{\alpha}\tilde{j}\right)i\Omega p\end{pmatrix},\end{aligned} \tag{16}$$

with $\tilde{H} = \gamma H_0 lc/(2\pi)$ and $\tilde{j} = b_j j_0$. The first two terms with prefactors A and B are exponentially damped and

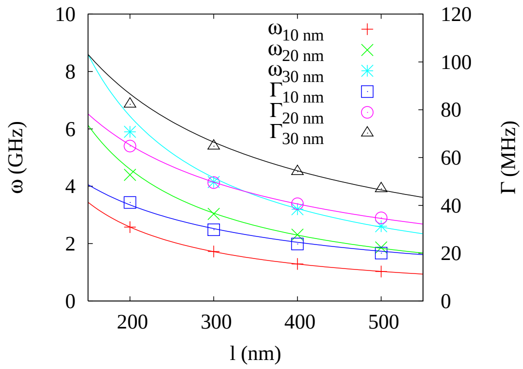

FIG. 2: (Color Online) Dependence of the frequency ω and the damping constant Γ on the length l for various thicknesses t of the system. The symbols denote numerical results while the lines are fits with the analytical results.

depend on the starting configuration. Independent of the source of excitation, i.e., field or current, the sense of rotation of the vortex is given by its polarization, i.e., $p = +1$ ($p = -1$) denotes a counterclockwise (clockwise) rotation of the vortex core. Changing the sign of the chirality has the same effect as turning the magnetic field by 180°. Similar to the motion of magnetic domain walls in thin nanowires [21] the vortex is driven by the current and the magnetic field as well as by their time derivatives.

At resonance the amplitude of the vortex core displacement in x- and y-direction is the same and the vortex performs a circular rotation. A vortex which is excited with a non-resonant frequency has an elliptic trajectory. The ratio between the semi-axes is given by the ratio between the frequency of the excitation and the resonance frequency.

To test the applicability of the approximations leading to the analytical result in Eq. (16) we performed micromagnetic simulations for magnetic thin-film elements with different lengths, thicknesses, polarizations, and chiralities. The material parameters of permalloy are used, i.e., an exchange constant of $A = 13 \cdot 10^{-12}$ J/m and a saturation magnetization of $M_s = 8 \cdot 10^5$ A/m. For the Gilbert damping we use a value of $\alpha = 0.01$ which is in the regime as found by recent experiments. [22–24] The degree of non-adiabaticity ξ is chosen to be equal to α. [11, 25]

For the micromagnetic simulations we extended the implementation of the Landau-Lifshitz-Gilbert equation in the Object Oriented Micro Magnetic Framework (OOMMF) by the additional current-dependent terms of Eq. (1). [21, 26] The simulation cells are 2 nm in x- and y-direction which is well below the exchange length of permalloy. One cell of thickness t was used in z-direction. As in the analytical model we substitute the Oersted field by a homogeneous magnetic field.

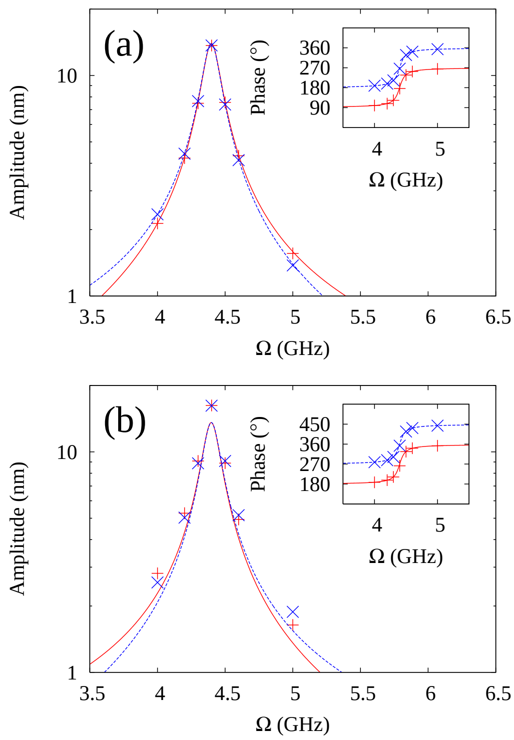

FIG. 3: (Color Online) Amplitude of the (a) current-driven and (b) field-driven vortex oscillation in x-direction (solid red line, pluses) and y-direction (dashed blue line, crosses) for a spin-polarized current density of $jP = 2.5 \cdot 10^{10}$ A/m^2 and a field of $H = 250$ A/m. The insets show the phases between the maximum of the applied current or field and the core displacement in x-direction (solid red line, pluses) and y-direction (dashed blue line, crosses). The symbols denote numerical results while the lines are derived from the analytical expression in Eq. (16).

At first the four ground states with $c \pm 1$ and $p \pm 1$ are calculated for each l and t. The ground states are then excited by a short current pulse. The frequency ω and the damping constant Γ are obtained by fitting the subsequent free oscillation with the first two terms in Eq. (16). Results are presented in Fig. 2 and exhibit a good agreement between the analytical model and the micromagnetic simulations. [27]

For the driven oscillation we choose a magnetic film element with length $l = 200$ nm and thickness $t = 20$ nm. This system size allows for reasonable computing time. The magnetization is excited with harmonic currents with a spin-polarized current density $jP = 2.5 \cdot 10^{10}$ A/m^2 in x-direction. The field excitation was performed with a harmonic field of $H = 250$ A/m

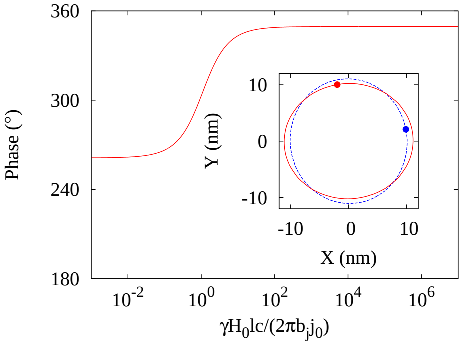

FIG. 4: (Color Online) Analytically calculated phase between the maximum current or magnetic field and the x-deflection of the vortex core for a 200 nm x 200 nm x 20 nm permalloy square excited with a frequency of $\Omega = 4.8$ GHz (above the resonance frequency of $\omega = 4.4$ GHz). The inset shows a section of the sample with the simulated trajectories of the vortex core excited with i) (solid red line) a spin-polarized current density with an amplitude of $jP = 1.2 \cdot 10^{11}$ A/m^2 and ii) (dashed blue line) a magnetic field with an amplitude of $H = 1000$ A/m. Points denote the position of the vortex at maximum current (i) and magnetic field (ii), respectively.

in y-direction. The amplitudes and the phases of the oscillation in x- and y-direction of a vortex with positive polarization and chirality are depicted in Fig. 3. In the current-driven oscillation an excellent accordance between analytical calculations and numerical simulations is found. In the field-driven case the amplitudes of the analytical solution are smaller than the amplitudes obtained from the micromagnetic simulations. These deviations are caused by the differences between the approximate magnetization depicted in Fig. 1 and the exact state. The phases between the maximum of the exciting magnetic field and the maximum deflection in x- and y-direction agree very well. Vortices with other polarization and chirality (not shown) yield the same accordance. [28]

From Eq. (16) one can see that the current and field induced forces on the vortex are of the same form. For experiments it is important to separate the Oersted-field and the spin-torque driven case. We describe the ratio between the field and current-induced forces on the vortex by $\tan\zeta = F_{\mathrm{Oe}}/F_{\mathrm{st}}$, i.e., a mixing angle of $\zeta = 0$ and $\zeta = \pm\pi/2$ denote the fully spin-torque driven and the fully field-driven case, respectively. There are two possibilities to determine the ratio of both forces. On the one hand for non-resonant excitations the trajectory of the vortex core is elliptical as illustrated in Fig. 4. According to Eq. (16) the direction of the major axis of the ellipse is determined by ζ. The amplitude of the vortex motion decreases very fast when the excitation frequency deviates from resonance, i.e., for experimental observation very high current densities with frequencies close to resonance are needed. On the other hand the excitation mechanisms can be distinguished using the phase of the vortex deflection. [14] As indicated by the dots in Fig. 4 the position of the vortex at maximum current depends on ζ, which can be determined from Eq. (16). The latter method is also applicable with excitations at resonance frequency.

In conclusion we derived an analytical expression for the current- and field-driven trajectory of a vortex in thin-film elements. The analytical result is compared to micromagnetic simulations. The accordance between both approaches is very good. The analytical expression enables us to determine the ratio between spin torque and Oersted field driven motion.

Financial support by the Deutsche Forschungsgemeinschaft via SFB 668 "Magnetismus vom Einzelatom zur Nanostruktur" and via Graduiertenkolleg 1286 "Functional metal-semiconductor hybrid systems" is gratefully acknowledged.

[1] L. Berger, Phys. Rev. B **54**, 9353 (1996).
[2] J. Slonczewski, J. Magn. Magn. Mater. **159**, L1 (1996).
[3] A. Wachowiak et al., Science **298**, 577 (2002).
[4] T. Shinjo et al., Science **289**, 930 (2000).
[5] S.-B. Choe et al., Science **304**, 420 (2004).
[6] B. Van Waeyenberge et al., Nature **444**, 461 (2006).
[7] J. Shibata et al., Phys. Rev. B **73**, 020403(R) (2006).
[8] H. Stoll et al., Appl. Phys. Lett. **84**, 3328 (2004).
[9] K. Y. Guslienko et al., Phys. Rev. Lett. **96**, 067205 (2006).
[10] J. Raabe et al., Phys. Rev. Lett. **94**, 217204 (2005).
[11] G. Meier et al., Phys. Rev. Lett. **98**, 187202 (2007).
[12] M. Kläui et al., Phys. Rev. Lett. **94**, 106601 (2005).
[13] J. He et al., Phys. Rev. B **73**, 184408 (2006).
[14] M. Bolte et al., unpublished.
[15] S. Zhang and Z. Li, Phys. Rev. Lett. **93**, 127204 (2004).
[16] A. A. Thiele, J. Appl. Phys. **45**, 377 (1974).
[17] Y. Nakatani et al., Nature Materials **2**, 521 (2003).
[18] D. L. Huber, Phys. Rev. B **26**, 3758 (1982).
[19] K. Y. Guslienko et al., Phys. Rev. B **71**, 144407 (2005).
[20] K. Y. Guslienko et al., J. Appl. Phys **91**, 8037 (2002).
[21] B. Krüger et al., Phys. Rev. B **75**, 054421 (2007).
[22] J. Nibarger et al., Appl. Phys. Lett. **82**, 2112 (2003).
[23] M. Schneider et al., Appl. Phys. Lett. **87**, 072509 (2005).
[24] Z. Liu et al., Phys. Rev. Lett. **98**, 087201 (2007).
[25] M. Hayashi et al., Phys. Rev. Lett. **96**, 197207 (2006).
[26] **OOMMF User's Guide, Version 1.0** M.J. Donahue and D.G. Porter Interagency Report **NISTIR 6376**, National Institute of Standards and Technology, Gaithersburg, MD (Sept 1999) (http://math.nist.gov/oommf/).
[27] Note: a is a fit parameter. The values used are 8.85 nm, 11.66 nm, and 13.59 nm for film thicknesses of 10 nm, 20 nm, and 30 nm, respectively.
[28] During the preparation of this manuscript a publication of Yamada et al. [29] came to our attention that contains first steps towards the inclusion of spin-polarized currents into the dynamics of vortices, however without consideration of the phase and the excentricity of the vortex motion.
[29] K. Yamada et al., Nature Materials **6**, 269 (2007).

Influence of chirality on the dynamics of current- and field-driven magnetic antivortices

André Drews,[1] Benjamin Krüger,[2] Markus Bolte,[1] and Guido Meier[1]
[1]*Institut für Angewandte Physik und Zentrum für Mikrostrukturforschung,*
Universität Hamburg, Jungiusstr. 11, 20355 Hamburg, Germany
[2]*I. Institut für Theoretische Physik, Universität Hamburg, Jungiusstr. 9, 20355 Hamburg, Germany*
(Dated: August 6, 2007)

Antivortices in ferromagnetic thin-film elements are in-plane magnetization configurations with a core pointing perpendicular to the plane. We find, that antivortices gyrate on elliptical orbits when excited by an alternating magnetic field or by a spin current. Their sense of gyration and the phase between high-frequency excitation and gyration are numerically investigated. Simultaneous current- and Oersted field-excitation for chiralities $c = 0$ and $c = 2$ can lead to a maximum enhancement or to an entire suppression of the amplitude of the antivortex core gyration, which is not found in magnetic vortices. This variation of the deflection of the antivortex core can be used to distinguish between spin torque and Oersted-field excitation in experiments.

PACS numbers: 75.60.Ch, 72.25.Ba, 76.50.+g

Magnetic vortices and antivortices exist in ferromagnetic thin-film elements. Due to the interplay of demagnetization and exchange energy the magnetization is forced out-of plane to form a core in the center. The orientation of the core, denoted as the polarization p, is highly interesting for technical applications, e.g., magnetic memory devices, as it can be binary-coded[1–3]. Magnetic vortices have been studied intensively in the last years. It has been shown, that when exciting a vortex by a magnetic field or by spin torque the core precesses[4–6] around its equilibrium position. The stray field exerts a force on the core, which is similar to that of a two-dimensional damped harmonic oscillator[7]. Hitherto the magnetic antivortex has not been studied so intensively. Antivortices appear, e.g., in clover shaped samples or cross-tie walls[8]. As illustrated in Fig. 1 their in-plane magnetization shows a twofold rotational symmetry different to the continuous symmetry of a vortex state. Due to their different in-plane configuration antivortex dynamics differs from vortex dynamics. An understanding of the dynamics of both, antivortex and vortex, is crucial for the description of vortex-antivortex creation and annihilation. These processes have recently received a lot of attention as they are predominant in cross-tie wall motion or vortex core switching[9,10].

Here we investigate the dynamical characteristics of the motion of antivortex cores, i.e., sense, phase, and amplitude of gyration. We then compare the antivortex dynamics to vortex dynamics and develop a notation that describes both. We show that generally the skyrmion number determines the sense of gyration. The chirality of the antivortex plays a role for the phase between exciting field and antivortex core position only for excitation with magnetic fields.

To classify vortices and antivortices the winding number n and the chirality c are defined by the relation[11] $\phi = n\beta + c\frac{\pi}{2}$ between the angle of the local magnetization ϕ and the angle in real space β with respect to the center of the (anti-)vortex core, as shown in Fig. 1. We assume that ϕ and β follow the mathematical sense of rotation. The chirality c corresponds to a constant phase between ϕ and β. Both, vortices with the winding number $n = 1$ and antivortices with the winding number $n = -1$ exhibit chiralities c of real numbers in the intervall $(-2, 2]$. In standard geometries such as discs or squares the vortex state solely possesses the chiralities $c = 1$ and $c = -1$. The chirality of an antivortex can be altered by rotations of the whole sample. Integer chiralities for both topological objects are depicted in Fig. 1. The winding

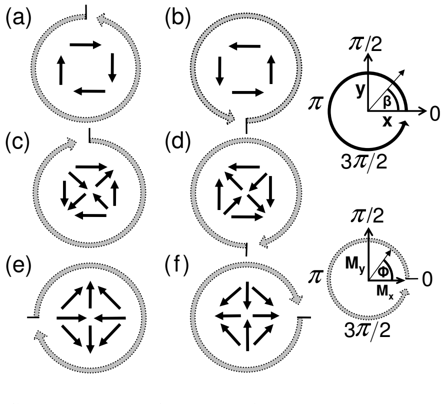

FIG. 1: Magnetic configurations of vortices with the winding number $n = 1$ and the chiralities (a) $c = -1$, (b) $c = 1$ and of antivortices with the winding number $n = -1$ and the integer chiralities (c) $c = 1$, (d) $c = -1$, (e) $c = 2$, and (f) $c = 0$. Black arrows illustrate the local magnetization. The black round arrow shows the angle in real space β. Dotted round arrows demonstrate the angle of the local magnetization as defined by $\phi = n\beta + c\frac{\pi}{2}$, the black line at the dotted round arrows indicates the angle $\phi = 0$.

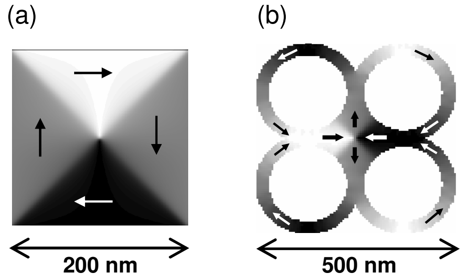

FIG. 2: Size and shape of (a) the vortex and (b) the antivortex sample.

number and the skyrmion number[12] $q = n \cdot p/2$ cannot be transformed by continuous operations such as rotations, hence both are topological charges[13,14]. Here, the skyrmion number is used to describe the sense of gyration of antivortices and vortices.

To simulate magnetic-field induced antivortex dynamics the OOMMF[15] code sped up by Runge-Kutta algorithms was used. The spin-torque effect was implemented using the Landau-Lifshitz-Gilbert equation extended by Zhang and Li[16,17],

$$\begin{aligned}\frac{d\boldsymbol{M}}{dt} =& -\gamma \boldsymbol{M}\times\left(\boldsymbol{H}_{\text{eff}} + \frac{\alpha}{M_S}\boldsymbol{M}\times\boldsymbol{H}_{\text{eff}}\right)\\ &-(1+\alpha\xi)\frac{b_j}{M_s^2}\boldsymbol{M}\times(\boldsymbol{M}\times(\boldsymbol{j}\cdot\nabla)\boldsymbol{M}) \qquad (1)\\ &-(\xi-\alpha)\frac{b_j}{M_s}\boldsymbol{M}\times(\boldsymbol{j}\cdot\nabla)\boldsymbol{M},\end{aligned}$$

where γ is the gyromagnetic ratio, α the Gilbert damping, ξ the ratio between spin flip and exchange relaxation time, and b_j the coupling constant between local current and magnetization. We simulated the excitation of a vortex in a $200 \times 200 \times 20$ nm^3 permalloy square and an antivortex in a $500 \times 500 \times 40$ nm^3 clover-shaped sample, as shown in Fig. 2. An external alternating magnetic field is applied in y-direction of amplitude $H = 70$ mT for the antivortex sample and $H = 50$ mT for the vortex sample. Different thicknesses of $t = 20$ nm and $t = 40$ nm for the vortex and antivortex sample were chosen in order to obtain similar eigenfrequencies for the two geometries. Current excitation of both structures was performed with a spin-polarized alternating current of amplitude $j \cdot P = 1 \cdot 10^{11}$ A/m^2 in x-direction. We assume a saturation magnetization $M_s = 8.6 \cdot 10^5$ A/m, an exchange constant $A = 1.3 \cdot 10^{-11}$ J/m, a Gilbert damping parameter $\alpha = 0.01$, and a ratio between spin flip and exchange relaxation time $\xi = 0.9\alpha$[18,19]. A cell size of $5 \times 5 \times 20$ nm^3 for the vortex and a cell size of $5 \times 5 \times 40$ nm^3 for the antivortex sample was chosen. Thus the lateral cell size is below the exchange length of permalloy of $l_{ex} = \sqrt{2A/\mu_0 M_s^2} \approx 5.3$ nm. The eigenfrequencies of both samples were determined by fitting the solution of a damped harmonic oscillator to the free relaxation of the (anti-)vortex cores yielding a free frequency of $\omega_V/2\pi = 744$ MHz for the vortex and $\omega_{AV}/2\pi = 759$ MHz for the antivortex. Because the frequency of the free oscillation is much larger than the damping ($\omega_f^2 \gg \Gamma^2$), the resonance frequency $\omega_r = \sqrt{\omega_f^2 + \Gamma^2}$ is approximately equal to the free frequency ω_f. To compare the phases of the core dynamics, zero of the time scale $t = 0$ is defined at the maximum of the harmonic excitations. Accordingly current and magnetic field both are cosine functions, i.e. $A(t) = A_0 \cos(\omega t)$. Both samples were excited below, at, and above resonance for all integer chiralities and polarizations. Exemplary results of the simulated current-induced motion of antivortex cores (polarization $p = 1$), and vortex cores (polarization $p = -1$) with the same skyrmion number $q = 1/2$ are presented in Fig. 3. The position of the current-driven vortex core excited quasistatically at $\Omega_0/2\pi = 398$ MHz, at resonance $\Omega_r/2\pi = 744$ MHz, and above resonance $\Omega_\infty/2\pi = 1034$ MHz is displayed in Fig. 3(b), (d), (f). The core moves on elliptical orbits. The semi-major axis of the ellipse at frequency Ω_0 points into y-direction, at resonance Ω_r the trajectory is a circle, and at the frequency Ω_∞ the semi-major axis of the ellipse points into the x-direction. Between the frequencies Ω_0 in Fig. 3(b) and Ω_∞ in Fig. 3(f) the angle of the core's

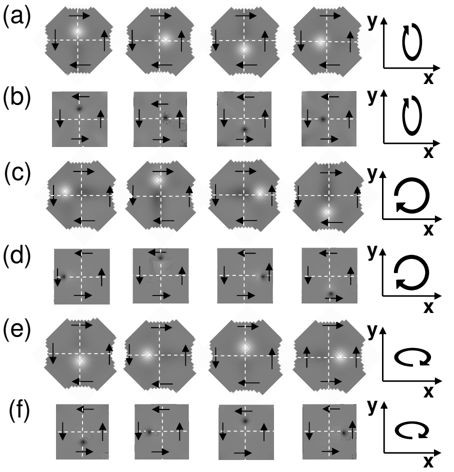

FIG. 3: Spatially resolved simulations of the current-induced (anti-)vortex core dynamics with the skyrmion number $q = -1/2$ and the chirality $c = 1$. The antivortex core and the vortex core were excited in (a) and (b) below resonance in (c) and (d) at resonance, and in (e) and (f) far above resonance. A scheme of the core's trajectory is shown on the right.

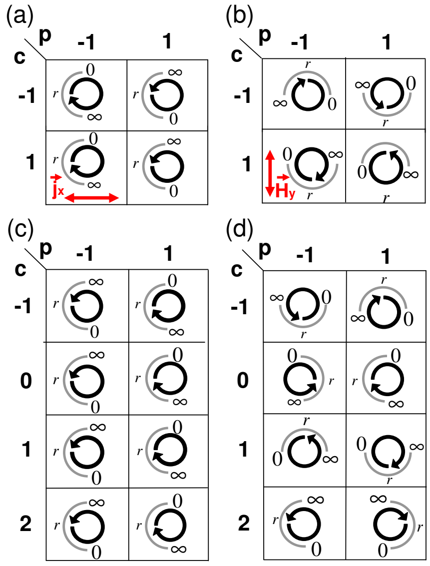

FIG. 4: (Color online) (a) Position of a current- and (b) a field-driven vortex core excited quasistatically Ω_0, at resonance Ω_r, and far above resonance Ω_∞ for all polarizations and integer chiralities at $t = 0$. The magnetic field is applied in y-direction, the spin current in x-direction. (c) Position of a current- and (d) of a field-driven antivortex core. The black arrows illustrate the trajectory of the (anti-)vortex core motion at the resonance frequency Ω_r.

position shifts by π. The antivortex core excited by an electrical current at frequencies $\Omega_0/2\pi = 398$ MHz, $\Omega_r/2\pi = 759$ MHz, and $\Omega_\infty/2\pi = 1034$ MHz in Fig. 3(a), (c), (e) shows the same elliptical trajectory and the same shift of the angle of the core's position between Ω_0 and Ω_∞. Hence, antivortices and vortices possessing equal skyrmion numbers show similar dynamics. For all polarizations and chiralities the senses of gyration and the phases between excitation and the vortex and the antivortex cores have been derived from simulations. The results are summarized in Fig 4. The simulated vortex dynamics shows, that the sense of gyration of the vortex core follows the right-hand rule, i.e., a positive polarization yields a gyration in mathematically positive direction. The gyration of the antivortex follows the left-hand rule, i.e, a positive polarization yields a negative sense of gyration of its core. In general two times the skyrmion number is equal to the mathematical sense of rotation, i.e., $2q = 1$ and $2q = -1$ denote a counterclockwise and clockwise gyration, respectively.

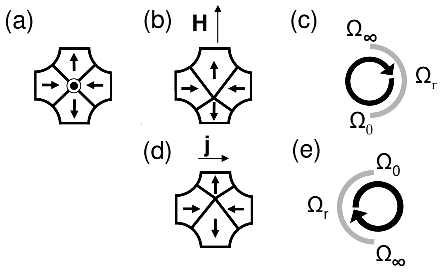

FIG. 5: Phenomenological consideration of the motion of an antivortex core. (a) Scheme of an antivortex with the chirality $c = 2$ and the polarization $p = 1$. (b) Excitation with a magnetic field in y-direction and (d) with a current in x-direction. (c) Frequency-dependent change of the initial phases for magnetic-field excitation and (e) for spin-polarized current excitation.

It is known, that the model of a harmonic oscillator can analytically describe the motion of a vortex core and its phase with respect to the excitation[7]. Antivortices and vortices with the same skyrmion number show the same dynamical behavior, as illustrated in Fig. 3 and Fig. 4. Hence, the harmonic oscillator model can also describe the antivortex dynamics. Considering the susceptibility of a driven harmonic oscillator and the position of the (anti-)vortex cores for the three frequencies Ω_0, Ω_r, and Ω_∞, the phase ζ between the current and the x-deflection of the (anti-)vortex core motion at all frequencies is

$$\zeta(\Omega, \omega_r) = -e^{2qi\left[\arctan\left(\frac{\omega_r^2-\Omega^2}{2\Gamma\Omega}\right)\right]}. \tag{2}$$

From this it follows, that electrical currents excite antivortices of different chiralities with the same phase. When exciting with an alternating magnetic field the phase of the (anti-)vortex dynamics is

$$\zeta(\Omega, \omega_r) = 2qe^{2qi\left[\arctan\left(\frac{\omega_r^2-\Omega^2}{2\Gamma\Omega}\right)\right]+\frac{\pi}{2}ci}. \tag{3}$$

For magnetic-field excitation the phase of the position of the core at time $t = 0$ depends on the chirality. The phase ζ is increased by $\pi/2$ when the chirality is increased by 1.

The dynamics of an antivortex core can be understood phenomenologically. Let us consider an antivortex with the chirality $c = 2$ and the polarization $p = 1$ excited in y-direction by a magnetic field and in x-direction by a current as illustrated in Fig. 5. In case of a quasi-static magnetic-field the domain, which is aligned parallel to the field, grows as shown in Fig. 5(b). The current's adiabatic spin-torque term can be written as an effective magnetic field

$$\boldsymbol{H_j} = \boldsymbol{M} \times \frac{b_j(\boldsymbol{j}\cdot\nabla)\boldsymbol{M}}{M_s^2\gamma} \tag{4}$$

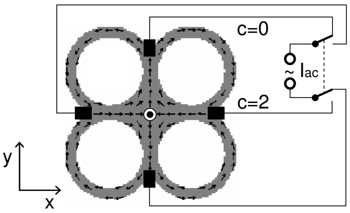

FIG. 6: Proposed experimental setup with electrical contacts to excite an antivortex with the polarization $p = 1$. The chirality depends on the direction of the exciting alternating-current through two contacts in y-direction (chirality $c = 0$) or x-direction (chirality $c = 2$). The chirality can be changed by using the toggle switch. In x-direction a quenched deflection and in y-direction an amplified deflection of the antivortex core is expected.

which leads to

$$\frac{d\boldsymbol{M}}{dt} = -\gamma \boldsymbol{M} \times \boldsymbol{H_j} - \frac{\alpha\gamma}{M_s}[\boldsymbol{M} \times (\boldsymbol{M} \times \boldsymbol{H_j})]. \quad (5)$$

This result resembles the Landau-Lifshitz-Gilbert form of the equation of motion. If the technical current direction is the positive x-direction, the effective field $\boldsymbol{H_j}$ points into the negative y-direction. This leads to a growth of the lower domain as shown in Fig. 5(d).

For the superposition of spin-torque and magnetic-field excitation we get from Eqs. (2) and (3)

$$2qe^{\frac{\pi}{2}ci} = \pm 1. \quad (6)$$

The plus sign holds for destructive and the minus sign for constructive interference. For a given skyrmion number q antivortex states possessing the chiralities $c = -1$ and $c = 1$ exhibit a phase shift of $-\pi/2$ either or $\pi/2$ between current and magnetic-field excitation. Antivortices with the chiralities $c = 0$ and $c = 2$ show a phase shift of 0 or π, i.e., a maximum variation of the amplitude.

From Eqn. (6) we obtain two solutions for destructive interference, namely, $c = 0$, $q = 1/2$ and $c = 2$, $q = -1/2$. If the contribution to the deflection due to the magnetic field and spin current is the same, the amplitude of the gyration of the antivortex core is completely suppressed. We note, that maximum amplitude modulation, i.e. quenching or doubling of the core deflection is not possible with vortices since no stable states for chiralities $c = 0$ and $c = 2$ exist.

In an experiment with combined Oersted fields and spin-polarized currents one can control the amplitude of the antivortex core motion by the direction of the alternating current. For the experimental proof of a quenched excitation we propose the setup illustrated in Fig. 6. Excitation by a spin current in the x-direction or y-direction through electrical contacts corresponds to a chirality of $c = 2$ or $c = 0$. For the positive polarization in Fig. 6 ($q = -1/2$) we expect a quenched motion for a current applied in x-direction. For a current applied in y-direction an amplified deflection is expected. The variation of the amplitude of antivortex cores with the chiralities $c = 0$ and $c = 2$ could also be used to determine the ratio between the forces on the antivortex core that are due to magnetic field and current, respectively.

In conclusion, we have demonstrated by micromagnetic simulations that antivortices can be caused to gyrate on elliptical orbits by a magnetic field or by spin torque. The sense of gyration of antivortices solely depends on the skyrmion number. The phase of antivortex motion excited by an alternating magnetic field depends also on the chirality. Antivortices with chiralities $c = 0$ and $c = 2$ that are excited simultaneously by spin torque and magnetic Oerstedt field show constructive and destructive superposition of the respective deflections. This can be used to experimentally investigate the influence of Oersted fields in current-induced antivortex dynamics.

Acknowledgments

We thank Ulrich Merkt and Daniela Pfannkuche for valuable discussions and encouragement. Financial support by the Deutsche Forschungsgemeinschaft via the Graduiertenkolleg 1286 "Functional metal-semiconductor hybrid systems" and via Sonderforschungsbereich 668 "Magnetismus vom Einzelatom zur Nanostruktur" as well as Sonderforschungsbereich 508 "Quantenmaterialien" is gratefully acknowledged.

---

[1] Y. Liu, S. Gliga, R. Hertel, and C. M. Schneider, cond. mat. **0702048** (2007).

[2] K. S. Buchanan, K. Y. Guslienko, S. B. Choe, A. Doran, A. Scholl, S. D. Bader, and V. Novosad, J. Appl. Phys. **97**, 10H503 (2005).

[3] K. Y. Guslienko and V. Novosad, J. Appl. Phys. **96**, 4451 (2004).

[4] B. Van Waeyenberge, A. Puzic, H. Stoll, K. W. Chou, T. Tylisczak, R. Hertel, M. Fähnle, H. Brückl, K. Rott, G. Reiss, et al., Nature **444**, 461 (2006).

[5] S. B. Choe, Y. Acremann, A. Scholl, A. Bauer, A. Doran, J. Stöhr, and H. A. Padmore, Science **304**, 420 (2004).

[6] J. Shibata, Y. Nakatani, G. Tatara, H. Kohno, and Y. Otani, Phys. Rev. B **73**, 020403R (2006).

[7] B. Krüger, A. Drews, M. Bolte, U. Merkt, D. Pfannkuche, and G. Meier, submitted (2007).

[8] K. Shigeto, T. Okuno, K. Mibu, T. Shinjo, and T. Ono, Appl. Phys. Lett. **80**, 4190 (2002).

[9] R. Hertel and C. M. Schneider, Phys. Rev. Lett. **97**, 1772021 (2006).

[10] A. Neudert, J. McCord, R. Schäfer, and L. Schultz, Phys. Rev. B. **75**, 1724041 (2007).

[11] J. He, Z. Li, and S. Zhang, Phys. Rev. B **73**, 184408 (2006).

[12] O. A. Tretiakov and O. Tschernyshyov, Phys. Rev. B **75**, 012408 (2007).

[13] A. Abanov and V. L. Pokrovsky, Phys. Rev. B **58**, R8889 (1998).

[14] V. L. Golo and A. M. Perelomov, Mathematical Physics **2**, 477 (1978).

[15] **OOMMF User's Guide, Version 1.0** M.J. Donahue and D.G. Porter Interagency Report **NISTIR 6376**, National Institute of Standards and Technology, Gaithersburg, MD (Sept 1999) (http://math.nist.gov/oommf/).

[16] S. Zhang and Z. Li, Phys. Rev. Lett. **93**, 127204 (2004).

[17] B. Krüger, D. Pfannkuche, M. Bolte, G. Meier, and U. Merkt, Phys. Rev. B. **75**, 054421 (2007).

[18] G. Meier, M. Bolte, R. Eiselt, B. Krüger, D. H. Kim, and P. Fischer, Phys. Rev. Lett **98**, 187202 (2007).

[19] M. Hayashi, L. Thomas, Y. B. Bazaliy, C. Rettner, R. Moriya, X. Jiang, and S. S. P. Parkin, Phys. Rev. Lett. **96**, 197207 (2006).

5 Conclusion and Outlook

The magnetization dynamics of micro- and nanometer-sized ferromagnetic elements has been investigated by micromagnetic simulations, magnetoresistance measurements, and X-ray microscopy. Summarizing the results described in Chapter 4, I combined micromagnetic simulations, magnetic-force microscopy, and X-ray microscopy to study the stray-field interaction in arrays of Fe nanostructures. I found that for distances less than 800 nm the elements interact strongly leading to an enlarged saturation magnetization and coercive field (see **[P10]**).

By simulating the response of micrometer-sized permalloy elements to magnetic field pulses the spin-wave eigenmodes were investigated and compared to theoretical approximations (see **[P9]** and **[P13]**). A strong dependence of the eigenmodes on the spatial symmetry of the exciting pulse and the static magnetization was observed, and the modes could be unambiguously identified with backward-volume and Damon–Eshbach modes. In another study thin permalloy rectangles were periodically excited by field pulses at a frequency close to the one of a higher harmonic of the main magnetic eigenmode. This led to a resonant amplification of the motion of the domain wall into an excited magnetization state (see **[P7]**).

In an investigation of the local anisotropic magnetoresistance in permalloy microstructures (**[P8]**), we used a combination of micromagnetic simulations, diffusive transport calculations, magnetic-force microscopy, and AMR measurements to associate AMR signals to transitions between magnetization configurations. We found that the actual local current distribution with respect to the magnetization can greatly alter the measured AMR signals. We therefore used the spatial resolution of X-ray microscopy to discriminate between different domain-wall types in permalloy wires. The measurements were performed simultaneously, so that changes in the AMR were successfully attributed to magnetization patterns observed by X-ray microscopy.

For my studies of the influence of spin-polarized currents on the magnetization dynamics of permalloy structures I built upon the above investigations. First I contributed to the extension of a micromagnetic simulation tool to include the adiabatic and the nonadiabatic spin-transfer torque terms. The tool was then used to simulate the ac-driven oscillation of a domain wall in a curved nanowire. An analytical model was developed that describes the domain-wall dynamics by a harmonic oscillator (see **[P12]** and **[P14]**). This model was successfully applied also to magnetic vortices and antivortices (see **[P17-P19]**, and **[P20]**). With quasi-static X-ray microscopy a randomness in the domain-wall motion in permalloy wires was observed (**[P16]**), and with time-resolved X-ray microscopy the dynamic phase relation between spin-polarized ac-currents and magnetic vortex gyration could be pinpointed (**[P18]**). From this we could determine the strength of a traversing current's Oersted field. Figure 5.1 shows the methods used for the studies on the respective topics.

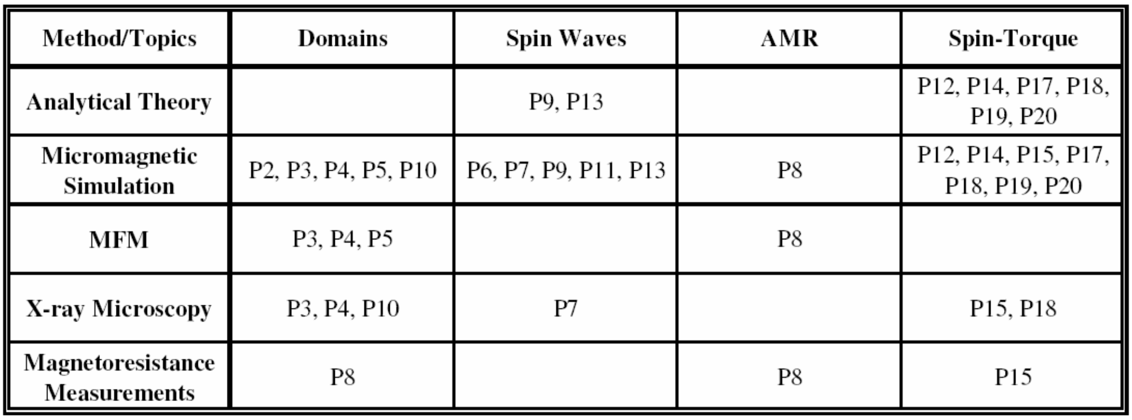

Method/Topics	Domains	Spin Waves	AMR	Spin-Torque
Analytical Theory		P9, P13		P12, P14, P17, P18, P19, P20
Micromagnetic Simulation	P2, P3, P4, P5, P10	P6, P7, P9, P11, P13	P8	P12, P14, P15, P17, P18, P19, P20
MFM	P3, P4, P5		P8	
X-ray Microscopy	P3, P4, P10	P7		P15, P18
Magnetoresistance Measurements	P8		P8	P15

Fig. 5.1: Table showing what methods were used to obtain results on the different topics in the respective journal articles.

Even though much has been learned in the course of this thesis, much more remains to be explored. Many questions still elude an answer, for example:

- How does current-induced domain-wall motion depend on the dynamics of the spin-polarized current, i.e., the rise time of a current pulse or the frequency of an ac current with respect to the domain-wall eigenfrequencies?
- What really is the value for the non-adiabaticity parameter?
- Do the same exponential laws govern stochastic spin-torque driven domain-wall motion as in the case of field-driven motion? What are the underlying mechanisms and what role does the temperature play?

To answer these and other questions, scientists will undoubtedly turn to micromagnetic simulations and time-resolved imaging techniques, as sensitive, time-resolved magnetoresistance measurements have become increasingly popular to investigate the dynamics of ever-smaller magnetic systems [115, 186].

6 List of Original Publications

Journal Articles

P1 M. Bolte, *"Simulation of Multi-Track Bit Detection with Channel Diversity through Detector Partitioning (using the Viterbi-Algorithm)",* Philips NatLab, Technical Note 2002/419.

P2 M. Bolte, D. P. F. Möller, and G. Meier, *"Simulation of Micromagnetic Phenomena",* Proceedings of the *18th European Simulation Multiconference* (ESM 2004), 407-412, SCS Publishing House, Ghent.

P3 G. Meier, R. Eiselt, M. Bolte, M. Barthelmeß, T. Eimüller, and P. Fischer, *"Comparative study of magnetization reversal in isolated and strayfield coupled microcontacts",* Appl. Phys. Lett. **85**, 1193-1195 (2004).

P4 M. Bolte, R. Eiselt, T. Eimüller, P. Fischer, and G. Meier, *"Micromagnetic simulation as a bridge between magnetic-force and magnetic-transmission x-ray microscopy",* J. Magn. Magn. Mat. **290-291**, 723-726 (2005).

P5 C. Pels, M. Barthelmeß, M. Bolte, A. Thieme, and G. Meier, *"Thickness and magnetic-field dependence of domain switching in isolated and interacting permalloy contacts",* J. Magn. Magn. Mat. **293**, 885-891 (2005).

P6 M. Bolte, G. Meier, and D. P. F. Möller, *"Understanding and predicting the electronic and dynamic behavior of nanoscale magnetic random access memory (MRAM) cells using micromagnetic modelling and simulation",* Proceedings of the *19th European Conference on Modelling and Simulation 2005* (ECMS 2005), 574-579, SCS Publishing House, Ghent.

P7 A. Krasyuk, F. Wegelin, S. A. Nepijko, H. J. Elmers, G. Schönhense, M. Bolte, and C. M. Schneider, *"Self-trapping of Magnetic Oscillation Modes in Landau Flux-Closure Structures",* Phys. Rev. Lett. **95**, 207201-1 - 207201-4 (2005). Also selected for the Virtual Journal of Nanoscale Science and Technology.

P8 M. Bolte, M. Steiner, C. Pels, M. Barthelmess, J. Kruse, U. Merkt, G. Meier, M. Holz, and D. Pfannkuche, *"Magnetotransport through domain patterns in permalloy rectangles",* Phys. Rev. B **72**, 224436-1 - 224436-8 (2005).

P9 M. Bolte, G. Meier, and C. Bayer, *"Spin-Wave Eigenmodes of Landau-Domain Patterns",* Phys. Rev. B **73**, 052406-1 - 052406-4 (2006). Also selected for the Virtual Journal of Nanoscale Science and Technology.

P10 M. Bolte, R. Eiselt, G. Meier, D.-H. Kim, and P. Fischer, *"Real space observation of dipolar interaction in arrays of Fe microelements",* J. Appl. Phys. **99**, 08H301-1 - 08H301-3 (2006).

P11 M. Bolte, G. Meier, M. Najafi, and D. P. F. Möller, *"Computation of Spin-Wave Spectra of Magnetic Nanostructures for Information Storage Systems",* Proceedings of the *20th European Conference on Modelling and Simulation* (ECMS) 2006, SE-136-1 - 136-6 (2006).

P12 B. Krüger, D. Pfannkuche, M. Bolte, G. Meier, and U. Merkt, *"Current-Driven Domain-Wall Dynamics in Curved Ferromagnetic Nanowires",* Phys. Rev. B **75**, 054421-1 - 054421-9 (2007). Also selected for the Virtual Journal of Nanoscale Science and Technology.

P13 M. Bolte, G. Meier, and C. Bayer, *"Symmetry dependence of spin-wave eigenmodes in Landau-domain patterns",* J. Magn. Magn. Mat. **316**, e526-e528 (2007).

P14 G. Meier, M. Bolte, U. Merkt, B. Krüger, and D. Pfannkuche, *"Current-induced domain-wall motion in permalloy semi rings",* J. Magn. Magn. Mat. **316**, e966-e968 (2007).

P15 G. Meier, M. Bolte, R. Eiselt, B. Krüger, D.-H. Kim, and P. Fischer, *"Direct Imaging of Current-Driven Stochastic Domain-Wall Motion and Deformation",* Phys. Rev. Lett., **98**, 187202-1 - 187202-4 (2007). Also selected for the Virtual Journal of Nanoscale Science and Technology and the Physical Review Focus Vol. **19**, story 14.

P16 M.-A. B. W. Bolte, G. Meier, M. Najafi, and D. P. F. Möller, *"Simulating Magnetic Storage Elements: Implementation of the Micromagnetic Model into MATLAB - Case Study for Standardizing Simulation Environments",* Proceedings of the SCS Simulation Summer Conference, San Diego, **SCS70** (2007).

P17 B. Krüger, A. Drews, M. Bolte, G. Meier, U. Merkt, and D. Pfannkuche, *"Harmonic Oscillator Model for current- and field-driven magnetic vortices"*, Phys. Rev. B accepted (2007).

P18 M. Bolte, G. Meier, R. Eiselt, L. Bocklage, A. Drews, B. Krüuger, T. Tyliszczak, B. Van Waeyenberge, K. W. Chou, G. Schütz, and H. Stoll, *"Direct Observation of Spin-Torque- and Oersted Field-Induced Magnetic Vortex Gyration with X-ray Microscopy",* submitted (2007).

P19 A. Drews, B. Krüger, M. Bolte, G. Meier, and U. Merkt, *"Influence of Chirality on Current- and Field-driven Dynamics of magnetic anti-vortices",* submitted (2007).

P20 B. Krüger, A. Drews, G. Meier, M. Bolte, D. Pfannkuche, and U. Merkt, *"Vortices and Antivortices as Harmonic Oscillators"*, J. Appl. Phys. accepted (2007).

Conference Contributions

C1 M. Bolte, *"Measurement and Simulation of Domains in Permalloy Microstructures"*, DPG spring conference, Regensburg, 9th March, 2004.

C2 P. Fischer, T. Eimüller, R. Eiselt, M. Bolte, and G. Meier, *"Comparative Study of magnetization reversal in stray-field coupled microcontacts"*, Joint European Magnetic Symposia (JEMS04), Dresden, Germany, 5th - 10th September, 2004.

C3 P. Fischer, T. Eimüller, M. Bolte, R. Eiselt, and G. Meier, *"Magnetization switching behaviour in stray-field coupled ferromagnetic microcontacts (HC-05)"*, 49th Annual MMM Conference, Jacksonville FL, USA, 7th - 11th November, 2004.

C4 M. Bolte, *"MTXM and MFM on stray-field coupled microelements"*, Poster contribution to the Dreikönigstreffen, Bad Honnef, 5th January, 2005.

C5 M. Bolte, M. Steiner, M. Holz, U. Merkt, and G. Meier, *"Local anisotropic magnetoresistance - simulation and measurements"*, Oral presentation at the DPG spring conference, Berlin, 5th March, 2005.

C6 M. Bolte and G. Meier, *"Symmetry of Collective Spin-Wave Eigenmodes in Landau Domain Structures"*, Poster contribution to the XRMS-Workshop, Swiss Light Source, Villigen, Switzerland, 12th November, 2005.

C7 M. Bolte, *"Spin-Wave Eigenmodes in Landau-Domain Patterns"*, DPG-Spring conference, Dresden, 30th March, 2006.

C8 C. M. Schneider, M. Bolte, A. Krasyuk, A. Oelsner, S. A. Nepijko, H.-J. Elmers, G. Schönhense, *"A View on Fast Magnetization Dynamics: Studies by XPEEM"*, Deutsche Tagung für Forschung mit Synchrotronstrahlung, Neutronen und Ionenstrahlen an Großgeräten 2006 (SNI 2006), 4th - 6th October, 2006.

C9 G. Meier, M. Bolte, R. Eiselt, U. Merkt, D.-H. Kim, and P. Fischer, *"Real space observation of dipolar interaction in arrays of iron and permalloy elements"*, Deutsche Tagung für Forschung mit Synchrotronstrahlung, Neutronen und Ionenstrahlen an Großgeräten 2006 (SNI 2006), 4th - 6th October, 2006.

C10 P. Fischer, D.-H. Kim, B.L. Mesler, R. Eiselt, M. Bolte, G. Meier, and E. H. Anderson, *"Imaging ultrafast spin dynamics with magnetic soft X-ray microscopy"*, Advanced Light Source Users Meeting, Berkeley CA 9th - 11th October, 2006.

C11 M. Bolte, H. Ziehlke, A. Drews, R. Eiselt, G. Meier, D.-H. Kim, B. L. Mesler, P. Fischer, B. Van Waeyenberge, A. Puzic, K. W. Chou, and H. Stoll, *"Current-induced magnetic vortex oscillations observed by time-resolved X-ray microscopy"*, 378th Wilhelm and Else Heraeus-Seminar in Bad Honnef (22nd -26th October, 2006) *"Spin-Torque in Magnetic Nanostructures"*. Best Poster Award.

C12 B. Krüger, D. Pfannkuche, M. Bolte, G. Meier, and U. Merkt, *"Current-Driven Domain wall dynamics in curved nanowires"*, 378th Wilhelm and Else Heraeus-Seminar in Bad Honnef (22nd -26th October, 2006) *"Spin-Torque in Magnetic Nanostructures"*.

C13 G. Meier, M. Bolte, R. Eiselt, U. Merkt, B. Krüger, D. Pfannkuche, D.-H. Kim, and P. Fischer, *"Vortex-domain wall motion and deformation by ns-current pulses observed by magnetic transmission x-ray microscopy"*, 378th Wilhelm and Else Heraeus-Seminar in Bad Honnef (22.-26.10.2006) *"Spin-Torque in Magnetic Nanostructures"*.

C14 M. Bolte, A. Drews, R. Eiselt, G. Meier, B. Krüger, D.-H. Kim, P. Fischer, B. Van Waeyenberge, A. Puzic, K. W. Chou, and H. Stoll, *"Soft X-Ray Microscopy of Current-induced Magnetic Vortex Oscillations and Domain-Wall Motion"*, 381st Wilhelm- and Else-Heraeus-Seminar, Bad Honnef, Germany, 3rd - 5th January, 2007.

C15 M. Bolte, R. Eiselt, H. Ziehlke, U. Merkt, G. Meier, D. Kim, and P. Fischer, *"X-ray Microscopy of Local Anisotropic Magnetoresistance (BD-01)"*, 10th Joint MMM/Intermag Conference, Baltimore, MD, USA, 7rd - 12th January, 2007.

C16 G. Meier, M. Bolte, R. Eiselt, U. Merkt, B. Krüger, D. Pfannkuche, D. Kim, and P. Fischer, *"Imaging nsec current-induced vortex-domain wall motion and deformation with magnetic soft x-ray microscopy (ED-01)"*, 10^{th} Joint MMM/Intermag Conference, Baltimore, MD, USA, 7^{rd} - 12^{th} January, 2007.

C17 M. Bolte, H. Ziehlke, R. Eiselt, G. Meier, D. Kim, and P. J. Fischer, *"Angular Dependence of the Magnetostatic Interaction in Arrays of Magnetic Nanostructures (GC-08)"*, 10^{th} Joint MMM/Intermag Conference, Baltimore, MD, USA, 7^{rd} - 12^{th} January, 2007.

C18 A. Drews, M. Bolte, B. Krüger, G. Meier, U. Merkt, B. Van Waeyenberge, A. Puzic, K. W. Chou, and H. Stoll, *"Current-induced magnetic vortex dynamics: micromagnetic simulations and time-resolved x-ray microscopy"*, DPG-Spring conference, Regensburg 28^{th} March, 2007.

C19 Benjamin Krüger, Daniela Pfannkuche, Markus Bolte, Guido Meier, and Ulrich Merkt, *"Current-driven domain walls in nanowires"*, DPG-Spring conference, Regensburg 28^{th} March, 2007.

C20 G. Meier, M. Bolte, R. Eiselt, U. Merkt, B. Krüger, D. Pfannkuche, D.-H. Kim, and P. Fischer, *"X-ray imaging of current driven stochastic domain-wall motion"*, DPG-Spring conference, Regensburg 28^{th} March, 2007.

C21 A. Drews, M. Bolte, B. Krüger, and G. Meier, *"Dynamics of ferromagnetic vortices and antivortices"*, International Summer School "Physics of Functional Micro- and Nanostructures" of the Research Training Group (Graduiertenkolleg) 1286, Poster Contribution, 20^{th}-$21st$ September, 2007.

C22 M. Najafi, B. Güde, M. Bolte, G. Meier, D. P. F. Möller, *"Efficient Algorithms for Micromagnetic Simulations"*, International Summer School "Physics of Functional Micro- and Nanostructures" of the Research Training Group (Graduiertenkolleg) 1286, Poster Contribution, 20^{th}-$21st$ September, 2007.

C23 A. Drews, M. Bolte, B. Krüger, and G. Meier, *"Chirality-dependent dynamics of current- and field-driven magnetic antivortices"*, 52^{nd} Magnetism and Magnetic Materials Conference, Tampa, FL, USA, 3^{rd} November, 2007.

C24 M. Bolte, R. Eiselt, L. Bocklage, A. Drews, G. Meier, B. Krüger, T. Tylisczak, B. Van Wayenberge, K. W. Chou, H. Stoll, and G. Schütz, *"Phase-sensitive and Time-resolved X-ray Microscopy for the Detection of Oersted fields in Spin-Torque*

Driven Magnetic Vortex Gyration", 52nd Magnetism and Magnetic Materials Conference, Tampa, FL, USA, 3rd November, 2007.

C25 B. Krüger, A. Drews, G. Meier, M. Bolte, D. Pfannkuche, and U. Merkt, *"Vortices and Antivortices as Harmonic Oscillators"*, 52nd Magnetism and Magnetic Materials Conference, Tampa, FL, USA, 3rd November, 2007.

Invited Talks

I1 M. Bolte, *"Measurement and Simulation of Micromagnetic Phenomena"*, Physics of Nanostructures Group (Prof. Dr. B. Koopmans), Technical University Eindhoven, The Netherlands, 31st March, 2005.

I2 M. Bolte, *"Measurement and Simulation of Nanomagnets for Ultrafast Data Storage"*, Center for Nanoscience (Prof. Dr. J. Kotthaus), Ludwig-Maximilians-Universität, Munich, Germany, 13th June, 2005.

I3 M. Bolte, *"Micromagnetic Simulation of Spin-Wave Eigenmodes in Landau-Domain Structures"*, Institute of Physics (Prof. Dr. G. Schönhense), Johannes Gutenberg Universität, Mainz, Germany, 29th November, 2005.

I4 M. Bolte, *"Micromagnetic Simulation of Spin-Wave Eigenmodes in Landau-Domain Structures"*, Magnetism Group (Prof. Dr. B. Hillebrands), Technische Universität Kaiserslautern, Kaiserslautern, Germany, 30th November, 2005.

I5 M. Bolte, *"Micromagnetic Simulation of Spin-Wave Eigenmodes in Magnetic Micro- and Nanostructures"*, ALS User Meeting, Berkeley, CA, USA, 12th April 2006.

I6 M. Bolte, *"Micromagnetic Simulation of Magnetization Dynamics and Current-Magnetization Interactions"*, SpinAps Center of Dr. Stuart Parkin, IBM Research Center Almaden, San Jose, CA, USA, 18th September, 2006.

I7 M. Bolte, *"Computersimulation in der Festkörperphysik - Am Beispiel neuer, ultraschneller magnetischer Speichermedien"*, ceremony in celebration of the donation of a server cluster by pro-com DATENSYSTEME GmbH to the PHYSnet of the University of Hamburg, 14th November, 2006.

I8 P. Fischer, B. Mesler, D.-H. Kim, M.-Y. Im, M. Bolte, R. Eiselt, G. Meier, and E.H. Anderson, *Magnetic soft X-ray microscopy – imaging spin structures and their dynamics on the nanoscale*, 1st International Symposium on Advanced Magnetic Materials and Applications (ISAMMA), Jeju island, Korea, 28th May - 1st June 2007

I9 M. Bolte, *"X-ray Microscopy and Magnetization Dynamics of Nanomagnets"*, SpinAps Center of Dr. Stuart Parkin, IBM Research Center Almaden, San Jose, CA, USA, 5th September, 2007.

I10 M. Bolte, *"Micromagnetic Simulations and X-ray imaging of ferromagnetic nanostructures"*, Research Group of Prof. Dr. James Harris, Department of Electrical Engineering, Stanford University, Stanford, CA, USA, 10th September, 2007.

I11 M. Bolte, *"Micromagnetic Modeling and Simulation"*, International Summer School "Physics of Functional Micro- and Nanostructures" of the Research Training Group (Graduiertenkolleg) 1286, Course 6, 27th September 2007.

I12 G. Meier, M. Bolte, R. Eiselt, B. Krüger, D.-H. Kim, and P. Fischer, *"X-ray imaging of current driven stochastic domain-wall motion"*, invited talk during the 52nd Magnetism and Magnetic Materials Conference, Tampa, FL, USA, 3rd November 2007.

Bibliography

[1] K. Binder, *Physik Journal* **3** (2004).

[2] W. Hillebrandt, E. Müller, *Physik Journal* **3** (2004).

[3] C. Lavalle, M. Rigol, A. Muramatsu, *Physik Journal* **3** (2004).

[4] T. Lippert, K. Schilling, *Physik Journal* **3** (2004).

[5] J. Ingham, I. J. Dunn, E. Heinzle, *Chemical Engineering Dynamics. An Introduction to Modelling and Computer Simulation* (Wiley-VCH, 2007).

[6] D. P. F. Möller, *European Simulation Multiconference 2000, SCSI Publ., Ghent, Belgium* (2000).

[7] W. Yang, ed., *IUTAM Symposium on Mechanics and Reliability of Actuating Materials* (Springer Netherlands, 2006).

[8] L. W. Nagel, D. O. Pederson, *University of California, Berkeley* (1973).

[9] J. F. Gantz, *et al.*, A forecast of worldwide information growth through 2010 - IDC White Paper, *Tech. rep.*, EMC (2007).

[10] Hitachi Global Storage, Deskstar7k1000 documentation, *Tech. rep.*, http://hitachigst.com (2007).

[11] Hitachi Global Storage, Go perpendicular, *Tech. rep.*, http://hitachigst.com (2007).

[12] R. L. White, R. M. H. Newt, R. F. W. Pease, *IEEE Trans. Magn.* **33**, 990 (1997).

[13] H. J. Richter, *et al.*, *Appl. Phys. Lett.* **88** (2006).

[14] A. P. Malozemoff, J. C. Slonczewski, *Magnetic Domain Walls in Bubble Material* (Academic Press, New York, 1979).

[15] A. H. Eschenfelder, ed., *Magnetic Bubble Technology* (Springer Verlag GmbH, 1981).

[16] M. Durlam, *et al.*, *IEDM Technical Digest* **34**, 6 (2003).

[17] Y. Saito, H. Sugiyama, *US Patent Application* **US 2005/0282379A1**, Dec 22 (2005).

[18] S. S. P. Parkin, *US Patent* **309**, 6,834,005 (2004).

[19] D. Meyners, K. Rott, H. Brückl, G. Reiss, J. Wecker, *J. Appl. Phys.* **99** (2006).

[20] A. Ney, C. Pampuch, R. Koch, K. H. Ploog, *Nature* **425** (2003).

[21] D. A. Allwood, *et al.*, *Science* **309**, 1688 (2005).

[22] L. Berger, *Phys. Rev. B* **54**, 9353 (1996).

[23] J. Slonczewski, *J. Magn. Magn. Mater.* **159**, L1 (1996).

[24] L. Berger, *J. Appl. Phys.* **55**, 1954 (1984).

[25] P. P. Freitas, L. Berger, *J. Appl. Phys.* **57**, 1266 (1985).

[26] G. Tatara, H. Kohno, *Phys. Rev. Lett.* **92**, 086601 (2004).

[27] S. Zhang, Z. Li, *Phys. Rev. B* **70**, 024417 (2004).

[28] S. Zhang, Z. Li, *Phys. Rev. Lett.* **93**, 127204 (2004).

[29] B. Krüger, D. Pfannkuche, M. Bolte, G. Meier, U. Merkt, *Phys. Rev. B* **75**, 054421 (2007).

[30] A. Yamaguchi, *et al.*, *Phys. Rev. Lett.* **92**, 077205 (2004).

[31] M. Kläui, *et al.*, *Phys. Rev. Lett.* **94**, 106601 (2005).

[32] A. Thiaville, Y. Nakatani, J. Miltat, Y. Suzuki, *Europhys. Lett.* **69 (6)**, 990 (2005).

[33] B. Hillebrands, K. Ounadjela, eds., *Spin Dynamics in Confined Systems I* (Springer Verlag, Berlin, Germany, 2004).

[34] Shen Kuo, *Dream Pool Assays* (China, 1086).

[35] P. C. Scholten, *Journ. Magn. Magn. Mat.* **149**, 57 (1995).

[36] A. Hubert, R. Schäfer, *Magnetic Domains: The Analysis of Magnetic Microstructures* (Springer, Berlin, Germany, 1998).

[37] C. Kittel, *Introduction to Solid State Physics, 5^{th} edition* (John Wiley and Sons, Inc., New York, 1976).

[38] J. Bardeen, L. N. Cooper, J. R. Schriefer, *Phys. Rev.* **108**, 1175 (1957).

[39] S. Chikazumi, *Physics of Ferromagnetism* (Oxford University Press, 1997).

[40] P. Weiss, *J. Phys.* **6**, 661 (1907).

[41] S. Goennenwein, M. Opel, *Vorlesungsskript zur Vorlesung Magnetismus (PH-E23-6) at the TU München* (Walther-Meissner-Institut, Garching, 2005).

[42] L. Landau, E. Lifshitz, *Physik. Z. Sowjetunion* **8**, 153 (1935).

[43] T. L. Gilbert, *Phys. Rev.* **100**, 1243 (1955).

[44] L. Néel, *C. R. Acad. Sci.* **241**, 533 (1955).

[45] F. Bloch, *Z. Phys.* **74**, 295 (1932).

[46] W. F. Brown jr., *Micromagnetics* (Interscience Publishers, New York, 1963).

[47] A. Aharoni, *Introduction to the Theory of Ferromagnetism* (Clarendon, Oxford, 1996).

[48] H. Kronmüller, M. Fähnle, *Micromagnetism and the Microstructure of Ferromagnetic Solids* (Cambridge University Press, Oxford, UK, 2003).

[49] J. D. Jackson, *Classical Electrodynamics* (John Wiley, New York, 1975).

[50] A. J. Newell, W. Williams, D. J. Dunlop, *J. Geophys. Res.* **98**, 9551 (1993).

[51] M. Najafi, Simulation der Austausch- und Streufeldwechselwirkung sowie der Magnetisierungsdynamik von Mikro- und Nanomagneten im Mikromagnetischen Model durch Matlab, Master's thesis, University of Hamburg, Germany (2007).

[52] V. Korenman, R. E. Prange, *Phys. Rev. B* **6**, 2769 (1972).

[53] B. Koopmans, J. J. M. Ruigrok, F. D. Longa, W. J. M. de Jonge, *Phys. Rev. Lett.* **95**, 267207 (2005).

[54] T. Silva, J. Nibarger, B. Rippard, B. Stamps, *APS Meeting Abstracts* p. 23011 (2004).

[55] M. Barthelmeß, Magnetic-force Microscopy and Micromagnetic Simulations on Domains of Nanostructured Ferromagnets, Ph.D. thesis, University of Hamburg, Germany (2004).

[56] S. Middelhoek, *J. Appl. Phys.* **34**, 1054 (1963).

[57] K. Ramstöck, W. Hartung, A. Hubert, *Phys. Status Solidi* **155**, 505 (1996).

[58] A. E. LaBonte, *J. Appl. Phys.* **40**, 2450 (1969).

[59] E. E. Huber, D. O. Smith, J. B. Goodenough, *J. Appl. Phys.* **29**, 294 (1958).

[60] M. Redjdal, A. Kakay, M. F. Ruane, F. B. Humphrey, *J. Appl. Phys.* **91**, 7547 (2002).

[61] T. Ishida, T. Kimura, Y. Otani, *Phys. Rev. B* **74**, 014424 (2006).

[62] V. Novosad, *et al.*, *Phys. Rev. B* **72**, 024455 (2005).

[63] B. Krüger, *et al.*, *Phys. Rev. Lett.* **XX**, XXX (2007).

[64] B. Van Waeyenberge, *et al.*, *Nature* **444**, 461 (2006).

[65] Yamada, Ono, *Nature Materials* **XX**, XX (2007).

[66] E. Stoner, E. P. Wohlfarth, *Phil. Trans. Roy. Soc* **240**, 599 (1948).

[67] Laboratoire Louis Néel, Centre National de la recherche scientifique (CNRS), found at http://lab-neel.grenoble.cnrs.fr/.

[68] E. Ising, Beitrag zur Theorie des Ferro- und Paramagnetismus, Ph.D. thesis, University of Hamburg, Germany (1924).

[69] B. A. Kalinikos, A. N. Slavin, *J. Phys. C* **19**, 7013 (1986).

[70] C. Bayer, Quantisierung und Lokalisierung von Spinwellen in mikrometerbreiten magnetischen Streifen, Master's thesis, Technische Universität Kaiserslautern (2003).

[71] G. T. Rado, J. R.Weertman, *J. Phys. Chem. Solids* **11**, 315 (1959).

[72] K. Y. Guslienko, A. N. Slavin, *Phys. Rev. B* **72**, 014463 (2005).

[73] C. Herring, C. Kittel, *Phys. Rev.* **81**, 869 (1951).

[74] C. Kittel, *Phys. Rev.* **73**, 155 (1948).

[75] R. W. Damon, J. R. Eshbach, *J. Phys. Chem. Solids* **19**, 308 (1961).

[76] J. Jorzick, *et al.*, *Phys. Rev. B* **60**, 15194 (1999).

[77] Y. Roussigné, S. M. Chérif, C. Dugautier, P. Moch, *Phys. Rev. B* **63**, 134429 (2001).

[78] K. Y. Guslienko, R. W. Chantrell, A. N. Slavin, *Phys. Rev. B* **68**, 024422 (2003).

[79] P. K. L. Drude, *Annalen der Physik* **306**, 566 (1900).

[80] A. Sommerfeld, H. Bethe, *Handbuch der Physik* **24**, 333 (1932).

[81] F. C. Williams Jr., E. N. Mitchell, *Jpn. J. Appl. Phys.* **7**, 739 (1968).

[82] K. Fuchs, *Proc. Cambridge Phil. Soc.* **34**, 100 (1938).

[83] E. H. Sondheimer, *Advances in Physics* **1**, 1 (1952).

[84] A. F. Mayadas, J. F. Janak, A. Gangulee, *J. Appl. Phys.* **45**, 2780 (1974).

[85] T. G. S. M. Rijks, S. K. J. Lenczowski, R. Coehoorn, W. J. M. de Jonge, *Phys. Rev. B* **56**, 362 (1997).

[86] A. F. Mayadas, M. Shatzkes, *Phys. Rev. B* **1**, 1382 (1970).

[87] N. Mott, *Proc. R. Soc.* **153**, 699 (1936).

[88] T. Valet, A. Fert, *Phys. Rev. B* **48**, 7099 (1993).

[89] D. R. Penn, M. D. Stiles, *Phys. Rev. B* **72**, 212410 (2005).

[90] S. Dubois, *et al.*, *Phys. Rev. B* **60**, 477 (1999).

[91] L. Piraux, S. Dubois, A. Fert, L. Beliard, *Eur. Phys. J. B* **4**, 413 (1998).

[92] C. E. Moreau, I. C. Moraru, N. O. Birge, J. William P. Pratt, *Appl. Phys. Lett.* **90**, 012101 (2007).

[93] R. Gross, A. Marx, *Grundlagen der Magnetoelektronik* (Walther-Meissner-Institut, Garching, 2000).

[94] T. McGuire, R. Potter, *IEEE Trans. Mag.* **11**, 1018 (1975).

[95] I. A. Campbell, A. Fert, O. Jaoul, *J. Phys. C* **3**, S95 (1970).

[96] H. Ebert, A. Vernes, J. Banhart, *Phys. Rev. B* **54**, 8479 (1996).

[97] M. Steiner, C. Pels, G. Meier, *J. Appl. Phys.* **95**, 6759 (2004).

[98] E. B. Myers, D. C. Ralph, J. A. Katine, R. N. Louie, R. A. Buhrman, *Science* **285**, 867 (1999).

[99] Y. B. Bazaliy, B. A. Jones, S.-C. Zhang, *Phys. Rev. B* **57**, R3213 (1998).

[100] M. Kläui, *et al.*, *Appl. Phys. Lett.* **83**, 105 (2003).

[101] J. Grollier, *et al.*, *Appl. Phys. Lett.* **83**, 509 (2003).

[102] M. Tsoi, R. Fontana, S. S. P. Parkin, *Appl. Phys. Lett.* **83**, 2617 (2003).

[103] N. Vernier, D. Allwood, D. Atkinson, M. Cooke, R. Cowburn, *Europhys. Lett.* **65**, 526 (2004).

[104] M. Yamanouchi, D. Chiba, F. Matsukura, H. Ohno, *Nature* **428**, 539 (2004).

[105] M. Kläui, *et al.*, *Phys. Rev. Lett.* **95**, 026601 (2005).

[106] M. Kläui, *et al.*, *Appl. Phys. Lett.* **88**, 232507 (2006).

[107] Y. Nakatani, A. Thiaville, J. Miltat, *Nature Materials* **2**, 521 (2003).

[108] X. Waintal, M. Viret, *Europhys. Lett.* **65**, 427 (2004).

[109] H. Koo, C. Krafft, R. D. Gomez, *Appl. Phys. Lett.* **81**, 862 (2002).

[110] G. Meier, *et al.*, *Phys. Rev. Lett.* **98**, 187202 (2007).

[111] A. Yamaguchi, *et al.*, *Appl. Phys. Lett.* **86**, 012511 (2005).

[112] A. Yamaguchi, *et al.*, *Phys. Rev. Lett.* **96**, 179904 (2006).

[113] M. Laufenberg, *et al.*, *Appl. Phys. Lett.* **88**, 052507 (2006).

[114] M. Laufenberg, *et al.*, *Phys. Rev. Lett.* **97**, 046602 (2006).

[115] M. Hayashi, *et al.*, *Phys. Rev. Lett.* **96**, 197207 (2006).

[116] A. Aharoni, *J. Appl. Phys.* **83**, 3432 (1999).

[117] S. Tandona, M. Beleggia, Y. Zhu, M. D. Graef, *J. Magn. Magn. Mat.* **271**, 9 (2004).

[118] S. Tandona, M. Beleggia, Y. Zhu, M. D. Graef, *J. Magn. Magn. Mat.* **271**, 27 (2004).

[119] A. Aharoni, *J. Magn. Magn. Mat.* **203**, 33 (1999).

[120] *µMAG – Micromagnetic Modeling Activity Group* found at: http://www.ctcms.nist.gov/rdm/mumag.html.

[121] *The Object Oriented MicroMagnetic Framework (OOMMF) project at ITL/NIST* found at: http://math.nist.gov/oommf.

[122] *LLG Micromagnetics Simulator* found at: http://llgmicro.home.mindspring.com/.

[123] *MicroMagus – Software for Micromagnetic Simulations* found at: http://www.micromagus.de/.

[124] *magpar – Parallel Finite Element Micromagnetics Package* found at: http://magnet.atp.tuwien.ac.at/scholz/magpar/.

[125] *RKMAG* found at: http://www.rkmag.com/.

[126] M. Bolte, Simulation of Micromagnetic Structure - Optimization and Extension of a Micromagnetic Simulation Tool, Master's thesis, University of Hamburg, Department of Physics (2004).

[127] http://www.mathworks.com/products/matlab.

[128] J. Fidler, T. Schrefl, *J. Phys. D: Appl. Phys.* **33**, R135 (2000).

[129] W. Scholz, Micromagnetic Simulation of Thermally Activated Switching in Fine Particles, Master's thesis, Institut für Angewandte und Technische Physik, Technische Universität Wien (1999).

[130] M. J. Donahue, R. D. McMichael, *Physica B* **233**, 272 (1996).

[131] C. J. García-Cervera, Z. Gimbutas, W. E, *J. Comp. Phys.* **184**, 37 (2003).

[132] M. Donahue, R. McMichael, *Magnetics, IEEE Transactions on* **43**, 2878 (2007).

[133] W. H. Press, S. A. Teukolsky, W. T. Vetterling, *Numerical Recipes in C: The Art of Scientific Computing* (Cambridge University Press, 1993).

[134] R. Hertel, *Z. f. Metallkunde* **93**, 957 (2002).

[135] X.-P. Wang, C. J. García-Cervera, W.E, *J. Comp. Phys.* **171**, 357 (2001).

[136] L. Lopez-Diaz, J. Eicke, E. Della Torre, *IEEE Trans. Magn.* **35**, 1207 (1999).

[137] E. Martínez, L. López-Díaz, L. Torres, C. J. García-Cervera, *J. Phys. D: Appl. Phys.* **40**, 942 (2007).

[138] M. Barthelmeß, A. Thieme, R. Eiselt, G. Meier, *J. Appl. Phys.* **93** (2003).

[139] M. Barthelmeß, C. Pels, A. Thieme, G. Meier, *J. Appl. Phys.* **95** (2004).

[140] Y. S. Huang, C. C. Wang, A. O. Adeyeye, *J. Appl. Phys.* **100**, 013909 (2006).

[141] E. D. Dahlberg, R. Proksch, *J. Magn. Magn. Mat.* **200**, 720 (1999).

[142] M. R. Freeman, B. C. Choi, *Science* **294**, 1484 (2001).

[143] T. Eimüller, Magnetic Imaging of Nanostructured Systems with Transmission X-ray Microscopy, Ph.D. thesis, Bayerische Julius-Maximillians-Universität Würzburg, Germany (2002).

[144] nanoscience instruments,*team nanotec hr-mfm75 magnetic force mode probes*, found at: http://store.nanoscience.com/.

[145] J. Lohau, S. Kirsch, A. Carl, G. Dumpich, E. Wassermann, *J. Appl. Phys.* **86** (1999).

[146] R. Engel-Herbert, D. M. Schaadt, T. Hesjedal, *J. Appl. Phys.* **99**, 113905 (2006).

[147] Y. Martin, H. K. Wickramasinghe, *Appl. Phys. Lett.* **50**, 1455 (1987).

[148] C. B. Prater, P. G. Maivald, K. J. Kjoller, M. G. Heaton, Tapping mode^{TM} imaging: Applications and technology, application notes, *Tech. rep.*, Digital Instruments (1995).

[149] J. M. García, *et al.*, *Appl. Phys. Lett.* **79**, 656 (2001).

[150] G. Meier, *et al.*, *Appl. Phys. Lett.* **85**, 1193 (2004).

[151] M. Bolte, R. Eiselt, T. Eimüller, P. Fischer, G. Meier, *J. Magn. Magn. Mat.* **290-291**, 723 (2005).

[152] C. Pels, M. Barthelmeß, M. Bolte, A. Thieme, G. Meier, *J. Magn. Magn. Mat.* **293** (2005).

[153] H. Ebert, *Rep. Prog. Phys.* **59**, 1665 (1996).

[154] G. Schütz, *et al.*, *Phys. Rev. Lett.* **58**, 737 (1984).

[155] P.Fischer, G.Schütz, G.Schmahl, P.Guttmann, D.Raasch, *Z. f. Phys. B* **101**, 313 (1996).

[156] B. T. Thole, P. Carra, F. Sette, G. van der Laan, *Phys. Rev. Lett.* **68**, 1943 (1992).

[157] J. Vogel, *et al.*, *J. Magn. Magn. Mat.* **165**, 96 (1997).

[158] H. Ohldag, *et al.*, *Phys. Rev. Lett.* **87**, 7201 (2001).

[159] J. Stöhr, *et al.*, *Phys. Rev. Lett.* **83**, 1862 (1999).

[160] F. Nolting, *et al.*, *Nature* **405**, 767 (2000).

[161] P. Fischer, *et al.*, *J. Appl. Phys.* **89** (2001).

[162] P. Fischer, *et al.*, *Rev. Sci. Instr.* **72** (2001).

[163] W. Chao, B. D. Harteneck, J. A. Liddle, E. H. Anderson, D. T. Attwood, *Nature* **435**, 1210 (2005).

[164] R. D. McMichael, M. J. Donahue, *IEEE Trans. Magn.* **33**, 4167 (1997).

[165] M. Kläui, *et al.*, *Appl. Phys. Lett.* **85**, 5637 (2004).

[166] Y. Nakatani, A. Thiaville, J. Miltat, *J. Magn. Magn. Mater.* **290**, 750 (2005).

[167] M. H. Park, *et al.*, *Phys. Rev. B* **73**, 094424 (2006).

[168] M. Kläui, C. A. F. Vaz, L. Lopez-Diaz, J. A. C. Bland, *J. Phys.: Condens. Matter* **15**, R985 (2003).

[169] M. Bolte, R. Eiselt, G. Meier, D.-H. Kim, P. Fischer, *J. Appl. Phys.* **99**, 08H301 (2006).

[170] L. F. Zhang, C. Xua, P. M. Hui, Y. Q. Ma, *J. Appl. Phys.* **97**, 103912 (2005).

[171] A. Krasyuk, *et al.*, *Physical Review Letters* **95**, 207201 (2005).

[172] M. Bolte, G. Meier, C. Bayer, *Phys. Rev. B* **73**, 052406 (2006).

[173] K.-D. Kammeyer, K. Kroschel, *Digitale Signalverarbeitung. Filterung und Spektralanalyse mit MATLAB-Übungen, 6th Edition* (Teubner Verlag, Wiesbaden, Germany, 2006).

[174] B. Heinrich, *et al.*, *Phys. Rev. Lett.* **59**, 1756 (1987).

[175] K. Perzlmaier, *et al.*, *Physical Review Letters* **94**, 057202 (2005).

[176] M. Buess, *et al.*, *Phys. Rev. Lett.* **93**, 077207 (2004).

[177] K. Y. Guslienko, X. F. Han, D. J. Keavney, R. Divan, S. D. Bader, *Phys. Rev. Lett.* **96**, 067205 (2006).

[178] H. Stoll, *et al.*, *Appl. Phys. Lett.* **84**, 3328 (2004).

[179] V. E. Demidov, S. O. Demokritov, B. Hillebrands, M. Laufenberg, P. P. Freitas, *Appl. Phys. Lett.* **85**, 2866 (2004).

[180] M. Bolte, G. Meier, C. Bayer, *J. Magn. Magn. Mat.* **316**, e526–e528 (2007).

[181] L. Vila, L. Piraux, J. M. George, G. Faini, *Appl. Phys. Lett.* **80**, 3805 (2002).

[182] T. Haug, A. Vogl, J. Zweck, C. H. Back, *Appl. Phys. Lett.* **88**, 082506 (2006).

[183] M. Steiner, Micromagnetism and Electrical Resistance of Ferromagnetic Electrodes for Spin-Injection Devices, Ph.D. thesis, University of Hamburg, Germany (2004).

[184] E. Saitoh, H. Miyajima, T. Yamaoka, G. Tatara, *Nature* **432**, 203 (2004).

[185] L. Thomas, *et al.*, *Nature* **443**, 197 (2006).

[186] M. Hayashi, *et al.*, *Phys. Rev. Lett.* **98**, 037204 (2007).

[187] J. A. Katine, F. J. Albert, R. A. Buhrman, E. B. Myers, D. C. Ralph, *Phys. Rev. Lett.* **84**, 3149 (2000).

[188] I. N. Krivorotov, *et al.*, *Science* **307**, 228 (2005).

[189] D. A. Allwood, *et al.*, *Science* **296**, 2003 (2002).

[190] R. P. Cowburn, *Patent Application* **309**, WO002004077451A1 (2004).

[191] B. Krüger, Current-Induced Domain-Wall Dynamics in Ferromagnetic Nanowires, Master's thesis, I. Institute of Theoretical Physics, University of Hamburg (2006).

[192] K. Shigeto, T. Okuno, K. Mibu, T. Shinjo, T. Ono, *Appl. Phys. Lett.* **80**, 4190 (2002).

[193] T. Shinjo, T. Okuno, R. Hassdorf, K. Shigeto, T. Ono, *Science* **289**, 930 (2000).

[194] A. Wachowiak, *et al.*, *Science* **298**, 577 (2002).

[195] J. Shibata, Y. Nakatani, G. Tatara, H. Kohno, Y. Otani, *Phys. Rev. B* **73**, 020403 (R) (2006).

[196] S.-B. Choe, *et al.*, *Science* **304**, 420 (2004).

[197] B. E. Argyle, E. Terrenzio, J. C. Slonczewski, *Phys. Rev. Lett.* **53**, 190 (1984).

[198] S. Kasai, Y. Nakatani, K. Kobayashi, H. Kohno, T. Ono, *Phys. Rev. Lett.* **97**, 107204 (2006).

[199] R. Hertel, C. M. Schneider, *Phys. Rev. Lett.* **97**, 177202 (2006).

[200] R. Hertel, S. Gliga, M. Fähnle, C. M. Schneider, *Phys. Rev. Lett.* **98**, 117201 (2007).

[201] J.-G. Caputo, Y. Gaididei, F. G. Mertens, D. D. Sheka, *Phys. Rev. Lett.* **98**, 056604 (2007).

[202] O. A. Tretiakov, O. Tchernyshyov, *Phys. Rev. B* **75**, 012408 (2007).

[203] D. D. Sheka, Y. Gaididei, F. G. Mertens, *condmat* **0706**, 3172 (2007).

Acknowledgements

This thesis was made at the *Institute of Applied Physics and Center for Microstructure Research* at the University of Hamburg in the research group of Professor Dr. Ulrich Merkt. Many people have contributed to this thesis. I have tried to fairly acknowledge the scientific contributions of the resepective individuals and groups in the corresponding sections. However, since there is so much more to the past three years of my life than science, I wish to thank
– Professor Dr. Ulrich Merkt. His concern, support and sacrifice for his students and staff is an example that hopefully will stay with me for the rest of my life. I wish to thank him for the meticulous reading of all my manuscripts, for raising the bar of expected performance, for helping to make ends meet for the young father of a large family, and for always taking time for me. He is in all respects worthy to be called a "Doktorvater". Thank you!
– Prof. Dr.-Ing. Dietmar P. F. Möller for his support and for encouraging me in all computer science related issues, for his enthusiasm for the work and the trust he always extended toward me.
– PD Dr. Guido Meier for so many things. First of all for being the best boss one could think of – open, approachable, fun-loving, and supportive. Thank you for the countless hours of explaining, discussing, and talking, also during beam times. Thank you for our friendship and for letting me be your PHA!
– Dr. René Eiselt for the many hours that we spent together during beam time, for his accuracy, dependability, honesty, and friendship.
– Benjamin Krüger for his patience in explaining to me the "simple and straight-forward" approximations used in the analytic description of domain-wall and vortex dynamics. I've come to deeply respect and trust him.
– Massoud Najafi for his experience in software engineering, his great job in writing his Matlab simulation code in only six months, and for calling upon me whenever he felt he needed to – even on weekends ;-).
– André Drews for his great enthusiasm for the work and his deep interest in so many things. I've come to appreciate his optimism and sensitive way.

– Bernd Güde for his support for our ’Simulation group’ and his nifty sense of humor.
– Stellan Bohlens for the great work he does and the many ’Franzbrötchen’.
– Dr. Christian Pels, Dr. Peter Baars, Dr. Marcus Steiner, Dr. Christopher Schierholz, Dr. Alexander van Staa, and Dr. Sebastian von Oehsen for their example in going before me and for keeping the group’s working atmosphere on a high fun level.
– Jan Podbielski for his many unannounced visits and the subsequent discussions that have always increased my understanding on spin waves. That caused me to to twist my fingers trying to match the magnetization vectors in rings ;-). I also thank him for the off-topic discussions and wish him all the best for his future.
– PD Dr. Peter Fischer, Dr. Dong-Hyun Kim, and their families for the support during beam times that caused them to spend many late-night hours away from their families,
– Dr. Hermann Stoll, Dr. Bartel Van Waeyenberge, Dr. Aleksandar Puzic, Kang Wei Chou, and Dennis Dolgos for the excellent and successful collaboration in the past almost two years at the STXM beam line and for the fruitful discussions about phases, chiralities and the like ;-)
– Dr. Christian Bayer who has an excellent gift of relating complex matters to normal mortals in ways they can understand. I thank him for the many in-depth discussions, but even more so for his kind and respectful character. I thank Professor Dr. B. Hillebrands for sharing his expertise with me and for supporting me in my academic career.
– Dr. Alexander Krasyuk for the good collaboration that extended far beyond mutual scientific benefit into the private life. I wish him and his family all the best. I also wish to thank Professor Dr. G. Schönhense, Professor Dr. H. J. Elmers, and Dr. S. A. Nepijko for the friendly discussions.
– Professor Dr. C. M. Schneider for being so approachable and friendly towards an unknown graduate student and everybody else.
– Dr. Mathias Kläui for many open and friendly discussions at conferences and for sharing with me his insight and expertise in many areas.
– Alex Thieme for writing the MFM code for OOMMF.
– Petra Roth, Carola Tenge, Barbara Truppe, and Andrea Beese for handling all the administrative work in such a professional way.
– The DFG for financial support via the Sonderforschungsbereich SFB 508 "Quantenmaterialien" and the Graduiertenkolleg "Functional Metal-Semiconductor Hybrid Systems".
– My parents for their continual love and support and for laying the foundations of what I am today.
– My wonderful wife and children who are my source of joy and happiness and make all the efforts worthwhile.